Machine Learning Applications in Spacecraft State and Environment Estimation

by

Srinagesh Sharma

A dissertation submitted in partial fulfillment
of the requirements for the degree of
Doctor of Philosophy
(Electrical Engineering:Systems)
in The University of Michigan
2018

Doctoral Committee:

Associate Professor James W. Cutler, Co-Chair
Associate Professor Clayton Scott, Co-Chair
Professor Brian Gilchrist
Professor Mark B. Moldwin

Srinagesh Sharma

srinag@umich.edu

ORCID iD: 0000-0001-5760-4161

Dedicated to my grandmother, Mahalakshmi Subbarao.

ACKNOWLEDGEMENTS

Doctoral work rarely, if ever, stands in isolation. It is the result of the presence of a strong ecosystem of support critical to the candidate. I would like to mention a few of the people to who made this thesis possible.

I would like to express my deep gratitude to my advisors Prof. James Cutler and Prof. Clayton Scott. Prof. Cutler, without your support, guidance, inspiration and your sense of possibility, this work would not exist. Thank you for providing me with understanding and insight on conceptualizing and executing research. I have also received an invaluable education on the design and engineering of systems to satisfy the lofty standards of space missions. Prof. Scott, thank you for your advice and for providing constructive and valuable feedback on research and on machine learning. I will forever strive to uphold the standards of thoroughness in research that you have set.

I would also like to thank the rest of my committee members, Prof. Brin Gilchrist and Prof. Mark Moldwin. Prof. Gilchrist, thank you for taking me in as your PhD student for the first four years and for providing feedback on my work whenever I needed it. Prof. Moldwin, thank you for your support and guidance on research.

I thank Sam Dolinar and John Hamkins from the information processing group at NASA JPL for their support and encouragement in the development of the orbit determination work as part of the Strategic University Research Partnership (SURP). I would also like to thank the various people involved with the development of the spacecraft missions that formed part of my research: MCubed-2, GRIFEX, CADRE and TBEx.

I would like to thank three generations of MXLers: Dan Spatcher, Prince Kuevor, Nathanael England, Daniel Gu, Joseph Yates, Tyler Rose, So-hee Kang, Charlie Rose, Kaitlyn Burke, Anton Frolenkov, Daniel Meinzer, Mike Mistaleski, Scott Tripp and many others. MXL has a unique culture of teamwork that has enabled me to learn a lot.

I thank my collaborators and colleagues: Aniket Deshmukh, Dae Young Lee, Rohit Gupta, Ehsan Taheri, Ben Kempke, Leonardo Regoli, Alex Walsh and Alexander Thuro. Aniket, our arguments on mathematics and machine learning have helped me hone my skills. Ehsan and Rohit, thank you for helping me understand dynamics and the fundamentals of differential geometry. Leonardo and Alex, thank you for your help with the magnetometer experiments.

I thank Raj Tejas Suryaprakash, Maruthi Ravichandran, Megha Acharya, Karthik Shivaram, Manu Akula, Chaitanya Garikipathi for some great times in Ann Arbor. Raj, thank you for the advice on research and for the truly awesome times. You have been an amazing roommate. I would like to thank Navaneeth Garakahalli, Swathi Gurudutt and Malini Rao. Navaneeth and Swathi, thank you for the time in Seattle. Malini, thank you for making it a point to meet me every time you can.

I thank my Uncle and Aunt, Raju and Vie Narasimhan for all your help and advice over the years. My breaks in the upper peninsula always resulted in breakthroughs in my research.

I would like to thank my parents and my brother. To my parents, Raghunath and Hema, thank you for your constant encouragement and support through my many years of study. To my brother, Sumukh, thank you for the fun conversations we had over the years.

Most importantly, I would like to thank my wife, Shreya, for her constant love, support and encouragement, without which this journey would have ended prematurely.

TABLE OF CONTENTS

DEDICATION ii

ACKNOWLEDGEMENTS iii

LIST OF TABLES viii

LIST OF FIGURES x

LIST OF APPENDICES xiii

ABSTRACT xv

CHAPTER

I Introduction 1

I.0.1 Orbit Determination 1

I.0.2 Magnetometer Interference Cancellation 3

I.1 Literature Review 4

I.1.1 Orbit Determination 5

I.1.2 Ground Station Network Architectures 6

I.1.3 Magnetometer Interference Cancellation 7

I.2 Thesis Statement 8

I.3 Proposed Approach 8

I.3.1 Orbit Determination 9

I.3.2 Network Architecture . . . 10
I.3.3 Magnetometer Interference Cancellation . . . 10
I.4 Contributions . . . 11
I.5 Dissertation Outline . . . 12

II Kernel Embedding Approach to Orbit Determination of Spacecraft Clusters 13

II.1 Introduction . . . 13
II.2 Orbit Determination as a Learning Problem . . . 15
II.2.1 OD Problem Setting . . . 15
II.2.2 Observability . . . 18
II.2.3 Machine Learning Setting . . . 19
II.3 Algorithm . . . 21
II.4 Learning Theory . . . 26
II.5 Results and Discussion . . . 28
II.5.1 System Architecture . . . 29
II.5.2 Doppler-Only OD . . . 31
II.5.3 Position Based OD . . . 40
II.5.4 Position Based OD - Lunar Orbit . . . 43
II.5.5 Position based OD - Comparison with EKF . . . 47
II.5.6 Discussion . . . 49
II.6 Conclusion . . . 51

III Collaborative Orbit Determination using Ground Station Networks 52

III.1 Introduction . . . 52
III.2 Parameters of Architecture . . . 53
III.2.1 Architecture Requirements for Orbit Determination . . . 56
III.3 Network Architecture . . . 58

III.3.1 Global Architecture . . . 58
III.3.2 Node Architecture . . . 60
III.4 Scheduling and Tracking . . . 62
III.4.1 Pointing Profiles . . . 64
III.5 Training Data Generation . . . 70
III.5.1 Orbit Distribution Selection . . . 71
III.5.2 Noise Distribution . . . 72
III.6 Results and Discussion . . . 73
III.6.1 Scenario 1: Simple Static Profiles . . . 73
III.6.2 Scenario 2: Complex Static Profiles . . . 77
III.6.3 Scenario 3: Dynamic Profile . . . 80
III.7 Conclusion . . . 81

IV Spacecraft Magnetometer Interference Cancellation 82
IV.1 Introduction . . . 82
IV.2 Spacecraft Magnetic Field Model . . . 85
IV.3 Interference Cancellation . . . 87
IV.4 Machine Learning Setting . . . 91
IV.4.1 A Contextual Bandit Problem . . . 93
IV.5 Algorithm . . . 93
IV.6 Learning Theoretic Analysis . . . 96
IV.7 Results and Discussion . . . 98
IV.7.1 Multi-class Classification . . . 99
IV.7.2 Experimental Spacecraft Magnetic Field Dataset . . . 100
IV.8 Conclusion . . . 110

V Conclusion and Future Work 111

Appendices 115

Bibliography **172**

LIST OF TABLES

TABLE

2.1 Two Line Element Parameters of the GRIFEX spacecraft. 36

2.2 Keplerian elements of the MCubed-2 spacecraft. 39

2.3 Classification error comparison. 43

2.4 Comparison of test errors 51

3.1 GSN Scheduling - Complex Static Profile 79

4.1 Statistics of interference 106

LIST OF FIGURES

FIGURE

1.1 TBEx Small Satellite with Multiple Magnetometers [1, 2] 11

2.1 System Architecture 32
2.2 MCubed-2 Raw RF Baseband Recordings from 02-10-2016 at 01:20:24 UTC 34
2.3 Doppler and Time feature vectors compared with Doppler from TLE Predicted Orbit post bias correction 35
2.4 Normalized errors of orbital parameters of test orbits based on GRIFEX Priors 37
2.5 RSW errors of test orbits based on GRIFEX Priors 37
2.6 Normalized errors of orbital parameters of test orbits based on MCubed-2 Priors 39
2.7 RSW Position Errors of test orbits based on MCubed-2 Priors 40
2.8 Deployment cones of spacecraft 1 & 2 41
2.9 Normalized errors of orbital parameters of test orbits of spacecraft 1 44
2.10 Normalized errors of orbital parameters of test orbits of spacecraft 2 45
2.11 Example lunar transfer orbits drawn from prior distribution 46
2.12 Normalized errors of orbital parameters of test orbits for trans-lunar scenario 47
2.13 Comparison of EKF and Learning Based OD 49

3.1 Global architecture 60
3.2 ASGS architecture 62
3.3 ODTrack Session 63

3.4 Antenna ellipsoid approximation and spherical cap 65
3.5 Selected ground stations and samples of initial position of the cluster based on P_Γ 74
3.6 Deploy cones of satellites from deployer 74
3.7 Directions of arrival corresponding to Doppler data observed by directional antennas 75
3.8 Simple static allocation: distribution of test data position error for satellite 1 76
3.9 Simple static allocation: distribution of test data velocity error for satellite 1 76
3.10 Simple static allocation: distribution of test data position error for satellite 2 76
3.11 Simple static allocation: distribution of test data velocity error for satellite 2 76
3.12 Simple static allocation: distribution of test data position error for satellite 3 76
3.13 Simple static allocation: distribution of test data velocity error for satellite 3 76
3.14 Simple static allocation: distribution of test data position error for satellite 4 77
3.15 Simple static allocation: distribution of test data velocity error for satellite 4 77
3.16 Complex static allocation: distribution of test data position error 79
3.17 Complex static allocation: distribution of test data velocity error 79
3.18 Dynamic allocation: distribution of test data position error 81
3.19 Dynamic allocation: distribution of test data velocity error 81

4.1 Simple regret evaluation of multi-class datasets 100
4.2 The GRIFEX CubeSat and the experimental setup for data generation, GRIFEX telemetry and additional subsystem modeled data was fed into the coils to generate interference 102
4.3 Simple regret of direct sensor selection with and without on-orbit modifications 103
4.4 Histogram of magnetic field interference from experimental setup 106
4.5 Evaluation of simple regret minimization with sensor combinations - with on-orbit dataset modification 107

4.6 Evaluation of simple regret minimization with sensor combinations - without on-orbit dataset modification 107
4.7 Time series of magnitude of magnetic field interference 108
4.8 Telemetry used in experimental setup 109

A.1 Example scenario dynamical system and measurements 127

C.1 Simple regret evaluation with $\beta = 0.1$ 165
C.2 Simple regret evaluation with $\beta = 0.5$ 166
C.3 Simple regret evaluation with $\beta = 2$ 167
C.4 Simple regret for Contextual Gap with History of 25 points 168
C.5 Time series of magnetic field interference - X direction 169
C.6 Time series of magnetic field interference - Y direction 170
C.7 Time series of magnetic field interference - Z direction 171

LIST OF APPENDICES

APPENDIX

A Appendix for Chapter 2 **115**

A.1 Background for Orbit Determination 115

A.1.1 Dynamical System 115

A.1.2 Sets and Probability 117

A.1.3 Recent Techniques from Machine Learning 118

A.2 Orbit Determination Problem Setting 123

A.3 Observability Analysis 127

A.4 Proofs for Theorems in Appendix A.3 133

A.4.1 Proof of Theorem A.1 134

A.4.2 Proof of Theorem A.2 135

A.4.3 Proof of Corollary A.1 137

A.5 Learning Theory 138

A.6 Analysis for Appendix A.5 141

A.6.1 Useful Theorems 143

A.6.2 Analysis of A_h and T_h 144

A.6.3 Proof of Theorem A.3 149

B Appendix for Chapter 3 **155**

B.1 Algorithms for Tracking 155

C Appendix for Chapter 4 **159**

C.1 Calibration of Combined Magnetometer Measurements 159

C.2 Decomposition of Loss 163

C.3 Additional Experimental Results 164

ABSTRACT

There are some problems in spacecraft systems engineering with highly non-linear characteristics and noise where traditional non-linear estimation techniques fail to yield accurate results. In this thesis, we consider approaching two such problems using kernel methods in machine learning. First, we present a novel formulation and solution to orbit determination of spacecraft and spacecraft groups which can be applied with very weakly observable and highly noisy scenarios. We present a ground station network architecture that can perform orbit determination using Doppler-only observations over the network. Second, we present a machine learning solution to the spacecraft magnetic field interference cancellation problem using distributed magnetometers paving the way for space magnetometry with boom-less CubeSats.

We present an approach to orbit determination under very broad conditions that are satisfied for n-body problems. We show that domain generalization and distribution regression techniques can learn to estimate orbits of a group of satellites and identify individual satellites especially with prior understanding of correlations between orbits and provide asymptotic convergence conditions. The approach presented requires only observability of the dynamical system and visibility of the spacecraft and is particularly useful for autonomous spacecraft operations using low-cost ground stations or sensors. With the absence of linear region constraints in the proposed method, we are able to identify orbits that are 800 km apart and reduce orbit uncertainty by 92.5% to under 60 km with noisy Doppler-only measurements.

We present an architecture for collaborative orbit determination using networked ground stations. We focus on clusters of satellites deployed in low Earth orbit and measurements of their Doppler-shifted transmissions made by low-gain antenna systems in a software-defined federated ground station network. We develop a network architecture enabling scheduling and tracking with uncertain orbit information. For the proposed network, we also present scheduling and coordinated tracking algorithms for tracking with the purpose of generating measurements for orbit determination. We validate our algorithms and architecture with its application to high fidelity simulations of different networked orbit determination scenarios. We demonstrate how these low-cost ground stations can be used to provide accurate and timely orbital tracking information for large satellite deployments, which is something that remains a challenge for current tracking systems.

Last, we present a novel approach and algorithm to the problem of magnetic field interference cancellation of time-varying interference using distributed magnetometers and spacecraft telemetry with particular emphasis on the computational and power requirements of CubeSats. The spacecraft magnetic field interference cancellation problem involves estimation of noise when the number of interfering sources far exceed the number of sensors required to decouple the noise from the signal. The proposed approach models this as a contextual bandit learning problem and the proposed algorithm learns to identify the optimal low-noise combination of distributed magnetometers based on indirect information gained on spacecraft currents through telemetry. Experimental results based on on-orbit spacecraft telemetry shows a 50% reduction in interference compared to the best magnetometer.

CHAPTER I

Introduction

Over the past two decades, the development of Pico and Nano-satellite technologies have drastically reduced cost and improved access to space providing platforms for low-cost space science and exploration [3, 4]. By the very nature of the environments in which these spacecraft operate, there are many problems in space systems with elusive solutions due to non-linearity, weak-observability, noise, under-determined behavior etc. This thesis focuses on two such problems - orbit determination and spacecraft noise environment estimation, and provides learning theoretic solutions to those problems.

I.0.1 Orbit Determination

Lower-cost access to space has enabled space missions consisting of numerous high-risk, low-cost spacecraft systems to be deployed near simultaneously in large numbers in orbits ranging from low Earth to deep space [5, 6, 7, 8]. Requirements for successful and efficient mission operations for such growing numbers of spacecrafts have led to the development of ground station networks with widely varying communications and costs [9, 10, 11]. Use of these networks for autonomous orbit determination would enhance the operational capability, improve usefulness, and potentially lower the cost of these new missions.

Existing orbit determination techniques provide accurate results, but have requirements particularly cumbersome for small spacecraft and passive objects that have high initial position uncertainty. Current *cooperative* measurements (or observations) use transponders or GPS receivers on spacecraft with orbit state estimation and refinement computed through initial orbit determination approaches and Kalman filters [12, 13]. However, transponder-based state estimation requires position uncertainty low enough to overcome link budget constraints which implies low initial uncertainty in spacecraft position, while GPS receivers only work near Earth. In addition, a number of Earth orbiting satellites lack direct navigation capabilities due to absence of GPS systems or transponders [14]. Meanwhile, *uncooperative* measurements such as radar and optical sitings also have requirements of low initial uncertainty and resolvability which limit their use to near Earth orbits. It would be useful to remove these above constraints, where just visibility of transmissions and identifiability of the state through such transmissions are the only required criteria.

Two additional important and difficult orbit determination needs are for near-Earth orbital debris and general tracking of celestial objects. Large numbers of short life-cycle deployments have resulted in slow decaying space debris whose tracking is critical for avoidance and mission survival [15, 16, 17, 18, 19].

Due to the large and growing number of debris objects, algorithms for autonomous tracking using varied, statistically independent and spatially distributed sets of observations would improve our space situational awareness. Tracking of celestial objects, such asteroids, have different observational characteristics and observations are available only over short sections of the trajectory.

We also consider the development of a network architecture for orbit determination. An *architecture* of a ground station network (GSN) consists of the physical layer abstractions, scheduling and tracking algorithms for tracking and operating a satellite using a network of ground stations. In this work, we consider the problem of constructing a ground station

network architecture to perform orbit determination as part of mission operations. We are interested in a GSN architecture to observe transmissions from a group or cluster of satellites when their initial orbital parameters are *uncertain* and belong to a *set* instead of being known with high accuracy.

The development of an architecture for orbit determination is a significant step towards achieving autonomous spacecraft operations, particularly for launch and early operations and for lost spacecraft tracking. For current ground station networks, scheduling and operations begin with the availability of a low uncertainty spacecraft state or orbit. This initial spacecraft orbit may be obtained through the deployment state of the upper stage, through two line elements generated by the Joint Space Operations Center [20, 21] and the capability to estimate the orbit when the orbit uncertainty is large is not part the network. We consider network architectures with the aim of extending scheduling and operational stages to include initial orbit determination using ground station networks.

I.0.2 Magnetometer Interference Cancellation

Spacecraft noise environment estimation has received recent interest in space magnetometry for analysis and understanding of space weather. Magnetic field measurements form important source of observations for space science, navigation and monitoring resulting in a recurring series of space missions for geomagnetic and interplanetary magnetic field analysis over the past half century [22, 23, 24, 25, 26, 27, 28]. Magnetic field measurements using satellites are affected by time varying interference generated by the spacecraft electrical environment. Historically, with large spacecraft, such noise was minimized by physically separating the sensor from the spacecraft using a rigid boom [29, 30, 27].

Due to ease of access to space, CubeSats have become popular as a high-risk low-cost alternative to space science measurements [4]. However, in such highly resource-constrained

satellites such as nano-satellites, there are additional challenges to space science magnetometry. First, structural constraints limit the construction, deployment, and use of long rigid booms, requiring sensors to be close to or inside the CubeSat. Second, for CubeSats with multiple magnetic sensors (magnetometers), there is the additional complexity of accessibility of sensor readings. Sensitive low noise magnetometers are influenced by the time-varying on-orbit environmental factors, such as temperature, radiation, spacecraft interference, requiring recurring calibration on-orbit. Such calibration procedures are computationally expensive, and as a consequence power constrained, limiting the number of sensors that can be calibrated at a measurement time step. Third, with distributed magnetometers or shortened booms, the measurements are affected by time-varying currents in the spacecraft that change based on different operational events such as data transmission, spacecraft maneuvers, power generation, etc.

There is a need for methods to mitigate spacecraft magnetic field interference in the CubeSat setting where the spacecraft are developed with low magnetic cleanliness, realistic sensors and with CubeSat computational constraints.

I.1 Literature Review

As described in the preceding section, there exist challenges in orbit determination and interference cancellation due to non-linearity and noise. Orbit determination and magnetic field analysis has been of interest since the very beginning of space exploration. For orbit determination, this historical development has resulted in a set of standard techniques that are applied to observation of cooperative and uncooperative measurements. For spacecraft magnetometry, while most historical literature has focused on magnetometry with large spacecraft, there has been recent interest in interference mitigation both due to the sensitivity and accuracy requirements for space science and due to a desire to use CubeSats for space

science analysis. These methods in literature are detailed below. The literature associated with the machine learning solutions can be found in the respective chapters.

I.1.1 Orbit Determination

The orbit determination problem is typically treated as a non-linear filtering problem where it is possible to use successive prediction-correction to estimate state vectors when the observations allow for good initial estimates [31, 32, 13, 33]. The standard technique for precision orbit determination is the extended Kalman filter (EKF) [31, 12, 32]. The EKF is a sub-optimal approximation of the Kalman filter for non-linear systems, which has been shown to converge asymptotically when the initial state of the system is in the linear region [34]. Batch processing with equivalent Gauss-Newton methods are also used [35].

A second popular approach is using Bayesian and particle filtering approaches for orbit determination [33], where a likelihood-conjugate prior distribution assumption is made regarding the filter parameters. In some approaches proposed by Lee [33], kernel methods are also used in particle filtering. However, the dynamical models are still linearized and EKF-based. There has been recent interest in developing methods for initial orbit determination using Gaussian mixture models [36, 37], where the distribution generated can be used as a prior distribution in developing a Gaussian mixture approximation of the batch least squares approach [36].

Unfortunately, when the observations have significant noise variances or the system is highly non-linear, successful initialization of non-linear filters may not be possible, such as with Doppler-only orbit determination. To the best of our knowledge, there exists no method to initialize filters through Doppler-only observations (Wright [13] concurs).

For celestial object tracking, short arc methods have become popular [38, 39, 40], where

individual orbital elements are computed based on analytic expressions of the orbit or by using genetic algorithms. Milani et. al [38, 41] restrict parts of initial conditions to an admissible region of orbits for very short arcs in which identification is feasible and use Delauney triangulations to compute the orbital parameters.

Current approaches to tracking and identifying debris are *uncooperative*, and are more complex than those for functional spacecraft, and due to maintaining identifiability, short arc methods are also used [42, 17, 43].

I.1.2 Ground Station Network Architectures

Ground station network architectures have been of particular interest over the past quarter century beginning with the design and development of the Deep Space Network (See [44] and the DESCANSO series for detailed descriptions of the DSN), the Air Force Satellite Control Network (AFSCN [45]) and ESTRACK [46, 47]. Increased access to space for commercial operations and educational institutions lead to newer ground station networks and network architectures [9, 48, 49, 50, 51, 52, 53, 54]. The standard ground station network subsystems required for operations and navigation consists of a set of N ground nodes which communicate through the network to a network operations and control (NOC) and Navigational subsystems for tracking [44, 55, 11]. The nodes have signal processing for telemetry, tracking systems (two way locked Doppler measurements, Delta-DOR, ranging etc.) and communication. The network is synchronized with a timing system such as GPS. Orbit determination and tracking is performed in ground station networks only when the uncertainty in the orbit of the satellite is small enough for locked tracking. A second system is required to provide this low uncertainty estimate of the orbit to the ground station network.

Scheduling and tracking algorithms form a second domain of research of spacecraft operations with networks. Over the past two decades, there has been analysis and develop-

ment of algorithms in single satellite scheduling [56, 45, 57, 53], multiple satellite scheduling [58, 59, 60] and on multiple satellite scheduling through inter-satellite communication links [61, 62]. The scheduling algorithms range from linear programming solutions to maximize data down-links [58, 57], genetic algorithm approaches [60], greedy algorithm approaches [45, 58] and probabilistic analyses [53].

I.1.3 Magnetometer Interference Cancellation

Due to the structural and noise constraints, methods for CubeSat magnetometry has shifted focus to shielding, usage of shorter booms, analysis using single and multiple sensors either on or near the spacecraft to estimate spacecraft noise behavior, and to choose either a sensor or a combination of sensors with minimum spacecraft magnetic field interference [30, 63, 64, 65].

Methods for magnetometer calibration and interference mitigation can be broadly classified into two areas of science measurements with large spacecraft and spacecraft attitude control. For science measurement, there are a variety of approaches to time-varying non-orthogonality corrections and spacecraft maneuver corrections for shielded spacecraft or spacecraft with a boom [66, 67, 68] and the second involves magnetometer calibration for spacecraft attitude control [69, 64, 70, 71, 65]. Leinweber [66] performs and updates detailed approaches for magnetometer error modeling (offsets, non-orthogonality, spin calibration, calibration using an EDI etc) but do not consider time-varying spacecraft interference. Recent work by Bromund et. al [72] builds on [66] and takes temperature calibration into account for magnetometer calibration.

Sheinker and Moldwin [30] present adaptive calibration with no reference magnetic field but under the assumption that the interference in one magnetometer is C times the interference of the other, for some constant C and assume independent and identically distributed noise behavior and calibrated sensors.

Crassidis et. al and Foster [65, 69] perform magnetometer calibration by considering only magnitude variations and compute non-linear least squares estimates. Springmann and Cutler [64] extend this approach to include time-varying bias from spacecraft currents and apply it to RAX spacecraft data [73]. They model significant current effects assuming a linear interference variation with dominant currents in the spacecraft and perform on-orbit calibration using a reference magnetic field (IGRF). They also assume that the interference is independent and identically distributed.

I.2 Thesis Statement

We propose solutions to the problems detailed in the preceding section based on a thesis on the versatility of machine learning:

"Learning systems can be used to solve complex non-linear and stochastic problems in space systems with elusive solutions by building precise connections to learning theory resulting in novel capabilities and understanding."

I.3 Proposed Approach

Machine Learning has become a ubiquitous tool providing solutions to complex real-world problems in many diverse areas such as health-care, climate science, financial systems, communications, and fundamental physics. Taking advantage of improved predictability with large amounts of high-dimensional data, machine learning has become a pervasive and versatile method.

We take advantage of the expressive powers of kernel methods in machine learning to provide solutions to orbit determination and interference cancellation [74]. In the orbit de-

termination problem, we take advantage of the ability of kernels to represent probability distributions and continuous functions. For interference cancellation, we use kernel based bandit approaches to overcome the significant constraints associated with CubeSat magnetometry.

I.3.1 Orbit Determination

Thus, in this thesis, we present a novel and general approach to orbit determination that is a batch method (all data are provided at once) which trades off computational complexity for significantly weaker observational requirements. The only requirements imposed are regularity of the observation and output spaces, observability over finite time and availability of observations sufficient to guarantee observability. This approach is applicable to both cooperative and uncooperative observational methods for orbit determination of general objects. It can be implemented by existing measurements systems as well as low-cost ground station networks that meet the relaxed requirements.

We propose a machine learning approach to estimate both the source of the observations and the corresponding orbital parameters. When the dynamic system of the orbital objects is observable, we show that the probability distribution from which the measurements are observed has a continuous map to the orbital parameters. Recent machine learning literature has dealt with the idea of distribution regression, where one is interested in learning a map from probability distributions to parameters. We introduce an extension to this problem, which we name *mixture distribution regression*, to estimate maps from samples of a mixture probability distribution.

I.3.2 Network Architecture

We construct a network architecture, scheduling and tracking algorithms to enable orbit determination. The network architecture uses spectrum monitoring algorithms with software defined ground stations to collect features of Doppler shift and signal identification that are used for orbit determination by the machine learning algorithm. We introduce and approach the new problem of Multiple Satellite Multiple Ground Station (or Multiple Resource) Scheduling Problem with Orbit Uncertainty (MMSP-OU) with the goal of scheduling for the purposes of observing network measurements of Doppler shift for orbit determination. We schedule and track to cover the set over which the initial orbital parameters can vary. We also introduce coordinated tracking and coordinated antenna pointing for realistic ground stations where the ground stations in the network aim to produce observations for any orbit in the uncertainty set.

I.3.3 Magnetometer Interference Cancellation

We consider the problem of minimizing interference with distributed magnetometers and spacecraft telemetry in the presence of interfering sources that far exceed the number of sensors. Using distributed magnetometers provides varied points of measurement of the true magnetic signal and noise throughout the spacecraft (see, for example the TBEx Spacecraft in Figure 1.1). All spacecraft collect some form of real-time telemetry (or context) information containing different parameters of the spacecraft such as solar panel currents, temperatures, momentum wheel information, real-time current consumption, etc. When the true magnetic field is known, it is possible to use telemetry or context information to predict the expected noise in a given sensor. We assume that there exist some points in time for which the true magnetic field is known and learn combinations of distributed magnetometer measurements as a function of telemetry that can minimize interference. We use this learned

behavior to minimize noise behavior over times for which the true magnetic field is unknown. We take CubeSat computational constraints into account by restricting the number of sensor combinations that can be accessed and calibrated real time to one and implement low complexity versions of the learning algorithm. We view this problem as a sequential decision making problem and show that it can be modeled as a novel machine learning problem of *contextual bandits* minimizing *simple regret*.

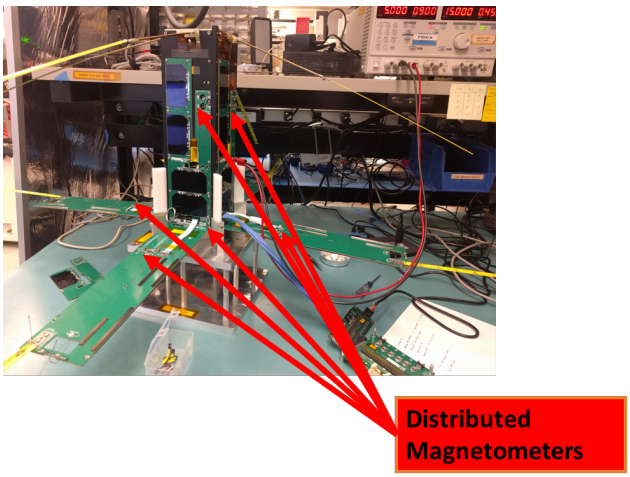

Figure 1.1: TBEx Small Satellite with Multiple Magnetometers [1, 2]

I.4 Contributions

This thesis introduces and solves three new problems in space systems in the two areas of orbit determination and magnetometer interference cancellation. In this process we introduce and solve two new problems in machine learning: mixture distribution regression and simple regret minimization for contextual bandits.

In orbit determination (OD), we present a novel formulation of the orbit determination problem of spacecraft clusters. We show that under broad conditions, the OD problem can be presented as a new problem of mixture distribution regression and present a two step solution to the problem. We present convergence properties of the algorithm and experimental results

for on-orbit spacecraft.

For collaborative orbit determination of ground station networks, we present a ground station network architecture for orbit determination. We also present scheduling and tracking algorithms for spacecraft when the orbits are uncertain. For tracking, we present three types of tracking algorithms based on the spread and evolution of the orbit uncertainties resulting in coordinated antenna pointing between the ground stations in the network. We validate our algorithms on synthetic data simulated for a ground station network.

We formulate the spacecraft magnetometer interference cancellation problem with CubeSat constraints as a new learning problem of simple regret minimization in contextual bandits. We present an algorithm for the learning problem based on theoretical results. We present results of the learning algorithm behavior for machine learning datasets and for a dataset based on telemetry gathered from the GRIFEX spacecraft. This work was done in collaboration with Aniket Deshmukh, my advisors Prof. Clayton Scott and Prof. James Cutler and my thesis committee member Prof. Mark Moldwin.

I.5 Dissertation Outline

This dissertation is organized as follows. Chapter II presents the approach, algorithm and experimental results for orbit determination of spacecraft clusters using mixture distribution regression. The precise development of Chapter II is presented in Appendix A. Chapter III presents the ground station network architecture, scheduling and tracking algorithms for collaborative orbit determination. Chapter IV presents the analysis reducing the magnetometer interference cancellation problem to a learning algorithm, the contextual gap algorithm for simple regret minimization with contextual bandits and experimental results on a lab-based experimental setup.

CHAPTER II

Kernel Embedding Approach to Orbit Determination of Spacecraft Clusters

II.1 Introduction

The goal of orbit determination is to estimate a vector representing a "state" of the satellite to facilitate trajectory prediction. To estimate parameters from a spacecraft cluster using machine learning, we have a two step approach. We first estimate the spacecraft ID from which each observation originated using a *domain generalization* method [75] followed by estimating the initial conditions of each spacecraft from the source IDs estimated using *distribution regression* [76].

In machine learning research, the areas of domain generalization [77] and distribution regression [78] have received increasing attention in the recent years. In the domain generalization setting, the learning system is given unlabeled data to be classified, and must do so by learning to generalize from labeled datasets that represent similar yet distinct classification problems. This can be done through a variety of approaches such as adaptive complexity regularization [77, 79, 80], mapping to common feature spaces [81, 82, 83] and transfer

learning through marginal distributions [75]. In distribution regression, the learning system learns a map from a set of distributions to a separable Hilbert space where the distribution is accessible only through its realizations [78, 76]. We will apply these methods to the orbit determination problem.

The contributions of this chapter are as follows: (1) We present a novel model and method using techniques recently developed in machine learning to perform orbit determination of objects in space. (2) We provide conditions under which such a system can be applied. (3) We present consistency analysis for the concatenated application of marginal transfer learning and distribution regression. (4) We present experimental results of orbit determination and classification for two low Earth orbiting satellites. (5) We compare the performance of this system with existing EKF based orbit determination systems in the presence of noise. (6) We present a synthetic orbit determination scenario of estimation of the orbit of a lunar spacecraft (a chaotic system) from one observation station with direction of arrival and range measurements.

This chapter is organized as follows. Section II.2 states the orbit determination problem, connects it to a machine learning problem and formally states the machine learning problem of mixture distribution regression. We present the algorithm for mixture distribution regression in Section II.3. The consistency analysis of the learning system is presented in Section II.4. We present a overview of the sampling and estimation architecture, experimental and synthetic data results in Section II.5. Conclusions are given in Section II.6.

Background on dynamical systems, probability and the machine learning methods used are presented in Appendix A.1. Appendix A.2 provides a precise description of the orbit determination problem with visibility constraints. Appendix A.3 provides the mathematical development connecting orbit determination in the control theoretic setting to a probabilistic setting. The learning theoretic analysis is presented in Appendix A.5. Proofs for the theorems in Appendices A.3 and A.5 are presented in Appendices A.4 and A.6.

II.2 Orbit Determination as a Learning Problem

The orbit determination (OD) problem described below with modifications for finite time observations and measurement uncertainty can be stated as a machine learning problem. We present the OD problem with these modifications, an analysis connecting OD in the control theoretic setting to a pure machine learning setting, and the problem of OD of spacecraft clusters as a machine learning problem.

II.2.1 OD Problem Setting

We consider the problem of orbit determination of a group of spacecraft, called a cluster, consisting of n_S spacecraft using observations from n_G sensors ($n_S, n_G \geq 1$). The spacecraft in the cluster have identification numbers (IDs) $\{1, 2, ..., n_S\}$ associated with them. The n_S spacecraft have orbital parameters or initial conditions, $\{\Gamma_i\}_{i=1}^{n_S}$, where each Γ_i belongs to $\tilde{\mathcal{J}}$, the space of orbital parameters. The spacecraft *cluster* has the initial condition $\Gamma = [\Gamma_1, \Gamma_2, \cdots, \Gamma_{n_S}]$ defined on $\mathcal{J} := \tilde{\mathcal{J}}^{n_s}$. Here we assume that the Γ is a realization of a *random variable* satisfying the probability distribution P_Γ which is known apriori and represents launch uncertainties, accuracy of pre-launch orbital ephemerides and in cases of orbit determination of lost spacecraft or space debris, the error accumulation of propagation from previously known state. With an initial condition Γ, the cluster evolves through time and its motion can be modeled through a dynamical system[1] and we denote the state of this cluster at time t as $\tilde{\Gamma}(t)$.

There are n_G ground sensors that observe the spacecraft cluster over a time period $\tilde{\mathcal{T}} \subset \mathbb{R}_+$. Any observations at ground station j, where $1 \leq j \leq n_G$, of the spacecraft cluster

[1] For a detailed description of the dynamical system with modifications for this setting see Appendix A.1.1.

will satisfy the system function[1] of the dynamical system, defined as $U_j(\Gamma, t) := q_{0,j}(\tilde{\Gamma}(t))$ where $q_{0,j}$ is the function that maps the state of the system to the observation. The overall dynamical system with observations from the ground station network has the system function $U(\Gamma, t) := [U_1(\Gamma, t), U_2(\Gamma, t), \cdots, U_{n_G}(\Gamma, t)]$.

The actual measurements from the spacecraft cluster observed over $\tilde{\mathcal{T}}$ will be noisy realizations of $U(\Gamma, t)$ for some random times $t \in \tilde{\mathcal{T}}$. We shall denote the times of measurements with the random variable T_S. The times at which these observations occur is determined by a probability distribution P_{T_S} defined over $\tilde{\mathcal{T}}$. A spacecraft i, where $1 \leq i \leq n_{S,}$, produces signals over the observation interval $\tilde{\mathcal{T}}$ according to the probability distribution $P_{T_S,i}$. Based on this, the cluster produces observations of these signals according to the mixture probability distribution $P_{T_S} := \sum_i \pi_i P_{T_S,i}$, where π_i is probability of observation produced by spacecraft i, given that an observation is produced by the cluster. We denote the support of P_{T_S} as $\mathcal{T} \subseteq \tilde{\mathcal{T}}$.

We denote the observation generated at time T_S from spacecraft i will be seen at ground station j as X_j and is a noisy version of $U_j(\Gamma_i, T_S)$. The source spacecraft i generating observation at time T_S is not known to the sensor network and has to be identified. The observations the *sensor network* produce at time T_S will be denoted by the random vector X, for $X := \begin{bmatrix} \tilde{X}_1 & \tilde{X}_2 & \cdots & \tilde{X}_{n_G} & T_S \end{bmatrix}$ defined over the space $\mathcal{X}$. We assume that the probability distribution of the noise generating X from U, $P(X|U(\Gamma_i, t))$ is known.

In the above setting, the distributions of the random variables are all known and generally, the function U is known only through a set of differential equations (for exact forms of the differential equations refer to Vallado [31]). The differential equations of U can be solved for measurement times T_S and hence examples of measurements for different spacecraft clusters can be drawn.

With this scenario, the orbit determination problem is stated as follows. Given P_Γ, P_{T_S},

$P(X|U)$ over the time interval $\tilde{\mathcal{T}}$, differential equations for U and n_T actual measurements $\{X_1, X_2, \cdots, X_{n_T}\}$ from the sensor network, can we estimate $\{\Gamma_i\}_{i=1}^{n_S}$, the orbital parameters of the spacecraft cluster?

Remarks 1. In reality, the sensor network observations are influenced by the sensor field of view and the horizon. For the precise problem statement taking visibility and its effects into account see Appendix A.2.

2. We present the theory with $n_S = 2$ and point to techniques in literature which can be used to extend the algorithm to general n_S.

3. The assumption on the absence of the spacecraft source knowledge associated with observations is motivated by scenarios that occur with clustered spacecraft deployments when tracking with Doppler and radar. With Doppler measurements of spacecraft transmissions, we do not require the transmissions to be decodable nor belong to different frequency bands (they can overlap). With radar, the individual spacecraft measurements are not required to be tagged, and do not need to be resolved if they are very close to one another.

4. Here we assume that the observation vectors $\{X_1, X_2, \cdots, X_{n_T}\}$ (including the time stamps) are independent and identically distributed (i.i.d.) from a probability distribution known prior to generation of observations, even though the observations may be generated sequentially in time. While traditional treatment of dynamic system observations are as sample paths of random processes, we differ in two aspects: we consider only finite time treatment and allow for multiple independent sets of sensors to produce $P(X|U)$.

II.2.2 Observability

When observability conditions are satisfied, the orbit determination problem can be reduced to the estimation of a map on the space of probability distributions of $\mathcal{X}$. Let $\mathcal{B}_\mathcal{X}$ denote the space of probability distributions on $\mathcal{X}$. Given the distribution of observations $P(T_S)$ and $P(X|U)$, the orbital parameter Γ induces a probability distribution $P(X|\Gamma) \in \mathcal{B}_\mathcal{X}$ such that $P(X|\Gamma) = \sum_i \pi_i P(X|\Gamma_i)$. The observations of a satellite cluster are i.i.d realizations of $X \sim P(X|\Gamma)$. For all the orbital parameters in $\mathcal{J}$, we denote the map $\Gamma \to P(X|\Gamma)$ by $\mu_X : \mathcal{J} \to \mathcal{B}_\mathcal{X}$. The range of μ_X is the set $R_\mathcal{X} := \{P(X|\Gamma)|\Gamma \in \mathcal{J}\}$ over which P_Γ induces a distribution ρ.

We make certain assumptions to simplify the nature of the probability distributions in the system and to avoid pathological cases. We assume the parameter space $\tilde{\mathcal{J}}$ and the observation space $\mathcal{X}$ are closed and bounded sets. We assume that the probability distribution P_{T_S} is a continuous probability distribution over the support $\mathcal{T} \subseteq \tilde{\mathcal{T}}$. We also assume that the variation of the probability distribution of noise $P(X|U(\Gamma_i, t))$ varies continuously with the change in the value of $U(\Gamma_i, t)$.

The system U is said to be observable over $\tilde{\mathcal{T}}$ if the state can be determined from the output of the dynamical system $U(\Gamma, t)$ for any $\Gamma \in \mathcal{J}$. For a system without control vectors, this implies that the initial state can be determined from the outputs. We can state the following equivalence between observability and the invertibility of μ_X:

Theorem A. *Under the assumptions stated, U is continuous and observable in $\mathcal{T}$ if and only if the inverse map $\mu_X^{-1} : R_\mathcal{X} \to \mathcal{J}$ exists and is continuous over the closed and bounded set $R_\mathcal{X} \subseteq \mathcal{B}_\mathcal{X}$.*

For precise statements of the assumptions and the preceding theorem, for the proofs and for extensions of Theorem A taking the field of view of the sensors into consideration, see

Appendix A.3.

Since the dynamical systems under consideration for the orbit determination problem are continuous, the above theorem states that if U is observable there exists a function $\lambda := \mu_X^{-1}$ from a subset of $\mathcal{B}_\mathcal{X}$ to the orbital parameters. The existence of this function holds under broad conditions for both the input and observation space. As a consequence, this theorem holds for all the various the formulations used for U (Lagrangian, Hamiltonian, etc.) and their corresponding orbital parameters (Keplerian, equinoctial, position-velocity and Poincare elements).

In the presence of a general estimator for maps from probability distributions to parameters that is independent of a dynamical system construction, Theorem A has significant implications. For a general set of observations, such an estimator can be used as a black box and would provide an experimental approach for verifying observability. Additionally, for any non-linear dynamical system formulation for which observability can be proven, the construction of a new estimator based on the dynamics is not necessary and the generalized estimator can provide initial estimates of the orbital parameters that independent of geometric or dynamical system considerations. Next, we propose such a general non-parametric technique to estimate the map λ that is independent of the formulation of U, the orbital parameters used and the type of observations.

II.2.3 Machine Learning Setting

We propose to estimate the function λ through a machine learning approach. While direct description of the probability distributions $P(X|\Gamma)$ is not possible, it is possible to generate realizations of example orbital parameters from P_Γ and generate example observations of a spacecraft cluster propagation. Using this, we generate training data in the following fashion: We synthetically generate J example deployment scenarios/tasks where for scenario

$j, 1 \leq j \leq J$, we first sample the initial condition $\Gamma^{(j)}$ of the cluster, propagate the cluster to generate observations and spacecraft IDs associated with the observation, $\{X_i^{(j)}, Y_i^{(j)}\}_{i=1}^{n_j}$. Using these J scenarios, we will train a learning algorithm to estimate the initial conditions for the test scenario Γ^T using only the observations $\{X_i^T\}_{i=1}^{n_T}$.

Using the training data, we now consider the problem of estimating λ as a machine learning problem. As described in the preceding subsections, we have an observation space $\mathcal{X}$ and a parameter space $\tilde{\mathcal{J}}$ and $\mathcal{B}_{\mathcal{X}}$ as the space of probability distributions on $\mathcal{X}$. For $i, 1 \leq i \leq n_S$, the orbital parameter Γ_i of spacecraft i induces a distribution $P_i := P(X|\Gamma_i)$ on $\mathcal{X}$. Given a realization (an example set of orbital parameters) Γ, there exists a mixture distribution $P(X|\Gamma) := \sum_i \pi_i P_i$ for which observations are seen at the sensors.

We are given J realizations of this system as training data. Specifically, we are given $\Gamma^{(j)} \overset{\text{i.i.d}}{\sim} P_\Gamma, 1 \leq j \leq J$ and realizations from the mixture distribution $P^{(j)}$ with mixture labels: $\{(X_i^{(j)}, Y_i^{(j)})\}_{i=1,j=1}^{n_j,J}$, where $Y_i^{(j)} \in \{1, 2, \cdots, n_S\}$ is the ID of the spacecraft from which $X_i^{(j)}$ is produced.

Separately, we are also given observations from a *test* scenario, P^T, $\{X_i^T\}_{i=1}^{n_T}$ for which the orbital parameter Γ^T is not known. We desire to learn the function $r : P^T \to \hat{\Gamma}^T$ such that $\|\Gamma^T - \hat{\Gamma}^T\| \to 0$. We assume a natural ordering in the components of the mixture distribution $P_i^T, 1 \leq i \leq n_S$ i.e., it is possible to label each component of the mixture and identify the labels from the mixture distribution.

The goal is to learn the function $r := [r_1, r_2, \cdots, r_{n_S}]$ such that $r_i : \mathcal{B}_{\mathcal{X}} \to \tilde{\mathcal{J}}$, $1 \leq i \leq n_S$, to minimize the empirical error

$$\hat{\mathcal{E}}(r) := \frac{1}{J} \sum_{j=1}^{J} \sum_{i=1}^{n_S} \|\Gamma_i^{(j)} - r_i(\widehat{P}^{(j)})\|_{\tilde{\mathcal{J}}}^2 + \sum_{i=1}^{n_S} \lambda_{2,i} \|r_i\|^2. \tag{2.1}$$

Note that this problem is a distribution regression problem with additional structure present

in the probability distributions in the form of labels or spacecraft IDs. Next, we present an algorithm that takes advantage of this additional structure to compute the function r through a two step process.

II.3 Algorithm

We propose a two step solution to the problem that takes advantage of the spacecraft ID information available in the mixture distribution $P(X|\Gamma)$. We name this method as *mixture distribution regression*. We are given training data of the form $\{\{X_i^{(j)}, Y_i^{(j)}\}_{i=1}^{n_j}, \Gamma^{(j)}\}_{j=1}^{J}$, which is separated into two parts of sizes J_{tl} and J_{dr} with $J = J_{tl} + J_{dr}$. The first part of the training set of size J_{tl} is used to train a learning system that can ID the spacecraft associated with each individual observation. This identification is performed using marginal transfer learning (also called marginal prediction) [75]. We use a modified form of the marginal predictor that provides, for each observation, the probability that it belongs to the different spacecraft in the cluster. We shall call these probabilities the estimated class posterior probabilities associated with the observations. The trained marginal predictor is used to compute the class posterior probabilities for the second part of the training data, J_{dr}. Spacecraft IDs or labels are then randomly assigned based on sampling from the class posterior probabilities. We shall use the term *predicted* labels or predicted IDs to distinguish the randomly sampled versions from the true spacecraft IDs. The true labels of the second part of the training data are discarded. In the next step, n_S distribution regression learning problem is solved such that the $i^{\text{th}}, 1 \leq i \leq n_S$ regressor is trained with *estimated* class conditional distributions of spacecraft ID i generated from the predicted labels.

For the rest of this chapter, we will describe the algorithm in the two class setting, $n_S = 2$, without loss of generality. Both marginal prediction and distribution regression learn continuous functions using kernels.

We define the *kernel* as a function $k : \mathcal{X} \times \mathcal{X} \to \mathbb{R}$ that is symmetric and positive definite. When $\mathcal{X}$ is a compact metric space, such as a closed and bounded subset of $\mathbb{R}^d$ (d-dimensional Euclidean space), it is possible to approximate continuous functions on $\mathcal{X}$ and capture a probability distribution on $\mathcal{X}$ using functions generated by the kernel. The functions generated by the kernel lie in a function space known as reproducing kernel Hilbert space (RKHS). This RKHS, $\mathcal{H}_k$, consists of the completion of the set of functions of the form $f(X) = \sum_i \alpha_i k(X_i, X)$ for $X \in \mathcal{X}, \alpha_i \in \mathbb{R}$. The kernel and the functions in the RKHS satisfy a reproducing property:

$$f(X) = \langle f, k(X, \cdot)\rangle_{\mathcal{H}}, \forall X \in \mathcal{X}.$$

Using the RKHS, it is possible to capture a probability distribution P on $\mathcal{X}$ as a function, called the mean embedding of P, defined as

$$\phi(P) := \int_{\mathcal{X}} k(x, \cdot) dP(x).$$

Kernels and the RKHS can be defined on more general spaces than compact subsets of $\mathbb{R}^d$. Marginal prediction and distribution regression require three particular extensions [2]:

1. It is possible to define a vector extension to kernels such that the kernel describes a function with a vector output (say $\mathbb{R}^d$). Such a kernel would map to the space of linear operators on $\mathbb{R}^d$, i.e., $\mathbb{R}^{d\times d}$.

2. It is possible to define kernels on the space of embeddings of probability distribution on $\mathcal{X}$. Let $\phi(\mathcal{B}_{\mathcal{X}})$ be the image of $\mathcal{B}_{\mathcal{X}}$ under the map ϕ. We can define a kernel on $\phi(\mathcal{B}_{\mathcal{X}})$, $K : \phi(\mathcal{B}_{\mathcal{X}}) \times \phi(\mathcal{B}_{\mathcal{X}}) \to \mathbb{R}$ with the RKHS, $\mathcal{H}_K$.

3. We can define a vector kernel on embeddings of $\mathcal{B}_{\mathcal{X}}$ to the space of linear operators on

[2] For a brief overview of transfer learning and distribution regression see Appendix A.1.3

on $\mathbb{R}^d$, i.e., $\mathbb{R}^{d\times d}$.

For the marginal predictor or transfer learning system [75] we define the three kernels:

- Kernel $k : \mathcal{X} \times \mathcal{X} \to \mathbb{R}$ for embedding probability distributions on $\mathcal{X}$. $\mathcal{H}_k$ is the RKHS associated with k. A probability distribution $P \in \mathcal{B}_\mathcal{X}$ can be embedded in $\mathcal{H}_k$ as

$$\phi_P := \phi(P) := \int_\mathcal{X} k(\cdot, x) dP(x)$$

- Kernel $K : \phi(\mathcal{B}_\mathcal{X}) \times \phi(\mathcal{B}_\mathcal{X}) \to \mathbb{R}$ a kernel operating on the embeddings of $\mathcal{B}_\mathcal{X}$ with RKHS $\mathcal{H}_K$. We shall denote the feature vector associated with kernel K as Ψ_K.

- Kernel $k' : \mathcal{X} \times \mathcal{X} \to \mathbb{R}$ a kernel operating on data points in $\mathcal{X}$ in the extended feature vector with RKHS $\mathcal{H}_{k'}$.

Using kernels K and k', we define the product kernel $k_P : (\mathcal{B}_\mathcal{X} \times \mathcal{X}) \times (\mathcal{B}_\mathcal{X} \times \mathcal{X}) \to \mathbb{R}$ as $k_P := K \cdot k$. Let $\mathcal{H}_{k_P}$ be the RKHS associated with the kernel k_P. Denote the finite version of a probability distribution P as $\hat{P}$. With the first part of the training data, the marginal predictor computes the function $\hat{g}$,

$$\hat{g} = \underset{g\in\mathcal{H}_{k_P}}{\arg\min} \frac{1}{J_{tl}} \sum_{j=1}^{J_{tl}} \frac{1}{n_j} \sum_{i=1}^{n_j} \ell(g(\hat{P}^{(j)}, X_i^{(j)}), Y_i^{(j)}) + \lambda_1 \|g\|^2.$$

We will use logistic regression as the loss function: $\ell(t, y) = \ln(1 + \exp(-yt))$. Instead of hard classification as proposed in [75], we estimate the posterior probabilities of the spacecraft IDs for samples from the test distribution P^T with samples $\{X_i^T\}_{i=1}^{n_T}$ as (note that $n_S = 2$)

$$\hat{P}(Y_i^T = 2 | X_i^T, P^T) = \frac{1}{1 + \exp(-\hat{g}(P^T, X_i^T))}$$

and $\hat{P}(Y_i^T = 1|X_i^T, P^T) = 1 - \hat{P}(Y_i^T = 2|X_i^T, P^T)$. The preceding estimate of the posterior probability holds because marginal transfer learning can be seen as classification in the extended feature space $\mathcal{X} \times \mathcal{B}_\mathcal{X}$ and the class posterior can be computed for classification problems using logistic regression [75, 84]. Using the preceding set of equations, for each task j in the second part of the training dataset, the posterior probabilities are sampled to generate labels $\{\hat{Y}_i^{(j)}\}_{i=1}^{n_j}$. The distribution regression system [76] requires two additional kernels.

- Kernel $\bar{k} : \mathcal{X} \times \mathcal{X} \to \mathbb{R}$ for embedding the probability distributions on $\mathcal{X}$ with RKHS $\mathcal{H}_{\bar{k}}$.

  A probability distribution $P \in \mathcal{B}_\mathcal{X}$ can be embedded in $\mathcal{H}_{\bar{k}}$ as

$$\xi_P := \xi(P) := \int_\mathcal{X} \bar{k}(\cdot, x) dP(x)$$

- Vector kernel $\mathfrak{K} : \xi(\mathcal{B}_\mathcal{X}) \times \xi(\mathcal{B}_\mathcal{X}) \to \mathcal{L}(\tilde{\mathcal{J}})$ for regressing from the embedding on $\mathcal{H}_{\bar{k}}$. $\mathfrak{K}$ has the RKHS $\mathcal{H}_\mathfrak{K}$. We shall denote the feature vector associated with kernel K as Ψ_K.

The predicted labels $\{\hat{Y}_i^{(j)}\}_{i=1}^{n_j}$ for each task j from the second part of the training data are used to estimate the n_S probability distributions. The kernel $\bar{k}$ is used to compute the mean embedding for the distribution of data estimated to be from the first spacecraft $Y = 1$ as

$$\hat{h}_1(\hat{P}^{(j)}) := \frac{1}{\hat{n}_{j,1}} \sum_{i=1}^{n_j} \mathbf{1}_{\{\hat{Y}_i^{(j)}=1\}} \bar{k}(X_i^{(j)}, \cdot),$$

where $\hat{n}_{j,1} := \sum_{i=1}^{n_j} \mathbf{1}_{\{\hat{Y}_i^{(j)}=1\}}$.

The conditional embeddings generated from the application of transfer learning, $\{\hat{h}_1(\hat{P}^{(j)})\}_{j=J_{tl}+1}^{J_{tl}+J_{dr}}$,

are used as training data for a distribution regression system minimizing the empirical loss

$$\hat{\mathcal{E}}(r_1 \circ \hat{h}_1) := \frac{1}{J_{dr}} \sum_{j=J_{tl}+1}^{J} \|\Gamma_1^{(j)} - r_1(\hat{h}_1(\hat{P}^{(j)}))\|_{\tilde{\mathcal{F}}}^2 + \lambda_{2,1}\|r_1\|^2, \tag{2.2}$$

to estimate the orbital parameters for the spacecraft with label 1 i.e., Γ_1. The second parameter Γ_2 is estimated similarly, using predicted labels of spacecraft ID 2. The detailed algorithm is described in Algorithm 2.1.

Algorithm 2.1: Mixture Distribution Regression

Input: Training Data $\{\{X_i^{(j)}, Y_i^{(j)}\}_{i=1}^{n_j}, \Gamma^{(j)}\}_{j=1}^{J}$, test data $\{X_i^T\}_{i=1}^{n_T}$.

Train marginal predictor with training data $\{\{X_i^{(j)}, Y_i^{(j)}\}_{i=1}^{n_j}\}_{j=1}^{J_{tl}}$

for $j = J_{tl}+1, J_{tl}+2, ..., J$ **do**

  for $i = 1, ..., n_j$ **do**

    Compute class posterior distribution

    $\hat{P}_{Y|X,i}^{(j)} := [P(Y_i^{(j)} = 1|X_i^{(j)}), \cdots, P(Y_i^{(j)} = n_S|X_i^{(j)})]$.

    Sample $\hat{Y}_i^{(j)} \sim \hat{P}_{Y|X,i}^{(j)}$.

  end

  Compute Embeddings of $\{\hat{P}(X|\Gamma_y^{(j)})\}_{y=1}^{n_S}$

end

for $y = 1, 2, ..., n_S$ **do**

  Train Distribution Regression to compute $\hat{r}_y$.

end

For test data $\{X_i^T\}_{i=1}^{n_T}$, predict labels $\{\hat{Y}_i^T\}_{i=1}^{n_T}$.

Use $\{\hat{Y}_i^T\}_{i=1}^{n_T}$ to compute class conditional embeddings $\{\hat{h}_y(\hat{P}^T)\}_{y=1}^{n_S}$.

Use Distribution regression with $\{\hat{h}_y(\hat{P}^T)\}_{y=1}^{n_S}$ to compute $(\hat{\Gamma}_1^T, \hat{\Gamma}_2^T, ..., \hat{\Gamma}_{n_S}^T)$.

II.4 Learning Theory

The data observed during actual measurements are not exactly represented by finite training data ($J < \infty$). This approximation leads to an error in the learning behavior, known as generalization error. We provide high probability upper bounds on the generalization error for mixture distribution regression. We show that under certain regularity conditions, as the amount of training data increases, the generalization error decreases under non-asymptotic conditions and goes to zero with high probability under asymptotic conditions.

We present generalization error bounds for a *soft label* version of mixture distribution regression where the estimated class posterior distributions are directly used for computing the embeddings associated with the labels (instead of random sampling of labels as discussed in section II.2.3). Standard probabilistic arguments can be used to show that as $n_j \to \infty$, the random sampled version approaches the soft label version of mixture distribution regression.

For generalization error bounds, we make the following boundedness and smoothness assumptions on the parameters of the learning algorithm.

1. The observation space $\mathcal{X}$ and the parameter space $\tilde{\mathcal{J}}$ are closed and bounded sets.

2. A kernel k is said to be universal if the functions in the RKHS associated with the kernel can approximate any continuous function to arbitrary precision. We assume that the kernels used for mixture distribution regression are universal, bounded and Hölder continuous.

3. The loss ℓ is the logistic loss.

4. There exists a map from the marginal distribution $P(X|\Gamma)$ to the class posterior distribution $P(Y|X)$.

The preceding assumptions are essential to constrain the learning algorithm to operate in well-behaved function spaces. Additionally, the assumptions that constrain the behavior of the input and output data (Assumptions 1 and 4) are broader than those that are specific to the OD problem stated in Section II.2.2. The observation and parameter space constraints in Assumption 1 are required for high probability measure concentration behavior of data, allowing learning behavior. Assumption 2 is required for accurate representation of continuous functions and probability distributions using the RKHS. Assumption 3 is necessary for accurate extraction of individual mixture components from the mixture distribution (See self-calibrated loss functions in [84]). Assumption 4 is required for application of Assumption 3 in the marginal transfer learning setting.

We denote by $\mathcal{S}_{tl}$ and $\mathcal{S}_{dr}$, the generalization errors of marginal transfer learning and distribution regression. Blanchard et. al [75] and Szabó et. al [76] provide generalization error bounds and consistency analysis for transfer learning and distribution regression respectively.

We provide generalization error bounds in terms of generalization errors of the the marginal transfer learning system and distribution regression. Let h_i^* denote the optimal solution of marginal transfer learning system for spacecraft ID i, i.e., the kernel embedding associated with the class conditional distribution $P(X|\Gamma_i)$ and let r_i^* denote the optimal solution for the distribution regressor: the map from h_i^* to Γ_i. We show that under certain regularity conditions that are satisfied for the orbit determination scenario, as $J_{tl} \to \infty$ and $J_{dr} \to \infty$, generalization error $\mathcal{E}(\hat{r}_i \circ \hat{h}_i) - \mathcal{E}(r_i^* \circ h_i^*) \to 0$.

The novelty and complexity of the proof comes from two areas. First, there is additional noise in the data for the distribution regression system that changes with increase in training data for the marginal transfer learning. Second, in the marginal transfer learning system, the logistic regression outputs are used to reconstruct embeddings of the class conditional distributions.

Theorem B. *For the mixture distribution regression setting, under the stated assumptions, for* $\delta > 0$,

$$\mathcal{E}(\hat{r}_i \circ \hat{h}_i) - \mathcal{E}(r_i^* \circ h_i^*) \leq C_1 \mathcal{S}_{tl}^{\beta} + C_2 \mathcal{S}_{tl}^{\beta/2} + C_3 \left(\sqrt{\frac{\log \delta^{-1}}{J_{dr}}} + \mathcal{S}_{tl} \right)^{\beta} + 4\mathcal{S}_{dr},$$

holds with high probability for constants C_1, C_2, C_3 *and* β.

For precise statements of the assumptions and Theorem B see Appendix A.5. For the complete proof of Theorem B see Appendix A.6.

Theorem B states that as long as the dynamical system of spacecraft cluster is observable by the sensor network, it is possible to estimate the orbital parameters of each spacecraft in the cluster with high probability to arbitrarily small error with sufficient amount of training data. Additionally, with sufficient amount of training data, this orbit determination can be performed even under weakly observable scenarios. The only limitations on the uncertainty distribution P_Γ is that it's support has to be bounded.

II.5 Results and Discussion

We consider four scenarios to test different aspects of the orbit determination system. The first is based on Doppler-only orbit determination and the last three on direction of arrival and range information. We present results with Doppler information collected by cognitive radio based algorithms on software-defined ground stations from on-orbit transmissions of MCubed-2 and GRIFEX spacecraft testing algorithmic behavior with high-noise, low-observability conditions. We then discuss the results for a simulated on-orbit deployment scenario of two spacecraft testing identification and orbit determination of satellites in a TLE lottery. The third scenario considers a lunar orbit where we test algorithmic behavior with a chaotic system. In the fourth scenario, we perform a comparison of a traditional or-

bit determination system based on the EKF with the proposed machine learning technique. Last, we shall discuss and provide comparisons of the different scenarios.

We present results with one and two ground stations. The mathematical theory is broad enough to allow for networked ground stations with multiple types of sensors, however, we shall leave this for future work. We begin with details of the system architecture for single ground station scenarios.

II.5.1 System Architecture

The general architecture of the sampling and the orbit estimation system is shown in Figure 2.1. The prior P_Γ, which represents the uncertainty of orbit parameters for learning, can be constructed either from launch characteristics and launch sequencing or from uncertainties in pre-launch TLEs. There are no limiting factors to P_Γ other than those described in Section II.2.2. It is necessary for the orbital elements used in this system to have parameters that are independent of each other in order to reduce computation requirements for training in the orbit determination step, since the kernel operator can be diagonal. The time sampling characteristics $P_{T|z}$ and the noise characteristics $P_{X|F}$ of the measurement system z must be estimated prior to generation of training data for the orbit determination. This estimation will depend on the deployment scenario. We provide examples of this for the Doppler-only orbit determination technique in Section II.5.2.

Sample generation is split into two subsystems: the propagator and the observer. The propagator generates samples of the dynamic systems U and V at sample time points. The dynamic system must be unbiased in its generation of data and its error must be bounded. This holds as long as the errors in the spherical harmonic coefficients of the gravity model are bounded and do not have a constant bias error. We present test scenarios with two propagators: SGP4 and an analytical propagator with a numerical integration-based set up. The

propagator sample time points are generated disregarding visibility and sensitivity information of the ground station. The observer system then combines the visibility information, the sensitivity information, and noise to generate samples X from $P(X|\Gamma)$ and the spacecraft id labeled $1, \cdots, n_S$ as detailed in Section II.2.

The learning system depends on the number of spacecraft. In the single spacecraft scenario, this training information is then fed to the two stage sampled regression for orbit determination. In the multiple spacecraft scenario, J_{tl} orbit distributions are first used to train the marginal predictor. The rest of the samples are then classified using the marginal predictor and then used to train an n_S bank of regressors, one for each spacecraft. As shown in Section II.4, this is necessary in the scenarios where identification of the spacecraft is not straightforward. Even though the marginal predictor with logistic regression is not sparse [84], the number of training scenarios for the marginal predictor, J_{tl} has been observed to be significantly lower than that of distribution regression J_{dr} to achieve low error for the spacecraft cluster datasets under consideration. Except for the serial behavior in training for the marginal predictor and the regressor, the system is entirely parallelizable. In fact, even though training for n_S regressors have to be performed, the number of kernel evaluations are equal to that of a single large regressor with all the data points. For the transfer learning system, to speed up evaluation, we used a random Fourier feature based transfer learning system proposed in Blanchard et. al[85]. The distribution regression system consisted of 13 hyper parameters: 6 for the kernel bandwidths of the embeddings, 6 for higher RKHS $\mathfrak{R}$ (as

in equation (2.3)) and one for the regularizer.

$$\mathfrak{K} = \begin{bmatrix} \mathfrak{K}_{\tilde{\gamma}_1} & 0 & 0 & 0 & 0 & 0 \\ 0 & \mathfrak{K}_{\tilde{\gamma}_2} & 0 & 0 & 0 & 0 \\ 0 & 0 & \mathfrak{K}_{\tilde{\gamma}_3} & 0 & 0 & 0 \\ 0 & 0 & 0 & \mathfrak{K}_{\tilde{\gamma}_4} & 0 & 0 \\ 0 & 0 & 0 & 0 & \mathfrak{K}_{\tilde{\gamma}_5} & 0 \\ 0 & 0 & 0 & 0 & 0 & \mathfrak{K}_{\tilde{\gamma}_6} \end{bmatrix} \tag{2.3}$$

Grid search with 5 fold cross validation was used for training. The Michigan High-Performance Cluster was used for training and testing. Preprocessed orbit feature vectors can then be fed into this system to perform orbit determination of the set of spacecraft. The preprocessing steps are dependant on the type of feature vectors used for orbit determination. In addition to the experimental results presented for the two spacecraft (MCubed-2 and GRIFEX), we also generate additional identically distributed sampling data to test performance of the system. For the direction of arrival and range (DOAR) systems we provide only synthetic results with data generated from analytical propagators.

II.5.2 Doppler-Only OD

The approach detailed in Section A.3 states that if observability criteria are satisfied, then Doppler information alone should be sufficient to perform orbit determination of spacecraft. While analytical verification of observability for Doppler based observations is highly complex and non-trivial, the approach detailed can be used to verify observability through the

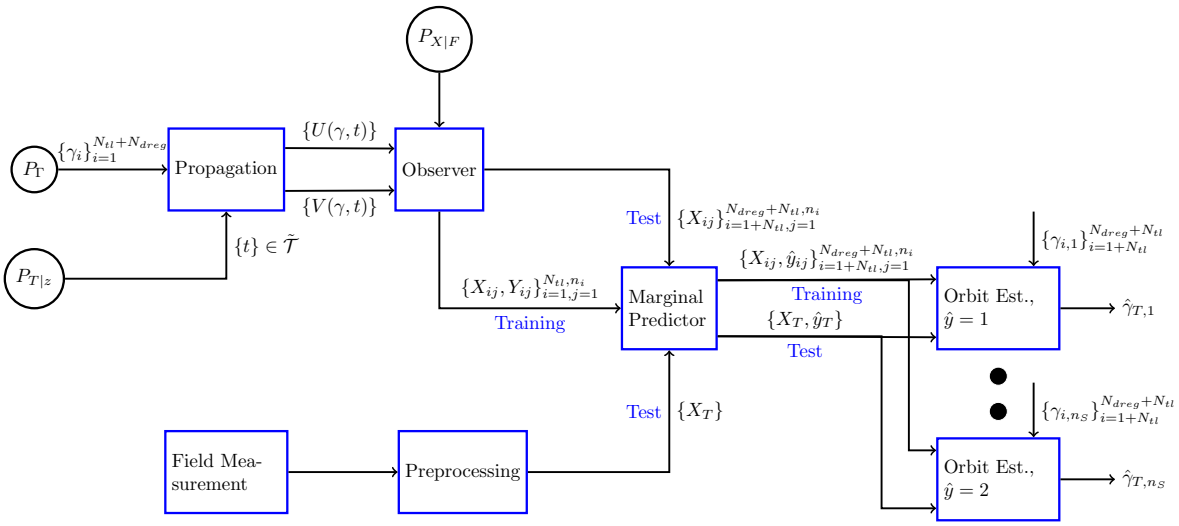

Figure 2.1: System Architecture

performance of the learning system.

We run orbit determination for two low Earth orbit spacecraft - MCubed/COVE-2 and GRIFEX [86, 87, 88]. Their orbits were determined over an interval spanning 4 passes for MCubed-2 and 3 passes for GRIFEX at the Ann Arbor ground station. This analysis was performed using extracted Doppler data from actual passes. Both satellites have UHF telemetry channels at 437.485 MHz and transmissions at 9600 bps, GMSK modulated waveforms. These transmissions will only be decodable when received energy per bit over noise crosses 13dB. However, decodability and identifiability are not a requirement for the proposed orbit determination technique.

Cognitive radio approaches in blind cyclostationary feature extraction [89] were used to extract Doppler, time, and data rate information. These algorithms were applied over recordings of raw, high-rate sampled data from an experimental, software-defined radio (SDR) based ground station. Complex baseband recordings were made of satellite transmissions with this SDR system for passes over Ann Arbor over a 6 hour interval starting at 23:00:00 UTC on 9 Feb. 2016. The recordings were limited to predicted intervals around passes

based on training data due to large file sizes of the recordings. Figure 2.2 shows an example recording for an MCubed-2 pass. Note the variation in received power is due to oscillations in pointing attitude.

Appropriate FIR filter banks were used on the baseband signal to filter the software defined radio harmonics and known constant frequency out of band RF transmissions such as those seen around the 380 second marks at 437.504 MHz. Note that we do not assume the presence of prior orbit information accurate enough to use directional antennas to decode signals associated with the spacecraft. A low-gain wide-beam antenna can be used to collect raw spectral information to extract parameters associated with transmissions. The raw RF baseband signals recordings also consisted of noise due to transmissions to the spacecraft from the ground station, which were eliminated using power thresholding (RF leakage for 500 W transmissions were at least 30 dB higher than beacons due to attenuation). CubeSat modulated telemetry transmissions at 9.6 kbps which was used to isolate Doppler of the spacecrafts [90]. Due to trivial classification requirements, data was manually classified before feeding into the orbit determination system.

Bias Correction For the learning algorithm to operate as expected the experimental and training data offsets should be identical. However, due to implementation issues, there were specific communications system characteristics both on the spacecraft and on the ground station which resulted in bias in the recorded data. On the satellite, temperature variations and imperfect frequency calibration transmission center frequency led to frequency bias. On the ground, there was a varying initial timing bias during the initialization of each recording (one recording per pass during the 6 hour interval). This was due to coding inefficiencies and speed in writing the large data (3 gigabytes for 10 minutes) to the file system.

The frequency bias was corrected with two frequency offset corrections - one for MCubed-2 and one for GRIFEX. The offsets were corrected by computing frequency offsets of a prior

pass with similar spacecraft temperatures. The timing bias was corrected with 7 time offset corrections for the 7 recording intervals (4 for MCubed-2 and 3 for GRIFEX). The time offsets were corrected by computing the time offset with respect to the TLE of the spacecrafts to align the points of maximum Doppler. The time offset corrections varied from 0 to 8 seconds. No other changes to the recordings were performed prior to extraction of features. Figure 2.3 shows an example of the extracted features and the JSpOC (Joint Space Operations Command) TLE post bias correction.

We do not expect to face this bias correction issue in future deployments of the orbit determination technique as center frequency behavior will be characterized prior to launch and the cognitive radio algorithms will be integrated into real-time operational software instead of being implemented over recordings in this experimental fashion.

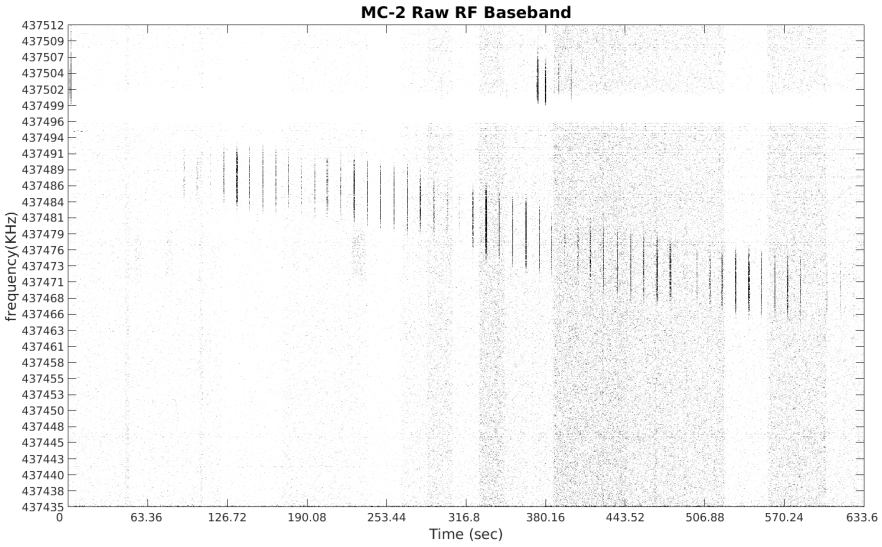

Figure 2.2: MCubed-2 Raw RF Baseband Recordings from 02-10-2016 at 01:20:24 UTC

The dynamic system for U and V used throughout this scenario is the SGP4 propagator. The learning systems are trained to estimate orbital elements specifically designed for TLE generation (not classical elements) and simplified propagators. U consists only of Doppler information and V consists of horizon information for the training data.

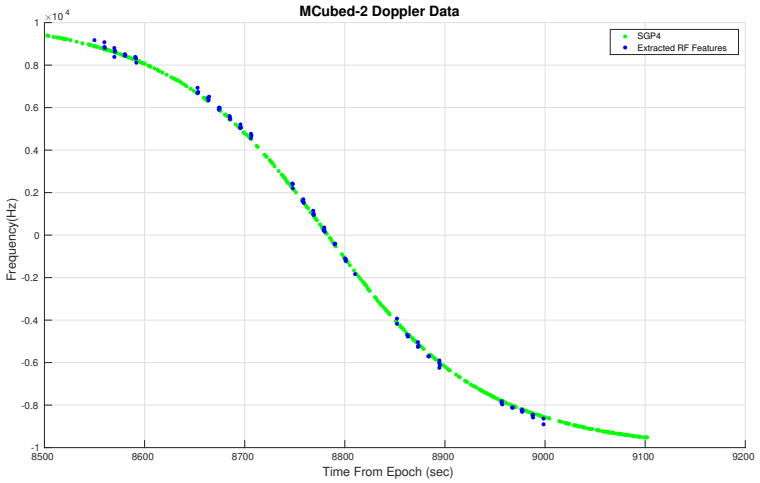

Figure 2.3: Doppler and Time feature vectors compared with Doppler from TLE Predicted Orbit post bias correction

GRIFEX Orbit Determination

GRIFEX orbit state was estimated from raw baseband RF transmission data observed over 3 passes and received during nominal operations. The priors were chosen to provide a sufficiently wide region of initial states to test orbit estimation. The prior P_Γ is

$$A \sim R_e + U(525, 555) \text{ km}, \qquad e \sim U(0.012, 0.017),$$
$$\Omega \sim U(120^\circ, 130^\circ), \qquad I \sim U(96^\circ, 101^\circ),$$
$$\omega \sim U(185^\circ, 200^\circ), \qquad M = U(35^\circ, 50^\circ).$$

P_Γ results in a variance in initial position of 765 km. Samples of 4000 orbits were used for training with the two stage sampled regressor (1.35×10^6 feature points in total). For testing purposes, in addition to the data acquired from on orbit transmissions, additional training data was generated with 200 test orbits for evaluation of the parameters from additional i.i.d samples. The noise distribution $P(X|F)$ was chosen to be uniform with a width of 200

Hz, similar in behavior to the noise from the Doppler observations. GRIFEX produces beacons and transmissions approximately every 10 seconds with an arbitrary initial offset (depending on operational characteristics) along with spacecraft responses due to nominal operations in between. We approximated the resulting transmission time-stamp distribution with a uniform distribution over $\tilde{\mathcal{T}}$.

From raw baseband signals, 534 feature vectors were extracted over 3 passes. The relevant TLE orbital parameters for the JSpOC TLE and the estimated values are shown in Table 2.1. The 200 additional simulated test orbits were also tested for orbit determination. The normalized errors in orbital elements for the 200 simulated test orbits for GRIFEX are shown in Figure 2.4 (normalized by the width of the support of the prior distribution). The radial, along-track and cross-track (RSW) and total errors for each of the test orbits are shown in Figure 2.5. Orbital elements were estimated for the epoch 01:00:00 2016/2/10 UTC.

Table 2.1: Two Line Element Parameters of the GRIFEX spacecraft.

	A(km)	e	I(deg)	Ω(deg)	ω(deg)	M(deg)
True (JSpOC Est.)	537.663	0.0152	99.089	123.2705	194.6996	40.8253
Estimated	534.673	0.0167	98.43	122.709	191.4	43.7795

The error in estimated initial position for the GRIFEX spacecraft is 30.05 km. The average error for the 200 test orbits was 47.24 km. The error magnitudes of the simulated test orbits are of the same order as that of the experimental data indicating that the fidelity of the training and test models mirror those of experimental data. Note that radial and cross-track errors are significantly lower for Doppler based observations. This is expected as along track information can be gained only through subtle changes in the Doppler curve when working with Doppler based observations and does not change the length of the passes or time between passes. Changes in radial information can be observed as it leads to changes in total variation of the Doppler curves and the timing between passes, resulting significantly better estimates. Changes in cross-track information leads to changes in the length of the

passes and total variation of Doppler of the different passes for low Earth orbits.

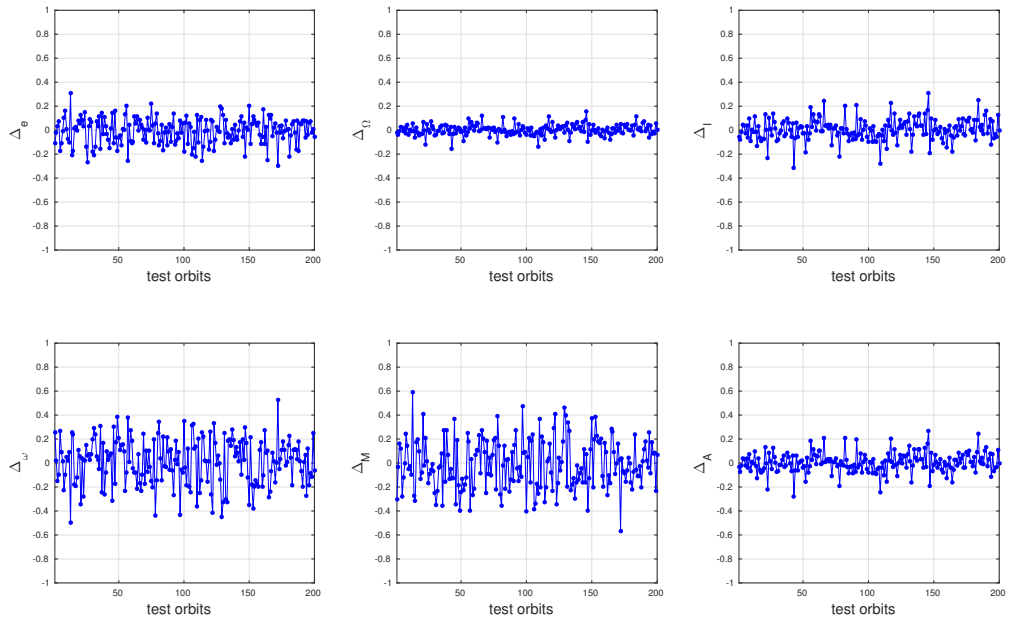

Figure 2.4: Normalized errors of orbital parameters of test orbits based on GRIFEX Priors

MCubed-2 Orbit Determination

MCubed-2 orbit determination was performed with data extracted over 4 passes. The priors for MCubed-2 were chosen to have smaller widths compared to the GRIFEX scenario for variations in RAAN and the argument of perigee to test for changes to estimation behavior while keeping the number of training data points approximately equal. The prior P_Γ used is

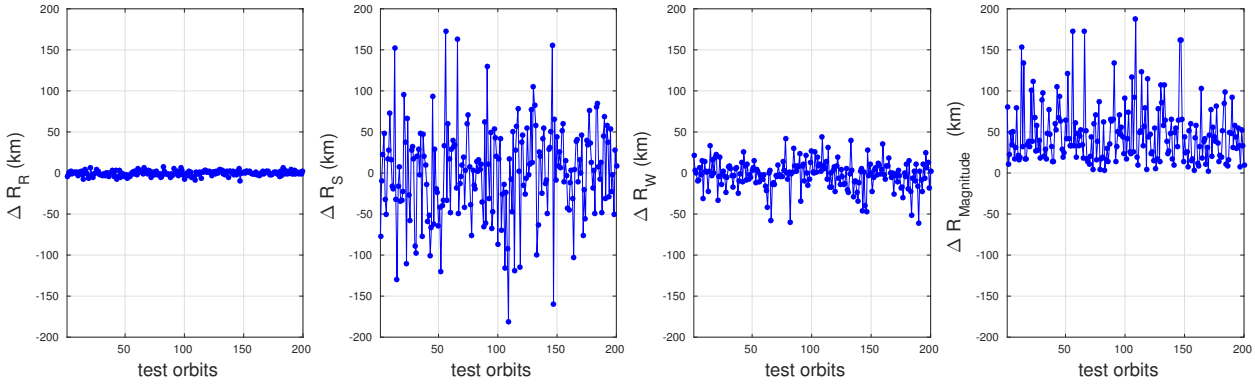

Figure 2.5: RSW errors of test orbits based on GRIFEX Priors

as follows.

$$A \sim R_e + U(635, 665) \text{ km}, \qquad e \sim U(0.025, 0.03),$$
$$\Omega \sim U(200^\circ, 205^\circ), \qquad I \sim U(117^\circ, 122^\circ),$$
$$\omega \sim U(65^\circ, 70^\circ), \qquad M = U(223^\circ, 233^\circ)$$

P_Γ results in a variance in initial position of 448 km. The training and testing setups were similar to GRIFEX. Samples of 4000 orbits were used for training the two stage sampled regressor (1.31×10^6 feature points in total) and 200 additional orbits were sampled for testing. The noise distribution $P(X|F)$ was chosen to be uniform with a width of 200 Hz. The probability of sampling in time were reduced corresponding to the behavior of MCubed-2.

MCubed-2 produces beacons approximately every 20 seconds with an arbitrary initial offset (depending on operational characteristics). The power levels of these beacons are modulated by the relative orientation of the antennas of the spacecraft and the ground (this can be seen in Figure 2.2). We reduce the sampling complexity of this distribution for training data generation by approximating it with a uniform distribution through $\tilde{\mathcal{T}}$ which is then selected by the horizon O. A total of 294 feature vectors were extracted over four passes for orbit determination. Table 2.2 shows the TLE estimated elements versus the estimates from the machine learning algorithm. In addition to the data acquired on orbit, additional data was generated for 200 test orbits for evaluation of the parameters. Figure 2.6 shows the normalized errors for each orbital element for the test orbits for MCubed-2 (normalized by the width of the support of the prior distribution). Orbital elements were estimated for the epoch: 23:00:00 2016/2/09 UTC.

The error in estimated initial position for the MCubed-2 spacecraft is 61.91 km. The

Table 2.2: Keplerian elements of the MCubed-2 spacecraft.

	A(km)	e	I(deg)	Ω(deg)	ω(deg)	M(deg)
True (JSpOC Estimates)	644.611	0.0273	120.493	201.978	67.501	225.47
Estimated	640.892	0.031	119.26	204.26	67.96	226.23

average error over the test orbits was 22.76 km. The RSW and total errors for the test orbits are shown in Figure 2.7. Note the improvement in estimation of the RAAN, inclination, mean anomaly and the semi-major axis and the RSW errors as compared to the estimates in GRIFEX. This is likely due to increased eccentricity, time of observation and decreased total variance in the initial position of the prior. This may also point to increased observability of parameters. Connections of observability metrics of this system to convergence bounds on learning algorithms should be explored in future work.

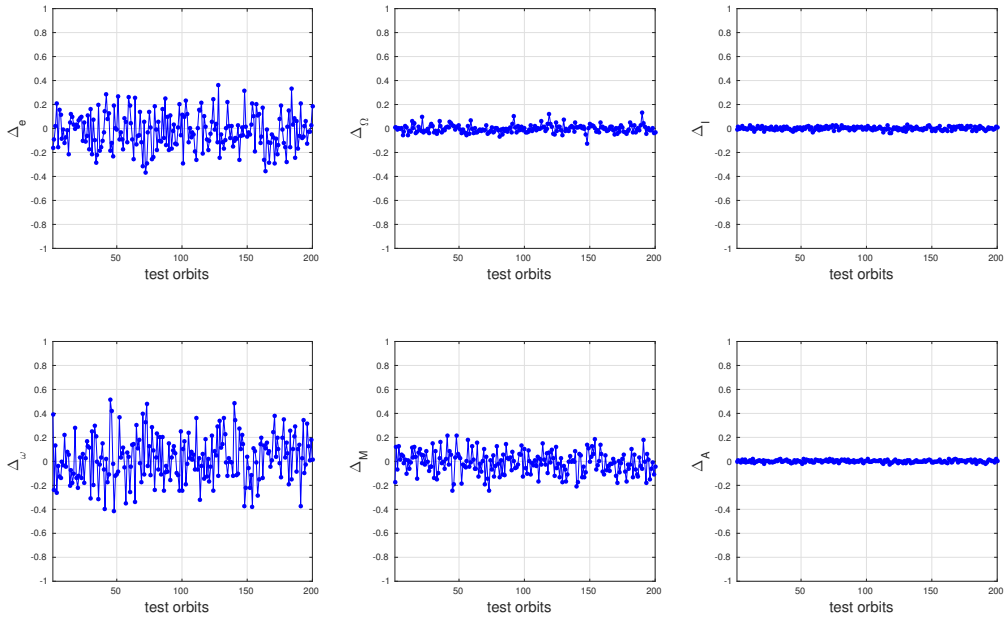

Figure 2.6: Normalized errors of orbital parameters of test orbits based on MCubed-2 Priors

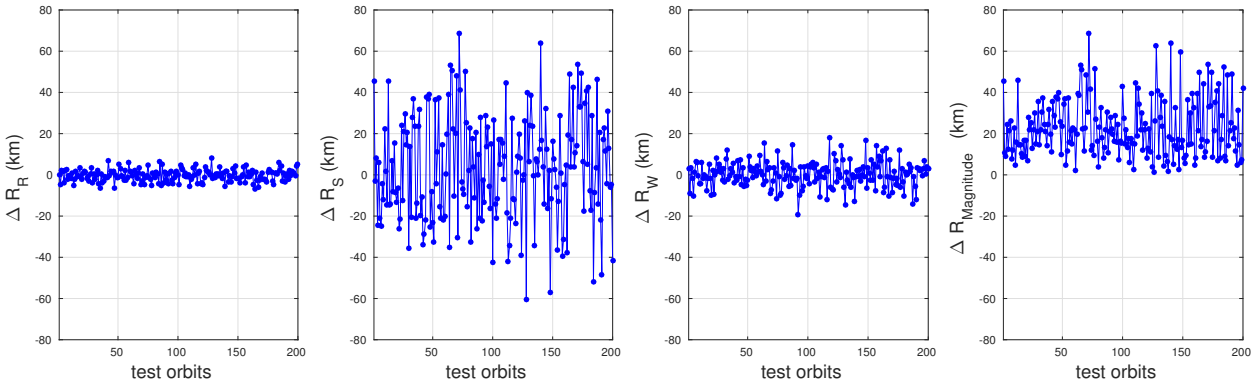

Figure 2.7: RSW Position Errors of test orbits based on MCubed-2 Priors

II.5.3 Position Based OD

We now present the results for a synthetic dataset simulating post deployment orbit determination of two spacecraft using position (direction of arrival and range data) from two ground stations (Ann Arbor and Chicago). This scenario simulates a TLE lottery, and shows that direction of arrival and range features from a noisy RADAR based system can be used to perform identification of the spacecraft based on orbit injection sequence in addition to orbit determination. It also demonstrates indirect generation of the priors of the spacecraft. The algorithm performs both the classification and regression tasks for orbit determination of both spacecraft. The sequence of deployment results in sample information for the classification algorithm to identify the different spacecraft. We shall first describe the details for generation of P_{Γ} and the propagators used, then describe the learning system and provide results.

Sampled Data Generation

The priors P_{Γ} for this scenario are not directly generated and require simulation of deployment scenarios. First, samples are drawn for a deployer spacecraft with the following distribution on orbital parameters:

$$A \sim R_e + U(650, 750) \text{ km}, \qquad e \sim U(0.03, 0.04),$$
$$\Omega \sim U(0^\circ, 5^\circ), \qquad I \sim U(70^\circ, 75^\circ),$$
$$\omega \sim U(350^\circ, 360^\circ), \qquad M = U(300^\circ, 310^\circ)$$

Two spacecraft are then deployed from the deployer spacecraft. The first spacecraft is provided with a change in velocity (Δv) of -0.5 m/s along the direction of velocity of the deployer. The second spacecraft is inserted 200 s after the first one and is provided with a Δv of +0.5 m/s along the direction of velocity of the deployer to allow the two spacecraft to separate. For both spacecraft, an additional 1.25 m/s is provided in the plane perpendicular to the velocity of the deployer in a direction drawn at random in this plane. The deployments cones of the two spacecraft from the deployer body fixed frame are as shown in Figure 2.8. The two spacecraft are then allowed to separate by a few km by propagation of their states for 6 hours to simulate passes of multiple small spacecraft whose positions can be resolved by a RADAR system. The distribution of the two spacecraft states at the 6 hour epoch is P_Γ. The training and test distributions are generated the same way.

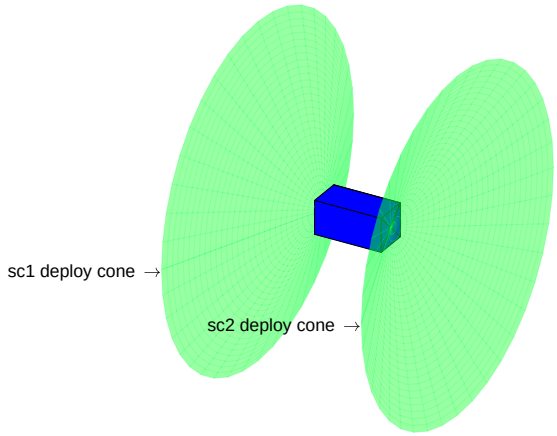

Figure 2.8: Deployment cones of spacecraft 1 & 2

The analytical propagator used to propagate the two spacecraft worked with the EGM96 gravitational model for spherical harmonics. Coefficients up to 4th order harmonics were taken into consideration along with precession and nutation characteristics, to provide sufficient model fidelity for the synthetic data. The time synchronization errors between the two ground stations were assumed to be negligible resulting in one time-stamp per measurement. The resulting feature vectors were direction of arrival and range information from both ground stations and the time-stamps. This synthetic data generated is similar to those generated by a bi-static RADAR, and therefore, measurements are generated only when the two spacecraft are in the horizons of both the ground stations. Noise in measurement ($P_{X|F}$) of 0.1° was added for azimuth and elevation measurements and 1 km for range measurements at both ground stations, which is generally greater than in practical systems, to test robustness to noise. Data for a total of 4700 orbits were generated. Around 70 feature vectors were generated per orbit per spacecraft for the training datasets. The total variance in initial position was 966 km for each spacecraft. The average separation of the two spacecraft at the epoch for orbit state estimation is 74.92 km.

Learning System

The first 500 orbit datasets were used along with identifiers for spacecraft to train the transfer learning system. A random Fourier feature approximation based transfer learning approach was applied to improve speed of training the data [85]. The performance of the algorithm was contrasted against its performance with the traditional logistic regression in which the data from all the orbits were pooled before classification (pooled classification). The test system consisted of the remaining 4200 orbits whose datapoints had to be classified. Traditional pooled classification systems do not work well for direction of arrival data as the meta-distributions of the two classes can be identical between two different orbit insertion scenarios. However, if the marginal distribution of both spacecraft is known, as it is for

Table 2.3: Classification error comparison.

Classification Method	% Training Error	% Test Error
Transfer Learning	0.48	0.74
Pooled Classification	45.77	49.42

transfer learning, the identity of the spacecrafts can be learned.

The output of the classifier is then fed to the regression system for orbit determination of both spacecraft. Note that the classified outputs are used in training to maintain consistency between the training and test distributions as reasoned in Section II.4. Classified points from the first 4000 orbits were used to train each regression system. The orbital elements used were the position and velocity vectors at the epoch instead of traditional Keplerian elements as the argument of perigee and the right ascension angles were no longer compact sets (i.e., it varied as $[x_1, 360) \cup [0, x_2]$, see Section A.3), even when the underlying space of probability distributions were compact. Classified points from 200 orbits were used to test orbital parameter estimates. The average error in estimation of the position of the first spacecraft is 20.06 km. The average error in estimation of the position of the second spacecraft is 19.36 km. Note that this is less than half the average separation of the two spacecraft, so the positions are identifiable and resolvable with information from a single pass. Figures 2.9 and 2.10 show the normalized errors of the orbital elements (normalized by the width of support of the prior).

II.5.4 Position Based OD - Lunar Orbit

The characteristics of the system described in Section A.3 are also satisfied for an N-body problem. In fact, if the data generation system was constructed with a general celestial dynamical system, no changes will be required to the orbit determination system even with N bodies. To test the empirical behavior of the algorithms we consider a lunar orbit transfer

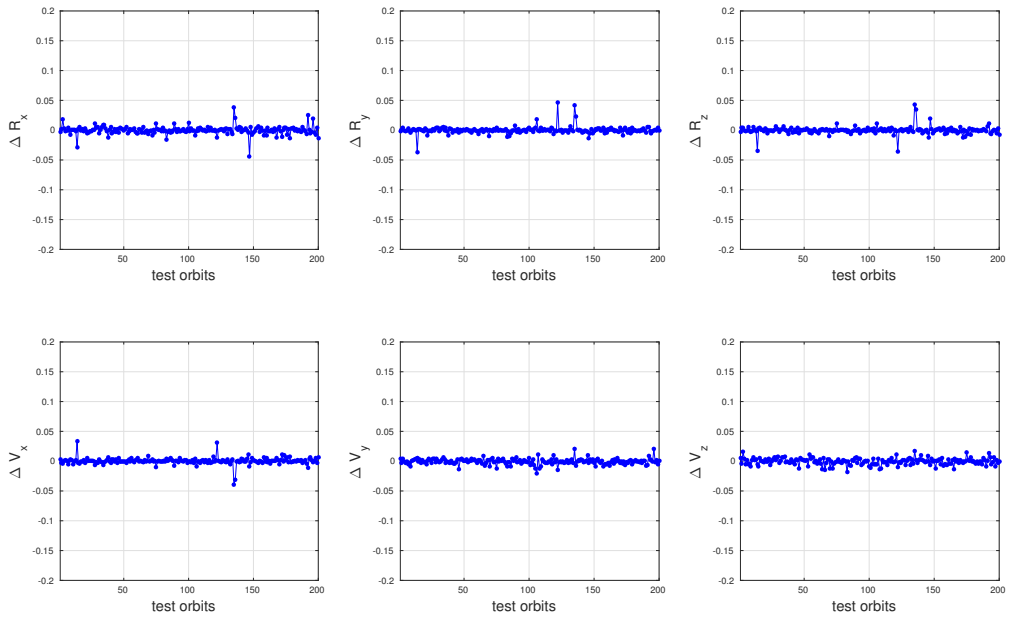

Figure 2.9: Normalized errors of orbital parameters of test orbits of spacecraft 1

scenario. The three body problem was the first described example of a chaotic system [91, 92, 93] where small changes in the initial orbital parameters lead to large changes in distributions associated with the data. We consider orbit estimation of a 4 day lunar transfer orbit with direction of arrival and range observations from one ground system over one pass. We first describe details of the propagation system and the orbit and prior design and then present the results of the orbit determination scenario.

Propagation and Orbit Design

For deep space orbit propagation, the propagator used in Section II.5.3 was extended to include accelerations from the Moon, Sun and Jupiter. To simplify and speed up computation, positions of these celestial objects were computed using JPL Ephemerides data. Further computational simplifications were performed by limiting sampling time to 300 seconds over a period of 4 days and interpolating for positions in between (Gaussian splines were used). Epoch for orbit insertion in this hypothetical scenario was chosen to be 18:00:00 1/1/2016 UTC.

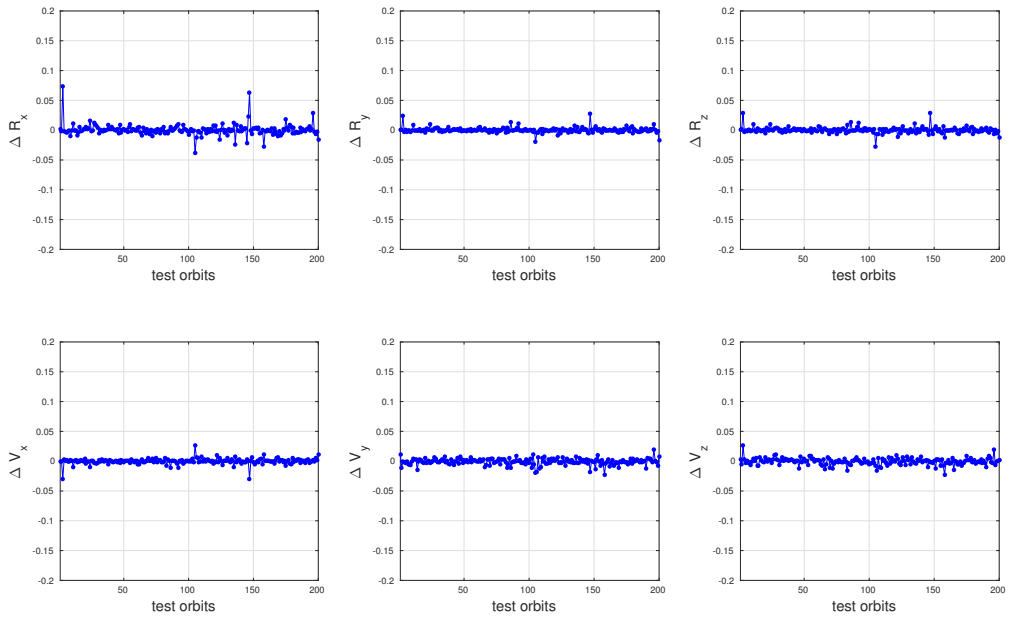

Figure 2.10: Normalized errors of orbital parameters of test orbits of spacecraft 2

The prior P_Γ was designed as follows. First, a 4 day direct lunar orbit [94] was designed to obtain a specific trans-lunar injection state. This state was then perturbed in position and velocity from samples drawn from a given set of distributions. An initial orbit using a circular restricted 3 body problem was constructed in a synodic frame. The synodic frame was transfered to a 3 dimensional system with the appropriate transformation. The circular lunar orbit was then replaced with JPL Ephemerides and the initial states were perturbed to obtain a transfer orbit. Lunar spherical harmonic coefficients were not taken into consideration and the moon was treated as a sphere due to negligible perturbation effects during the test period. The orbits designed were similar to the 4 day injection orbits described in Parker [94]. The initial state of this orbit was used as initial input parameters to the distribution P_Γ. The perturbations for position and velocity were designed as compact sets of conic sections with the following distributions (States are in spherical coordinates):

$$R_r \sim R_{r,init} + U(0, 0.05R_{r,init}) \text{ km}, \qquad V_r \sim V_{r,init} + U(-0.02V_{r,init}, 0.02V_{r,init}),$$

$$R_\theta \sim U(R_{\theta,init} - 2^\circ, R_{\theta,init} + 2^\circ), \qquad V_\theta \sim U(V_{\theta,init} - 1^\circ, V_{\theta,init} + 1^\circ),$$

$$R_\phi \sim U(R_{\phi,init} - 2^\circ, R_{\phi,init} + 2^\circ), \qquad V_\phi \sim U(V_{\phi,init} - 1^\circ, V_{\phi,init} + 1^\circ).$$

This prior results in an effective variance of 203 km in initial position. The samples drawn from the above distributions are then used to evaluate the orbit determination system. Figure 2.11 shows the paths generated by the analytical propagator in the Earth Centered Inertial (ECI) frame for 20 sample states drawn from P_Γ. A uniform distribution over time was used to generate observation vectors from one ground station. The number of samples were chosen to result in approximately one sample every 3 minutes over one pass (<12 hour period). Note that this 12 hour period does not begin during orbit insertion but 6 hours after insertion (This is due to the fact that the spacecraft is not in view of the chosen ground station during orbit insertion. Besides interpolation errors generated by the propagator, no additional noise was added to the system to generate observations.

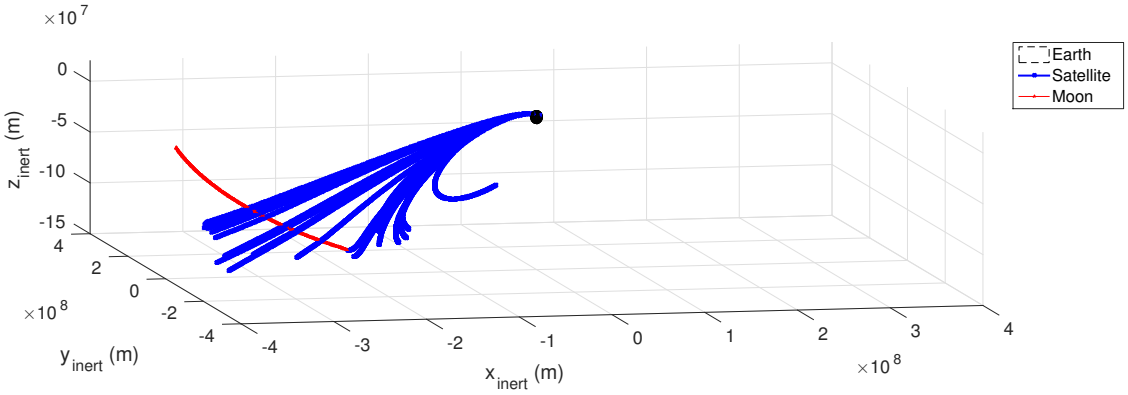

Figure 2.11: Example lunar transfer orbits drawn from prior distribution

Learning System

Similar to the other scenarios, 4000 orbits were generated for training and 200 for testing. The preprocessing step was modified to normalize time period and range variations. Besides this no changes were performed to the learning algorithm. Figure 2.12 shows the normalized errors in the estimates (normalized by the width of the support of the prior of each element). The average error in position estimation was 4km. This error is lower in comparison to similar scenarios which use direction and range information for orbit estimation. Note that due to finite sampling and chaotic nature of the orbits, outliers will exist with very low

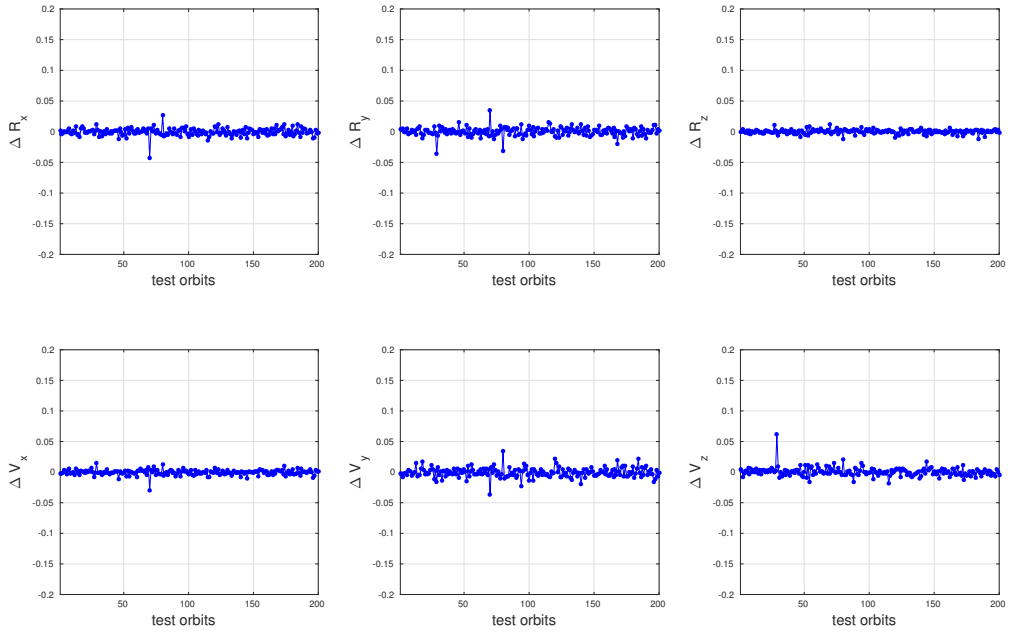

Figure 2.12: Normalized errors of orbital parameters of test orbits for trans-lunar scenario

probability.

II.5.5 Position based OD - Comparison with EKF

We compare the performance of the learning technique proposed with a traditional orbit determination system based on the EKF. The propagators used were the same as described in Section II.5.3. We shall first describe the exact characteristics of the orbit determination system used to compare against and then provide details of synthetic data generated for comparison.

Sample Data Generation

The probability distribution over orbital parameters chosen for this scenario was designed from two perspectives. First the preliminary orbit determination system's performance with large noise added to the observations should be sufficient to force the EKF out of its linear

region. Second, the noise added should be admitted by the data preprocessing and 6σ editing filters used in state of the art EKF based orbit determination algorithms [13]. Orbits with relatively high eccentricity were chosen with the following priors:

$$A \sim R_e + U(5000, 5400) \text{ km}, \qquad e \sim U(0.4, 0.35),$$
$$\Omega \sim U(350^\circ, 5^\circ), \qquad I \sim U(70^\circ, 75^\circ),$$
$$\omega \sim U(0^\circ, 10^\circ), \qquad M = U(300^\circ, 320^\circ)$$

The propagator described in Section II.5.3 was used to generate data over one pass. Uniform noise with width of $0.2^\circ, 0.2^\circ, 2$ km is added to the azimuth, elevation and range measurements respectively. A total of 4200 random orbits were generated.

EKF Based OD

This orbit determination system consisted of a preliminary orbit determination system for initialization followed by the EKF. The preliminary orbit determination system used was Herrick-Gibbs [31]. The preliminary orbit determination was conducted on points on a section of the orbit near the perigee and the points were chosen such that the time period between the points was about 10 minutes, based on the results of the performance with the ascending Molniya scenarios in Schaeperkoetter [95]. The preliminary OD system was followed by an EKF with 6σ data editing (see Wright [13]). The dynamic system used for propagation of the EKF is identical to the propagator used for generation of the observations. This was done to compare the performance of the EKF in scenarios with significantly noisy observations.

For a parity in comparison of the two techniques the same set of orbits were used for

parameter selection for the EKF and training of the machine learning based OD system. The first 4000 orbits were used to generate the error covariance matrices for the EKF. The 4000 orbits were also used to train the machine learning algorithm (5 fold cross validation). No changes to the learning algorithm were made from the previous sections. Both the EKF and the learning based OD system were tested on the data points generated from the last 200 orbits. Figure 2.13 shows the initial position errors for the 200 orbits under test. Note that if the EKF diverges to a point where no observations lie in the 6σ range the measurement editor will edit out all further observations limiting further updates. As can be seen, the learning based orbit determination system has significant performance advantage over the EKF, albeit under significantly larger computational requirements. The few outliers for the learning based system will converge to zero in probability with increase in training data as detailed in Section II.4.

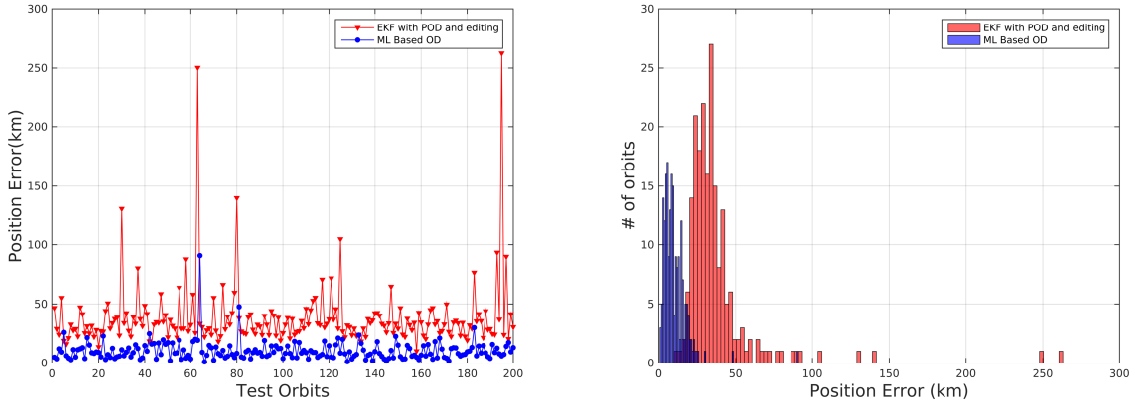

Figure 2.13: Comparison of EKF and Learning Based OD

II.5.6 Discussion

A summary of the position error results is shown in Table 2.4. For Doppler based orbit determination, the Along-track and Cross-track errors are larger. This is a direct consequence of the fact that each individual point contains very little actual position information and position can only be gained from the changes in the probability distribution that generate the

points. Radial Errors as low as radial information can be gained from zero Doppler cross-over points. The synthetic test data error magnitudes are of the same order as the errors produced by the experimental datasets. If the data generation systems are not sufficiently realistic, there can be discrepancies in the test errors and the errors produced by the experimental datasets, as the learned system will not directly correspond to the experimental data. This requirement also applies to the noise modeling of the Doppler measurements. While the MC2 orbit determination position errors are larger in comparison to GRIFEX, the equivalent comparison in terms of the orbital elements themselves produces the opposite result. This is a consequence of the fact that the optimization to compute orbital elements does not directly correspond to reducing position errors as the transformation between the two is not linear.

With a constant number of training orbits (4000), decreasing uncertainty and improving observability improves accuracy. This behavior can be seen in two scenarios. The accuracy of Doppler-only OD is lower in comparison to Position based orbit determination due to differences in observability and noise effects. The accuracy is highest for chaotic orbits with small initial spaces, where small changes in the initial condition produce very large changes in the orbit. Note here that while the lunar orbit scenario observation intervals were for 10 hours, the average transmissions characteristics produced equivalently lower number of transmissions per orbit such that the datasets of the position based orbit determination systems had the same order of training and test data points per orbit as in the LEO case.

For position based orbit determination, the along-track errors are larger. This behavior is expected as velocity information cannot be directly gained from the features. The sum of average and RMS errors for the two satellites is less than the average separation between the satellites, and the spacecraft can be resolved in the orbit insertion scenario. Note that for the position based OD scenarios, noise of $(0.1^\circ, 0.1^\circ, 1\text{km})$ were added to the (Azimuth, Elevation, Range) measurements.

Table 2.4: Comparison of test errors

	Prior Position Std. Dev (km)	$\lvert\tilde{\mathcal{T}}\rvert$ (hr)	Radial Error (km)	Along-track Error (km)	Cross-track Error (km)	Total Error (km)
GRIFEX Synthetic	765	4.5	2.96	56.6	17.49	59.31
GRIFEX Experimental	765	4.5	6.92	7.33	-28.30	30.05
MC2 Synthetic	448	7	2.86	25.85	6.19	26.73
MC2 Experimental	448	7	13.46	28.97	-53.04	61.91
Position Synthetic (LEO) 1	966	1	15.76	38.85	10.79	43.29
Position Synthetic (LEO) 2	966	1	10.60	25.34	2.71	27.6
Positon Synthetic (Lunar)	203	10	1.32	5.26	1.40	5.6

II.6 Conclusion

We presented the orbit determination problem of multiple spacecraft from a learning theoretic perspective. The learning system allows for estimation of spacecraft orbits over a very broad set of conditions. The learning algorithm requires only bounded and compact space specifications without the need for initialization in the linear region of the estimator, unlike traditional non-linear estimators. We showed that the combined algorithm is consistent when the mapping is continuous and the classifiers are well defined. We presented experimental results for Doppler-only orbit determination scenarios with operational spacecraft and synthetic deep space orbit scenarios. We also provide comparisons with the EKF in a synthetic scenario with large measurement noise, where the proposed approach overcomes the divergence limitations of the EKF. The learning approach can also be used to perform state estimation in weakly observable, unactuated dynamic systems with random and noisy observations over finite time periods.

CHAPTER III

Collaborative Orbit Determination using Ground Station Networks

III.1 Introduction

We now consider the problem of constructing a ground station network architecture to perform orbit determination as part of mission operations. We are interested in a GSN architecture to observe transmissions from a group or cluster of n_S satellites when their initial orbital parameters are *uncertain* and belong to a *set* $\mathcal{J}$ instead of being known with high accuracy. We do not assume that these transmissions be decodable, just that they can be observed and their Doppler shifts measured by spectrum monitoring algorithms.

In Chapter II, we showed that when the orbital parameters governing spacecraft dynamics are observable from a large number of noisy observations which satisfy certain broad regularity conditions, it is possible to estimate orbital parameters even when the orbit uncertainty does not satisfy linear region constraints required by standard orbit determination techniques such as the EKF. Using this technique it is possible to perform orbit determination using Doppler only observations gained from a ground station network. In this chapter, we develop

a network architecture that enables orbit determination with low-cost, distributed ground stations.

This chapter is organized as follows: Section III.2 expands on the problem setup developed in [96] with design variables required for practical ground station networks and details the requirements of the architecture. Section III.3 develops physical layer ground station network architectures for orbit determination, Section III.4 provides resource allocation information associated with an orbit determination tracking session, Section III.5 provides additional details of training data generation applicable to practical ground station networks and Section III.6 provides results for a synthetic orbit determination scenarios over a ground station network. Section III.7 concludes the chapter.

III.2 Parameters of Architecture

For this GSN architecture, we provide formal definitions of the parameters required for its design and control. We are interested in architectures for set of n_S spacecraft orbits to be determined using a network with n_{GSN} ground stations over an observation period $\tilde{\mathcal{T}}$. The n_S spacecrafts have orbital parameters $[\gamma_1, \gamma_2, \cdots \gamma_{n_S}]$. We shall view the orbital parameters as random variables and satisfy a probability distribution P_Γ for $\gamma := [\gamma_1, \gamma_2, \cdots \gamma_{n_S}]$. The marginal probability distribution, P_{Γ_i}, of a satellite $i, 1 \leq i \leq n_S$, is defined over a set $\tilde{\mathcal{J}}$ (for simplicity, we assume that the sets are the same for all the satellites). The set $\tilde{\mathcal{J}}$ represents the possible set of orbital parameters that the satellites in the cluster can have.

The i^{th} spacecraft produces transmissions at time stamps T_S over a time period $\tilde{\mathcal{T}}$ according to the probability distribution $P_i(T_S|z)$, where z is a parameter that determines the probability distribution (more on z later). The n_S satellites in total produce observations according to a mixture probability distribution $P(T_S|z) := \sum_{i=1}^{n_S} P_i(T_S|z)$.

Given P_Γ and observations, the network's goal is to perform orbit determination with a set of n_G ground stations, where $n_G \leq n_{GSN}$. We define the dynamical system that describes the motion of a spacecraft i with an observer ground station $j, 1 \leq j \leq n_G$, as $U_j(\gamma_i, t)$. Further, let $U_j(\gamma, t) := [U_j(\gamma_1, t), U_j(\gamma_2, t), \cdots, U_j(\gamma_{n_S}, t)]$ be the dynamical system of the spacecraft cluster as seen from observer j. Over any subset n_G of ground stations as observers, we describe the total the spacecraft cluster dynamic system as $U(\gamma, t)$. Similarly, we define $V(\gamma, t)$ as the dynamic system describing the direction of the satellite cluster from the n_G ground stations where $V_j(\gamma_i, t)$ gives the direction (azimuth and elevation) of satellite i from ground station j. At time T_S, spacecraft i randomly generates, according to probability $P_i(T_S|z)$, noiseless measurement samples $F = [F_1, F_2, \cdots, F_{n_G}, T_S]$ which is observed by the ground station network, where $F_j = U(\gamma_i, T_S)$. Since we don't assume decodability of the transmissions and make no assumptions on frequencies of transmission, we do not require that the identity of the spacecraft producing the transmission be known (it can be any of the n_S spacecraft randomly generating observations). Ground station j can observe $[X_j, T_j]$, a noisy version (noise both in value X_j and in time synchronization T_j) of the noiseless measurement $[F_j, T_S]$, only if the satellite producing the transmissions lies inside the horizon mask of ground station j, H_j. For a given ground station j, the GS architecture determines and controls two sets of design variables:

1. Based on hardware characteristics and coverage, the network provides a visibility region O_j which governs when ground station j will produce observations (note $O_j \subseteq H_j$). Measurement samples are obtained only if $V_j(\gamma, t) \in O_j$. The pointing profile is a set of antenna pointing angles that define the visibility region O_j of spacecraft passes of spacecraft with an initial state that belong to the support of P_Γ.

2. The parameter z is network variable made up of four broad sets of parameters for each spacecraft i: $z_{ts}(i), z_{nc}(i), z_{sc}(i)$ and $z_{fv}(i)$. $z_{ts}(i)$ is the timing uncertainty variable capturing the synchronization uncertainty in the network and the propagation uncer-

tainty of measuring the signals of spacecraft i. $z_{nc}(i)$ denotes the hyper parameters associated with the noise characteristics for measuring signals of the spacecraft. $z_{sc}(i)$ denotes the characteristics of the transmission systems of the spacecraft that are used for measurements. $z_{fv}(i)$ denotes the parameters controlling identification of the cyclostationary feature vectors associated with spacecraft transmissions, such as bandwidth and coding rate identification parameters, noise and signal power thresholds required to determine the features of a particular spacecraft by a ground station. The choice of parameters in z_{fv} is correlated to z_{sc} through communication systems design (See [97, 90, 98, 89]). Based on the network measurement system characteristics, the network shall provide the system parameters z_{ts}, z_{nc} and the corresponding probability distributions. The ground station produces measurements $[X_i, T_i]$. The probability distributions associated with the network observation measurements $P([X_i, T_i]|F_i, T_S, z)$ are known to the network. For example, X_i can consist of cyclostationarity based features of narrow band communication systems with probability distributions as described in [97, 90] and $P(T_i|T_S, z)$ is the GS timing system uncertainty. We encapsulate the network variables influencing the probability distributions through variable z.

The network as a whole obtains measurements $[X, T] = [X_1, X_2, \cdots, X_{n_G}, T_1, T_2, \cdots, T_{n_G}]$ over the time sets of observation in $\tilde{\mathcal{T}}$. The design parameters of the network are optimized for the goal of enabling orbit determination. In [96], we show that if U is observable and continuous over the visibility regions $\{O_j\}_{j=1}^{n_G}$ of the ground station network, it is possible to estimate the orbital parameters of the cluster of satellites. The design variables are chosen to satisfy these requirements of observability, continuity and visibility. For this purpose, the global variables that need to be selected and controlled by the architecture for the orbit determination problem are as follows:

- The selection of n_G ground stations in the network over time $\tilde{\mathcal{T}}$ as operational scheduling of an orbit determination (OD) session.

- The identification of a pointing profiles for ground stations with directional antenna patterns.

- Variable controlling imperfect synchronization between ground stations z_{ts}, and probability distributions controlling time delays between spacecraft transmissions and measurements.

The design variables and architecture need to satisfy the assumptions of the learning system for orbit determination detailed in [96]. This results in a set of requirements for the GSN.

III.2.1 Architecture Requirements for Orbit Determination

The physical layer design of the network, the scheduling system and tracking algorithms need to satisfy fundamental requirements regarding the nature of the observations collected such as compactness of the support of P_Γ, Observability and continuity of the effective dynamical system, guarantees of observations over the scheduled and tracked intervals and continuity of the measuring system distribution over the tracking intervals.

1. Compactness of the support of P_Γ: The support of the probability distribution that governs the uncertainty in orbit parameters should be closed and bounded. This requirement is guaranteed since total kinetic energy imparted for spacecraft orbit injections are finite and since we are assuming that no further propulsion occurs during orbit determination. Construction of P_Γ is discussed in Section III.5.1.

2. Observability and continuity of effective dynamic system: The effective dynamic system presented by the observations of the ground station system when the observations can only belong to the those that can be detected by the antennas in the GS network nodes should satisfy observability and continuity requirements. According to the theory

established in [96], if the effective dynamic system is observable and continuous then there exists a continuous map from the set of observations over interval $\mathcal{T}$ to the orbital parameters. The architecture presented will guarantee a continuous effective dynamic system and we shall guarantee observability by low prediction errors of the map learned by the learning cluster. Low prediction errors on test data implies that the underling system is identifiable and therefore observable over $\mathcal{T}$. This guarantees that with sufficient number of observations, the orbits of the satellites can be determined.

3. Guaranteeing observations over the scheduled intervals: To guarantee sufficient number of observations from the spacecraft during the tracking intervals, we will assume that there exist intervals of size τ in $\mathcal{T}$ such that τ is much smaller than the effective pass interval over which at-least one observation is guaranteed. In GS network terms, τ upper bounds the time between transmission intervals of the satellite. This criteria is generally satisfied by beacon intervals of CubeSats (more details in Section III.4).

4. Continuity of the measuring system distribution over the tracking interval: There are two parts to satisfying this requirement: time continuity of measurement intervals tracked and continuity of the noise distribution $P(X|F, z)$ with respect to F. We guarantee time continuity through the scheduling and tracking algorithms developed in Section III.4. The continuity in the distribution of noise is generally satisfied for all types of measurements in orbit determination of Doppler, ranging, D-DOR etc. For the Doppler measurements we focus on in this chapter, this condition is satisfied for narrowband communication systems as discussed in [97, 90].

In the following sections, we present a network topology and design considerations associated with deployment of an OD session over a federated ground station network. We present physical layer abstractions associated with a ground station network architecture for orbit determination. Global Network architectures for orbit determination require augmentation of the Network Operations Center with a learning cluster consisting of computing nodes.

Node level architectures require cognitive radio approaches for spectrum monitoring with software defined radios. Detailed network architectures are presented in Section III.3.

We develop algorithms for selection of nodes for OD, scheduling and operations at the network level and operations of the ground stations at the node level for the purposes of orbit determination. Orbit determination will be performed over a set of individual tracking intervals which we define as an *ODTrack Session*. Algorithmically, there are three components to the tracking and scheduling algorithms:

- Selection of ground stations of the network.
- Selection of time intervals of tracking (Sessions of tracking).
- Selecting a pointing direction for the GS antennas for tracking uncertain passes.

Details of the session architecture are discussed in Section III.4.

III.3 Network Architecture

We present network layouts for integration of orbit determination systems into the network architecture. We first present global network architectures and then consider node-level architectures.

III.3.1 Global Architecture

The global architecture is as shown in figure 3.1. The architecture augments the standard federated ground station network architecture with a learning cluster. The instantiation and control of the ODTrack session will be performed by the NOC with information provided by the learning cluster. The ODTrack Session will be in operation during pass intervals in

the session interval $\tilde{\mathcal{T}}$. Prior to instantiation of the ODTrack session, state uncertainty P_Γ is calculated by using state uncertainties of spacecraft deployer along with satellite deployment sequences or from TLE uncertainty projections. We shall consider computation of P_Γ in section III.5.1.

Learning Cluster For OD track session, the NOC scheduler initializes learning cluster with state uncertainties $\mathcal{J}, P_\Gamma$, observation interval $\tilde{\mathcal{T}}$, noise characteristics z_{ts}, z_{nc}, spacecraft behaviors z_{sc}, z_{fv} and the parametrized version of the distribution $P(X|F, z)$. This contains sufficient information to construct datasets for scheduling, tracking and training. The NOC instantiates an ODTrack session in learning cluster with P_Γ, z and $\tilde{\mathcal{T}}$. During instantiation of the ODTrack session, the data generation system in the learning cluster determines the subset of all available ground stations with appropriate noise level and signal strength requirements for orbit determination. Learning Cluster then computes specific schedules for a subset of these ground stations and provides *pointing profiles* $\{APP_j\}_{j=\{1,2,..n_G\}}$ for the corresponding ground stations. The pointing profiles will consist of a set of a session level elements for the ground stations selected for spectrum monitoring. Session level elements engage the ground station system over different intervals [9]. The NOC uses $\{APP_j\}$ with encoding and decoding (codec) information to reserve $n_G(\leq n_{GSN})$ nodes over interval $\tilde{\mathcal{T}}$ (Session layers $\{S_j\}$). The details of this procedure is presented in III.4.

Post instantiation, the learning cluster enters the training phase for full training data generation and hyper-parameter estimation (cross validation). The generation and cross validation phases are fully parallelizable, internally and with network data collection. Training data generation will consist of highly accurate system models for orbit propagation and noise sampling. It will also take uncertainties in time synchronization between ground stations. Details of the data generation system are discussed in section III.5.

The learning cluster will also have a network interface to the nodes of the GS network.

During the OD Track session, the GS nodes will provide the learning cluster with information required to construct the feature vectors for orbit determination. Information from ground station i will consist of features obtained by ground station and result from the spectrum monitoring operations that will be performed at the nodes. The OD algorithm proposed in Chapter II does not require ordering of the packets and it is assumed that all the packets will be received in random order by the end of the last session layer instantiation by the ODTrack session. The cluster will perform marginal transfer learning to determine the feature vectors to be used for the orbit determination of the different spacecraft.

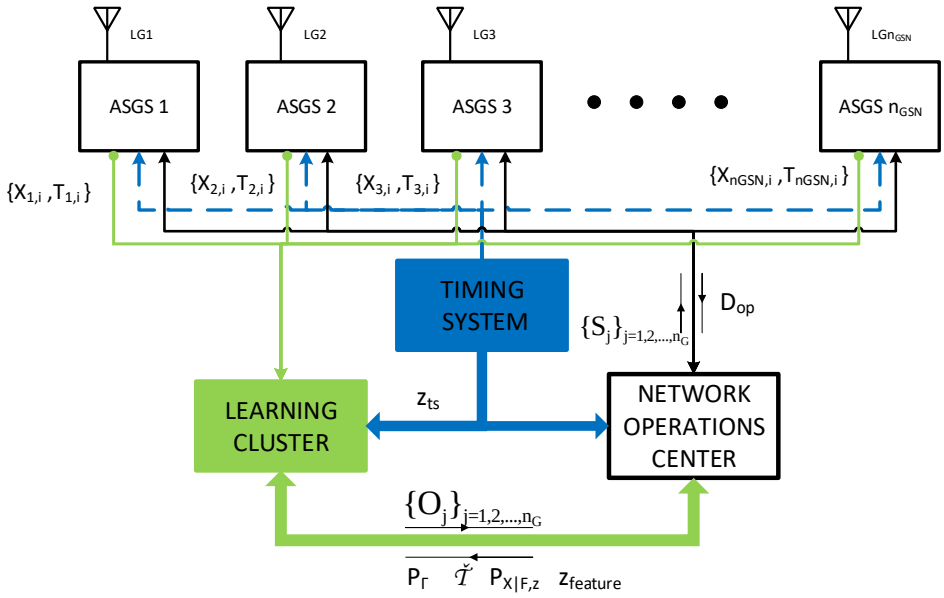

Figure 3.1: Global architecture

III.3.2 Node Architecture

The information generated by the learning cluster can be used to track spacecraft using **Augmented Software Ground Stations (ASGS)**. The broad architectures of the ASGS are shown in figure 3.2. ASGS performs spectrum monitoring for noise characterization and identification of presence of modulated transmissions, in addition to operations. During all session layer operations the ASGS maintains a real time noise floor estimate. The Software

Ground Station has a series of adaptive filter-banks with variable session layer characteristics which depend on the type of session layer instantiated. For standard operations sessions, only the band around the center frequency of operation is under consideration and all other information is filtered out. The system behaves as a normal software defined ground station[9, 99]. The ground station makes the noise floor estimates available to the learning cluster to compute pointing profiles.

During ODTrack sessions, when tracking spacecraft transmissions, autonomous radio [100] or cognitive radio approaches [89, 101] is used in obtaining modulation characteristics. Spectral analysis is performed only when the received power is greater than the noise floor by a threshold (P_{thres}). Selection of P_{thres} depends on link budget parameters associated with the group of spacecraft. P_{thres} is determined by signal detection false alarm rates and the probability distributions of the features being estimated. Sections of the complex baseband samples are time stamped using the timing system. When detection of features are successful, the average UTC time stamps of the features over the integration times are also attached to the features. Perfect synchronization is not expected between ground stations however, the probability distribution of timing errors are assumed to be known to the learning cluster. The feature detection algorithm is not required to decode any unique identifications of the transmissions. The identification of the transmissions will be performed at the learning cluster. In the presence of multiple modulation peaks at different frequencies, multiple identification should be performed through identification of autocorrelation peaks (See [98]).

The antenna characteristics driving the selection of the n_G ground stations are 3dB beamwidths and antenna gains sufficient to satisfy modified link budget requirements. The two selection rules guiding antenna selection can be stated as follows:

- Ground stations which meet P_{thres} requirements for Antenna Gain - 3dB are first selected.

- Among these ground stations, ground stations that can capture the largest power over the largest percentage of the passes are selected.

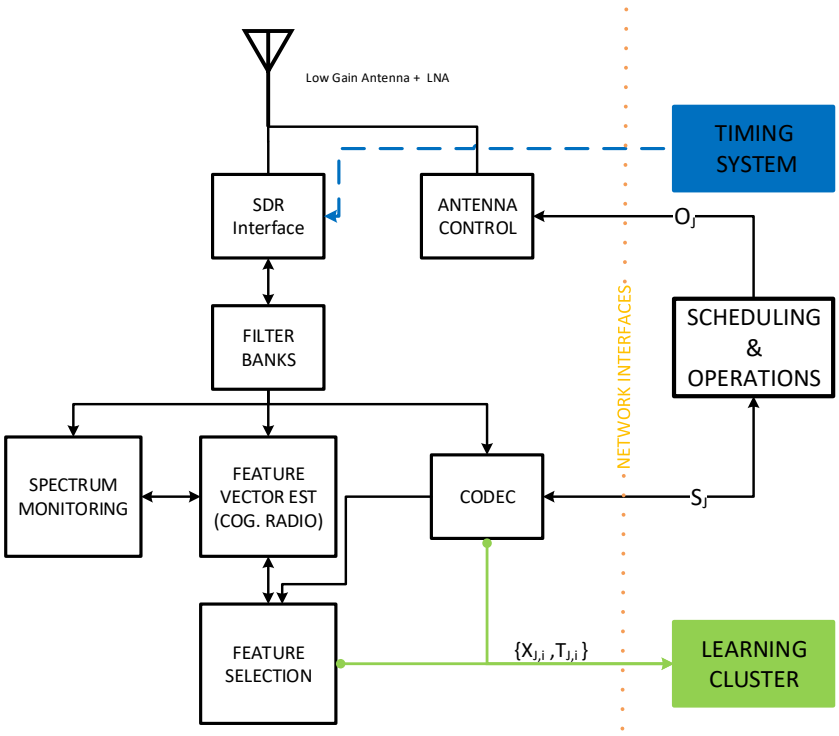

Figure 3.2: ASGS architecture

III.4 Scheduling and Tracking

Scheduling and tracking with uncertainty involves session instantiation and tracking to operate over passes defined over the set of orbits with initial conditions in $\mathcal{J}$. For this scenario session instantiation defines intervals over which ground stations have to be reserved and tracking parameters are captured through a sequence of antenna pointing directions. These algorithms do not depend on the exact nature of the prior P_Γ but on its effective support $\mathcal{J} := \cup_{i=1}^{n_S} \tilde{\mathcal{J}}_i$. We will discuss scheduling and tracking algorithms assuming that we are given $\mathcal{J}$ and then discuss details of construction of P_Γ in section III.5.

We use a finite approximation of $\mathcal{J}$ and $\mathcal{T}$ for computational purposes since $\mathcal{J}$ and $\mathcal{T}$

are closed and bounded sets consisting of a union of intervals. We approximate $\mathcal{J}$ using an ϵ-net[1] $\mathcal{J}_\epsilon$ to estimate the scheduling and tracking parameters. Since the dynamics of the spacecraft are continuous with respect to the initial condition, an ϵ-net should sufficiently approximate the scheduling parameters. A lattice (or grid) of points in $\mathcal{J}$ provides a sufficient construction of the net [102]. Similarly, we define a net $\mathcal{T}_\tau$ over $\mathcal{T}$.

All ground stations in the network that are available during $\mathcal{T}$ are taken into consideration for computation of reservation intervals and pointing profiles. Once pointing profiles are selected, the number of pass intervals available for the estimation of each orbit in $\mathcal{J}_\epsilon$ are computed. The minimum number of ground stations that provide sufficient pass intervals for all the orbits in $\mathcal{J}_\epsilon$ are then selected for orbit determination.

The first step in scheduling involves identification of pass intervals of $\mathcal{J}$ required for session level resource acquisition. The ODTrack session is a set of ground station contact intervals or passes (see Figure 3.3). In the terminology specific to [9], the ODTrack session is a group of individual sessions as shown in figure 3.3. The reservation intervals of ground station $j, 1 \leq j \leq n_G$ corresponds to the intervals during which any object with its orbit parameter in $\mathcal{J}$ will lie in the horizon of ground station j. More precisely, the ODTrack session will be made up of a group of time intervals or pass schedules $S_{jl}, l = 1, 2...L_j, 1 \leq j \leq n_G$ where L_j is the total number of pass intervals of ground station j. The schedules are such that the scheduled intervals at-least cover the measurement intervals (times intervals in a pass where the spacecraft can transmit). This implies that $\bigcup_l S_{jl} \supseteq \bigcup_{\gamma \in \mathcal{J}} \{t \in \mathcal{T}, V(\gamma, t) \in H_j)\}$

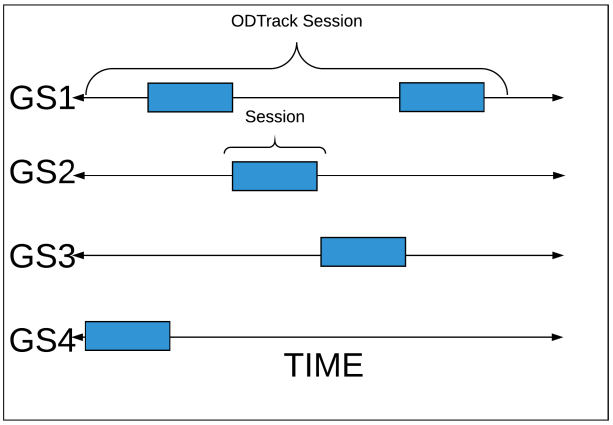

Figure 3.3: ODTrack Session

[1] See Appendix A.1 for the definition of ϵ-net

where H_j is the station mask for ground station j. We compute this by first computing the union of pass intervals for all the orbits in $\mathcal{J}_\epsilon$, $\bigcup_{\gamma \in \mathcal{J}_\epsilon} \{t \in \mathcal{T}_\tau, V(\gamma, t) \in H_j)\}$ and then identifying the pass intervals $I_{jl} := [I_{start,jl}, I_{end,jl}], 1 \leq l \leq L_j$. A correction for the net approximation is then used to produce the reservation intervals for ground station j as $S_{jl} := [I_{start,jl} - C_t\tau - C_\gamma\epsilon, I_{end,jl} + C_t\tau + C_\gamma\epsilon]$ where C_t, C_γ are the lipschitz constants of $V(\gamma, t)$ with respect to time and initial conditions.

Next, we consider tracking algorithms for orbit determination. Since we are dealing with ground stations, we define the set of pointing directions and time associated with a particular ground station as a *pointing profile*.

III.4.1 Pointing Profiles

The goal of pointing profiles is to maximize identifiable (not necessarily decodable) signals that can be picked up from spacecraft. For ground station j and pass interval l, it is a set APP_{jl}, of antenna pointing directions and time. It can used to construct the visibility regions O_j for ground station $j = 1, 2..n_G$, the region of observation over which measurements will be observed for ground station j as $O_j := \bigcup_{l \in L_j} APP_{jl}$. There are different types of pointing profiles that depends on the size of the set $\mathcal{J}$ in comparison to the coverage provided by the antennas of the ground station network. When the orbit uncertainty set is small enough that every orbit in the set can be seen the horizon coverage of the antenna, the ground station can effectively track the full satellite cluster with it's antennas. In this case, the pointing profiles are dynamic. Otherwise the pointing profiles are static (Point and listen configuration). When the uncertainty is large in the average along track direction, a simple static antenna pointing profile is used. When the cross track uncertainty is large, complex static pointing profiles are used.

We assume that the ground stations in the network have directional antennas. We use the ellipsoid approximation for the main beam of the antennas in a ground station. This results in spherical caps of coverage on the horizon (the horizon is half a unit sphere) whose angular widths corresponds to the 3dB beam-width of the antennas. The spherical cap can be rotated and translated on the half sphere representing the horizon (Figure 3.4). The pointing profile is a set of directions of the center of this spherical cap and the times of pointing at these directions.

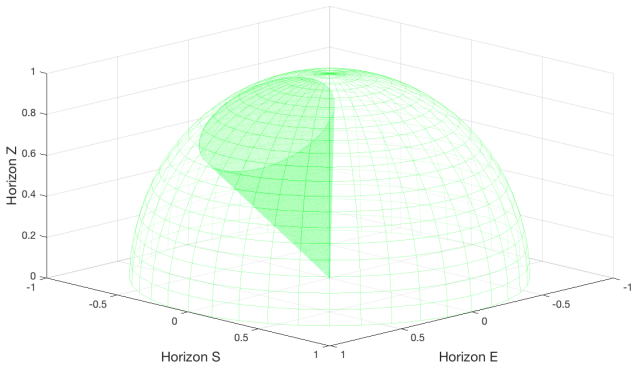

Figure 3.4: Antenna ellipsoid approximation and spherical cap

We provide definitions required for description of pointing profiles. Let $A(r, \phi)$ denote a spherical cap centered at direction $r \in S^2$ with angle ϕ representing the width of the spherical cap. We denote the spherical cap for ground station j centered along r_j with beam width ϕ_j as $A_j(r_j, \phi_j)$ and let $A_{ref,j}$ denote its spherical cap along a reference (parking) direction. For $s_1, s_2 \in S^2$, the geodesic distance is defined as $d_G(s_1, s_2) := \arccos(\langle s_1, s_2 \rangle)$. For a closed set $W \subseteq S^2$, we define the geodesic width of W as

$$w_G(W) := \max_{s_1, s_2 \in W} d_G(s_1, s_2),$$

and the minimal spherical cap A_W of W as the spherical cap with the smallest area such that $W \subseteq A_W$, i.e., if s_1^*, s_2^* are such that

$$(s_1', s_2') := \arg\max_{s_1, s_2 \in W} d_G(s_1, s_2),$$

then

$$A_W = A\left(\frac{s_1' + s_2'}{\|s_1' + s_2'\|}, 0.5 w_G(W)\right)$$

Dynamic Profiles Dynamic profiles provide a set of tracking sequences per pass interval of a ground station. This profiles can be used only when the angular spread of the uncertainty set at every pass is smaller than the antenna beam-widths of the ground station.

Consider a ground station j with a rotation controlled antenna. Let $V_j(\mathcal{J}_\epsilon, t)$ denote the image of $\mathcal{J}_\epsilon$ at time t. The dynamic profile is chosen when the dynamic geodesic ratio defined as

$$R_{dynamic} := \max_{t \in \mathcal{T}_\tau} \frac{w_G(V_j(\mathcal{J}_\epsilon, t)) + C_\gamma \epsilon}{w_G(A_{ref,j})},$$

is less than unity over enough ground station passes to achieve observability. If this condition is met the satellite cluster can be tracked whenever it lies over the horizon of the ground station since the angular width of all the orbits in $\mathcal{J}$ at any time is smaller than the angular width of the antenna,i.e., $\forall t \in \mathcal{T}$,

$$\bigcup_i \{V_j(\tilde{\mathcal{J}}_i, t) \cap H_j\} \subset A_j(r) \subset H_j \tag{3.1}$$

for some $r \in S^2$. At every time step, the antennas point at the center of the smallest enclosing spherical cap that can be constructed around the set of directions for all orbits in $\mathcal{J}_\epsilon$ at a given time t. Thus, the pointing profile is the set of centers of the minimal spherical caps of the set $\{t \in \mathcal{T}_\tau, V_j(\mathcal{J}_\epsilon, t) \cap H_j\}$ and can be computed as

$$APP_{jl} := \{\left(\frac{s_1'(t) + s_2'(t)}{\|s_1'(t) + s_2'(t)\|}, t\right), (s_1'(t), s_2'(t)) := \underset{s_1, s_2 \in V_j(\mathcal{J}_\epsilon, t) \cap H_j}{\arg\max} d_G(s_1, s_2), \quad t \in S_{jl}\}$$

Static Profiles Static pointing profiles provide one orientation per pass interval of a ground station. A disadvantage of static pointing profiles is that the pass length is limited by the antenna beam-width. Due to this, more conservative allocation is necessary. We discuss two types of static pointing profiles. One when the average cross track uncertainty is small and the second when footprint of $\mathcal{J}$ is large.

The static pointing profiles target to center around the azimuth and elevations of the average Doppler shift seen by orbits with initial conditions in $\mathcal{J}_\epsilon$. Let $S_{jl}(\gamma), \gamma \in \mathcal{J}_\epsilon$ denote the pass interval at ground station j of orbit γ such that $S_{jl}(\gamma) \subseteq S_{jl}$. We define the average Doppler shift as seen during ground station pass interval S_{jl} as

$$F_{avg,jl}(\gamma) = \frac{1}{|S(\gamma)|} \sum_{t \in S_{jl}(\gamma)} U(\gamma, t), \qquad \gamma \in \mathcal{J}_\epsilon.$$

We first compute the time $t_{avg,jl}(\gamma)$ at which the Doppler shift of $F_{avg}(\gamma)$ was achieved. This computation can either be achieved using interpolation or by directly using the propagator. We then compute the azimuth and elevation points at which the average Doppler shifts occurred and we compute the average direction set $D_{avg,jl} := \{V(\gamma, t_{avg,jl}(\gamma)), \gamma \in \mathcal{J}_\epsilon\}$. This set is then used to compute the static geodesic ratio as

$$R_{static} = \frac{w_G(D_{avg,jl})}{w_G(A_{ref,jl})}.$$

The simple and complex static profiles are based on whether R_{static} is larger or smaller than a threshold R_{thres}. The selection of R_{static} as the parameter for selection of static profiles is based on its insensitivity to along-track and mean motion uncertainties. In a large number of clustered satellite deployments, the orbits of the spacecraft are designed to separate with time. In many cases, along track separation occurs faster than cross track separation in such deployments as upper stage deployment sequences impart different along track ejection velocities. The simple static profile is designed to allow a point and listen configuration for the ground stations encountered along the orbit.

The selection of R_{thres} is determined based on the minimum length of the pass of a ground station required to guarantee observation of points from the satellite cluster. It involves a trade off between the cross-track width of $\mathcal{J}$ and the desired path lengths for orbit determination. A larger threshold guarantees longer effective observation lengths with

smaller cross-track uncertainties and a smaller threshold guarantees a larger coverage of uncertainties but smaller effective pass lengths. Experimental results show that for typical low cost COTS ground stations with medium gain antennas tracking LEO deployments, a threshold value less than 0.7 is sufficient for beacon time intervals of $\tau = 10s$ to have sufficient number of observations (See Section III.6.1).

When $R_{static} < R_{thres}$, the antenna pointing direction for parking and recording using the ASGS is computed as the center of the minimal spherical cap of $D_{avg,jl}$. For

$$s_1', s_2' = \underset{s_1, s_2 \in D_{avg,jl}}{\arg\max}\ d_G(s_1, s_2), \tag{3.2}$$

the simple static pointing profile is computed as

$$APP_{jl} = \left(\frac{s_1' + s_2'}{\|s_1' + s_2'\|}, S_{jl} \right).$$

This pointing profile allows parking the antennas at $\frac{s_1' + s_2'}{\|s_1' + s_2'\|}$ and listening over S_{jl} at ground station j, recording the observations required for orbit determination and feeding the information back to the learning cluster for orbit determination.

When $R_{static} > R_{thres}$, the cross-track uncertainties are larger than what can be tracked with a single directional antenna. This case occurs with large inclination, RAAN and altitude uncertainties.

With large uncertainties, the number of solutions to the tracking problem can vary from 0 (infeasible) to an exponential number, based on the locations of ground stations and the set $\mathcal{J}$. When the number of ground stations available in the network do not provide sufficient pass intervals for OD even with the assumption that the ground stations receive with isotropic antennas, the problem of selecting directional antenna pointing profiles becomes infeasible. When all the ground stations provide access to all the orbits in $\mathcal{J}_\epsilon$, then the profile solution is

not unique and can be stated as a case of the set-cover problem (where we are using antenna coverage sets to cover $\mathcal{J}_\epsilon$, which is NP Hard. We tackle this problem in two steps: first by verifying necessary conditions for feasibility and second by using a greedy algorithm to cover all the orbits in $\mathcal{J}$.

If the solution of orbit determination with Doppler requires the observation of k pass intervals with directional antennas, then the presence of k intervals with the assumption of omni-directional antennas for observation has to be feasible for all orbits in $\mathcal{J}_\epsilon$. This criteria is computed by using the sampled data from $\mathcal{J}_\epsilon$ and measuring the minimum number of passes over orbits in $\mathcal{J}_\epsilon$. Once this criteria is satisfied a greedy algorithm is applied to compute a solution. If the greedy algorithm fails to cover all the orbits, then the algorithm can be initialized at different initial conditions and in the absence of feasibility with all initialization, the uncertainty is deemed untrackable.

We present the greedy algorithm with two assumptions: that the prior is defined in a classical element scenario and that $\mathcal{J}$ is an interval in $\mathbb{R}^6$. We work with classical elements as ground station coverage of a particular orbit is most drastically affected, in terms of its path on the horizon, due to change in inclination and the ascending node. The goal of the algorithm is to provide n_P pass intervals for all orbits in $\mathcal{J}$. The first step is to perform an ordered sorting of $\mathcal{J}_\epsilon$, with sorting priority between elements as $[RAAN, I, a, e, \omega, M]$. We initialize an empty set $\mathcal{I}_\epsilon := \{\}$. The first element is used as the initialization point s. Over all the pass intervals for orbit s, the ground stations with the largest antenna beam-widths are chosen. The selected ground stations antenna profile is selected. The orbits that are covered by the antenna profile are then added to $\mathcal{I}_\epsilon$ from the sorted orbit set. Note that since the dynamical systems for the spacecraft are continuous and the antenna caps are convex, I_ϵ will cover an interval of the orbits in $\mathcal{J}_\epsilon$. This procedure is iterated over the set of orbits not covered ($\mathcal{J}_\epsilon \setminus \mathcal{I}_\epsilon$) until all the orbits are in $\mathcal{I}_\epsilon$. The effective number of passes seen per orbit in this scenario using the selected antenna profiles are then tabulated. The

procedure is repeated until all orbits are covered at least n_P times. If the number of ground stations are insufficient, the procedure is declared infeasible and more ground stations have to be added for orbit determination.

The selection of the antenna profile requires the sorted version of $\mathcal{J}_\epsilon$ and the initialization point s. For all the orbits in $\mathcal{J}_\epsilon$ which have passes over the selected ground station, the distance matrix $D_{avg,jl}$ is computed. Starting at s a minimum distance spanning tree is constructed incrementally such that at every step, the maximum geodesic width of the set of vertices in the tree is less than the threshold for the ground station antenna. Once this threshold is met, the antenna is centered between the vertices meeting the maximum geodesic width. Note that this algorithm can be implemented efficiently by maintaining a two heaps that are updated with every vertex addition. The set of vertices covered and the antenna pointing profile is then returned.

For a high level description of algorithms for the pointing profiles described see Appendix B.1

III.5 Training Data Generation

The training data generation for the learning algorithm for orbit determination needs to simulate and generate realistic samples of observations from deployment scenarios (including changes in observations induced by the architecture such as timing uncertainty and noise). There are two areas of design consideration in the generation of training data that have been taken into account: the selection of the orbit distribution (P_Γ) and the noise associated with observations at the ground stations and the timing synchronization errors between the ground stations.

III.5.1 Orbit Distribution Selection

P_Γ represents the uncertainty in orbit parameters. For Doppler based orbit determination of spacecraft, there are two common scenarios for which orbit determination is required. One is the post insertion early orbit phase (EOP) where the spacecraft deployed are in close proximity, and diverge with time. The second is when prior orbit determination or TLE errors accumulate and tracking for the purposes of nominal operations is no longer possible.

Launch and Early Orbit Phase P_Γ is constructed from launch uncertainties when orbit determination has to be performed in the absence of upper stage (deployer) state vectors. There are at least three sources of deviation. The first is the launch vehicle orbit insertion accuracy (for example, insertion accuracy parameters for Minotaur V [103]). The essential advantage in our algorithms is that direct description of P_Γ is not required, only a description sufficient to draw samples are necessary. This is particularly useful as indirect distributional modeling such as dispersion studies of both experimental and simulated launch conditions for atmospheric ascent guidance can be used (See [104, 105, 106] and the reference therein for launch simulation).

The other two sources of uncertainty we consider are are wind profiles of launch day scenarios [106] and launch windows. LEO launches without RAAN correction requirements [107] will result in a larger uncertainty distribution. Note that the probability distributions of these parameters have to be constructed (directly or indirectly drawn) for all the orbital parameters under consideration at a particular epoch, unlike in ascent guidance where only 3 or 4 of the orbit parameters are considered (Semi-major axis, inclination and eccentricity). This can be performed by simply drawing different orbit initial conditions based on expected variation of launch times and propagating to insertion as performed for dispersion studies.

Mid-mission Orbit information degrades with time due to atmospheric uncertainties and orbit determination/TLE inaccuracies and other perturbations [108]. If the spacecraft have transponder or ranging capabilities, then orbit information can be updated with the stated approaches. However, if the evolution of error is large enough that the transmissions are no-longer decodable, then the inaccuracy information can be used to draw samples of P_Γ.

Link budget limitations have to be taken into considerations while selection of the prior and the ground stations. If there is discrepancy between the simulated training and observed test data regarding the presence and absence of observations due to the link budget, then the learning algorithm accuracies will differ while field testing. This requires that the transmissions used in measurements satisfy link requirements of the ground station nodes performing spectrum monitoring to identify measurements.

III.5.2 Noise Distribution

The training data generation system has certain intricacies associated with a practical GSNs which we shall now describe. For practical ground station networks, the timing parts of the noise distribution $P(X|F,z)$ i.e., $P(T_j|T_S,z)$ are non-trivial. There are two points of importance here. The first is timing uncertainty associated with ground stations. With imperfect synchronization between ground stations, exact timing behaviors are unknown. Training data generation will characterize the probability distribution associated with imperfect time keeping of each ground station. Samples drawn for the set of points associated with each individual orbit and ground station will have one individual randomly drawn time profile. Time profiles of the ground station will be different for every new orbit dataset created.

The next one is deep space propagation delay in reception of measurements. Deep space time delays are split into two components. The first component that is orbit dependent

(initial condition dependent) is taken into consideration in the dynamic system. This components accounts for the propagation delay to a reference point (Eg: the center of the earth) and is connected to T_S. The second component is dependent only on T_S, varies through the rotation of the earth and is taken into account for $P(T_j|T_S, z)$.

The noise associated with Doppler observations also have to be taken into account. There is sufficient analysis of communication system and noise behaviors that this can either be modeled prior to launch, or using standard communication system behaviors [97, 90]. The learning algorithm requires accurate representation of the test data during training times for consistency in results.

III.6 Results and Discussion

We present Doppler only orbit determination results with the architecture and algorithms proposed for three scenarios testing the different tracking profiles proposed. Since the algorithms proposed are independent of the number of spacecraft in a spacecraft cluster, we present only one scenario with spacecraft deployment. The other two scenarios are with one satellite.

III.6.1 Scenario 1: Simple Static Profiles

This scenario considers simple static allocation. The scenario consists of 4 spacecraft deployed from a deployer spacecraft. The deployer craft has an orbit uncertainty defined as (randomly chosen)

$$A \sim R_e + U(450, 550) \text{ km}, \qquad e \sim U(0.04, 0.05),$$

$$\Omega \sim U(40^\circ, 45^\circ), \qquad I \sim U(70^\circ, 75^\circ),$$

$$\omega \sim U(55^\circ, 60^\circ), \qquad M \sim U(250^\circ, 260^\circ),$$

where $U(a, b)$ is the uniform distribution from a to b. The deployer propagates for 6 hours and then deploys 4 spacecraft randomly along the 4 cones (Figure 3.6). The propagation is performed using a high fidelity analytical propagator which takes into account perturbations up to the 10^{th} order.

Spacecraft are deployed in time intervals of 200 seconds. The four satellite were injected with ejection velocity components of $\begin{bmatrix} -1.5 & -0.5 & 0.5 & 1.5 \end{bmatrix}$ m/s in a direction selected randomly in the plane perpendicular to the local horizontal. A additional velocity of 1.25 m/s in a random direction perpendicular to the ram direction was added to each deployment. The insertion cones for the deployer spacecraft as as shown in Figure 3.6. Total uncertainty in position of satellites is 863km. The average separation between the spacecraft at epoch was 36km. Figure 3.5 shows the GS locations and the position uncertainty of the satellites. The samples of the prior distributions for the four satellites are obtained by simulating deployment for each orbit scenario.

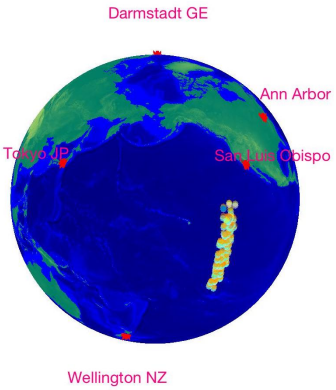

Figure 3.5: Selected ground stations and samples of initial position of the cluster based on P_Γ

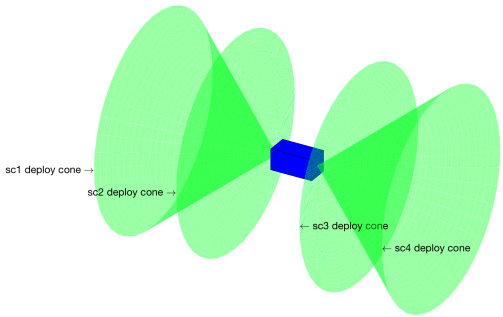

Figure 3.6: Deploy cones of satellites from deployer

Orbit determination performed with 5 ground stations ground stations which observe over a 6 hour interval, situated in Ann Arbor, San Luis Obispo, Darmsdadt in Germany, Wellington in New Zealand and Tokyo. The 6 hour interval contained 7 passes intervals from

these 5 ground stations. Uniform Doppler measurement noise $\sim 2.5\%\Delta f_{max.doppler}$ (500 Hz at 436MHz) was added to the measurements. Time synchronization error between ground stations was chosen as a uniform distribution : $Unif([-1,1])ms$. Each ground station has a rotation controllable antenna of 42° beam-width. An ϵ-net of size 200 was used to estimate the scheduling and tracking parameters. Since the width of $\mathcal{J}$ is very large in the along track direction (this can be seen in figure 3.5), but narrow along the cross track directions, a simple static profile was used. A static profile threshold used was $R_{thres} = 2$. For 3 of the 7 passes, the computed estimate of R_{static} was 3 and hence a simple static profile was used. The pointing directions were computed based on the algorithms presented. Figure 3.7 shows the directions of arrival corresponding to the Doppler data measurements used for training the learning cluster. It can be seen that the training data is pruned to include only those Doppler points that can be seen by the antennas.

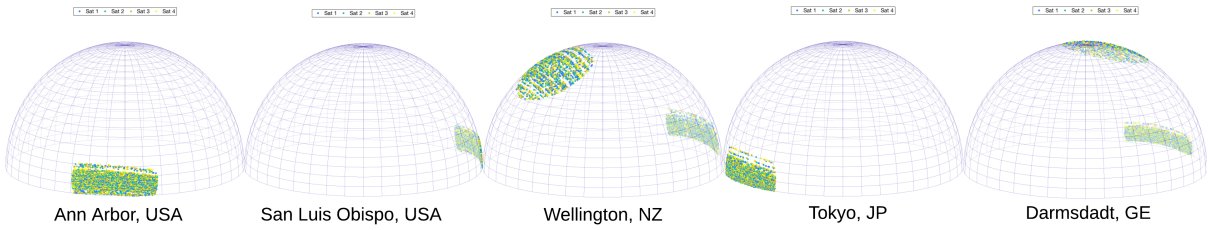

Figure 3.7: Directions of arrival corresponding to Doppler data observed by directional antennas

The machine learning based orbit determination (MLOD) was performed for the data simulated from the preceding scenario. Data for 4200 example deployments were generated with initial conditions described previously. 4000 of these deployments were used as training data and the rest 200 as test data, to test the performance of the MLOD algorithm with the stated architecture. Figures 3.8 - 3.15 show the histogram of position and velocity errors of the test orbits. The average position error is 21.44 km and the average velocity error is 20 m/s.

The uncertainty in position of the test orbits has reduced from 863 km to 21.44 km.

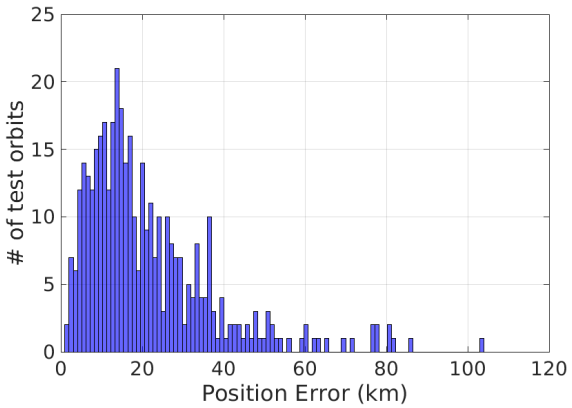

Figure 3.8: Simple static allocation: distribution of test data position error for satellite 1

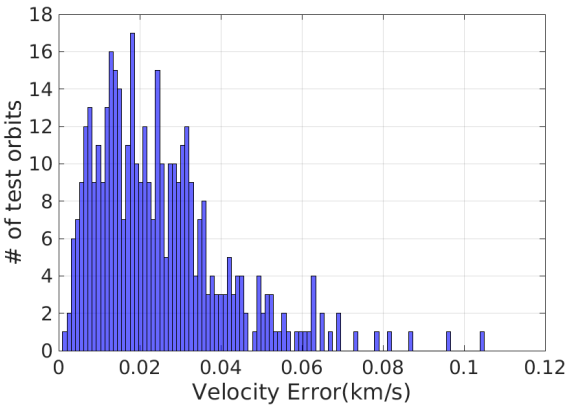

Figure 3.9: Simple static allocation: distribution of test data velocity error for satellite 1

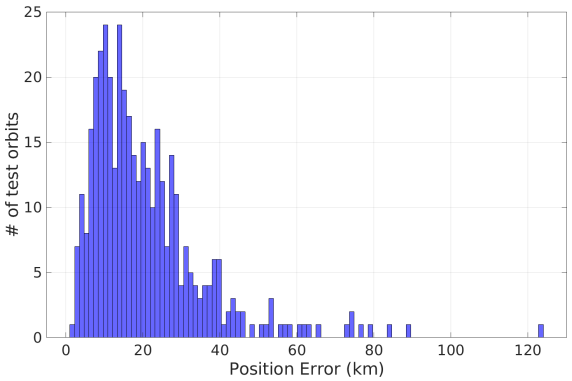

Figure 3.10: Simple static allocation: distribution of test data position error for satellite 2

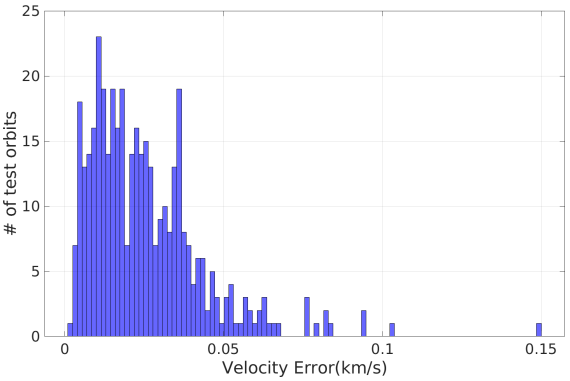

Figure 3.11: Simple static allocation: distribution of test data velocity error for satellite 2

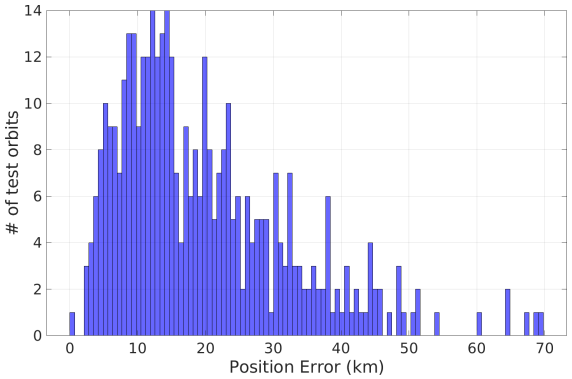

Figure 3.12: Simple static allocation: distribution of test data position error for satellite 3

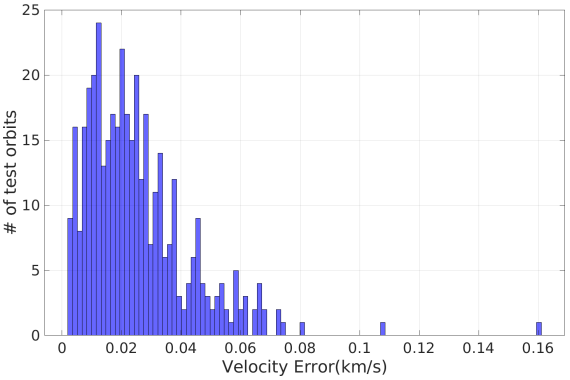

Figure 3.13: Simple static allocation: distribution of test data velocity error for satellite 3

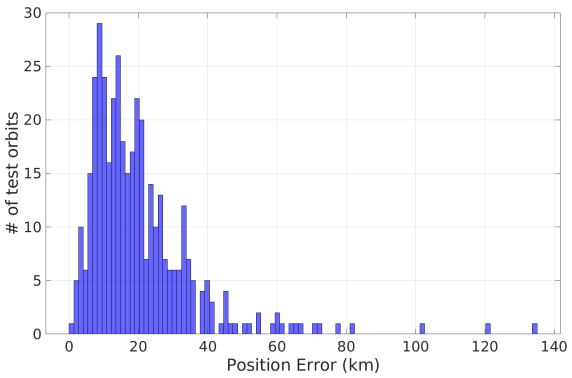

Figure 3.14: Simple static allocation: distribution of test data position error for satellite 4

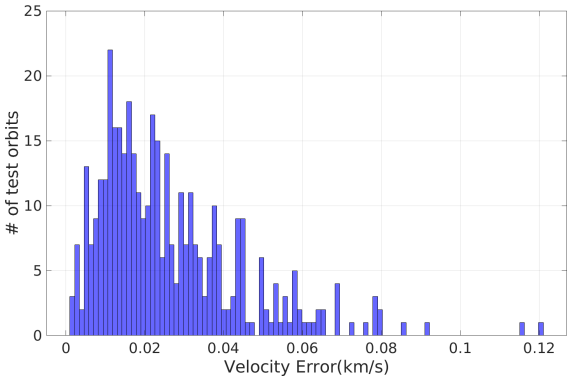

Figure 3.15: Simple static allocation: distribution of test data velocity error for satellite 4

This is sufficient for a UHF ground station to track, decode, operate the spacecraft and perform precision orbit determination with either a second phase of MLOD or by an EKF. The estimation accuracy is also sufficient to resolve the spacecrafts deployed. The velocity error is 20 m/s, which allows accurate propagation of the orbits to further improve estimates using standard fine tracking measurements of transponders and standard methods such as the EKF.

III.6.2 Scenario 2: Complex Static Profiles

This scenario demonstrates an orbit determination example for complex static allocation. The scenario consists of orbit determination of one spacecraft using a network of 10 ground stations. The orbit uncertainty is chosen to generate a large uncertainty with the RAAN, with the uncertainty similar to that produced by a launch window interval of 2 hours. The rest of the orbital parameter uncertainties, such as uncertainty in inclination are exaggerated for demonstration of the network architecture behaviors (standard launch vehicle injection accuracy for inclination is less than 1°). The distribution P_{Γ} is as follows.

$$A \sim R_e + U(500, 550) \text{ km}, \qquad e \sim U(0.04, 0.045),$$
$$\Omega \sim U(270^\circ, 300^\circ), \qquad I \sim U(45^\circ, 50^\circ),$$
$$\omega \sim U(20^\circ, 30^\circ), \qquad M \sim U(90^\circ, 100^\circ),$$

Similar to Section III.6.1, an analytical orbit propagator with 100 perturbation coefficients was used. The standard deviation of the position uncertainty is 855.68 km.

The satellite orbits were observed over a 3 hour interval using a network of ten ground stations. All the ground stations had identical antennas with a 9 dB gain ($\sim 67^\circ$ ellipsoid beam-width), typical of a patch antenna. The ground stations can point the antennas at any direction in the horizon. The spacecraft Doppler measurements have a noise of 100 Hz. The timing uncertainty between the ground stations is less than or equal to 1 ms.

A random net with 300 points was used to approximate $\mathcal{J}$. Over the 3 hour interval, six of the ten ground stations had 10 passes in total for the orbits in $\mathcal{J}_\epsilon$. A complex static profile was used with a threshold of $R_{static} = 0.7$. Since the prior distribution P_Γ is very large, no single ground station can see all the possible orbits. A minimum of 3 passes for all the orbits in $\mathcal{J}_\epsilon$ was set as a requirement for the orbit determination algorithm. The greedy algorithm choose 2 passes for the first cover, 3 passes for the second and 4 passes for the third and provided corresponding antenna pointing profiles. Using this the scheduling of the network was trimmed to only the pass intervals required by the orbit determination algorithm. The details of the ground stations and the passes selected by the complex static profile are provided in Table 3.1. This was then used to perform orbit determination. Training and test data were generated from the priors and the propagators for 4000 training orbits and 400 test orbits.

The position and velocity errors are as shown in figures 3.16 and 3.17. The average error

in position estimation is 40.11 km and the average velocity error is 46 m/s. This is larger than the errors produced in the simple static allocation scenario because an increased RAAN uncertainty leads to lower number of measurements visible for the test orbits. However, a position error of 40.11 km is sufficient to continue performing tracking with high gain resources and refine orbit determination estimates.

Table 3.1: GSN Scheduling - Complex Static Profile

Ground Station Name	GS Location (lat, lon, h(m))	Total Number of Passes	Number of Passes Selected
Ann Arbor, USA	(42.27; -83.72; 230)	0	0
San Luis Obispo, USA	(35.28; -120.66; 36)	0	0
Wellington, NZ	(-41.3; 174.78; 34)	2	2
Tokyo, JP	(35.685; 139.751; 64)	1	0
Darmstadt, GE	(49.8706; 8.649; 194)	2	2
Bogota, CO	(10.4; -75.283; 90)	2	2
Cape Town, SA	(-33.917; 18.417; 74)	0	0
Honolulu, USA	(21.307; -157.858; 19)	0	0
Salisbury, SA, AU	(-34.767; 138.633; 31)	2	1
York, UK	(53.967; -1.083; 63)	2	2

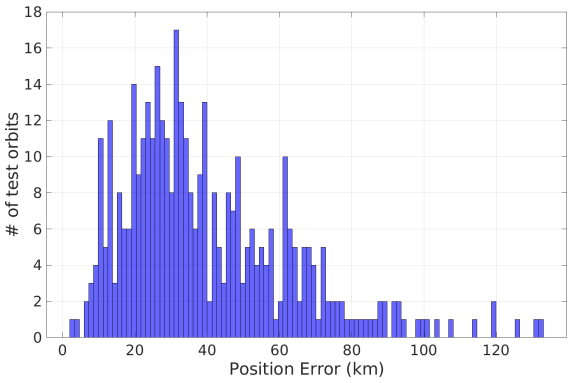

Figure 3.16: Complex static allocation: distribution of test data position error

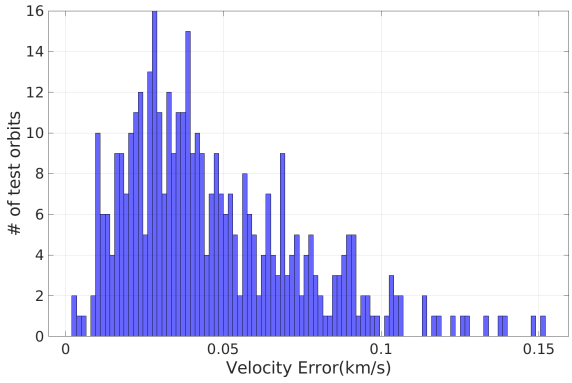

Figure 3.17: Complex static allocation: distribution of test data velocity error

III.6.3 Scenario 3: Dynamic Profile

We present a dynamic profile orbit determination scenario with a short observation interval and a network of 10 ground stations. A common problem with low initial uncertainty tracking is that the error's tend to accumulate. This scenario analyzes error minimization under very short intervals of Doppler observations ($<$ 1 orbit). The variation chosen for the angular orbital parameters was limited to one degree. The prior orbital parameters are

$$A \sim R_e + U(800, 825) \text{ km}, \qquad e \sim U(0.05, 0.055),$$
$$\Omega \sim 49.5^\circ + U(-0.5^\circ, 0.5^\circ), \qquad I \sim 30^\circ + U(-0.5^\circ, 0.5^\circ),$$
$$\omega \sim U(60^\circ, 62^\circ), \qquad M \sim U(45^\circ, 2^\circ),$$

The variance in the initial position with the preceding prior distribution was 100 km, small enough to be tracked by a wide beam antenna. The observation rate chosen corresponds to an observation every $\sim$ 10s. The number of training and test orbits were chosen similar to the previous scenarios.

The scheduling algorithm chose 4 of the 10 ground stations for tracking. The observation interval for this scenario was 70 minutes. Note that due to the short length of the observation interval, even the semi-major axis information has to be indirectly derived from the Doppler shifts, unlike in multiple pass observations where the zero Doppler shift points for two successive passes at a ground station provides the semi-major axis information. The position and velocity errors are as shown in figures 3.18 and 3.19. The average error in position estimation is 36 km and the average velocity error is 27.9 m/s. This is sufficient to continue tracking with dynamic allocation for further orbits and reduce the prediction errors.

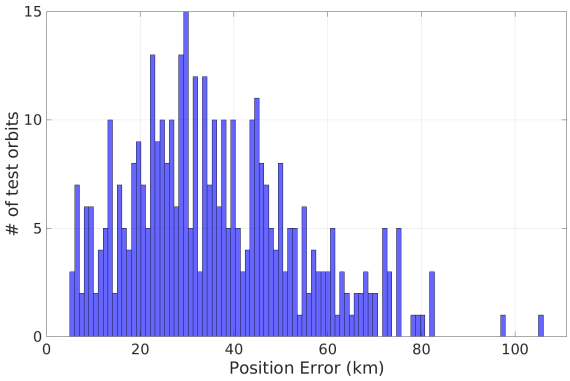

Figure 3.18: Dynamic allocation: distribution of test data position error

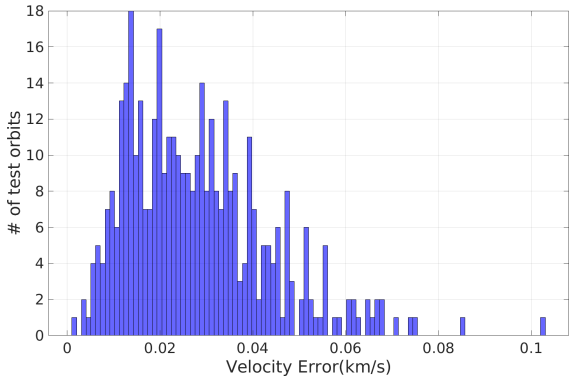

Figure 3.19: Dynamic allocation: distribution of test data velocity error

III.7 Conclusion

We present a ground station network architecture, scheduling and tracking algorithms for tracking spacecraft clusters when the orbital parameters have a large uncertainty. The network architecture is developed on the spectrum monitoring capabilities of an autonomous software ground station. The algorithms presented perform *co-ordinated tracking* of spacecraft clusters where even though each ground station receives partial tracking information, the network receives complete tracking data augmenting standard GSN architectures to include coarse and precision orbit determination capabilities through collaboration.

CHAPTER IV

Spacecraft Magnetometer Interference Cancellation

IV.1 Introduction

In this chapter, we consider the problem of spacecraft magnetic field interference cancellation. The requirements of CubeSat computational constraints, requirement of a reference magnetic field to compute loss, the iterative and imperfect nature of identification of sensor non-orthogonality (when sensor non-orthogonality is estimated in the presence of noise and the absence of knowledge of the magnetic field) provides two main constraints to the magnetometer interference cancellation problem: partial feedback, the absence of a perfect understanding of the interference.

We minimize interference by adaptively selecting weighted combinations of magnetometer measurements based on telemetry information. The adaptive sensor selection algorithm ("learner") switches between two phases. In one phase, the interference can be computed due to the knowledge of the true magnetic field at that time step - the *exploration* phase. In the second phase, the interference cannot be computed, but in this phase, the measurements are necessary to meet scientific objectives, and the interference will affect the measurements selected. In this phase, the algorithm selects the best sensor combination by exploiting the

information it gained in the exploration phase. We shall name this the *exploitation* phase.

In a machine learning setting, this can be viewed as a *contextual bandit* problem. Contextual bandits are a variant of the Multi-Armed Bandit problem. The multi-armed bandit (MAB) is a framework for sequential decision making where, at every time step, the learner selects (or “pulls") one of several possible actions (or “arms"), and received a reward based on the selected action. The performance of the learner is judged based on the notion of *regret*. The regret of the learner is the difference between the maximum possible reward and the reward resulting from the chosen action. In the classical MAB setting, the goal is to minimize the sum of all regrets, or *cumulative regret*, which naturally leads to an exploration/exploitation trade-off problem [109]. If the learner explores too little, it may never find an optimal arm which will increase its cumulative regret. If the learner explores too much, it may select suboptimal actions too often which will also increase its cumulative regret. There are a variety of algorithms that solve this exploration/exploitation trade-off problem [109, 110, 111, 112, 113].

Historically, adaptive sensing has been viewed in a decision process framework where the learner takes actions on selecting the sensor based on previous data collected. There have been many proposed solutions based on Markov decision processes (MDPs) and partially observable MDPs, with optimality bounds for cumulative regret [114, 115, 116, 117, 118]. In fact, sensor management and sequential resource allocation was one of the original motivating settings for the MAB problem [119, 113, 114], with the goal of cumulative regret minimization. We are interested in an adaptive sensing setting where the optimal decisions and rewards also depend on the context, but where the actions can be separated into pure exploration and pure exploitation phases, with no actual loss during exploration (since true magnetic field is known), and with no feedback during pure exploitation.

The contextual bandit problem extends the classical MAB setting, with the addition of time-varying side information, or *context* or telemetry, made available at every time step.

The best arm at every time step depends on the context, and intuitively the learner seeks to determine the best arm as a function of context. To date, work on contextual bandits has studied cumulative regret minimization, which is motivated by applications in health care, web advertisement recommendations and news article recommendations [120]. The contextual bandit setting is also called associative reinforcement learning [110] and linear bandits [112, 121].

In classical (non-contextual) MABs, the goal of the learner isn't always to minimize the cumulative regret. In some applications, there is a *pure exploration* phase during which the learning incurs no regret (i.e., no penalty for suboptimal decisions), and performance is measured in terms of *simple regret*, which is the regret assessed at the end of the pure exploration phase. For example, in top-arm identification, the learner must guess the arm with highest expected reward at the end of the exploration phase. Simple regret minimization clearly motivates different strategies, since there is no penalty for suboptimal decisions during the exploration phase. Fixed budget and fixed confidence are two main theoretical frameworks in which simple regret is generally analyzed [122, 123, 124, 125].

In this chapter, we extend the idea of simple regret minimization to contextual bandits. In the interference cancellation setting, at times when the true magnetic field is known, the learner can explore noise behaviors among distributed magnetometers and when the true magnetic field is unknown, the learner has to exploit its understanding of noise to provide accurate magnetometer measurements. In this setting, there is a pure exploration phase during which no regret is incurred, following by a *pure exploitation* phase during which regret is incurred, but there is no feedback so the learner cannot update its policy. To our knowledge, previous work has not addressed novel algorithms for this setting. The work of [126] provides ϵ-optimal simple regret guarantees for the policy of uniform sampling of arms in the independent and identically distributed data (i.i.d) setting. In the work of [127, 128, 129, 130] there is a single best arm even when contexts are observed. Our

algorithm, Contextual Gap, generalizes the idea of [127] to the contextual bandits setting.

We make following contributions: 1. We formulate the spacecraft magnetometer interference cancellation problem in the machine learning setting. 2. We formulate a novel machine learning problem: that of simple regret minimization for contextual bandits. 3. We develop an algorithm, Contextual Gap, for this setting, based on theoretical guarantees. 4. We present experimental results on data generated based on on-orbit telemetry of the GRIFEX CubeSat and on other machine learning datasets.

This chapter is organized as follows. In Section 2, we present the magnetic field models for spacecraft interference and sensor calibration. In Section 3, we reduce the problem of interference cancellation to a machine learning setting. In Section 4, we state the machine learning problem formally and in Section 5, we propose the Contextual Gap algorithm to solve this new problem. In Section 6, we present a brief overview of the learning theoretic analysis and in Section 7, we present and discuss experimental results. Section 8 concludes the chapter.

IV.2 Spacecraft Magnetic Field Model

We perform interference cancellation with a realistic spacecraft model, distributed sensors and with computational and power constraints normally encountered with CubeSats. We are interested in measuring the *true* magnetic field $Q_T(t) = [Q_X(t), Q_Y(t), Q_Z(t)]$ at measurement times $t \in \mathbb{N} = \{1, 2, 3, ..\}$.

Consider a spin-stabilized spacecraft spinning about the z axis at an angular velocity ω and has M 3-axis magnetometers, measuring the magnetic fields $Q_{S,m}(t), 1 \leq m \leq M$. The sensors have imperfect non-orthogonality behavior and a measurement of $Q_T(t)$ by sensor i produces $G_i O_t Q_T(t) + S_i$ where $O_t \in SO(3)$ is the rotation matrix for the rotation of the

spacecraft at time t and $G_i \in \mathbb{R}^{3\times3}, S_i \in \mathbb{R}^3$ are the slow varying sensor non-orthogonality matrix and offset for sensor i [67, 66, 72]. G_i has the small signal structure

$$G_i = \begin{bmatrix} G_{i,1} & G_{i,1}\Delta\varphi_{i,1} & G_{i,1}\Delta\theta_{i,1} \\ -G_{i,2}\Delta\varphi_{i,2} & G_{i,2} & G_{i,2}\Delta\theta_{i,2} \\ G_{i,3}\Delta\theta_{i,3}\cos(\varphi_{i,3}) & G_{i,3}\Delta\theta_{i,3}\sin(\varphi_{i,3}) & G_{i,3} \end{bmatrix}$$

G_i, S_i are unknown and can be estimated at time t by estimation of spin-harmonics and sensor modeling [67, 72].

The sensor measurements by the spacecraft are influenced by magnetic field interference due to currents running through the systems of the spacecraft. We denote the total number of current loops in the spacecraft that interfere with the measurements as N, (generally $N >> M$). Let $I_S(t) = [I_1(t), I_2(t), \cdots, I_N(t)]$ denote the vector of all current loops in the spacecraft that generate magnetic field interference. Due to the additive properties of magnetic force fields, the sensors measure the magnetic field

$$Q_{S,m} = G_m(O_t Q_T(t) + V_m(t)) + S_m, \qquad 1 \le m \le M \tag{4.1}$$

where $V_m(t) = \sum_{n=1}^{N} v_{mn}(I_n(t))$ and $v_{mn}(I_n(t))$ is the magnetic field strength of current loop n measured by sensor m.

The spacecraft collects telemetry or context x_t at each time step t to provide indirect information about the interference such that $V_m(t) = h_m(x_t) + \xi_{m,t}$. This telemetry information can include major supply currents, battery, reaction wheel currents or reaction wheel speeds and torque applied, solar panel output currents, sub-system temperatures, etc. We shall denote the telemetry space (the topological space to which x_t belongs) as $\mathcal{X}$. For the rest of

this chapter, we shall refer to x_t as telemetry or context interchangeably.

We assume that for some times $t \in \mathcal{T} \subset \mathbb{N}$ with $|\mathcal{T}| = T$, the true magnetic field $Q_T(t)$ is known and for a magnetic field measurement from sensor i, it is possible to compute the amount of noise seen by the sensor i at telemetry state x_t using the loss function $\|Q_T(t) - \hat{G}_i^{-1}(t)(Q_{S,i}(t) - \hat{S}_i(t))\|^2$, where $\hat{G}_i(t), \hat{S}_i(t)$ are estimates of G_i, S_i at time t computed without access to the true magnetic field by computing the spin harmonics induced by non-orthogonal sensors (as in [67]). The estimation of non-orthogonality requires storage and analysis of the past L samples of data to extract spin components. This is computationally expensive and requires iterative application of least-squares solutions or computation of averaging estimates as in [67, 66]. Due to this and due to the computational constraints of CubeSats, we impose the condition that only one sensor measurement can be accessed at a time-step.

In this setting, given the true magnetic fields for times $Q_T(t)$ we would like to like to provide accurate estimates of Q_T for times $t \in \mathbb{N} \setminus \mathcal{T}$.

Remarks

1. $\hat{G}_i$ can be recovered accurately only when the spacecraft is noiseless.

2. Generally $\mathcal{T}$ is known for certain non-contiguous time steps. For simplicity in explanation and without loss of generality we will assume that $\mathcal{T} = \{1, 2, 3, \cdots, T\}$.

3. We assume that using high definition geomagnetic models with Swarm data (e.g.,: [131]), we can provide accurate estimates of the geomagnetic field at some points of the spacecraft's orbit.

IV.3 Interference Cancellation

We propose to adaptively select low noise combinations of sensor measurements for each axis of measurement based on spacecraft telemetry information to generate low noise measure-

ments of Q_T. The magnetic field interference is linearly additive and certain combinations of magnetometer measurements will have lower noise estimates. The complete removal of interference in scenarios where the number of independent interfering sources are significantly greater than the number of magnetometers is an infeasible problem (the problem is under-determined). However, it is feasible to evaluate combinations of magnetometer measurements to minimize interference based on spacecraft electrical state. The spacecraft telemetry x_t provides indirect information on spacecraft currents, and therefore, on the strength and directions of the interference. Based on this, we consider combining sensor measurements based on the telemetry to minimize noise.

More precisely, we are interested in the magnetic field measurements $Q_W(t) := \sum_m W_m Q_{S,m}(t)$ such that

$$W_m = \begin{bmatrix} w_{m,1} & 0 & 0 \\ 0 & w_{m,2} & 0 \\ 0 & 0 & w_{m,3} \end{bmatrix}$$

and $\sum_m w_{m,j}(x_t) = 1, j = 1, 2, 3$. We propose to use such combinations of measurements with the realistic sensor calibration models proposed in Section IV.2. With the sensor model as stated in Section IV.2, we can re-write the magnetic field measurement produced by $Q_W(t)$ as

$$\begin{aligned} Q_W(t) &= \sum_{m=1}^{M} W_m G_m (O_t Q_T(t) + V_m(t)) + W_m S_m(t) \\ &= G_W(O_t Q_T(t) + V_W(t)) + S_W(t), \end{aligned} \tag{4.2}$$

where $G_W = \sum_m W_m G_m$, $V_W(t) = G_W^{-1} \sum_m W_m G_m V_m(t)$ (If the small signal approximations hold, then G_W is invertible). From equation 4.2 it can be seen that with the model described in section IV.2, sensor combinations can be treated as new sensors with calibration parame-

ters that are unique to the combination. When the gains along the axes are comparable among all the magnetometers, spin-calibration methods can be applied to combinations of magnetometer measurements. For details of the small signal approximations for G_W and its applicability to spin-calibration methods see Appendix C.1.

Using standard techniques, we can provide an estimate G_W, $\hat{G}_W$. In the presence of noise, the calibration corrections for G_W, S_W are inaccurate. In particular, the larger the average noise for a particular combination W, the larger the error in estimation of the calibration parameters. A sensor combination W with lower average noise will lead to better non-orthogonality and spin correction. The estimates of $\hat{G}_W$ can be used for $t \in \mathcal{T}$ to obtain an indirect and noisy estimate of the interference.

For times $t \in \mathcal{T}$ when an estimate of the interference can be provided, it can be shown that for a fixed sensor combination W, the loss l_W can be decomposed into two parts as

$$l_W = f_W(x_t) - \zeta_t$$

where $f_W : \mathcal{X} \to \mathbb{R}$ is a function that maps the telemetry at time t to interference and ζ_t is random variable that perturbs f_W, and depends on the unobserved interference, imperfect calibration and the true magnetic field. Of the two parts, the first part, f_W, depends on the telemetry x_t and allows optimization. The exact nature of $f_W(x_t)$ depends on the construction of the spacecraft or CubeSat and the type of telemetry under consideration. The second part, ζ_t, is a *random process* that depends on the average magnitude of interference and the true magnetic field. When the spin correction has low error, the unobservable interference (the part of the interference that cannot be inferred from telemetry) dominates the random process behavior. We will focus on the loss behavior with respect to the telemetry and denote the loss random variable as $\ell_W(x_t)$ such that

$$\ell_W(x_t) = f_W(x_t) - \zeta_t$$

We are interested in adaptive selection of W from telemetry x_t to minimize average interference for each $t \in \mathbb{N} \setminus \mathcal{T}$. Define the action space $\mathcal{W}$ as search space for interference minimization:

$$\mathcal{W} = \{(W_1, W_2, \cdots W_m) | \sum_m w_{m,i} = 1, |w_{m,i}| \leq C_W, i = 1, 2, 3\}.$$

We aim to estimate a function $W : \mathcal{X} \rightarrow \mathcal{W}$ such that for $t \in \mathcal{T}'$, the expected loss is minimized for any $x_t \in \mathcal{X}$, i.e.,

$$W(x_t) = \arg\min_{W' \in \mathcal{W}} \mathbb{E}[\ell_{W'}(x_t)].$$

We would like to note here that even though the system being optimized is $f_W(x_t)$ a direct optimization of $\ell_W(x_t)$ has to be performed as we do not have access to $f_W(x_t)$. The non-orthogonality parameters $\hat{G}_W^{-1}, \hat{S}_W(t)$ have to be computed for every combination W only after selection of W by computation of $Q_W(t)$ for the previous L time steps followed by the application of spin-correction techniques.

Finite Approximation A complete search to optimize over $\mathcal{W}$ real-time with CubeSat computational constraints is intractable particularly when the unobservable interference behavior is not independent and identically distributed. To satisfy computational constraints we propose to optimize over a finite approximation of $\mathcal{W}$. To do so we shall make the following assumption about $f_W(x_t)$:

A-I $f_W(x_t)$ is uniformly continuous with respect to sensor combination W for all x_t.

The above assumption implies that for any $\delta > 0$, there exists an $\epsilon > 0$ such that

$\sum_m \|W_m - W'_m\|_F \leq \epsilon$ implies $|f_W(x_t) - f_{W'}(x_t)| < \delta$. With the preceding assumption we consider an ϵ-net $\mathcal{W}_\epsilon = \{W_\epsilon^{(1)}, W_\epsilon^{(2)}, \cdots, W_\epsilon^{(A)}\}$ of size $|\mathcal{W}_\epsilon| = A$ such that for any $W \in \mathcal{W}$, $\min_{W' \in \mathcal{W}_\epsilon} \sum_m \|W_m - W'_m\| \leq \epsilon$. With Assumption **A-I**, minimizing over the ϵ-net provides the δ approximation to the optimizer:

$$\left| \min_{W' \in \mathcal{W}} \mathbb{E}[\ell_{W'}(x_t)] - \min_{W' \in \mathcal{W}_\epsilon} \mathbb{E}[\ell_{W'}(x_t)] \right| \leq \delta$$

$\mathcal{W}_\epsilon$ can be constructed by construction of three $(\epsilon/3)$-nets on M-dimensional simplexes scaled by C_W, offset by $C_W - 1$ and then creating a 3D grid which will consist of values of $\mathcal{W}_\epsilon$. We are interested in estimation of the function

$$W(x_t) = \arg\min_{W' \in \mathcal{W}_\epsilon} \mathbb{E}[\ell_{W'}(x_t)] \tag{4.3}$$

The following section presents equation (4.3) in a machine learning setting as a contextual bandit problem minimizing simple regret. At every time step t, the learning algorithm will select an action $a \in \{1, 2, ..., A\}$ to choose the sensor combination $W_\epsilon^{(a)}$.

IV.4 Machine Learning Setting

We model the interference minimization scenario as a contextual bandit problem where the learning algorithm has to learn to identify (over times $t \in \mathcal{T}$), the sensor combination with the least noise. It then uses the learned behavior over the times for which magnetometer measurements are necessary. We denote the telemetry or context space as $\mathcal{X}$. Let $\{x_t\}_{t=1}^{\infty}$ denote the sequence of observed telemetry. Over $\mathcal{W}_\epsilon$ the total number of sensor combinations are A. For each x_t, the learner is required to choose an action or *arm* $a \in [A]$ (the action or

arm is the selection of a sensor combination), where $[A] := \{1, 2, ..., A\}$.

The learning algorithm learns on the basis of a *reward* r_a, such that $r_a := -l_{W_\epsilon^{(a)}}$. Simplifying notation, for arm $a \in [A]$, we label $f_a : \mathcal{X} \to \mathbb{R}$ defined as $f_a := -f_{W_\epsilon^{(a)}}$ as the function that determines the expected reward for context x when action a is selected. Let a_t denote the action selected at time t, from Section IV.3 the reward at time t obeys $r_t := f_{a_t}(x_t) + \zeta_t$, where ζ_t is unobservable noise. We assume that for each a, f_a belongs to a reproducing kernel Hilbert space (RKHS) defined on $\mathcal{X}$. Without loss of generality, we assume that $\mathcal{T} = \{1, 2, ...T\}$. We shall define the first T time steps for which the true magnetic field is known as the *exploration phase* where the learner observes context x_t, chooses arm a_t and obtains reward r_t. The time steps after T belong to an *exploitation phase* where the learner observes context x_t, chooses arm a_t and earns an implicit reward r_t that is not returned to the learner.

The telemetry and the unobservable noise are not independent and identically distributed with time, and the unobservable noise component depends on the previous noise behavior and previous telemetry. To handle this general behavior a general probabilistic framework is adopted, similar to [121] and [132]. Let $\mathcal{X}$ be the compact space endowed with a finite positive Borel measure. We assume that ζ_t is a zero mean, ρ-conditionally sub-Gaussian random variable, i.e., ζ_t is such that for some $\rho > 0$ and $\forall \gamma \in \mathbb{R}$,

$$\mathbb{E}[e^{\gamma \zeta_t} | \mathcal{F}_{t-1}] \leq \exp\left(\frac{\gamma^2 \rho^2}{2}\right). \tag{4.4}$$

We also define the following terms. Let $D_{a,t}$ be the set of all the time indices when arm a was selected up to time $t-1$ and $|D_{a,t}| = N_{a,t}$. Let $X_{a,t}$ be the data matrix whose rows are $\{x_\tau\}_{\tau \in D_{a,t}}$ and similarly let $Y_{a,t}$ denote the column vector of rewards $\{r_\tau\}_{\tau \in D_{a,t}}$. Thus, $X_{a,t} \in \mathbb{R}^{d \times N_{a,t}}$ and $Y_{a,t} \in \mathbb{R}^{N_{a,t}}$.

IV.4.1 A Contextual Bandit Problem

At every time step t, the learner observes context x_t. During the exploration phase $1, \cdots, T$, the learner chooses a series of actions to explore and learn the mapping f_a from the context to the reward. During the evaluation phase $t > T$, the goal is to select the best arm that depends on the context. We define the *simple regret* associated with choosing arm $a \in [A]$, given context x, as:

$$R_a(x) := f^*(x) - f_a(x), \tag{4.5}$$

where $f^*(x) := \max_{i \in [A]} f_i(x)$ is the expected reward for the best arm for context x and $f_a(x)$ is the expected reward for selected arm a. The learner aims to minimize the simple regret for $t > T$. The goal is to determine policies for exploration and exploitation such that $\forall \epsilon > 0, \forall x, P(R_{a_t}(x) > \epsilon | x) \to 0$ as $T \to \infty$, where a_t is a selected arm at some $t > T$. The following section presents an algorithm to solve this problem.

IV.5 Algorithm

Estimating functions $f_a, a \in [A]$ from the context space to the reward space is an important step towards achieving the goal which allows the learner to estimate the expected reward for given context and thereby allowing it to choose the best arm for a given context. Let $k : \mathcal{X} \times \mathcal{X} \to \mathbb{R}$ be a symmetric positive definite kernel function on $\mathcal{X}$, $\mathcal{H}$ be the corresponding RKHS and $\phi(x) = k(\cdot, x)$ be the associated canonical feature map. Let $\phi(X_{a,t}) := [\phi(x_j)]_{j \in D_{a,t}}$. We define the kernel matrix associated with $X_{a,t}$ as $K_{a,t} := \phi(X_{a,t})^T \phi(X_{a,t}) \in \mathbb{R}^{N_{a,t} \times N_{a,t}}$ and the kernel vector of context x as $k_{a,t}(x) := \phi(X_{a,t})^T \phi(x)$. Let $I_{a,t}$ be the identity matrix of size $N_{a,t}$. To estimate the function f_a at time t, we solve the following minimization problem (also called as Kernel ridge regression): $\hat{f}_{a,t}(x) = \arg\min_{f_a \in \mathcal{H}} \sum_{j \in D_{a,t}} (f_a(x_j) - r_j)^2 + \lambda \|f_a\|^2$. The solution

to kernel ridge regression estimate of f_a can be computed as $\hat{f}_{a,t}(x) = k_{a,t}(x)^T(K_{a,t} + \lambda I_{a,t})^{-1}Y_{a,t}$ with variance in the estimate, $\hat{\sigma}^2_{a,t}(x) := k(x,x) - k_{a,t}(x)^T(K_{a,t} + \lambda I_{a,t})^{-1}k_{a,t}(x)$ [132]. The following theorem is a slightly modified version of Theorem 2.1 in [132] which allows us to define high probability upper and lower confidence bounds on $f_a(x)$.

Theorem IV.1 (Restatement of Theorem 2.1 in [132]). *Consider the contextual bandit scenario described in section IV.4. For any $\beta > 0$, with probability at least $1 - e^{-\beta^2}$, it holds simultaneously over all $x \in \mathcal{X}$ and all $t \leq T$,*

$$|f_a(x) - \hat{f}_{a,t}(x)| \leq (C_1\beta + C_2)\frac{\hat{\sigma}_{a,t}(x)}{\sqrt{\lambda}} \tag{4.6}$$

where $C_1 = \rho\sqrt{2}$ and $C_2 = \rho\sqrt{\sum_{\tau=2}^{T} \ln(1 + \frac{1}{\lambda}\hat{\sigma}_{a,\tau-1}(x_\tau))} + \sqrt{\lambda}\|f_a\|_{\mathcal{H}}$.

We express the upper and lower confidence bounds of $f_a(x)$ as $U_{a,t}(x) = \hat{f}_{a,t}(x) + (C_1\beta + C_2)\frac{\hat{\sigma}_{a,t}(x)}{\sqrt{\lambda}}$ and $L_{a,t}(x) = \hat{f}_{a,t}(x) - (C_1\beta + C_2)\frac{\hat{\sigma}_{a,t}(x)}{\sqrt{\lambda}}$. The algorithm extends the Bayes Gap algorithm [127] to the contextual setting. We define the *contextual gap* as $B_{a,t}(x) = \max_{i \neq a} U_{i,t}(x) - L_{a,t}(x)$ and the confidence estimates $s_{a,t}(x) = 2(C_1\beta + C_2)\frac{\hat{\sigma}_{a,t}(x)}{\sqrt{\lambda}}$. After a burn-in phase where each arm is sampled in order for some number of rounds N_λ, the algorithm works by exploring the best and the second best arms and increasing the confidence in reward estimates during the exploration phase. In the exploitation phase, for a given context x, the contextual gap for all time steps in the exploration phase are evaluated. The arm with the smallest gap over all time history for the given context x is chosen as the best arm associated with context x. Because there is no feedback during the exploitation phase, the algorithm moves to the next exploitation step without feedback or modification to the learning history. The exact description is presented in Algorithm 4.1.

During the exploitation phase, looking back at all history may be computationally prohibitive, in which case, in practice, we just select the best arm as $J_T(x_t), \forall t > T$. As described

Algorithm 4.1: Contextual-Gap

Input: Number of arms A, Time Steps T, parameter β, regularization parameter λ, burn-in phase constant N_λ.

for $t = 1, ..., AN_\lambda$ **do**

  Observe context x_t.

  Choose $a_t = t \mod A$.

  Receive reward $r_t \in \mathbb{R}$.

end

for $t = AN_\lambda + 1, \ldots, T$ **do**

  Observe context x_t.

  Learn reward estimators $\hat{f}_{a,t}(x_t)$ and confidence estimators $s_{a,t}(x_t)$ based on history.

  $U_{a,t}(x_t) = \hat{f}_{a,t}(x_t) + \frac{s_{a,t}(x_t)}{2}$, $L_{a,t}(x_t) = \hat{f}_{a,t}(x_t) - \frac{s_{a,t}(x_t)}{2}$.

  $B_{a,t}(x_t) = \max_{i \neq a} U_{i,t}(x_t) - L_{a,t}(x_t)$.

  $J_t(x_t) = \arg\min_a B_{a,t}(x_t), j_t(x_t) = \arg\max_{a \neq J_t(x_t)} U_{a,t}(x_t)$.

  Choose $a_t = \arg\max_{a \in \{j_t(x_t), J_t(x_t)\}} s_{a,t}(x_t)$.

  Receive reward $r_t \in \mathbb{R}$.

end

for $t > T$ **do**

  Observe context x_t.

  for $\tau = AN_\lambda + 1, \ldots, T$ **do**

    Evaluate and collect $J_\tau(x_t), B_{J_\tau(x_t)}(x_t)$.

  end

  $\iota = \arg\min_{AN_\lambda + 1 \leq \tau \leq T} B_{J_\tau(x_t),t}(x_t)$

  Choose $\Omega_t = J_\iota(x_t)$.

end

in the experimental section, this works well in practice. Let N_λ be the minimum number of tries that arm a has to be selected prior to the guarantee of regret bounds. Theoretically, N_λ has to be bigger than a certain number defined in Section IV.6, but for experimental results we keep $N_\lambda = 1$. The following section details high probability bounds on the simple regret of the contextual-gap algorithm.

IV.6 Learning Theoretic Analysis

We now analyze high probability simple regret bounds which depend on the gap quantity $\Delta_a(x) := |\max_{i \neq a} f_i(x) - f_a(x)|$. The bounds are presented in the non-i.i.d setting described in Section IV.4. For the confidence interval to be useful, it needs to shrink to zero with high probability over the feature space as each arm is pulled more and more. This requires smallest non zero eigenvalue of sample covariance matrix of data for each arm to be lower bounded by a certain value. The lower bound on eigenvalue of the sample covariance matrix is used to shrink the confidence intervals with high probability under certain assumptions. We bound the simple regret using the lower bounds on the eigenvalues, the gap quantity, and the special exploration strategy described in the algorithm 4.1. We make additional assumptions to the problem setting described.

A I $\mathcal{X} \subset \mathbb{R}^d$ is a compact space endowed with a finite positive Borel measure.

A II Kernel $k : \mathcal{X} \times \mathcal{X} \to \mathbb{R}$ is bounded by a constant L, the canonical feature map $\phi : \mathcal{X} \to \mathcal{H}$ of k is a continuous function, and $\mathcal{H}$ is separable and $f_a \in \mathcal{H}$.

We denote $\mathbb{E}_{t-1}[\cdot] := \mathbb{E}[\cdot|\phi(x_1), \phi(x_2), \cdots, \phi(x_{t-1})]$ and by $\lambda_r(A)$ the r^{th} largest eigenvalue of a compact self adjoint operator A. For a context x, the operator $\phi(x)\phi(x)^T : \mathcal{H} \to \mathcal{H}$ is a compact self-adjoint operator. We define the cumulative operator $V_t := \sum_{s=1}^{t-1} \mathbb{E}_s[\phi(x_t)\phi(x_t)^T]$. Based on this notation, we make the following assumption:

A III There exists a subspace of dimension d^* with projection P, and a constant $\lambda_x > 0$, such that $\forall t$, $\lambda_r(P^T \mathbb{E}_{t-1}[\phi(x_t)\phi(x_t)^T]P) > \lambda_x$ for $r \leq d^*$ and $\lambda_r((I-P)^T \mathbb{E}_{t-1}[\phi(x_t)\phi(x_t)^T](I-P)) = 0, \forall r > 0$.

Assumption **A III** implies that there exists a subspace of dimension d^* such that eigenvalues of V_t in the subspace grow linearly with time and are zero outside the subspace. This assumption allows us to lower bound, with high probability, the r^{th} eigenvalue of the cumulative sample covariance operator $S_t := \sum_{s=1}^{t} \phi(x_s)\phi(x_s)^T$ so that it is possible to learn the reward behavior in the low energy directions of the context at the same rate as the high energy ones with high probability.

Let $N_\lambda := \max\left(\frac{2(1-\lambda)}{\lambda_x}, d^*, \frac{256}{\lambda_x^2}\log(\frac{128\tilde{d}}{\lambda_x^2\delta})\right)$. The condition of $N_{a,t} > N_\lambda$ in Algorithm 4.1 results in a minimum number of tries that arm a has to be selected prior to the guarantee of regret bounds. In $N_\lambda := \max\left(\frac{2(1-\lambda)}{\lambda_x}, d^*, \frac{256}{\lambda_x^2}\log(\frac{128\tilde{d}}{\lambda_x^2\delta})\right)$, the first and third term in the max are needed so that we can give concentration bounds on eigenvalues and prove that confidence width shrinks. The second term is needed because one has to get at least d^* contexts for every arm so that at least some energy is added to the lowest eigenvalues.

The high probability monotonic upper bound on the confidence estimate can be used to upper bound the simple regret. The upper bound depends on a context-based hardness quantity defined for each arm a (similar to [127]) as

$$H_{a,\epsilon}(x) = \max(\frac{1}{2}(\Delta_a(x) + \epsilon), \epsilon). \tag{4.7}$$

Denote its lowest value as $H_{a,\epsilon} := \inf_{x \in \mathcal{X}} H_{a,\epsilon}(x)$. Let total hardness be defined as $H_\epsilon := \sum_{a \in [A]} H_{a,\epsilon}^{-2}$. The recommended arm Ω_t after time $t \geq T$ is defined as $\Omega_t = J_{\arg\min_{AN_\lambda+1 \leq \tau \leq T} B_{J_\tau(x_t),t}(x_t)}(x_t)$ from algorithm 4.1. We now upper bound the simple regret as follows:

Theorem IV.2. *Consider a contextual bandit problem as defined in Section IV.4 with as-*

sumptions ***A I-A III****. For* $0 < \delta \leq \frac{1}{8}$ *and* $N_\lambda := \max\left(\frac{2(1-\lambda)}{\lambda_x}, d^*, \frac{256}{\lambda_x^2}\log(\frac{128\tilde{d}}{\lambda_x^2\delta})\right)$*, let*

$$\beta = \sqrt{\frac{\lambda_x(T - N_\lambda(A-1)) + 2A\lambda}{16C_1^2 H_\epsilon}} - \frac{C_2}{C_1}. \tag{4.8}$$

For all $t > T$*,*

$$P(R_{\Omega_t}(x) < \epsilon | x) \geq 1 - A(T - AN_\lambda)e^{-\beta^2} - A\delta. \tag{4.9}$$

Note that the term C_2 in (4.8) grows logarithmically in T. For β to be positive, T should be greater than $\frac{16H_\epsilon C_2^2 - 2A\lambda}{\lambda_x} + N_\lambda(A-1)$. We compare the term $e^{-\beta^2}$ in our bound with the one in [126]. Uniform sampling technique in [126] leads to a bound which depends on $Ce^{-cT^{\frac{2}{(d_1+d)}}} \leq Ce^{-cT^{\frac{2}{2+d_2}}}$, where $d_1 \geq 2$, d is the dimension of the context and constants C, c, which is very slow. But in our case, it leads to $C'Te^{c'T}$ for constants C', c'. Comparing the equations, we can conclude that our bound is superior for $\forall d \geq 1$.

IV.7 Results and Discussion

We present results from three different cases and two different experimental setups, first from online multi-class classification with partial feedback, and second from a lab generated non-i.i.d spacecraft magnetic field as described in section 2 with direct magnetometer selection and the third from a lab-generated non-i.i.d dataset with combinations of magnetometers as arms. The datasets were split into cross-validation and evaluation datasets and each of those datasets were further split into exploration and exploitation phases. Due to the prohibitive computational complexity of the exploitation phase of the proposed algorithm, a simplification was made to choose the best arm $J_T(x)$ as the recommended arm during the exploitation phase instead of going back all the way in history. We use the Gaussian kernel and tune the bandwidth of the kernel, and the regularization parameter for both our method

and Kernel-UCB. The exploration parameter $\alpha = C_1\beta + C_2$ is set to 1 for the results in this section and we show results for different values of α in the supplementary material.

We present simple regret comparisons of the contextual gap algorithm against Kernel-UCB [133], which is designed to optimize cumulative regret as a test both of the sub-optimality of cumulative regret minimizations in minimizing simple regret and to test the performance of the simple regret minimization algorithm.

IV.7.1 Multi-class Classification

We present results of contextual simple regret minimization for multiclass datasets. At every time step, we get an example or feature vector and we need to select the class to which example belongs. Each class is treated like an arm or action. If we select the best arm (true class) we get a reward of one, otherwise we get a reward of zero. This setting is different from standard online multiclass classification, because we don't learn the true class if our selection is wrong. We present results over three standard machine learning multi-class datasets: MNIST [134], USPS [135] and Letter [136]. The simple regret plots for Contextual Gap and Kernel-UCB are presented. The plots are generated by varying the length of the exploration phase and keeping the exploitation dataset constant for evaluation of simple regret. It can be seen that the simple regret of the contextual gap converges faster than the simple regret of Kernel-UCB. Since the datasets are i.i.d in nature, multiple simple regret evaluations are performed by shuffling the evaluation datasets, and the average curves are reported.

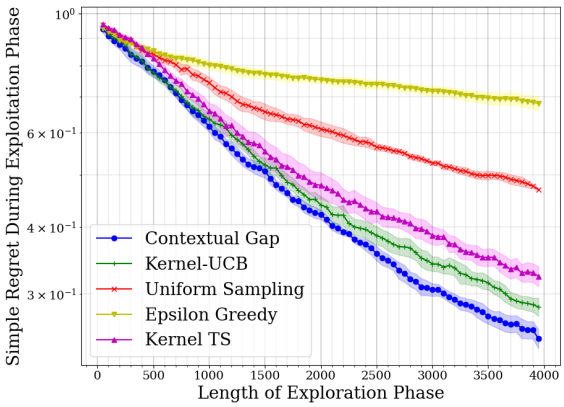

(a) Letter dataset

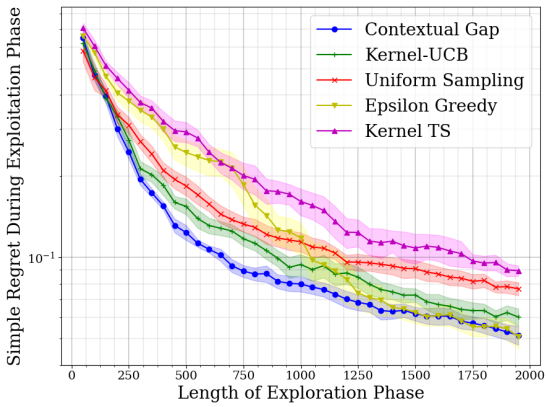

(b) USPS dataset

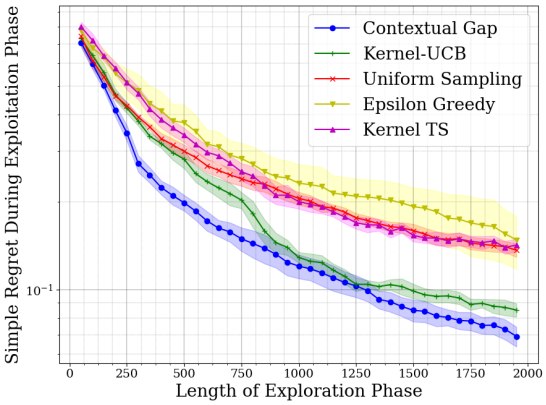

(c) MNIST dataset

Figure 4.1: Simple regret evaluation of multi-class datasets

IV.7.2 Experimental Spacecraft Magnetic Field Dataset

Interference minimization using contextual gap algorithm was tested on a lab generated, realistic spacecraft magnetic field dataset with telemetry downloaded from on-orbit spacecraft (*non-i.i.d* contexts). In spacecraft magnetic field data, we are interested in identifying the least noisy sensor or combination of sensors for every time step (see Sections IV.2 and IV.3).

Experimental Setup

The lab-based experimental setup consisted of a combination of simulated electrical behavior and telemetry downloaded from the GRIFEX satellite [88, 87]. The experimental setup consisted of 8 magnetic coils generating interference and 3 magnetometers performing measurements placed in a structure similar to a 4U CubeSat in an electromagnetically shielded environment. The currents generating magnetic fields at the 8 coils were derived from currents that would be generated from subsystems in a spin-stabilized CubeSat. Three subsystems were taken into consideration: reaction wheels, solar panels and the electrical power system (EPS).

Reaction wheel currents were simulated from a realistic spacecraft model similar to those used for Multi-disciplinary Design Optimization (MDO) of CubeSats [137]. Angular velocity and torque measurements were used in telemetry for the learning algorithm.

The solar panel magnetic noise was generated based on panel currents and panel temperatures from GRIFEX telemetry applied to panel models. Non-ideal solar panels do not have a deterministic uniform current density distributed across the panels [138, 139]. Each of the four solar panels were broken down into 100 current elements with randomly chosen densities and a small linear temperature variation was introduced for each current element (different current elements had different temperature variations).

Electrical Power System (EPS) interference was based on 5 CubeSat current loops - unregulated power feeds from the solar panels into EPS and unregulated battery current out of the EPS. For EPS, the correlations between currents and the placement of the coils were similar to the placement of the panel current loops and their correlations on GRIFEX.

In addition to the above subsystems, unobservable noise were added prior to generating spacecraft interference from the coils. The unobservable noise was modeled as low magnitude

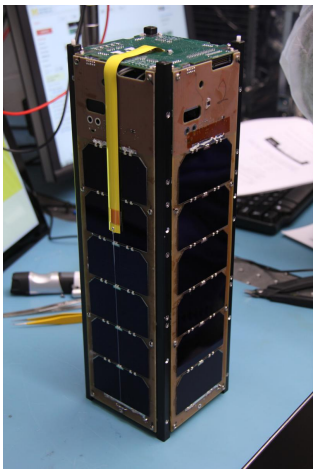

(a) GRIFEX CubeSat

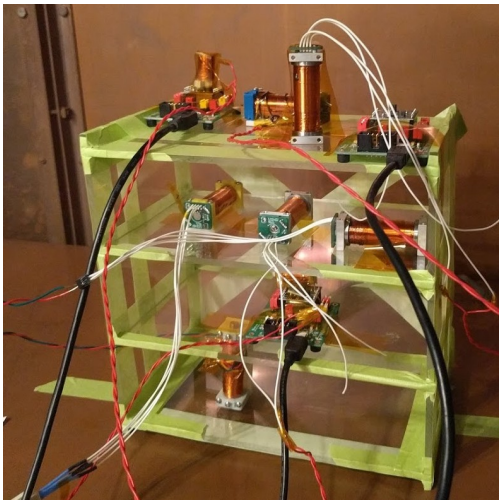

(b) Coil and sensor setup

Figure 4.2: The GRIFEX CubeSat and the experimental setup for data generation, GRIFEX telemetry and additional subsystem modeled data was fed into the coils to generate interference

i.i.d uniform noise.

The telemetry x_t consisted of a 15 dimensional vector consisting of simulated reaction wheel speed and torque, GRIFEX solar panel currents, solar panel temperatures and battery currents. Magnetic field interference data were collected using three sensors (arms), and sensor readings were downloaded for all three sensors at all times steps, although the learning algorithm does not know these in advance and must select one action per time step.

Direct Sensor Selection

We test the behavior of the learning algorithm by restricting W_ϵ to the sensors themselves ($\epsilon = C_W/\sqrt{M-1}$). In this scenario, the true magnetic field was computed using a magnetic field model (POMME 11 [140]). The spin correction was assumed to be perfect ($\widehat{G}_W = G_W$) and therefore noise in the reward process was produced only by the unobserved noise ξ_t.

We test algorithmic behavior in two different settings: with and without on-orbit modifi-

cation. The underlying data is time series based with the telemetry collected from GRIFEX. We make an on-orbit modification to simulate algorithmic behavior when the exploration and exploitation phases do not occur on successive data-points. Due to the cyclic nature of the spacecraft orbits and the rotations, we achieve this effect by shuffling the dataset once for the exploration and exploitation phases while evaluating the data. The cross validation for both datasets is done with time-series data (not shuffled) similar to what would be available prior to deployment. Figures 4.3a and 4.3b show the simple regret minimization curves for the spacecraft dataset with and without on-orbit modifications.

Due to the nature of the magnetic field interference, there exists large variability in reward for certain regions of the context space, implying that consistent exploration of the best and second best arms provides improved results. This large variability is more pronounced without the on-orbit correction, due to the nature of the time series data (See Figures 4.7, 4.8 for the time series of interference and telemetry). Due to this, the Contextual Gap algorithm shows jumps in simple regret evaluations when newer dimensions in contexts are explored resulting in a temporary increase in the uncertainty estimate.

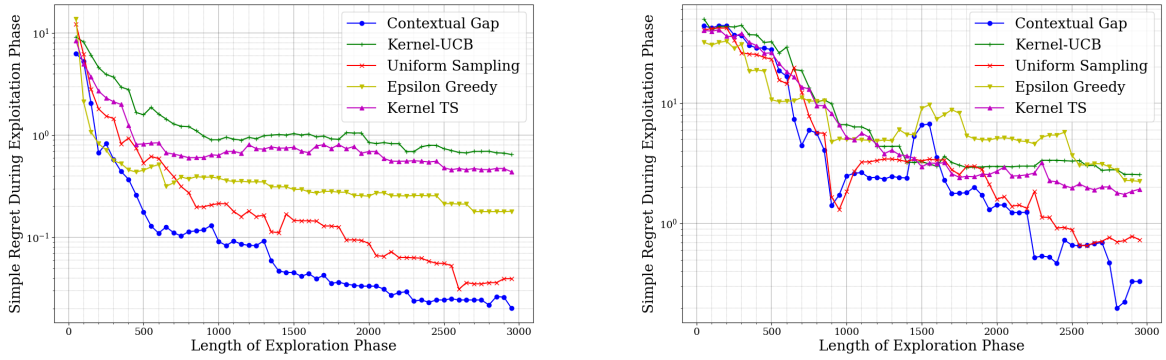

(a) Spacecraft dataset - with on-orbit modification

(b) Spacecraft dataset - without on-orbit modification

Figure 4.3: Simple regret of direct sensor selection with and without on-orbit modifications

Selection of Sensor Combinations

In this scenario, we analyze interference minimization through selection of sensor combinations in the presence of rotational effects and imperfect calibration. The interference experimentally generated was added to a simulated spinning spacecraft. The spacecraft spin was restricted along the z-axis. The true magnetic field in the body fixed frame was chosen as constant for the dataset.

Along each dimension, ten sensor combinations were sampled from a simplex. This resulted in a total of 1000 arms. However, among the arms selected, most of the 1000 arms are sub-optimal (higher interference) most of the time. A subset of the arms that were the best among the arms for more than 1.67% of the total number of evaluations were selected. (The total dataset consists of 6000 data points, of this only those arms that were optimal for at-least a hundred time samples were selected). This resulted in a total of 11 arms.

During pre-processing of the dataset, the true estimates of combined sensor correction matrix G_W were perturbed with random noise to test the effects of imperfect sensor correction. For testing, the rewards of all the arms were computed for the dataset. During on-orbit operation, only the estimates of the sensor combinations selected have to be computed per time step. Figure 4.4 shows the histogram of the minimum interference values with sensor combinations, with individual sensors, and the interference of the individual magnetometers. The statistics associated with the interference seen by each of the sensors and the optimal sensor combinations are presented in Table 4.1. The cross validation and test datasets for application of the learning algorithm were constructed similar to the direct sensor selection scenario with and without on-orbit modifications.

The simple regret for the contextual gap algorithm is as shown in Figure 4.5b and 4.6b. The histogram of the best arm selection among the 11 sensor combinations is shown along with the results of the Contextual Gap algorithm for the exploitation phases for the two

cases in Figure 4.5a and 4.6a. From Figures 4.5b, 4.6b, with increase in the exploration phase, the simple regret decreases. A decrease in simple regret implies that the Contextual Gap algorithm learns to adaptively chooses the sensor combination with an interference that is the smallest among the possible combinations (arms) under consideration. Smaller the regret, smaller the difference between the selected combinations and the lowest interference a particular set of sensor combinations can provide.

It can be seen that with increasing training data the contextual gap algorithm learns to identify sensor combinations with low regret. At the end of the exploration period, since the simple regret evaluations are non-zero, the optimal sensor selection is imperfect. The learning theoretic bounds presented in the preceding section show that this simple regret will go to zero with an increase in the length of the exploration phase.

The time series of the interference magnitude and the telemetry used for the exploitation phase without on-orbit correction is shown in Figure 4.7 and Figure 4.8. The interference along individual directions in the spacecraft body fixed frame is provided in Appendix C.3. Note that even if the magnitude of interference is low along certain directions, with the implemented scenario, the interference along the X, Y and Z directions may be higher. This effect can be corrected with a finer selection of sensor combinations. Selecting larger number of combinations for the Contextual Gap algorithm to optimize over also implies a longer a exploration phase. A trade off of the learning time versus interference with fewer number of arms has to be analyzed prior to on-orbit implementation of the Contextual Gap algorithm.

Table 4.1: Statistics of interference

	Mean (nT)	Median (nT)	Std dev. (nT)
Sensor 1	16.81	15.34	9.09
Sensor 2	36.99	33.74	18.92
Sensor 3	75.45	72.59	19.24
Sensor Minimum	15.81	14.79	7.91
Sensor Minimum Combination	7.21	6.16	4.50

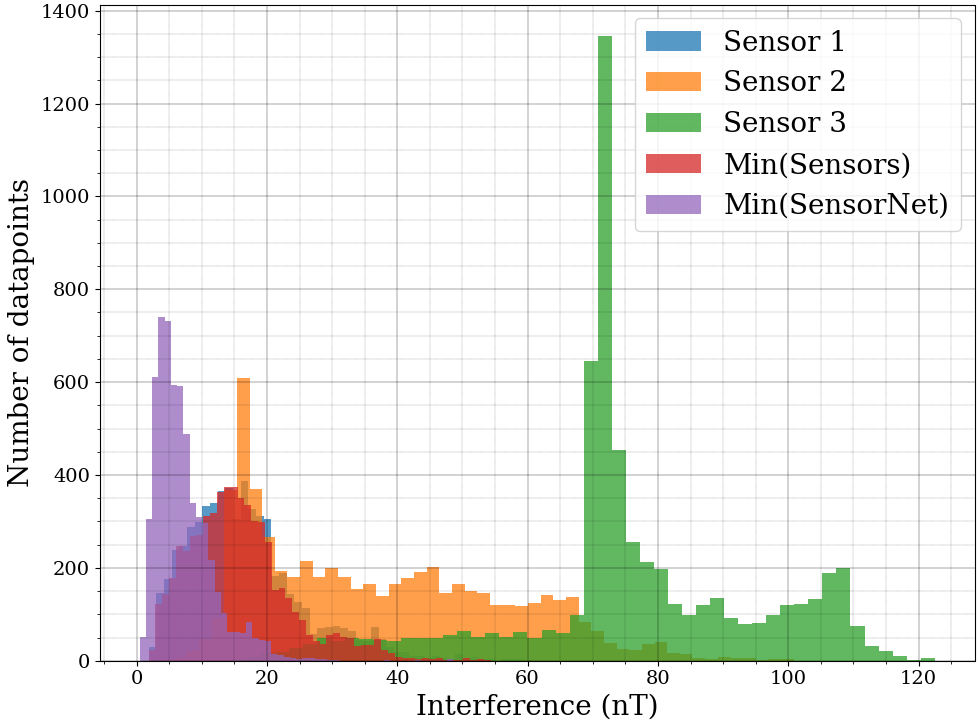

Figure 4.4: Histogram of magnetic field interference from experimental setup

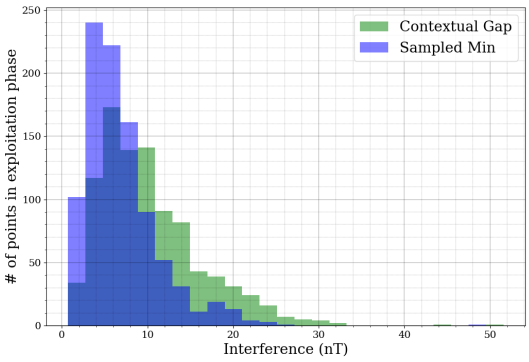

(a) Histogram of interference

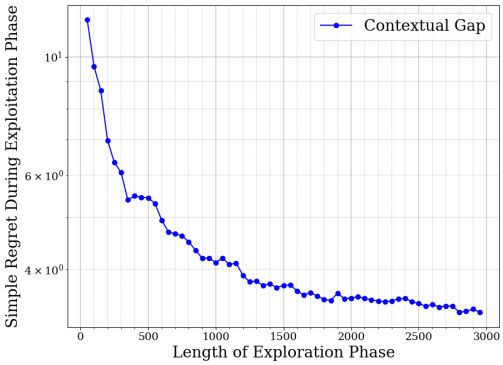

(b) Simple regret evaluation

Figure 4.5: Evaluation of simple regret minimization with sensor combinations - with on-orbit dataset modification

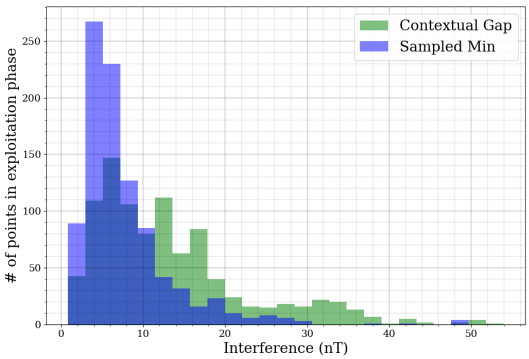

(a) Histogram of interference

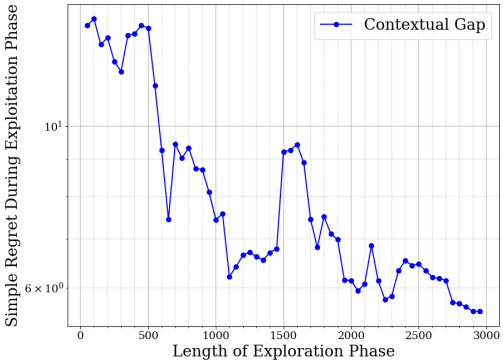

(b) Simple regret evaluation

Figure 4.6: Evaluation of simple regret minimization with sensor combinations - without on-orbit dataset modification

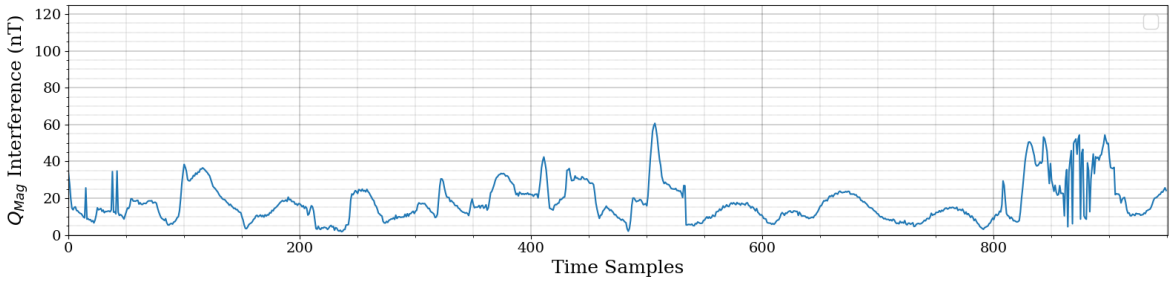

(a) Interference of Magnetometer 1

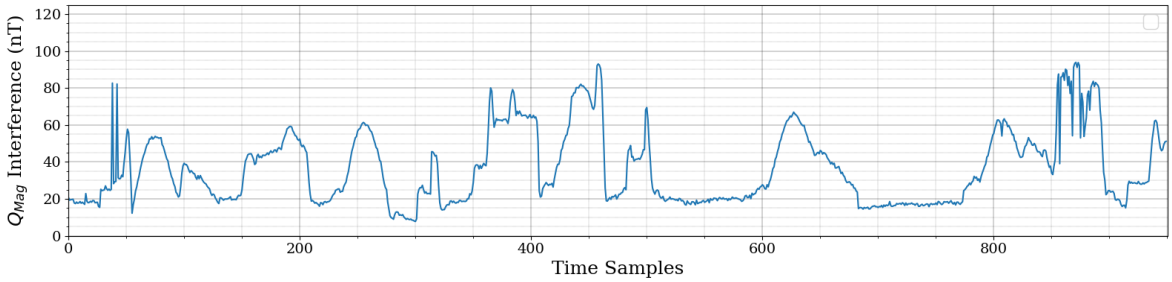

(b) Interference of Magnetometer 2

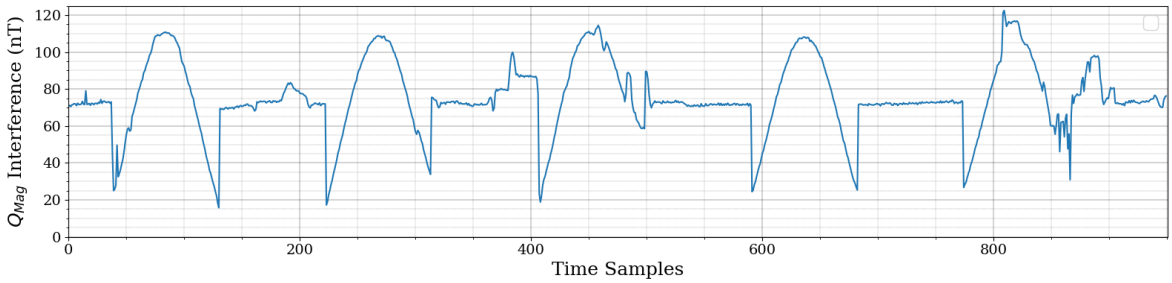

(c) Interference of Magnetometer 3

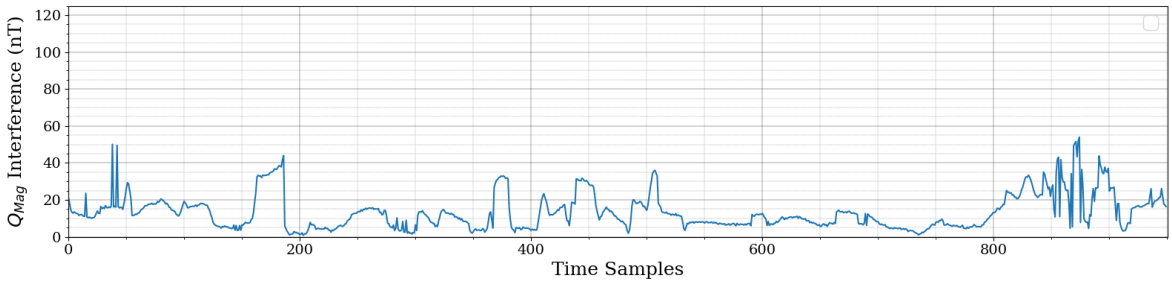

(d) Contextual Gap with 11 arms

Figure 4.7: Time series of magnitude of magnetic field interference

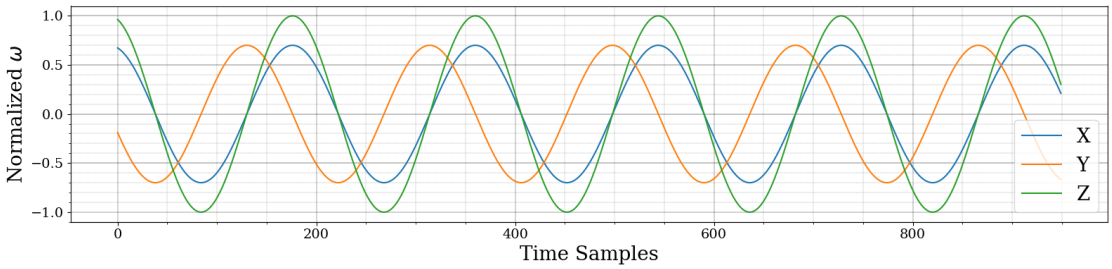

(a) Telemetry - angular velocity (synthetic)

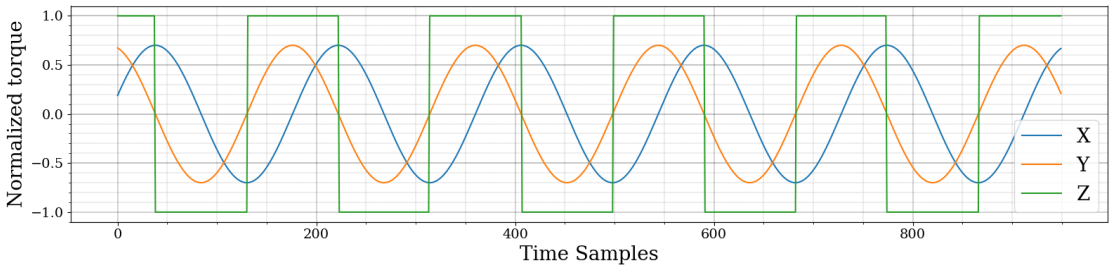

(b) Telemetry - torque (synthetic)

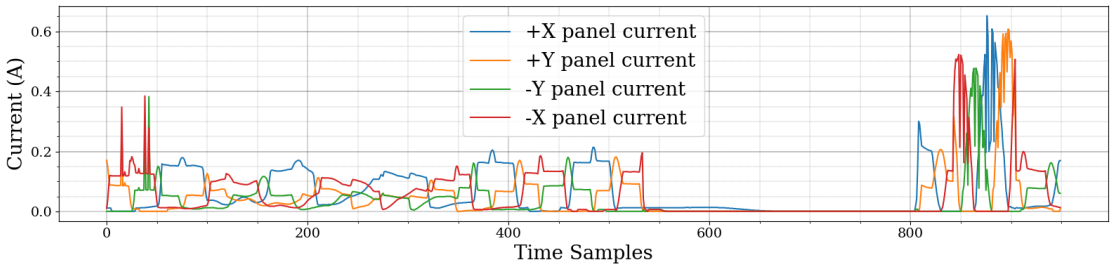

(c) Telemetry - solar panel currents (GRIFEX)

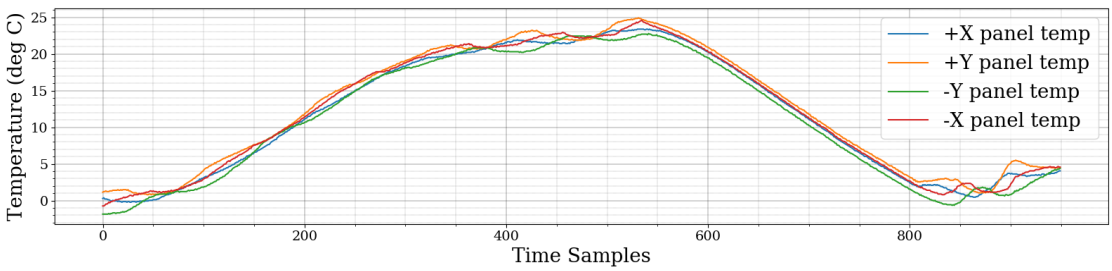

(d) Telemetry - solar panel temperatures (GRIFEX)

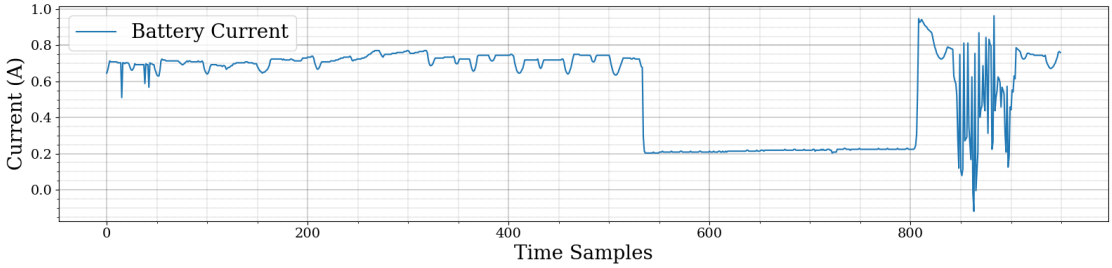

(e) Telemetry - battery (EPS) current (GRIFEX)

Figure 4.8: Telemetry used in experimental setup

IV.8 Conclusion

This chapter discussed a novel approach to the minimization of time-varying interference in spacecraft magnetometry. We showed that the problem can be modeled as a novel machine learning problem: one of simple regret minimization in the contextual bandit setting. We presented an algorithm, called Contextual Gap, for simple regret minimization based on theoretical bounds. For the proposed algorithm, we show empirical results on three multiclass datasets and a lab-based spacecraft magnetometer dataset based on on-orbit telemetry of the GRIFEX spacecraft.

CHAPTER V

Conclusion and Future Work

We have developed learning algorithms for orbit determination and spacecraft magnetometer interference cancellation. In addition, we also developed network architecture for implementation of Doppler based orbit determination. The learning algorithms developed operate under very general conditions. The orbit determination (OD) algorithm requires only visibility of the spacecraft cluster and observability of the dynamical system. The network architecture provides algorithms to track spacecraft clusters under the conditions required for OD with sufficient density of ground stations. The magnetic field interference cancellation algorithm works with CubeSat computational constraints and under realistic telemetry conditions.

In Chapter II, we provided an orbit determination algorithm for spacecraft clusters as the solution of a new machine learning problem of mixture distribution regression. We empirically demonstrated the generality of the orbit determination through different OD scenarios (experimental Doppler-only scenario, position based OD, a lunar orbit scenario and a low Earth orbit scenario for comparison with an EKF). We also demonstrated robustness to noise and the absence of initial estimate requirements with comparisons to EKF and show convergence of the mixture distribution regression based orbit determination algorithm when

the EKF diverges. To authors knowledge, this is the only Doppler only algorithm for orbit determination.

In Chapter III, we analyzed the new problem of MMSP-OU with the goal of maximizing measurements for orbit determination. The addition of a learning cluster provides a method for computing coordinated tracking algorithms with software defined ground stations. We proposed algorithms that can track spacecraft clusters with the standard launch window uncertainties in low Earth orbit.

In Chapter IV, we developed a novel way to minimize spacecraft magnetic field interference with distributed magnetometers and spacecraft telemetry. The proposed algorithm is a solution of the new machine learning problem of simple regret minimization in the contextual bandit setting. To the authors knowledge, this is the first solution to the minimizing spatially distributed time varying spacecraft noise under CubeSat computational constraints and when the noise sources far exceed the number of sensors.

This thesis forms the first forays into viewing these problems in spacecraft subsystems from a machine learning perspective and therefore opens up many different possibilities for future work. In many CubeSat deployments, due to the orbital parameters being tied to the dynamics of the upper stage, there exists strong correlation between the orbital parameters. Mixture distribution regression can be modified to use vector kernel operators to take advantage of correlation between the orbits in the spacecraft cluster. The batch version of mixture distribution regression is limited in updating the initial estimates with batch data. An on-line version of mixture distribution regression where data can be received and the orbital estimates can updated with time with additional measurements is of interest. A third direction for future work is to further study the connections between the magnitude of observability and convergence of the learning algorithm.

There are two areas of future work related to improvements and deployment of the ground

station network for OD. First, spectrum monitoring using software ground stations will also pick up measurements by extraneous ground transmissions in the band of operation, which will require adaptive selection of these transmissions for which training data generation may not be possible. This can be achieved by extending the marginal transfer learning to an $(n_S + 1)$-class version where training data for one of the classes is not provided. A second area of future work involves combining independent sensor measurements from observations other than those provided by the ground station network, such as direction of arrival, range and GPS measurements.

The approach developed in Chapter IV opens up areas of future work both in spacecraft systems and in machine learning. The distributed magnetometers learn minimum interference combinations. Since the number of interfering sources are larger than the number of magnetometers, this minimum is non-zero. This suggests a need for spacecraft bus architectures that provide regions of low magnetic field interference which complement the learning algorithm in minimization of magnetometer interference. In addition, on-orbit testing of the interference cancellation algorithm is required prior to field deployments of the contextual gap algorithm. In machine learning, there is scope for extension of this setting to reinforcement learning with the addition of the spacecraft attitude state. Since the telemetry and the magnetic field information already contain partial attitude information, the addition of low resolution magnetic reference and attitude estimation feedback can be used for a reinforcement learning setting for CubeSat ADCS.

We state in this work that learning systems can be used to solve complex non-linear and stochastic problems in space systems with elusive solutions by building precise connections to learning theory resulting in novel capabilities and understanding. Through this thesis we developed learning systems of mixture distribution regression, contextual bandits and greedy algorithms. We showed that these learning systems can solve complex non-linear and stochastic problems in space systems with elusive solutions such as orbit determination in

weakly observable settings and magnetic field interference cancellation in the presence of a large number of interfering sources. We showed that these solutions hold due to precise connections between observability and the existence of a map for mixture distribution regression and between the magnetic field interference and the reward in a contextual bandit setting. We have novel capabilities of Doppler-only orbit determination using ground station networks, a method for spacecraft magnetic field interference minimization with distributed magnetometers and novel algorithms for new machine learning problems of mixture distribution regression and simple regret minimization using contextual bandits. These novel capabilities provide a stepping stone for the integration of artificial intelligence in space technologies and in developing solutions to some of the most complex frontiers of humankind.

It is exciting to look forward to the technological innovations in space exploration and artificial intelligence that these methods and algorithms will help enable.

APPENDIX A

Appendix for Chapter 2

A.1 Background for Orbit Determination

In this section we introduce theoretical concepts in dynamical systems, probability, set theory and machine learning that are necessary for statement and analysis of the orbit determination problem. We restrict their definitions to the setting used in the thesis.

A.1.1 Dynamical System

The motion of a satellite and the observations associated with its motion can be described by a dynamical system. Spacecraft motion is represented as the variation of states in a state space with time. We define the state space as a metric space $(\mathcal{M}, d_{\mathcal{M}})$ with a smooth manifold $\mathcal{M}$ and a distance metric $d_{\mathcal{M}}$ (known as the Reimannian distance metric or the geodesic distance). For a point $m \in \mathcal{M}$, we define the tangent space $\mathfrak{T}_m\mathcal{M}$ of $\mathcal{M}$ as the set of all tangent vectors at m. We further define the tangent bundle associated with the manifold $\mathcal{M}$ as $\mathfrak{T}\mathcal{M} := \bigcup_{m\in\mathcal{M}} \mathfrak{T}_m\mathcal{M}$. We define the flow of a dynamical system as the function $\chi : \mathcal{M} \times \mathbb{R} \to \mathcal{M}$ which satisfies two properties:

1. For some $\Gamma \in \mathcal{M}$, $\chi(\Gamma, 0) = \Gamma$.

2. $\chi(\chi(\Gamma, t_1), t_2) = \chi(\chi(\Gamma, t_2), t_1) = \chi(\Gamma, t_1 + t_2)$ for $t_1, t_2 \in \mathbb{R}_+$.

The initial condition of the dynamical system is defined as $\Gamma \in \mathcal{M}$ such that $\chi(\Gamma, 0) = \Gamma$. The state of the dynamical system at time t is defined as $\tilde{\Gamma}(t) := \chi(\Gamma, t)$.

Generally, the flow of the spacecraft motion cannot be described in closed form and its evolution with time is described as the solution of a differential equation, defined using,

1. A vector field $w_0 : \mathcal{M} \times \mathbb{R}_+ \to T\mathcal{M}$ such that

$$\frac{d\tilde{\Gamma}(t)}{dt} = w_0(\tilde{\Gamma}(t), t),$$

   i.e., w_0 maps a state $\tilde{\Gamma}(t) \in \mathcal{M}$ to a point in its tangent space $T_{\tilde{\Gamma}(t)}\mathcal{M}$.

2. The initial condition $\tilde{\Gamma}(0) := \Gamma$.

In estimation problems in control theory, the state is not directly accessible and the evolution of the dynamical system is accessible only through an observer. We define the observer as a function $q_0 : \mathcal{M} \to \mathcal{Z}$ that maps a state $\tilde{\Gamma}(t)$ to a measurement or observation $z(t) \in \mathcal{Z}$ where $\mathcal{Z}$ is a metric space. Finally, we define the system function of the dynamical system as $U : \mathcal{M} \times \mathbb{R}_+ \to \mathcal{Z}$ as the overall function which maps initial condition $\Gamma \in \mathcal{M}$ and time $t \in \mathbb{R}_+$ to the observation z at time t i.e., $U(\Gamma, t) := q_0(\chi(\Gamma, t))$. [1]

In this thesis, we will restrict the initial conditions to lie in a compact subset $\mathcal{J} \subset \mathcal{M}$ and the time evolution to lie in an interval $\tilde{\mathcal{T}} \subset \mathbb{R}_+$. Due to continuity of the flow, the image $\chi(\mathcal{J}, \tilde{\mathcal{T}}) \subset \mathcal{M}$, is compact. We will assume that q_0 maps from $\chi(\mathcal{J}, \tilde{\mathcal{T}})$ to a compact metric space $\tilde{\mathcal{F}} \subset \mathcal{Z}$ with metric $d_{\tilde{F}}$ (these assumptions will be described formally later). In this thesis, we will work with dynamic systems with system function U restricted to the input

[1] For further details of the geometric structure of mechanical systems see Arnold[141] or Appendix A of Holm[142]. For definitions of the observation function and system function see Hermann and Krenner [143].

space $\mathcal{J} \times \tilde{\mathcal{T}}$ and the output space $\tilde{\mathcal{F}}$, i.e., $U : \mathcal{J} \times \tilde{\mathcal{T}} \to \tilde{\mathcal{F}}$. We will refer to $\mathcal{J}$ as the space of initial conditions or parameter space synonymously.

The dynamic system function U is said to be observable in $\mathcal{T} \subseteq \tilde{\mathcal{T}}$ if the partial inverse function $U^{-1} : (\mathcal{T} \to \tilde{\mathcal{F}}) \to \mathcal{J}$ such that $U^{-1}(U(\Gamma, \cdot)) = \Gamma$ exists and is unique almost everywhere. This definition of observability is more in line with identifiability and subsumes the definition of non-linear observability used in traditional control theory settings.

Applied here, the state $\tilde{\Gamma}(t)$ of a satellite at any time t can be described by its position and velocity at t. The dynamical system is created by the gravitational fields of celestial objects around the spacecraft. In this formulation, the tangent space $\mathfrak{T}_{\tilde{\Gamma}(t)}\mathcal{M}$ consists of points of velocity and acceleration of the satellite. The observer can be a ground sensor which measures direction $\tilde{f} \in \tilde{\mathcal{F}} = S^2$ (in the three dimensional sphere) of the spacecraft from the sensor and the observer function q_0 maps the state of the spacecraft to its direction with respect to the sensor.

A.1.2 Sets and Probability

Definition A.1 (Prokhorov Metric)**.** Let $(\mathcal{X}, d_{\mathcal{X}})$ be a compact metric space, with compact space $\mathcal{X}$ and metric $d_{\mathcal{X}}$. $\mathcal{X}$ is endowed with the Borel σ-algebra $\mathfrak{F}_{\mathcal{X}}$ induced by $d_{\mathcal{X}}$. Let $\mathcal{B}_{\mathcal{X}}$ be the space of probability distributions on $(\mathcal{X}, \mathfrak{F}_{\mathcal{X}})$. For $P_1, P_2 \in \mathcal{B}_{\mathcal{X}}$, the Prokhorov metric d_P is defined as

$$d_P(P_1, P_2) := \inf\{a \in [0,1] : P_1(A) \leq P_2(A^a) + a \ \ \forall A \in \mathfrak{F}_{\mathcal{X}} \text{ and vice versa}\} \tag{A.1}$$

where $A^a = \{x \in \mathcal{X} : \left(\inf_{x' \in \mathcal{X}} d_{\mathcal{X}}(x, x')\right) < a\}$. In this setting, $(\mathcal{B}_{\mathcal{X}}, d_P)$ is a metric space and d_P is said to induce a weak topology on $\mathcal{B}_{\mathcal{X}}$. [2]

[2] For further details see Section 6, ch. 1 of Billingsley[144].

Definition A.2 (Probability kernel function)**.** Consider two random variables X, Y defined on topological spaces $\mathcal{X}$ and $\mathcal{Y}$. The conditional probability distribution is a map $\mu : \mathcal{Y} \to \mathcal{B}_{\mathcal{X}}$ such that for $y \in \mathcal{Y}$, $P(X|y) := \mu(y)$ and $P(X \in A|Y) := \mu(Y)(X \in A)$ for $A \in \mathfrak{F}_{\mathcal{X}}$. We define the functional form of the conditional distribution μ as the probability kernel function. [3]

Definition A.3 (Set Distance)**.** Let $\mathfrak{m}$ be the Borel measure. Consider two measurable sets A, B with symmetric difference defined as $A\Delta B := A \setminus B \cup B \setminus A$. We define the set distance between two measurable sets A and B to be $d_S(A, B) := \mathfrak{m}(A\Delta B)$,

Definition A.4 (ϵ-Ball)**.** Let $\mathcal{X}$ be a compact metric space with metric $d_{\mathcal{X}}$. For any $x \in \mathcal{X}$, we define the ϵ-ball as the set

$$B_\epsilon(x, d_{\mathcal{X}}) := \{x' \in \mathcal{X} | d_{\mathcal{X}}(x, x') < \epsilon\}$$

Definition A.5 (ϵ-net)**.** Let $(\mathcal{J}, d_{\mathcal{J}})$ be a compact metric space. We say that a subset $\mathcal{A} \subset \mathcal{J}$ is an ϵ-net of $\mathcal{J}$ if

$$\inf_{a \in \mathcal{A}} d_{\mathcal{J}}(a, \gamma) < \epsilon,$$

for any $\gamma \in \mathcal{J}$.

A.1.3 Recent Techniques from Machine Learning

Now we present a brief background of two machine learning techniques recently proposed in literature to solve the problem of mixture distribution regression: distribution regression [76] and transfer learning [75].

[3] For more information and for construction of the probability kernel function, see Lemma 1.37 and Chapter 5 in Kallenberg[145].

Distribution regression and kernels Distribution regression [76] is a technique to estimate the mappings from the space of probability distributions on an observation space to a parameter space, when the only access to the probability distribution is through its observations [76].

Consider an observation space $\mathcal{X}$ and a parameter space $\mathcal{J}$. Let $\mathcal{B}_{\mathcal{X}}$ be the set of all probability distributions defined on $\mathcal{X}$. In the distribution regression setting, we are given J training *tasks*, $\{\{X_i^{(j)}\}_{i=1}^{n_j}, \Gamma^{(j)}\}_{j=1}^{J}$ where each training task $(\{X_i^{(j)}\}_{i=1}^{n_j}, \Gamma^{(j)})$ consists of a set of observations $\{X_i^{(j)}\}_{i=1}^{n_j}, X_i^{(j)} \in \mathcal{X}$ and a parameter $\Gamma^{(j)} \in \mathcal{J}$. For task j, observations $\{X_i^{(j)}\}_{i=1}^{n_j}$ are independent and identically distributed (i.i.d) draws from a probability distribution $P^{(j)} \in \mathcal{B}_{\mathcal{X}}$. Separate from this, we are also given a *test* task, $\{X_i^T\}_{i=1}^{n_T}$, observed from a similar but distinct probability distribution $P^T \in \mathcal{B}_{\mathcal{X}}$. The parameter Γ^T for the test task is unknown and has to be estimated from the training data.

We are interested in learning a function $r : \mathcal{B}_{\mathcal{X}} \to \mathcal{J}$ using the training data such that as the number of training tasks $J \to \infty$, the estimated parameter, using the learnt function r and the test observations, converges to the true parameter, i.e, $\|\Gamma^T - r(P^T)\| \to 0$.

In distribution regression, the function r is learnt using kernels. When $\mathcal{X}$ is a compact metric space, such as a closed and bounded subset of $\mathbb{R}^d$ (d-dimensional Euclidean space), it is possible to capture a probability distribution on $\mathcal{X}$ using a reproducing kernel Hilbert space (RKHS). We define the *kernel* as a function $\bar{k} : \mathcal{X} \times \mathcal{X} \to \mathbb{R}$ that is symmetric and positive definite. The reproducing kernel Hilbert space (RKHS) $\mathcal{H}_{\bar{k}}$, consists of the completion of the set of functions of the form $f(X) = \sum_i \alpha_i \bar{k}(X_i, X)$ for $X \in \mathcal{X}, \alpha_i \in \mathbb{R}$. The RKHS has a reproducing property:

$$f(X) = \langle f, \bar{k}(X, \cdot) \rangle, \forall X \in \mathcal{X}.$$

The kernel $\bar{k}$ can also be associated with a feature vector, defined as the map $\Psi_{\bar{k}} : \mathcal{X} \to \mathcal{H}_{\bar{k}}$ such that

$$\bar{k}(X_1, X_2) = \langle \Psi_{\bar{k}}(X_1), \Psi_{\bar{k}}(X_2) \rangle,$$

for $X_1, X_2 \in \mathcal{X}$. It is possible to define a vector extension to kernels such that the kernel describes a function with a vector output (Say $\mathbb{R}^d$). Such a kernel would map to the space of linear operators on $\mathbb{R}^d$, i.e., $\mathbb{R}^{d \times d}$.

Using the RKHS, it is possible to capture a probability distribution P on $\mathcal{X}$ as a function, called the mean embedding of P, defined as

$$\xi(P) := \int_{\mathcal{X}} \bar{k}(x, \cdot) dP(x).$$

For the j^{th} training task $(\{X_i^{(j)}\}_{i=1}^{n_j}, \Gamma^{(j)})$, denote $\widehat{P}^{(j)}$ as the finite reconstruction of $P^{(j)}$ from $\{X_i^{(j)}\}_{i=1}^{n_j}$. We can compute the empirical mean embedding as

$$\xi(\widehat{P}^{(j)}) := \frac{1}{n_j} \sum_{i=1}^{n_j} \bar{k}(X_i^{(j)}, \cdot).$$

Distribution regression performs regression over the mean embeddings and computes a function in $\mathcal{H}_{\mathfrak{K}}$. Given the training data, distribution regression solves the optimization

$$\widehat{r} = \underset{r \in \mathcal{H}_{\mathfrak{K}}}{\arg\min} \frac{1}{J} \sum_{j=1}^{J} \|r(\widehat{P}^{(j)}) - \Gamma^{(j)}\|_{\mathcal{J}}^2 + \lambda_2 \|r\|_{\mathcal{H}}^2,$$

and produces the estimate

$$\widehat{r}(\widehat{P}^{T}) = k_r (K + \lambda_2 I)^{-1} [\Gamma^{(1)}, \Gamma^{(2)}, \cdots, \Gamma^{(J)}]',$$

where $K := [\Re(\xi(\widehat{P}_i), \xi(\widehat{P}_j))]_{i=1,j=1}^{J,J}$ is the kernel matrix, $k_r := [\Re(\xi(\widehat{P}_j), \xi(\widehat{P}^T))]_{j=1}^{J}$ is the column vector of $\xi(\widehat{P}^T)$ with respect to the training distribution embeddings and $\lambda_2 \in \mathbb{R}$ is a regularization parameter [76].

The guarantees of convergence of the estimate provided by $\hat{r}$ is computed using the generalization error,

$$\mathcal{E}(r) := \mathbb{E}[\|\Gamma^T - r(P^T)\|],$$

where $\mathbb{E}$ is the expectation. Szabó et. al[76] show that the difference $\mathcal{E}(\hat{r}) - \inf_r \mathcal{E}(r) \to 0$ as $J \to \infty$ and $n_j \to \infty$.

When the kernel functions $\bar{k}, \Re$ have a *universality* property [146, 147], the mean embedding of $\bar{k}$ is injective and the RKHS $\mathcal{H}_\Re$ is dense in the space of continuous functions (any continuous function can be approximated with high accuracy). As we show in Section A.3, this property is particularly useful because the orbit determination setting provides a continuous map from the distribution of observations to the orbital parameters.

Marginal Transfer Learning Marginal transfer learning [75] is a form of domain generalization (DG). In the domain generalization problem, one has to learn a classifier to produce an identity (ID) or label for the observations through labeled data provided for similar yet distinct scenarios.

Consider an observation space $\mathcal{X}$ and a label or ID space $\mathcal{Y} = \{1, 2, .., n_S\}$. Let the space of distributions over $\mathcal{X} \times \mathcal{Y}$ be $\mathcal{B}_{\mathcal{X}\times\mathcal{Y}}$ and let ρ_{XY} be a probability distribution on $\mathcal{B}_{\mathcal{X}\times\mathcal{Y}}$. We are given training data from J tasks $\{X_i^{(j)}, Y_i^{(j)}\}_{i=1,j=1}^{n_j,J}$ such that $(X_i^{(j)}, Y_i^{(j)}) \overset{\text{i.i.d}}{\sim} P_{XY}^{(j)}$, $P_{XY}^{(j)} \overset{\text{i.i.d}}{\sim} \rho_{XY}$ and we are given a loss function $\ell : \mathbb{R} \times \mathcal{Y} \to \mathbb{R}_+$. Separately we are given unlabeled observations from a test task $\{X_i^T\}_{i=1}^{n_T}$ for $P_{XY}^T \sim \rho_{XY}$ for which the labels $\{Y_i^T\}_{i=1}^{n_T}$

are not observed and we are interested in predicting an ID for each observation in the test task.

The prediction of labels for the test task is similar but distinct from the training data, since the underlying probability distribution over which the data is drawn is similar but distinct. Marginal transfer learning approaches this problem by learning the classifier over an *extended* observation space $\mathcal{X} \times \mathcal{B}_{\mathcal{X}}$, i.e., it includes the probability distribution of the observations. In particular, marginal transfer learning computes a function $g : \mathcal{B}_{\mathcal{X}} \times \mathcal{X} \to \mathbb{R}$ where $\mathcal{B}_{\mathcal{X}}$ is the space of probability distributions defined on $\mathcal{X}$, so that for the test task $\{X_i^T\}_{i=1}^{n_T}$, the predicted labels are close to the true labels and the average loss $\frac{1}{n_T}\sum_{i=1}^{n_T} \ell(g(X_i^T, P^T), Y_i^T) \to 0$.

Let k be a kernel $k : \mathcal{X} \times \mathcal{X} \to \mathbb{R}$ on $\mathcal{X}$. Using k, we generate mean embeddings $\phi(P) := \int_{\mathcal{X}} k(x, \cdot) dP(x)$, of probability distribution P defined on $\mathcal{X}$. On $\phi(\mathcal{B}_{\mathcal{X}})$, the set of mean embeddings associated with $\mathcal{B}_{\mathcal{X}}$, let K be a kernel $K : \phi(\mathcal{B}_{\mathcal{X}}) \times \phi(\mathcal{B}_{\mathcal{X}}) \to \mathbb{R}$. Additionally, let k' be another kernel $k' : \mathcal{X} \times \mathcal{X} \to \mathbb{R}$ defined on data points $x \in \mathcal{X}$. In marginal transfer learning, given a loss function $\ell : \mathbb{R} \times \mathcal{Y} \to \mathbb{R}_+$, we seek the estimate [75]

$$\widehat{g} = \underset{g \in \mathcal{H}_{k_{PX}}}{\arg\min} \frac{1}{J}\sum_{j=1}^{J} \frac{1}{n_j}\sum_{i=1}^{n_j} \ell(g(\phi(\widehat{P}_X^{(j)}), X_i^{(j)}), Y_i^{(j)}) + \lambda_1 \|g\|^2_{\mathcal{H}_{k_{PX}}},$$

where $\widehat{P}_X^{(j)}$ is the finite reconstruction of $P_X^{(j)}$ and $\mathcal{H}_{k_{PX}}$ is the RKHS associated with a *product* kernel $k_{PX} : (\phi(\mathcal{B}_{\mathcal{X}}) \times \mathcal{X}) \times (\phi(\mathcal{B}_{\mathcal{X}}) \times \mathcal{X}) \to \mathbb{R}$ defined as the product of kernels K and k' as $k_{PX}((P_X, X)(P_{X'}, X')) := K(\phi(P_X), \phi(P_{X'}))k'(X, X')$. The optimization problem can be stated as a quadratic program. For further details refer to Blanchard et. al[75].

Convergence guarantees are provided through the average generalization error,

$$I(g, \ell, n_T) := \mathbb{E}_{P_{XY}^T \sim \rho_{XY}} \mathbb{E}_{(X,Y)^T \sim (P_{XY}^T)^{\otimes n_T}} \left[\frac{1}{n_T}\sum_{i=1}^{n_T} \ell(g(\widehat{P}_X^T, X_i^T), Y_i^T) \right].$$

where $\mathbb{E}$ is the expectation. With an infinite test sample ($n_T = \infty$), the average generalization error is equal to

$$I(g, \ell, \infty) := \mathbb{E}_{P_{XY} \sim \rho_{XY}} \mathbb{E}_{(X,Y)\sim(P_{XY})} \Big[\ell(g(P, X), Y) \Big].$$

Blanchard et. al[75] show that as the amount of training data increases, $I(\hat{g}, \ell, n_T) - \inf_g I(g, \ell, \infty) \to 0$. We will denote the optimal solution of the marginal transfer learner as g^*, i.e.,

$$g^* = \arg\min_{g \in \mathcal{H}_{k_{P_X}}} I(g, \ell, \infty)$$

We shall use marginal transfer learning/marginal prediction to ID the spacecraft in the cluster that produced an observation.

A.2 Orbit Determination Problem Setting

We consider the problem of orbit determination of a group of spacecraft, called a cluster, consisting of n_S spacecraft using observations from n_G sensors ($n_S, n_G \geq 1$). The spacecraft in the cluster have IDs $\{1, 2, ..., n_S\}$ associated with them. There are n_S instances of dynamical system flow and n_G observers. We have n_S objects whose initial conditions are $\{\Gamma_i\}_{i=1}^{n_S}$, where each Γ_i belongs to the space $\tilde{\mathcal{J}}$, the space of initial conditions. The spacecraft *cluster* has the initial condition $\Gamma = [\Gamma_1, \Gamma_2, \cdots, \Gamma_{n_S}]$ defined on $\mathcal{J} := \tilde{\mathcal{J}}^{n_s}$. Here we assume that Γ is a realization of a random variable satisfying the probability distribution P_Γ, which is known prior to orbit determination. For a cluster with initial condition Γ, the spacecraft cluster evolves through time and at time t, the cluster has the state $\tilde{\Gamma}(t) := \chi(\Gamma, t) := [\chi(\Gamma_1, t), \chi(\Gamma_2, t), \cdots, \chi(\Gamma_{n_S}, t)]$.

We shall use the terminology orbital parameters synonymously with initial conditions.

The n_G ground sensors observe the spacecraft cluster over a time period $\tilde{\mathcal{T}} \subset \mathbb{R}_+$. For each ground station $j, 1 \leq j \leq n_G$ and initial condition Γ, the dynamical system flow χ and the observation function $q_{0,j}$ results in the system function $U_j(\Gamma, t) := q_{0,j}(\chi(\Gamma, t))$. The overall dynamical system with observations from the ground station network has the system function $U(\Gamma, t) := [U_1(\Gamma, t), U_2(\Gamma, t), \cdots, U_{n_G}(\Gamma, t)]$.

The actual measurements from the spacecraft cluster that will be observed over $\tilde{\mathcal{T}}$ will be noisy realizations of $U(\Gamma, t)$ for some random times $t \in \tilde{\mathcal{T}}$. We shall denote the times of measurements with the random variable T_S. The times at which these observations will be seen is determined by two factors: A probability distribution P_{T_S} defined over $\tilde{\mathcal{T}}$ and the field of view of the ground sensors. A spacecraft $i, 1 \leq i \leq n_S$ produces signals over the observation interval $\tilde{\mathcal{T}}$ according to the probability distribution $P_{T_S,i}$. Based on this, the cluster produces observations of these signals according to probability distribution $P_{T_S} := \sum_i \pi_i P_{T_S,i}$, where π_i is probability of observation produced by spacecraft i, given that an observation is produced by the cluster. We denote the support of P_{T_S} as $\mathcal{T} \subseteq \tilde{\mathcal{T}}$.

The sensors (or ground stations) have a dynamic field of view due to the presence of the Earth creating a horizon. The network can receive an observation from a satellite in the cluster only if at least one of the ground stations has the satellite in its field of view. The direction vectors of the cluster from ground station j is described by a second system function $V_j : \mathcal{J} \times \tilde{\mathcal{T}} \to S^2$, where S^2 is the three dimensional sphere. For a specific spacecraft with initial condition Γ_i, $V_j(\Gamma_i, t)$ is a vector in S^2. Let $O_j \subset S^2$ denote the field of view of ground station $j, 1 \leq j \leq n_G$. Ground station j can produce observations of satellite i with initial condition Γ_i only if $V_j(\Gamma_i, t) \in O_j$. Based on this, we write that the measurements are produced by the network for orbit initial state Γ according to a conditional probability that is limited by O_j i.e., for a set $\mathcal{B}$ in the Borel $\sigma-$ algebra $\mathfrak{F}_{\tilde{\mathcal{T}}}$,

$$P(T_S \in B|\Gamma) := \frac{P_{T_S}(T_S \in B \cap \bigcup_{j=1}^{n_G}\{t \in \tilde{\mathcal{T}} : V_j(\Gamma, t) \in O_j\})}{P_{T_S}(T_S \in \bigcup_{j=1}^{n_G}\{t \in \tilde{\mathcal{T}} : V_j(\Gamma, t) \in O_j\})} \qquad \forall B \in \mathfrak{F}_{\tilde{\mathcal{T}}}.$$

Taking horizon visibility into account, we define the effective observation function of the dynamic system as $W : \mathcal{J} \to (\tilde{\mathcal{T}} \to \tilde{\mathcal{F}})$, which maps the initial conditions $\mathcal{J}$ to the space of functions that map from $\tilde{\mathcal{T}}$ to $\tilde{\mathcal{F}}$ such that for $t \in \tilde{\mathcal{T}}$,

$$W(\Gamma)(t) := [W_1(\Gamma)(t), W_2(\Gamma)(t), \cdots, W_{n_G}(\Gamma)(t)],$$

and

$$W_j(\Gamma)(t) = \begin{bmatrix} U_j(\Gamma_1, t)\mathbf{1}_{V_j(\Gamma_1,t)\in O_j} & U_j(\Gamma_2, t)\mathbf{1}_{V_j(\Gamma_2,t)\in O_j} & \cdots & U_j(\Gamma_{n_S}, t)\mathbf{1}_{V_j(\Gamma_{n_S},t)\in O_j} \end{bmatrix}.$$

For an observation generated at time T_S from spacecraft i, the noiseless version of measurements of ground station j is defined as $F_j := U_j(\Gamma_i, T_S)\mathbf{1}_{V_j(\Gamma_1,T_S)\in O_j}$. The source spacecraft i generating observation at time T_S is not known to the sensor network and has to be estimated. The noiseless version of the observations the *sensor network* produces at time T_S will be denoted by the random vector $\tilde{F}$, for $\tilde{F} := \begin{bmatrix} F_1 & F_2 & \cdots & F_{n_G} \end{bmatrix}$ defined over the compact space $\tilde{\mathcal{F}}$ and the noiseless versions of the observations of the sensor network will be denoted as $F := [\tilde{F}, T_S]$. The actual measurements of the sensor network are noisy versions of F, which we shall denote by the random variable X defined on the observation space $\mathcal{X}$ and will be generated according to the probability distribution $P(X|F)$ which, we shall assume, is known.

In the above setting, the distributions of the random variables are all known, the sets $O_j, 1 \leq j \leq n_G$ are all known but the flow χ (and therefore U, V) is known only through a set of differential equations as discussed in Section A.1.1 (For exact forms of the differential equations refer to Vallado[31]). The differential equations of U, V can be solved for measurement times T_S and hence examples of measurements for different spacecraft clusters can be drawn.

With this scenario, the orbit determination problem can be stated as follows. Given $P_\Gamma, P_{T_S}, P_{X|F}$ over the time interval $\tilde{\mathcal{T}}$, differential equations for U, V and actual measurements $\{X_1, X_2, \cdots, X_{n_T}\}$, can we estimate $\{\Gamma_i\}_{i=1}^{n_S}$, the orbital parameters or initial conditions?

Example We can consider the scenario of orbit determination of one spacecraft (MCubed-2) using one ground station (Ann Arbor, MI, USA). Over an observation interval of 6 hours, $\tilde{\mathcal{T}} := [epoch, epoch + 6hours]$, the observations will be performed by a Radio Frequency (RF) ground station observing Doppler measurements $\tilde{F} = Doppler$, from spacecraft RF transmissions, at transmission times T_S. The Doppler system function is estimated using the range rate differential equations U_1, as seen in Figure A.1. The observations will be visible only when the spacecraft is above the horizon $Elevation \in [0, 90^\circ]$ for $V_1 = Elevation$ and $O_1 = [0, 90^\circ]$. The effective observation function W is U limited by visibility, and the Doppler observations are seen when the ground station measures transmissions. P_{T_S} can be constructed based on the beacon (beacons are periodic transmissions of the satellite health) and tumbling characteristics of the spacecraft. Figure A.1 shows the functions U_1, W_1, the regions where $V_1(\Gamma, t) \in O_1$ and the observations $F = [\tilde{F}, T_S]$.

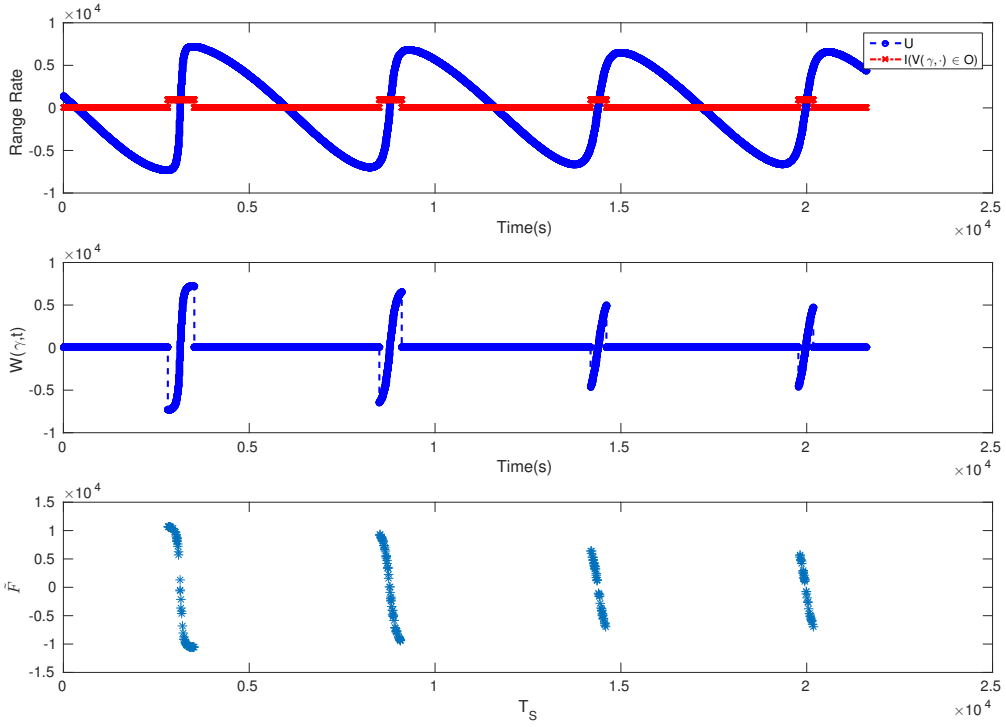

Figure A.1: Example scenario dynamical system and measurements

A.3 Observability Analysis

In this section, we present precise analysis reducing the orbit determination problem to the estimation of a map on the space of probability distributions of $\mathcal{X}$. Consider the orbit determination scenario from Section A.2. Given the distribution of timestamps of observations $P(T_S)$, a probability distribution on the spacecraft output vectors, F, is induced by the set of spacecraft orbit parameters, $\Gamma = [\Gamma_1, \Gamma_2, \cdots, \Gamma_{n_S}]$. Samples of F generate samples of measurements, X, at the sensor network.

Based on this, the probability distribution is split as

$$P(\Gamma, F, X) = P(\Gamma)P(F|\Gamma)P(X|F). \tag{A.2}$$

The conditional probability distribution $P(F|\Gamma)$ is shaped by the deterministic non-linear dynamic model describing the system and operating on T_S as discussed in Section A.2. Define $W(\Gamma)^{-1}$ as the pre-image of $W(\Gamma)$. For sets C and B in the σ-fields of $\tilde{F}$ and T_S, the conditional distribution $P(F|\Gamma)$ of a system can now be written as

$$P(F \in C \times B|\Gamma) = P(\tilde{F} \in C, T_S \in B|\Gamma) = P(T_S \in B \bigcap W(\Gamma)^{-1}(C)|\Gamma), \tag{A.3}$$

for $\Gamma \in \mathcal{J}$. The measure $P(X|F)$ then produces noisy observations.

Given this system, we next present mathematical analysis to provide insight into consequences of observability on the system. The distribution P_Γ induces a probability measure ρ on $R_\mathcal{X}$, a set of probability measures on $\mathcal{X}$(the set is $\{P(X|\Gamma), \Gamma \in \mathcal{J}\}$). $R_\mathcal{X}$ is a subset of $\mathcal{B}_\mathcal{X}$, the set of all Borel probability measures on $\mathcal{X}$. We show that if the system is observable, there exists a continuous map from $R_\mathcal{X} \subseteq \mathcal{B}_\mathcal{X}$ to $\mathcal{J}$ which can describe the orbital parameters. This continuous map can be learnt from random samples of the probability distributions drawn as random samples from the space of probability distribution $\mathcal{B}_\mathcal{X}$ using machine learning techniques and can then be used to estimate initial conditions for test datasets generated by spacecraft.

For the system defined in Appendix A.2, we make the following assumptions on the spaces $\mathcal{J}, \mathcal{F}, \mathcal{X}, \tilde{\mathcal{T}}$ and the probability distributions associated with them in order to characterize the effect of W on the probabilistic system:

A I $(\tilde{\mathcal{F}}, d_{\tilde{F}}), (\mathcal{X}, d_X)$ are compact metric spaces, $\tilde{\mathcal{J}}$ is a compact subset of a smooth manifold defined over $\mathbb{R}^{\tilde{d}}$ for some $\tilde{d} < \infty$ and $\tilde{\mathcal{T}}$ is a compact subset of $\mathbb{R}_+$ endowed with the regular Borel measure $\mathfrak{m}$.

A II P_{T_S} is absolutely continuous over support $\mathcal{T} \subseteq \tilde{\mathcal{T}}$.

A III The probability kernel function from $\mathcal{F} \to \mathcal{P}(\mathcal{X})$, for $\mathcal{P}(\mathcal{X}) \subseteq \mathcal{B}_{\mathcal{X}}$, is a homeomorphism in the weak topology induced by the Prokhorov metric $(\mathcal{B}_{\mathcal{X}}, d_P)$.

Let $\mathfrak{F}_{\mathcal{X}}$ be the σ-algebra induced by open (or closed) balls on $\mathcal{X}$ (Borel σ-algebra).

Assumption **A I** limits the analysis of the system to those that are most suitable to characterization in terms of probability measures, which is most systems of interest. Assumption **A II** requires the probability distribution of measurements over the observation time admits a density. Assumption **A III** is required for noise characteristics of the system where we assume that if the underlying noiseless parameters (such as directional of arrival, Doppler change or RADAR measurements) change, so does the probability distribution of the measurement system and this change is continuous. As a working example for assumption **A III**, when one measures range rate or Doppler shift of spacecraft signal transmissions with narrowband communication systems, it has been shown that the correlation function from which the feature vector X is obtained can be written as the sum of a distribution depending on Doppler shifted frequency and a residual [97, 90].

We define distance metrics $d_{U,p}, 1 \leq p < \infty$ on the set of functions defined on $\mathcal{T}$ to $\tilde{\mathcal{F}}$. For two functions c_1, c_2 with domain $\tilde{\mathcal{T}}$ and range $\subseteq \tilde{\mathcal{F}}$, we define the distance $d_{U,p}$ as

$$d_{U,p}(c_1, c_2) = \left[\int_{\mathcal{T}} (d_{\tilde{\mathcal{F}}}(c_1(t), c_2(t)))^p d\mathfrak{m} \right]^{\frac{1}{p}} \tag{A.4}$$

for $1 \leq p < \infty$ and

$$d_{U,\infty}(c_1, c_2) = \sup_{t \in \mathcal{T}} d_{\tilde{\mathcal{F}}}(c_1(t), c_2(t)) \tag{A.5}$$

when they exist. For a first step analysis, we ignore the effect of visibility V and consider the case where points in $U(\Gamma, t)$ for some $\Gamma \in \mathcal{J}$ and $t \in \mathcal{T}$ will always be observed.i.e., the observations aren't modulated by field of view and sensor specific horizon considerations and observations are produced through out $\mathcal{T}$ i.e., $P(T_S|\Gamma) = P_{T_S}$. In doing so, we can analyze the

probability distributions $\{P(X|\Gamma) : \Gamma \in \mathcal{J}\}$ and the nature of the probability kernel function associated with $P(X|\Gamma)$ using the following theorem.

Theorem A.1. *For the system defined by equations* (A.2) - (A.3) *with assumptions* ***A I*** *and* ***A III****, if* U *is observable in* $\mathcal{T}$ *and Lipschitz continuous in* $d_{U,\infty}$ *with respect to* Γ *in* $\mathcal{J}$ *then there exists a continuous inverse mapping* $\lambda : R_{\mathcal{X}} \to \mathcal{J}$ *for a compact set* $R_{\mathcal{X}} \subseteq \mathcal{B}_{\mathcal{X}}$ *on the topology* $(\mathcal{B}_{\mathcal{X}}, d_P)$.

See Appendix A.4.1 for proof.

Next, we introduce the effect of visibility only on the dynamics. We capitalize on the continuous and differentiable behavior of V seen in most astrodynamic systems. If V_j is differentiable and continuous then the corresponding indicator functions $\mathbf{1}_{V_j(\Gamma,t)\in O_j}$ will be continuous in $d_{U,p}$ for some p when it exists. We consider the behavior of functions continuous in $d_{U,p}$ to study the effect of V on W.

Theorem A.2. *For the system defined by equations* (A.2) - (A.3) *with assumptions* ***A I****,* ***A II*** *and* ***A III****,* W *is observable in* $\mathcal{T}$ *and continuous in* $d_{U,p}$ *for* $1 \leq p < \infty$ *if and only if there exists a continuous inverse map* $\lambda : R_{\mathcal{X}} \to \mathcal{J}$ *for a compact set* $R_{\mathcal{X}} \subseteq \mathcal{B}_{\mathcal{X}}$ *on the topology* $(\mathcal{B}_{\mathcal{X}}, d_P)$

See Appendix A.4.2 for proof.

Remark

- We are not assuming that the dynamic system itself be Borel measurable or in a metric topology. We are assuming that the resulting observation function have these characteristics. This is especially true in the case of a generating system based on Hamiltonian dynamics (using Poincaré elements for U) where the topology is locally Lebesgue, but observations such as position and Doppler over n_G ground stations are mapped to a metric space.

- When set $\mathcal{J}$ is such that $\|\Gamma\| \leq C_\Gamma$ as a consequence of assumption **A I**, the norm

$\|\lambda\|_\rho^2 \leq C_\Gamma^2$, where ρ is the probability distribution induced on $\mathcal{B}_\mathcal{X}$ by P_Γ. This will be useful in Appendix A.5, for convergence rate analysis.

The above two theorems state that in a system where the time intervals of observation are independent of the initial conditions, when the system is observable and is continuous in certain metric spaces they are also continuous in the space of probability distributions seen by the observations $B_\mathcal{X}$. This allows us to work with probability distributions instead of the observation function of the dynamic system.

In a practical implementation of this system, unless in a very constrained setting, is it generally the case that the visibility of observations is dependent on the orbit, as the region of observations is limited by the horizon of the ground stations or their sensitivity in parts of the horizon. We address this scenario next.

Now, consider the scenario where the presence of observations is also governed by the state of the visibility dynamical system V (which provides direction of arrival estimates). Let $\mathcal{T}(\Gamma)$ denote the preimage of O with respect to a particular Gamma:

$$\mathcal{T}(\Gamma) = \bigcup_{j=1}^{n_G} \{t \in \tilde{\mathcal{T}} : V_j(\Gamma)(t) \in O_j\}. \tag{A.6}$$

It is to be noted that in this scenario all ground stations may not be able to generate observations, only the ground stations for which $V_j(t) \in O_j, 1 \leq j \leq n_G$ will produce observations. We will assume that in the event that at least one of the ground stations generate observations, the rest will generate an observation of zero and we shall work with the observation function $W(\Gamma)$.

Using the definition of $\mathcal{T}(\Gamma)$, we extend Theorem A.2 to work with scenarios where the compact set of observations are a set of intervals (multiple satellite passes) where only some ground stations produce measurements. To do this, we first modify the assumption on

continuous distributions as follows

A II-A $P(T_S|\Gamma)$ is absolutely continuous over the support $\mathcal{T}(\Gamma) \subseteq \mathcal{T}, \forall \Gamma \in \mathcal{J}$.

Using this assumption, a corollary to Theorem A.2 can be stated as follows.

Corollary A.1. *For the system defined by equations* (A.2) - (A.3), (A.6) - (A.7) *and assumptions* ***A I***, ***A II-A*** *and* ***A III***, *if* V *continuous in* Γ, *differentiable in* t *and* $\mathfrak{m}(\bigcup_{j\in\{1,2,\cdots,n_G\}} \{t : \frac{\partial V_j}{\partial t} = 0\}) = 0$ *then the following are equivalent*

- W *is observable and continuous in* $d_{U,p}, 1 \leq p < \infty$ *over* $\Gamma \in \mathcal{J}$.
- *there exists a continuous inverse map* $\lambda : R_{\mathcal{X}} \to \mathcal{J}$ *for compact* $R_{\mathcal{X}} \subseteq \mathcal{B}_{\mathcal{X}}$ *on the topology* $(\mathcal{B}_{\mathcal{X}}, d_P)$.

See Appendix A.4.3 for proof.

Note that the condition of observability over $\mathcal{T}(\Gamma)$ is significantly stronger than observability over $\mathcal{T}$. It is, however, a weaker assumption compared to observability at every $t \in \mathcal{T}$. A simple example for low Earth orbits where the system may be observable over $\mathcal{T}(\Gamma)$ but is not observable for every $t \in \mathcal{T}$ occurs when estimating orbits with Doppler shift based measurements. In cases when one of initial conditions (the right ascension of the ascending nodes) differ by a small amount with all other initial conditions being identical, there will exist regions where the measurements are identical for significant sections of $\mathcal{T}(\Gamma)$. They will, however, be observable over $\mathcal{T}(\Gamma)$ as the point of the zero Doppler shift will differ in time and one of the points of where the zero doppler measurements occur belong to $\mathcal{T}(\Gamma)$ due to the low earth orbit characteristic.

Corollary A.1 essentially states that in the scenario with n_G ground stations producing observations, (observations which are generated from an i.i.d process over a time interval) a continuous map to the initial conditions exist from a compact subset of the space of proba-

bility distributions of the observation random variable X exists if two conditions are satisfied. First the observation function of the dynamic system is observable over the times when the probability of observations being generated are non-zero. Second, it is required that the rate of change of the visibility system V is non-zero almost everywhere. For the scenario where O represents the horizon and $V(\Gamma, t)$ represents the elevation of the spacecraft with respect to the ground station, corollary A.1 requires that for scenarios where the times of observation is modulated by the elevation, the rate of change of elevation with respect to the ground station is non-zero almost everywhere. This is guaranteed by Newton's laws of gravitation for all cases except Geostationary orbits. However, for geostationary orbits $\mathcal{T}(\Gamma) = \mathcal{T}$ and the continuous map still exists according to theorem A.2. In an orbit determination scenario with direction of arrival estimates, this implies that if the observability and continuity conditions in theorem A.1, A.2 and corollary A.1 are satisfied (which is necessary for any estimator to be consistent), then there exists a continuous mapping from the probability distributions of the direction of arrival measurements observed to the orbital parameters. This continuous mapping also exists even when observations are spread across multiple ground stations in time $\mathcal{T}$.

A.4 Proofs for Theorems in Appendix A.3

We shall denote the probability kernel function of $P(F|\Gamma)$ as

$$\mu(\Gamma)(D) := P(\tilde{F} \in C, T_S \in B|\Gamma) = P(T_S \in B \bigcap W(\Gamma)^{-1}(C)|T_S \in \mathcal{T}(\Gamma), \Gamma), \tag{A.7}$$

A.4.1 Proof of Theorem A.1

Proof. If U is observable and continuous then there exists a continuous bijective mapping from $\mathcal{J}$ onto $U(\mathcal{J},\cdot)$. For such a bijective mapping U, let the probability kernel function associated with $P(F \in \cdot|\Gamma) = \mu(\Gamma)$. By continuity of U, for a given δ we have ϵ such that $\Gamma_1, \Gamma_2 \in \mathcal{J}$ with $d_{\mathcal{J}}(\Gamma_1,\Gamma_2) < \epsilon$ implies $d_{\tilde{F}}(U(\Gamma_1)(t), U(\Gamma_2)(t)) < \delta$, $\forall t \in \tilde{\mathcal{T}}$.

Consider sets $C \in \mathfrak{F}_{\tilde{\mathcal{F}}}, B \in \mathfrak{F}_{\mathcal{T}_S}$. Let $U(\Gamma)^{-1}(C) := \{t \in \mathcal{T}|U(\Gamma,t) \in C\}$. From the $\epsilon-\delta$ definition of continuity, for any $t \in U(\Gamma_1)^{-1}(C)$ we can find a point $f \in U(\Gamma_2, C^{\delta})$ such that $d_{\tilde{\mathcal{F}}}(U(\Gamma_1,t),f) < \delta$. The probability kernel function in the absence of visibility constraints can be written as

$$\begin{aligned}\mu(\Gamma)(C\times B) &:= P(\tilde{F}\in C, T_S \in B|\Gamma=\Gamma) = P(\tilde{F}\in C, T_S\in B)\\ &= P_{T_S}(T_S \in B \cap U(\Gamma)^{-1}(C))\end{aligned}$$

The previous continuity argument over U implies that for every set $D = C\times B$, we have $\tilde{D} = C^{\delta}\times B \subseteq D^{\delta}$ such that $\mu(\Gamma_1)(D) = \mu(\Gamma_2)(\tilde{D})$ and therefore $\mu(\Gamma_1)(D) \le \mu(\Gamma_2)(D^{\delta}) + \delta$. Using a similar argument $\mu(\Gamma_2)(D) \le \mu(\Gamma_1)(D^{\delta}) + \delta$. This implies that

$$\begin{aligned}d_P(\mu(\Gamma_1),\mu(\Gamma_2)) &= \inf\{\alpha : \mu(\Gamma_1)(D) \le \mu(\Gamma_2)(D^{\alpha}) + \alpha \text{ and } \mu(\Gamma_2) \le \mu(\Gamma_1)(D^{\alpha}) + \alpha,\ \forall D \in \mathfrak{F}_{\mathcal{F}}\}\\ &< \delta\end{aligned}$$

Also, as U is observable over $\mathcal{J}$, if $\Gamma_1 \neq \Gamma_2$, then there exists $D \in \mathfrak{F}_{\mathcal{F}}$ such that $\mu(\Gamma_1)(D) \neq \mu(\Gamma_2)(D)$. Therefore, there exists a continuous function from $\tilde{R}_{\mathcal{F}}$ to $\mathcal{J}$ for $\tilde{R}_{\mathcal{F}} \subseteq \mathcal{B}_{\mathcal{F}}$. Since the kernel function from $\mathcal{F}$ to $\mathcal{B}_{\mathcal{X}}$ is bijective and continuous from assumption **A III**, the hypothesis holds.

□

A.4.2 Proof of Theorem A.2

Proof. ($\Rightarrow$) Let $\nu(\Gamma)$ be the density function of the probability measure $\mu(\Gamma)$ (This exists by assumption **A II**). Fix $\epsilon' > 0$. For ϵ', pick δ and ϵ such that $\epsilon' > [\sup_{\Gamma \in \mathcal{J}, t \in \mathcal{T}} \nu(\Gamma)(t)]\epsilon > \delta > 0$. By continuity of $W(\Gamma)$ in $d_{U,p}$, for the given δ, ϵ, there exists δ' such that $d_{\mathcal{J}}(\Gamma_1, \Gamma_2) < \delta' \Rightarrow d_{U,p}(W(\Gamma_1), W(\Gamma_2)) < \delta\epsilon^{1/p}$.

Let $\mathcal{T}_\delta = \{t \in \mathcal{T} : d_{\tilde{\mathcal{F}}}(W(\Gamma_1)(t), W(\Gamma_2)(t)) > \delta\}$. We have, for any such Γ_1, Γ_2 defined previously,

$$d_{U,p}(W(\Gamma_1), W(\Gamma_2)) = \left[\int_{\mathcal{T}} d_{\tilde{\mathcal{F}}}(W(\Gamma_1), W(\Gamma_2)) d\mathfrak{m}\right]^{\frac{1}{p}} \geq$$
$$\geq \left[\int_{\mathcal{T}_\delta} d_{\tilde{\mathcal{F}}}(W(\Gamma_1), W(\Gamma_2)) d\mathfrak{m}\right]^{\frac{1}{p}} \geq \delta \mathfrak{m}(\mathcal{T}_\delta)^{1/p}.$$

Since $d_{U,p}(W(\Gamma_1), W(\Gamma_2)) < \delta\epsilon^{1/p}$, this argument implies that $\mathfrak{m}(\mathcal{T}_\delta) < \epsilon$

Now, consider any set $D = B \times C \in \mathfrak{F}_{\mathcal{F}}$ ($B \in \mathfrak{F}_{\mathcal{T}}$ and $C \in \mathfrak{F}_{\tilde{\mathcal{F}}}$ since they are all Borel sigma algebras). Define $W(\Gamma)^{-1}(C) := \{t \in \mathcal{T} | W(\Gamma)(t) \in C\}$, the preimage of $W(\Gamma)$. When $\mathfrak{m}(\mathcal{T}_\delta) < \epsilon$, it follows from the definition of $\mathcal{T}_\delta$ that $W(\Gamma_1)^{-1}(C) \cap (\mathcal{T} \setminus \mathcal{T}_\delta) \subseteq W(\Gamma_2)^{-1}(C^\delta) \cap (\mathcal{T} \setminus \mathcal{T}_\delta)$ and vice versa.

Additionally, we also have that

$$P_{T_S}(B \cap W(\Gamma_1)^{-1}(C) \cap \mathcal{T}_\delta) \leq P_{T_S}(B \cap \mathcal{T}_\delta) \leq P_{T_S}(\mathcal{T}_\delta) \leq P_{T_S}(\mathcal{T}_\delta) + P_{T_S}(B \cap W(\Gamma_2)^{-1}(C^\delta) \cap \mathcal{T}_\delta).$$

Let $\tilde{\epsilon} := P_T(\mathcal{T}_\delta)$. Consider $\mu(\Gamma_1)(D)$,

$$\mu(\Gamma_1)(D) = P_{T_S}(B \cap W(\Gamma_1)^{-1}(C)).$$

We split the probability into events in $(\mathcal{T} \setminus \mathcal{T}_\delta)$ and $\mathcal{T}_\delta$,

$$\mu(\Gamma_1)(D) = P_{T_S}(B \cap W(\Gamma_1)^{-1}(C) \cap \mathcal{T} \setminus \mathcal{T}_\delta) + P_{T_S}(B \cap W(\Gamma_1)^{-1}(C) \cap \mathcal{T}_\delta).$$

Using the preceding argument,

$$\mu(\Gamma_1)(D) \leq P_{T_S}(B \cap W(\Gamma_2)^{-1}(C^\delta) \cap \mathcal{T} \setminus \mathcal{T}_\delta) + P_{T_S}(B \cap W(\Gamma_2)^{-1}(C) \cap \mathcal{T}_\delta) + P_{T_S}(T_\delta).$$

Using the definition of $P_{T_S}(\mathcal{T}_\delta)$,

$$\mu(\Gamma_1)(D) \leq P_{T_S}(B \cap W(\Gamma_2)^{-1}(C^\delta) \cap \mathcal{T} \setminus \mathcal{T}_\delta) + P_{T_S}(B \cap W(\Gamma_2)^{-1}(C) \cap \mathcal{T}_\delta) + \int_{\mathcal{T}_\delta} \nu(\Gamma)(t) d\mathfrak{m}(t)$$

From the supremum of $\nu(\Gamma)(t)$ and from the previous argument that $\mathfrak{m}(\mathcal{T}_\delta) < \epsilon$,

$$\mu(\Gamma_1)(D) \leq P_{T_S}(B \cap W(\Gamma_2)^{-1}(C^\delta) \cap \mathcal{T} \setminus \mathcal{T}_\delta) + P_{T_S}(B \cap W(\Gamma_2)^{-1}(C) \cap \mathcal{T}_\delta) + [\sup_{\Gamma \in \mathcal{J}, t \in \mathcal{T}} \nu(\Gamma)(t)]\epsilon.$$

By construction of ϵ' and C^δ,

$$\begin{aligned}\mu(\Gamma_1)(D) &\leq P_{T_S}(B \cap W(\Gamma_1)^{-1}(C^\delta)) + \epsilon' \\ &\leq \mu(\Gamma_2)(D^{\epsilon'}) + \epsilon'.\end{aligned}$$

By a similar argument, we also have $\mu(\Gamma_2)(D) \leq \mu(\Gamma_1)(D^{\epsilon'}) + \epsilon'$. Therefore $d_P(\mu(\Gamma_1), \mu(\Gamma_2)) < \epsilon'$.

Also, as W is observable over $\mathcal{J}$, if $\Gamma_1 \neq \Gamma_2$, then there exists $D \in \mathfrak{F}_\mathcal{F}$ such that $\mu(\Gamma_1)(D) \neq \mu(\Gamma_2)(D)$ (injective map). Since $\mathcal{J}$ is compact, μ forms a continuous and injective map to $R_\mathcal{F} \subseteq \mathcal{B}_\mathcal{F}$ and $(\mathcal{B}_\mathcal{F}, d_P)$ is a compact metric space (Prokhorov's theorem), we have that the image $R_\mathcal{F} = \mu(\mathcal{J})$ is compact. The existance of a continuous and injective map onto a compact metric space implies the existance of an inverse map, therefore there exists a continuous map $\lambda : R_\mathcal{X} \to \mathcal{J}$ (see Rudin[148]) .

($\Leftarrow$) Proof by contradiction. Assume there exists a homeomorphic map $\lambda : R_{\mathcal{F}} \to \mathcal{J}$ from a compact metric space $(R_{\mathcal{F}}, d_P)$. Additionally, assume that equations (A.2) - (A.3) hold and $\lambda^{-1} = \mu$ almost everywhere, but U is not continuous for some particular Γ_1,i.e, $\exists \epsilon > 0$ such that for any ball $B_\delta(\Gamma_1, \|\cdot\|_2)$, $W(B_\delta(\Gamma_1, \|\cdot\|_2)) \not\subseteq B_\epsilon(W(\Gamma_1), d_{U,p})$. This also implies the resulting mapping is not continuous in measure at Γ_1, since, for some $\epsilon' > 0$ and for any $\delta > 0$, the image of $B_\delta(\Gamma_1, d_{U,p})$ under map μ, $\mu(B_\delta(\Gamma_1, d_{U,p})) \not\subseteq B_{\epsilon'}(\mu(\Gamma_1), d_P)$ (Following similar arguments as in the direct case). This, however, is a contradiction as λ^{-1} is continuous. □

A.4.3 Proof of Corollary A.1

Proof. P_{T_S} is absolutely continuous with respect to the Lebesgue measure (limited to the Borel σ-algebra). If $\mathcal{T}(\Gamma)$ is continuous in Γ and can be expressed as a union of intervals, we have for every $\delta > 0$, ϵ_1, ϵ_2 such that $d_{\mathcal{J}}(\Gamma_1, \Gamma_2) < \epsilon_1 \Rightarrow d_S(\mathcal{T}(\Gamma_1), \mathcal{T}(\Gamma_2)) < \epsilon_2 \Rightarrow d_P(\mu(\Gamma_1), \mu(\Gamma_2)) < \delta$.

Define $\mathcal{T}_i(\Gamma) = \{t \in \tilde{\mathcal{T}} : V_i(\Gamma)(t) \in O_i\}$ for $i \in \{1, 2, \cdots, n_G\}$. Let $\mathcal{T}_i^{\epsilon}(\Gamma) = \{t \in \tilde{\mathcal{T}} : V_i(\Gamma)(t) \in O_i^{\epsilon}\}$ and $\mathcal{T}_i^{-\epsilon}(\Gamma) = \{t \in \tilde{\mathcal{T}} : V_i(\Gamma)(t) \in O_i^{-\epsilon}\}$ where $O_i^{\epsilon} = \{o \in \mathbb{R}^n | d_G(o, O_i) < \epsilon\}$ for distance metric d_G on the three dimensional sphere and $O_i^{-\epsilon} = ((O_i^c)^{\epsilon})^c$.

Since V is continuous in Γ, we have $\mathcal{T}_i^{-2\epsilon}(\Gamma_1) \subseteq \mathcal{T}_i^{-\epsilon}(\Gamma_2) \subseteq \mathcal{T}_i(\Gamma_1) \subseteq \mathcal{T}_i^{\epsilon}(\Gamma_2) \subseteq \mathcal{T}_i^{2\epsilon}(\Gamma_1)$. For a given Γ, by definition, $\mathcal{T}_i(\Gamma) \subseteq \mathcal{T}_i^{\epsilon}(\Gamma)$. If the two sets $\mathcal{T}_i(\Gamma)$ and $\mathcal{T}_i^{\epsilon}(\Gamma)$ are equal for all Γ, then the continuity condition is satisfied trivially and therefore we only need to consider the case when $\mathcal{T}_i(\Gamma) \subset \mathcal{T}_i^{\epsilon}(\Gamma)$. For a given ϵ consider $\mathcal{T}_i^{-\epsilon}(\Gamma) \Delta \mathcal{T}_i^{\epsilon}(\Gamma)$ i.e., the pre-image of $O_i^{-\epsilon} \Delta O_i^{\epsilon} = \bigcup_{p \in Bd(O_i)} B_\epsilon(p, d_G)$. We have, from the definition of the Lebesgue measure, $d_S(\mathcal{T}_i^{-\epsilon}(\Gamma), \mathcal{T}_i^{\epsilon}(\Gamma)) \leq \mathfrak{m}(R_{O_i,\epsilon}) + \mathfrak{m}(\bigcup_j C_j \cap V_i(\Gamma)^{-1}(O_i^{-\epsilon} \Delta O_i^{\epsilon}))$, where $R_{O_i,\epsilon}$ is the set where the derivative of $V_i(\Gamma)$ with respect to t is zero in $O_i^{-\epsilon} \Delta O_i^{\epsilon}$ and C_j is a countable covering of the set $\tilde{\mathcal{T}} \setminus R_{O_i,\epsilon}$ over the neighborhoods of points where the implicit function theorem can be applied.

Therefore, we have that when $\mathfrak{m}(R_{O_i,\epsilon}) = 0$, for any $\epsilon_2 > 0$, $\exists$ an ϵ_3 such that $d_S(O_i^{-\alpha}, O_i^{\alpha}) < \epsilon_3$ implies $d_S(\mathcal{T}_i^{-\alpha}(\Gamma), \mathcal{T}_i^{\alpha}(\Gamma)) < \epsilon_2$, which implies continuity of $\mathcal{T}_i(\Gamma)$ and $\mathcal{T}(\Gamma)$ with respect to Γ. The rest of the proof follows from theorem A.2. □

A.5 Learning Theory

We present generalization error bounds on the mixture distribution regression presented in Section II.3 in terms of the generalization errors of the marginal transfer learning and distribution regression system. We show that, as the amount of training data J_{tl} and J_{dr} increases, the generalization error in estimation of the orbital parameters of the spacecraft cluster goes to zero. We provide generalization error bounds for a *soft label* version of the mixture distribution algorithm, where the spacecraft IDs are assigned with probabilities in the estimated class posterior distributions, instead of sampling them from the estimated class posterior distributions.

We denote the probability distribution on $\mathcal{B}_{\mathcal{X}} \times \mathcal{J}$ that is induced by the prior P_Γ as $\rho(P, \Gamma)$. For the development of learning theoretic bounds, we will work directly with conditional embeddings generated directly by the estimated class conditional distributions instead of sampling the class IDs. For $B \in \mathfrak{F}_{\mathcal{X}}$ and $P \in \mathcal{B}_{\mathcal{X}}$, the estimated class conditional probability can be written as

$$\hat{P}_i(X \in B) := \hat{P}(X \in B | Y = i) := \frac{\hat{P}(Y = i | X \in B)}{\hat{\pi}_i} P(X \in B),$$

where $\hat{\pi}_i = \int_{\mathcal{X}} \hat{P}(Y = i|X) dP(X)$. Using this definition, we re-define the conditional embeddings generated by transfer learning in the soft label setting, for class $y \in \{1, 2, ..., n_S\}$, as

$$\hat{h}_y(P) := \int_{\mathcal{X}} \bar{k}(X, \cdot) \frac{\hat{P}(Y = y|X)}{\hat{\pi}_i} dP.$$

Based on the definitions in Section II.3, the equivalent finite sample version of the class conditional embeddings, for training task j, for class y, can be written as

$$\hat{h}_y(\hat{P}^{(j)}) = \frac{1}{n_j} \sum_{i=1}^{n_j} \bar{k}(X_i^{(j)}, \cdot) \frac{\hat{P}(Y_i^{(j)} = y|X_i^{(j)})}{\hat{\pi}_i},$$

where $\hat{\pi}_i = \frac{1}{n_j} \sum_{i=1}^{n_j} \hat{P}(Y_i^{(j)} = i|X_i^{(j)})$.

The average error for the estimated mixture distribution regression of class i is defined as

$$\mathcal{E}(\hat{r}_i \circ \hat{h}_i) := \mathbb{E}_{(P,\Gamma)\sim\rho}\left[\|\Gamma_i - \hat{r}_i(\hat{h}_i(P))\|\right]$$

Denote the optimal conditional embedding for class i as h_i^* and the optimal regressor for class i as r_i^*, i.e., for $P = \sum_i \pi_i P_i$,

$$h_i^*(P) = \int_{\mathcal{X}} \bar{k}(X, \cdot) dP_i(X)$$

and

$$r_i^* = \arg\min_{r \in \mathcal{H}_{\mathfrak{K}}} \mathcal{E}(r \circ h_i^*).$$

We provide error bounds on $\mathcal{E}(\hat{r}_i \circ \hat{h}_i) - \mathcal{E}(r_i^* \circ h_i^*)$ under the following assumptions:

L I $\tilde{\mathcal{J}}$ is a compact subset of a real separable Hilbert space and $\mathcal{X}$ is a compact metric space.

L II Kernels $k, k', \bar{k}, K$ and $\mathfrak{K}$ are universal and bounded by constants $B_k^2, B_{k'}^2, B_{\bar{k}}^2, B_K^2, B_{\mathfrak{K}}^2$

respectively. In addition, the cannonical feature vectors associated with kernels K and $\mathfrak{K}$, $\Psi_K : \mathcal{H}_k \to \mathcal{H}_K$ and $\Psi_{\mathfrak{K}} : \mathcal{H}_{\bar{k}} \to \mathcal{H}_{\mathfrak{K}}$ are Hölder continuous with constants α and β and scaling factors $\mathfrak{L}_K, \mathfrak{L}_{\mathfrak{K}}$. i.e.,

$$\forall v, w \in \mathcal{H}_k \qquad \|\Psi_K(v) - \Psi_K(w)\|_{\mathcal{H}_K} \leq \mathfrak{L}_K \|v - w\|^{\alpha}_{\mathcal{H}_k}$$

and

$$\forall v, w \in \mathcal{H}_{\bar{k}} \qquad \|\Psi_{\mathfrak{K}}(v) - \Psi_{\mathfrak{K}}(w)\|_{\mathcal{H}_{\mathfrak{K}}} \leq \mathfrak{L}_{\mathfrak{K}} \|v - w\|^{\beta}_{\mathcal{H}_k}$$

L III The loss function ℓ is the logistic loss and is L_ℓ-Lipschitz in its first variable and bounded by B_ℓ.

L IV Given a marginal probability distribution $P_X \in \mathcal{B}_{\mathcal{X}}$, the posterior conditional distribution is a deterministic function of P_X, i.e., $P(Y|X) = Z(P_X)$ for some deterministic function Z.

Note that the assumption **L I** is more general than **A III**. The assumption **L II** is satisfied by Gaussian kernels and exponential inner product kernels. Assumption **L IV** is satisfied for the orbit determination scenario due to observability and the existence of the map λ. Using these assumptions, the generalization error is bounded by the following theorem.

Theorem A.3 (Error bound on mixture distribution regression)**.** *For the mixture distribution regression setting assume that the conditions **L I** - **L IV** are satisfied. Then, for $\delta > 0$ and $1 \geq \delta_2 > 0$, with probability $1 - 2\delta - \delta_2$,*

$$\mathcal{E}(\hat{r}_i \circ \hat{h}_i) - \mathcal{E}(r_i^* \circ h_i^*) \leq C_1 \mathcal{S}_{tl}^{\beta} + C_2 \mathcal{S}_{tl}^{\beta/2} + C_3 \left(\sqrt{\frac{\log \delta^{-1}}{J_{dr}}} + \mathcal{S}_{tl} \right)^{\beta} + 4\mathcal{S}_{dr},$$

where

$$\mathcal{S}_{tl} := I(\hat{g}, \ell, \infty) - I(g^*, \ell, \infty),$$

$$\mathcal{S}_{dr} := \mathcal{E}(\hat{r}_i \circ h_i^*) - \mathcal{E}(r_i^* \circ h_i^*),$$

$C_1 := \frac{2C_\Gamma^2 B_\Re^2 L_\Re}{\lambda_{2,i}^2}\left(\frac{2B_{\bar{k}}}{c_Y}\right)^{2\beta}$, $C_2 := \frac{C_\Gamma^2 B_\Re \sqrt{L_\Re}}{\lambda_{2,i}}\left(1 + \frac{B_\Re}{\lambda_{2,i}}\right)\left(\frac{2B_{\bar{k}}}{c_Y}\right)^{\beta}$, $C_3 := \frac{4}{\lambda_{2,i}}\left(2 + \frac{B_\Re^4}{\lambda_{2,i}^2}\right)C_\Gamma^2 L_\Re\left(\frac{2B_{\bar{k}}}{c_Y}\right)^{2\beta}$ *and* $c_Y = \pi_i\hat{\pi}_i$ *provided* $J_{dr} \geq 64\log(\frac{6}{\delta_2})\frac{B_\Re \mathcal{N}(\lambda_{2,i})}{\lambda_{2,i}}$, $\lambda_{2,i} \leq \|T_{h_i^*}\|_{\mathcal{L}(\mathcal{H}_\Re)}$ *and* $c_Y > 0$ *for effective rank* $\mathcal{N}(\lambda_{2,i})$ *and spectral operator* $T_{h_i^*}$.

Note that c_Y is guaranteed to be greater than zero when the generalization error of transfer learning $\mathcal{S}_{tl} < \pi_i$ (i.e., every class has observations so that the empirical estimate $\hat{pi}_i > 0$.

The proof is presented in Appendix A.6.3.

The bounds for $\mathcal{S}_{tl}$ and $\mathcal{S}_{dr}$ are provided by Blanchard et. al [75] and Szabó et. al[76] respectively. From Theorem A.3, it can be seen that as $J_{tl} \to \infty$, $J_{dr} \to \infty$ and $n_j \to \infty, 1 \leq j \leq J$ and the transfer learning and distribution regression systems converge, then the mixture distribution regression system converges as well.

A.6 Analysis for Appendix A.5

The development of the proof of Theorem A.3 involves extensions to current learning theory literature. This section presents definitions, background, the intermediate theorems required for the proof of theorem A.3.

Preliminaries We define the kernel operator associated with a kernel $\Re$ at point $\xi(P)$, as $\Re_{\xi(P)}$ and it's adjoint as $\Re^*_{\xi(P)}$. This corresponds to the mapping $\Re_{\xi(P)} : \tilde{\mathcal{J}} \to \mathcal{H}_\Re$ such that for $\gamma \in \tilde{\mathcal{J}}$

$$\Re_{\xi(P)}\gamma := \Re(\cdot, \xi(P))\gamma.$$

For details and properties of the kernel operator and its adjoint see [149, 150]. We define $L^2(\mathcal{B}_{\mathcal{X}} \times \tilde{\mathcal{J}}, \rho, \tilde{\mathcal{J}})$ as the space of functions from $\mathcal{B}_{\mathcal{X}} \times \tilde{\mathcal{J}}$ onto $\tilde{\mathcal{J}}$ that are square integrable in the measure ρ. Let $\mathcal{L}(L^2)$ be the space of linear operators on $L^2(\mathcal{B}_{\mathcal{X}} \times \tilde{\mathcal{J}}, \rho, \tilde{\mathcal{J}})$, let $\mathcal{L}(\mathcal{H}_{\bar{k}}, \tilde{\mathcal{J}})$ denote the space of linear operators on functions mapping from $\mathcal{H}_{\bar{k}}$ to $\tilde{\mathcal{J}}$ and let $\mathcal{L}_2(\mathcal{H}_{\bar{k}}, \tilde{\mathcal{J}})$ denote the space of Hilbert Schmidt operators on functions mapping from $\mathcal{H}_{\bar{k}}$ to $\tilde{\mathcal{J}}$.

We define the linear operator $A_{h_i} : \mathcal{H}_{\Re} \to L^2(\mathcal{B}_{\mathcal{X}} \times \tilde{\mathcal{J}}, \rho, \tilde{\mathcal{J}})$ such that for $r_i \in \mathcal{H}_{\Re}$

$$(A_{h_i} r_i)(P, \Gamma_i) = \Re^*_{h_i(P)} r_i$$

This essentially implies that

$$(A_{h_i} r_i)(P, \Gamma_i) = r_i \circ h_i(P),$$

A_{h_i} is the canonical injection of $\mathcal{H}_{\Re}$ under the transformation h_i. Let ρ_P denote the marginal distribution of ρ with respect to P:

$$\rho_P(P) = \int_{\Gamma \in \mathcal{J}} d\rho(P, \Gamma).$$

We define the Hilbert-Schmidt operators $T_{h_i(P)} = \Re_{h_i(P)} \Re^*_{h_i(P)}$ and

$$T_{h_i} = \int_{\mathcal{B}_{\mathcal{X}}} T_{h_i(P)} d\rho_P(P).$$

Using the spectral operator for the optimal transfer learning function h_i^*, we define the effective rank as $\mathcal{N}(\lambda_{2,i}) := \mathrm{Tr}((T_{h_i^*} + \lambda_{2,i})^{-1} T_{h_i^*})$

The proof strategy for Theorem A.3 is as follows:

1. We first derive the conditions for convergence of $A_{\hat{h}_i}$ the embedding of the classified output in theorem A.7.

2. Next, we extend on the conditions to derive rates for the empirical version of the

spectral operator T_{h_i} in Corollary A.2.

3. We then use these arguments in section A.6.3 to provide high probability upper bounds for $\mathcal{E}(\hat{r}_i \circ \hat{h}_i) - \mathcal{E}(r_i^* \circ h_i^*)$ in theorem A.3.

The proof depends on the property of the extended feature space in marginal transfer learning and on the self-calibration property of logistic loss. In the infinite sample setting, the marginal transfer learning system can be seen as a standard support vector machine on the extended, infinite dimensional feature space $\mathcal{B}_{\mathcal{X}} \times \mathcal{X}$. For the marginal transfer learning system, let

$$\eta(X, P) := \mathbb{E}_{P_{Y|X} \sim \rho_{Y|X}} \big[P(Y = 1|X) \big]. \tag{A.8}$$

In particular, when Assumption **L IV** holds, $\rho(P_{Y|X}) := \delta_{Z(P_X)}$,

$$\eta(X, P_X) := \mathbb{E}_{P_{Y|X} \sim \delta_{Z(P_X)}} \big[P(Y = 1|X) \big] := Z(P_X)(Y = 1|X = x).$$

The self calibration properties of the logistic loss (see Steinwart and Christmann[84]) when applied to the extended feature space of marginal transfer learning imply that

$$\int_{\mathcal{B}_{\mathcal{X}}} \int_{X} |\eta(X, P) - \hat{P}(Y = 1|X)|^2 dP d\rho_P(P) \leq I(\hat{g}, \ell, \infty) - I(g^*, \ell, \infty) \tag{A.9}$$

The derivation of the above equation is identical to example 3.66 in [84] with the extended feature vector (P, X).

A.6.1 Useful Theorems

For the theorem below, we will assume that for the transfer learning setting $n_j = n_{tl}$ for all $1 \leq j \leq J_{tl}$.

Theorem A.4 (Universal consistency of MTL, Cor. 5.4 of [75]). *Assume that loss ℓ is L_ℓ lipschitz in the first variable, is bounded by B_l and that assumptions **L I**, **L II** are satisfied for $\mathcal{X}$ and kernels k, K and k'. Assume that J_{tl}, n_{tl} grow to infinity in such a way that $J_{tl} = O(n_{tl}^p)$ for some $p > 0$. Then if $\lambda_{1,j}$ is a sequence such that $\lambda_{1,j} \to 0$ and $\lambda_{1,j}\sqrt{\frac{j}{\log j}} \to \infty$, it holds that*

$$I(\hat{g}, \ell, \infty) \to \inf_{g \in \mathcal{B}_\mathcal{X} \times \mathcal{X} \to \mathbb{R}} I(g, \ell, \infty)$$

in probability.

A.6.2 Analysis of A_h and T_h

Theorem A.5. *If assumptions **L I** and **L II** hold for the given system, A_{h_i} is a bounded operator from $\mathcal{H}_\mathfrak{K}$ to $L^2(\mathcal{B}_\mathcal{X} \times \tilde{\mathcal{J}}, \rho, \tilde{\mathcal{J}})$, the adjoint $A_{h_i}^* : L^2(\mathcal{B}_\mathcal{X} \times \tilde{\mathcal{J}}, \rho, \tilde{\mathcal{J}}) \to \mathcal{H}_\mathfrak{K}$ is*

$$A_{h_i}^* s = \int_{\mathcal{B}_\mathcal{X} \times \mathcal{J}} \mathfrak{K}_{h_i(P)} s(P, \Gamma_i) d\rho(P, \Gamma_i)$$

where the integral converges in $\mathcal{H}_\mathfrak{K}$ and $A_{h_i}^* A_{h_i}$ is the Hilbert-Schmidt operator on $\mathcal{H}_\mathfrak{K}$:

$$T_{h_i} = \int_{\mathcal{B}_\mathcal{X}} T_{h_i(P)} d\rho_P(P)$$

for $T_{h_i(P)} = \mathfrak{K}_{h_i(P)} \mathfrak{K}_{h_i(P)}^*$.

Theorem A.6. *If assumptions **L I**, **L II** hold, r_i^* is a minimizer of expected risk $\mathcal{E}(\cdot)$ under the composition map h_i^* iff it satisfies*

$$T_{h_i^*} r_i^* = A_{h_i^*}^* \Gamma_i$$

The proofs are straightforward and follow the same line of arguments as presented in

[149] and [150].

We shall first present bounds on A_{h_i} for the transfer learning system before we move on to the bounds of the complete system.

Theorem A.7. *Consider a mixture distribution regression system and assume that the conditions* ***L I*** *-* ***L III*** *are satisfied. Then,*

$$\|(A_{\hat{h}_i} - A_{h_i^*})\|_{\mathcal{L}(L^2)} \leq C_h \big(I(\hat{g}, \ell, \infty) - I(g^*, \ell, \infty)\big)^{\beta/2},$$

where $C_h = \big(\frac{2B_{\bar{k}}}{c_Y}\big)^{\beta} \sqrt{L_{\mathfrak{K}}}$ *and* $c_Y := \pi_i \hat{\pi}_i$.

Proof. Without loss of generality, we will provide the convergence bounds for $i = 1$ and the label space $\mathcal{Y} := \{0, 1\}$. Let $\mathcal{Z} = \mathcal{B}_{\mathcal{X}} \times \tilde{\mathcal{J}}$. We have

$$\begin{aligned}
\|(A_{\hat{h}_1} - A_{h_1^*})r_1\|_{\rho}^2 &= \int_{\mathcal{Z}} \|(\mathfrak{K}^*_{\hat{h}_1(P)} - \mathfrak{K}^*_{h_1^*(P)})r_1\|_{\tilde{\mathcal{J}}}^2 d\rho(P, \Gamma_1) \\
&\leq \|r_1\|_{\mathcal{H}_{\bar{k}}}^2 \int_{\mathcal{Z}} \|(\mathfrak{K}^*_{\hat{h}_1(P)} - \mathfrak{K}^*_{h_1^*(P)})\|_{\mathcal{L}(\mathcal{H}_{\mathfrak{K}}, \tilde{\mathcal{J}})}^2 d\rho \\
&= \|r_1\|_{\mathcal{H}_{\bar{k}}}^2 \int_{\mathcal{Z}} \|(\mathfrak{K}_{\hat{h}_1(P)} - \mathfrak{K}_{h_1^*(P)})^*\|_{\mathcal{L}(\mathcal{H}_{\mathfrak{K}}, \tilde{\mathcal{J}})}^2 d\rho.
\end{aligned}$$

Using $\|\cdot\|_{\mathcal{L}} \leq \|\cdot\|_{\mathcal{L}_2}$ and the Hölder condition,

$$\begin{aligned}
\|(A_{\hat{h}_1} - A_{h_1^*})r_1\|_{\rho}^2 &\leq \|r_1\|_{\mathcal{H}_{\bar{k}}}^2 \int_{\mathcal{Z}} \|(\mathfrak{K}_{\hat{h}_1(P)} - \mathfrak{K}_{h_1^*(P)})\|_{\mathcal{L}_2(\tilde{\mathcal{J}}, \mathcal{H}_{\mathfrak{K}})}^2 d\rho \\
&\leq \|r_1\|_{\mathcal{H}_{\bar{k}}}^2 L_{\mathfrak{K}} \int_{\mathcal{B}_{\mathcal{X}}} \|\hat{h}_1(P) - h_1^*(P)\|_{\mathcal{H}_{\bar{k}}}^{2\beta} d\rho(P_X).
\end{aligned}$$

From the definition of $\hat{h}_1$ and h_1^*,

$$\begin{aligned}\|(A_{\hat{h}_1} - A_{h_1^*})r_1\|_\rho^2 &\leq \|r_1\|_{\mathcal{H}_{\bar{k}}}^2 L_{\mathfrak{K}} \int_{\mathcal{B}_X} \left\| \int_{\mathcal{X}} \bar{k}(x,\cdot) d\hat{P}_1(x) - \int_{\mathcal{X}} \bar{k}(x,\cdot) dP_1(x) \right\|_{\mathcal{H}_{\bar{k}}}^{2\beta} d\rho_P(P_X) \\ &= \|r_1\|_{\mathcal{H}_{\bar{k}}}^2 L_{\mathfrak{K}} \int_{\mathcal{B}_X} \left\| \int_{\mathcal{X}} \bar{k}(x,\cdot) \left(\frac{\widehat{P}(Y=i|x)}{\widehat{P}(Y=i)} - \frac{P(Y=i|x)}{P(Y=i)} \right) dP_X \right\|_{\mathcal{H}_{\bar{k}}}^{2\beta} d\rho_P(P_X).\end{aligned}$$

From convexity of $\|\cdot\|_{\mathcal{H}_{\bar{k}}}$ and Jensen's inequality,

$$\begin{aligned}\|(A_{\hat{h}_1} - A_{h_1^*})r_1\|_\rho^2 &\leq \|r_1\|_{\mathcal{H}_{\bar{k}}}^2 L_{\mathfrak{K}} \int_{\mathcal{B}_X} \left(\int_{\mathcal{X}} \|\bar{k}(x,\cdot)\|_{\mathcal{H}_{\bar{k}}} \left| \frac{\widehat{P}(Y=1|x)}{\widehat{P}(Y=1)} - \frac{P(Y=1|x)}{P(Y=1)} \right| dP_X \right)^{2\beta} d\rho_P(P_X) \\ &\leq \|r_1\|_{\mathcal{H}_{\bar{k}}}^2 L_{\mathfrak{K}} B_{\bar{k}}^{2\beta} \int_{\mathcal{B}_X} \left(\int_{\mathcal{X}} \left| \frac{\widehat{P}(Y=1|x)}{\widehat{P}(Y=1)} - \frac{P(Y=1|x)}{P(Y=1)} \right| dP_X \right)^{2\beta} d\rho_P(P_X) \\ &\leq \|r_1\|_{\mathcal{H}_{\bar{k}}}^2 L_{\mathfrak{K}} B_{\bar{k}}^{2\beta} \int_{\mathcal{B}_X} H^{2\beta} d\rho_P(P_X)\end{aligned}$$

Where $H := \int_{\mathcal{X}} \left| \frac{\widehat{P}(Y=1|x)}{\widehat{P}(Y=1)} - \frac{P(Y=1|x)}{P(Y=1)} \right| dP_X$. We will continue to simplify H. Let $c_Y := P(Y=1)\widehat{P}(Y=1)$.

$$\begin{aligned}H &= \int_{\mathcal{X}} \frac{|\widehat{P}(Y=1|x)P(Y=1) - P(Y=1|x)\widehat{P}(Y=1)|}{c_Y} dP_X \\ &\leq \frac{1}{c_Y} \int_{\mathcal{X}} \left(|\widehat{P}(Y=1|x) - P(Y=1|x)| + |P(Y=1) - \widehat{P}(Y=1)| \right) dP_X \\ &\leq \frac{1}{c_Y} \left(\int_{\mathcal{X}} |\widehat{P}(Y=1|x) - P(Y=1|x)| dP_X + |P(Y=1) - \widehat{P}(Y=1)| \right) \\ &\leq \frac{1}{c_Y} \left(\int_{\mathcal{X}} |\widehat{P}(Y=1|x) - P(Y=1|x)| dP_X + \left| \int_{\mathcal{X}} P(Y=1|x) dP_X - \int_{\mathcal{X}} \widehat{P}(Y=1|x) dP_X \right| \right) \\ &\leq \frac{2}{c_Y} \int_{\mathcal{X}} |\widehat{P}(Y=1|x) - P(Y=1|x)| dP_X,\end{aligned}$$

where the second step comes from the fact that for 4 numbers $0 \leq a, b, c, d \leq 1$, $|ab - cd| \leq |a - c| + |b - d|$.

Therefore we have

$$\|(A_{\hat{h}_1} - A_{h_1^*})r_1\|_\rho^2 \leq \frac{2^{2\beta}\|r_1\|_{\mathcal{H}_{\bar{k}}}^2 L_{\mathfrak{K}} B_{\bar{k}}^{2\beta}}{c_Y^{2\beta}} \int_{\mathcal{B}_X} \left(\int_{\mathcal{X}} |\widehat{P}(Y=1|x) - P(Y=1|x)| dP_X \right)^{2\beta} d\rho_P(P_X)$$
$$= \frac{2^{2\beta}\|r_1\|_{\mathcal{H}_{\bar{k}}}^2 L_{\mathfrak{K}} B_{\bar{k}}^{2\beta}}{c_Y^{2\beta}} \int_{\mathcal{B}_X} \left(\int_{\mathcal{X}} \left| \eta(X, P_X) - \frac{1}{1+\exp(-g(X,P_X))} \right| dP_X \right)^{2\beta} d\rho_P(P_X)$$

Using cauchy-schwarz inequality,

$$\|(A_{\hat{h}_1} - A_{h_1^*})r_1\|_\rho^2 \leq \frac{2^{2\beta}\|r_1\|_{\mathcal{H}_{\bar{k}}}^2 L_{\mathfrak{K}} B_{\bar{k}}^{2\beta}}{c_Y^{2\beta}} \int_{\mathcal{B}_X} \left(\int_{\mathcal{X}} \left| \eta(X, P_X) - \frac{1}{1+\exp(-g(X,P_X))} \right|^2 dP_X \right)^{\beta} d\rho_P(P_X)$$

Using the concavity of $(\cdot)^\beta$ and the Jensen's inequality,

$$\|(A_{\hat{h}_1} - A_{h_1^*})r_1\|_\rho^2 \leq \frac{2^{2\beta}\|r_1\|_{\mathcal{H}_{\bar{k}}}^2 L_{\mathfrak{K}} B_{\bar{k}}^{2\beta}}{c_Y^{2\beta}} \left(\int_{\mathcal{B}_X} \int_{\mathcal{X}} \left| \eta(X, P_X) - \frac{1}{1+\exp(-g(X,P_X))} \right|^2 dP_X d\rho_P(P_X) \right)^{\beta}$$
$$\leq \frac{2^{2\beta}\|r_1\|_{\mathcal{H}_{\bar{k}}}^2 L_{\mathfrak{K}} B_{\bar{k}}^{2\beta}}{c_Y^{2\beta}} \left(I(\hat{g}, \ell, \infty) - I(g^*, \ell, \infty) \right)^{\beta}$$

The theorem follows from the definition of the norm.

□

Corollary A.2. *Consider a mixture distribution regression system and assume that the conditions* ***L I*** *-* ***L III*** *are satisfied. Then, with probability* $1 - \delta$*,*

$$\|(\hat{T}_{\hat{h}_i} - \hat{T}_{h_i^*})r_i\|^2 \leq C_{h,2} \left(\sqrt{\frac{\log \delta^{-1}}{J_{dr}}} + \left(I(\hat{g}, \ell, \infty) - I(g^*, \ell, \infty) \right) \right)^{\beta}$$

where $C_{h,2} := \dfrac{2^{2+2\beta}\|r_i\|^2 B_{\mathfrak{K}}^2 B_{\bar{k}}^{2\beta} L_{\mathfrak{K}}}{c_Y^{2\beta}}$ *and* $c_Y := \pi_i \hat{\pi}_i$.

Proof. We consider the training data for the distribution regression to have J_{dr} tasks. With-

out loss of generality, we will provide the convergence bounds for $i = 1$. The proof is similar to that of Theorem A.7. The training dataset consists of points drawn from probability distributions $\{P^{(j)}\}_{j=J_{tl}+1}^{J}$. Let $[J_{dr}] = \{J_{tl}+1, \cdots, J\}$. We have

$$\|(\hat{T}_{\hat{h}_1} - \hat{T}_{h_1^*})r_1\|^2 \leq \frac{1}{J_{dr}} \sum_{j\in[J_{dr}]} \|(\mathfrak{K}_{\hat{h}_1(P^{(j)})}\mathfrak{K}^*_{\hat{h}_1(P^{(j)})} - \mathfrak{K}_{h_1^*(P^{(j)})}\mathfrak{K}^*_{h_1^*(P^{(j)})})r_1\|^2$$

Adding and subtracting $\mathfrak{K}_{\hat{h}_1(P^{(j)})}\mathfrak{K}^*_{h_1^*(P^{(j)})}$ and using the properties of norm,

$$\|(\hat{T}_{\hat{h}_1} - \hat{T}_{h_1^*})r_1\|^2 \leq \frac{\|r_1\|^2}{J_{dr}} \sum_{j\in[J_{dr}]} \|(\mathfrak{K}_{\hat{h}_1(P^{(j)})}\mathfrak{K}^*_{\hat{h}_1(P^{(j)})} - \mathfrak{K}_{\hat{h}_1(P^{(j)})}\mathfrak{K}^*_{h_1^*(P^{(j)})} + \mathfrak{K}_{\hat{h}_1(P^{(j)})}\mathfrak{K}^*_{h_1^*(P^{(j)})} - \mathfrak{K}_{h_1^*(P^{(j)})}\mathfrak{K}^*_{h_1^*(P^{(j)})})\|^2.$$

Using the inequality $\|f_1 + f_2\|^2 \leq 2(\|f_1\|^2 + \|f_2\|^2)$,

$$\|(\hat{T}_{\hat{h}_1} - \hat{T}_{h_1^*})r_1\|^2 \leq \frac{2\|r_1\|^2}{J_{dr}} \sum_{j\in[J_{dr}]} \|(\mathfrak{K}_{\hat{h}_1(P^{(j)})}\mathfrak{K}^*_{\hat{h}_1(P^{(j)})} - \mathfrak{K}_{\hat{h}_1(P^{(j)})}\mathfrak{K}^*_{h_1^*(P^{(j)})}\|^2 + \|\mathfrak{K}_{\hat{h}_1(P^{(j)})}\mathfrak{K}^*_{h_1^*(P^{(j)})} - \mathfrak{K}_{h_1^*(P^{(j)})}\mathfrak{K}^*_{h_1^*(P^{(j)})})\|^2.$$

Using Cauchy-Schwarz inequality and the bound on kernel $\mathfrak{K}$,

$$\|(\hat{T}_{\hat{h}_1} - \hat{T}_{h_1^*})r_1\|^2 \leq \frac{4\|r_1\|^2 B_{\mathfrak{K}}^2}{J_{dr}} \sum_{j\in[J_{dr}]} \|\mathfrak{K}_{\hat{h}_1(P^{(j)})} - \mathfrak{K}_{h_1^*(P^{(j)})}\|^2.$$

Using the hölder continuity of $\mathfrak{K}$,

$$\|(\hat{T}_{\hat{h}_1} - \hat{T}_{h_1^*})r_1\|^2 \leq \frac{4\|r_1\|^2 B_{\mathfrak{K}}^2 L_{\mathfrak{K}}}{J_{dr}} \sum_{j\in[J_{dr}]} \|\hat{h}_1(P^{(j)}) - h_1^*(P^{(j)})\|^{2\beta}$$

Following arguments identical to those presented in theorem A.7 we have

$$\|(\hat{T}_{\hat{h}_1} - \hat{T}_{h_1^*})r_1\|^2 \leq \frac{2^{2+2\beta}\|r_1\|^2 B_{\mathfrak{K}}^2 B_{\bar{k}}^{2\beta} L_{\mathfrak{K}}}{J_{dr} c_Y^{2\beta}} \sum_{j\in[J_{dr}]} \left(\int_{\mathcal{X}} \left| \eta(X, P^{(j)}) - \hat{P}(Y = 1|X) \right|^2 dP^{(j)} \right)^{\beta}$$

Using Jensen's inequality,

$$\|(\hat{T}_{\hat{h}_1} - \hat{T}_{h_1^*})r_1\|^2 \leq \frac{2^{2+2\beta}\|r_1\|^2 B_{\mathfrak{K}}^2 B_{\bar{k}}^{2\beta} L_{\mathfrak{K}}}{c_Y^{2\beta}} \left(\frac{1}{J_{dr}} \sum_{j \in [J_{dr}]} \int_{\mathcal{X}} \left| \eta(X, P^{(j)}) - \hat{P}(Y = 1|X) \right|^2 dP^{(j)} \right)^{\beta}$$

Denoting the term inside the summation as $\tilde{H}$ we have, using Azuma-Mcdiarmid's inequality, with probability $1 - \delta$,

$$\|(\hat{T}_{\hat{h}_1} - \hat{T}_{h_1^*})r_1\|^2 \leq \frac{2^{2+2\beta}\|r_1\|^2 B_{\mathfrak{K}}^2 B_{\bar{k}}^{2\beta} L_{\mathfrak{K}}}{c_Y^{2\beta}} \left(\sqrt{\frac{\log \delta^{-1}}{J_{dr}}} + \mathbb{E}_{P_X}[\tilde{H}] \right)^{\beta}$$

Using equation A.9,

$$\|(\hat{T}_{\hat{h}_1} - \hat{T}_{h_1^*})r_1\|^2 \leq \frac{2^{2+2\beta}\|r_1\|^2 B_{\mathfrak{K}}^2 B_{\bar{k}}^{2\beta} L_{\mathfrak{K}}}{c_Y^{2\beta}} \left(\sqrt{\frac{\log \delta^{-1}}{J_{dr}}} + \left(I(\hat{g}, \ell, \infty) - I(g^*, \ell, \infty) \right) \right)^{\beta}$$

□

A.6.3 Proof of Theorem A.3

Proof. For simplification of notation, we write $\hat{r} = \hat{r}_i$ and $r_{\mathcal{H}} := r_i^*$. By the definition of $\mathcal{E}$, we can write

$$\mathcal{E}(\hat{r} \circ \hat{h}_i) - \mathcal{E}(r_{\mathcal{H}} \circ h_i^*) = \|A_{\hat{h}_i}\hat{r} - \Gamma_i\|_\rho^2 - \|A_{h_i^*} r_{\mathcal{H}} - \Gamma_i\|_\rho^2.$$

Completing the squares,

$$\mathcal{E}(\hat{r} \circ \hat{h}_i) - \mathcal{E}(r_{\mathcal{H}} \circ h_i^*) = \|A_{\hat{h}_i}\hat{r} - A_{h_i^*} r_{\mathcal{H}}\|_\rho^2 + 2\langle A_{\hat{h}_i}\hat{r} - A_{h_i^*} r_{\mathcal{H}}, A_{h_i^*} r_{\mathcal{H}} - \Gamma_i \rangle_\rho.$$

Adding and subtracting $A_{h_i^*}\hat{r}$ and then using the inequality $\|\sum_{i=1}^{N} f_i\|^2 \leq N\sum_{i=1}^{N}\|f_i\|^2$,

$$\begin{aligned}\mathcal{E}(\hat{r}\circ\hat{h}_i) - \mathcal{E}(r_{\mathcal{H}}\circ h_i^*) &= \|A_{\hat{h}_i}\hat{r} - A_{h_i^*}\hat{r} + A_{h_i^*}\hat{r} - A_{h_i^*}r_{\mathcal{H}}\|_\rho^2 + 2\langle A_{\hat{h}_i}\hat{r} - A_{h_i^*}r_{\mathcal{H}}, A_{h_i^*}r_{\mathcal{H}} - \Gamma_i\rangle_\rho \\ &\leq 2(\|A_{\hat{h}_i}\hat{r} - A_{h_i^*}\hat{r}\|_\rho^2 + \|A_{h_i^*}\hat{r} - A_{h_i^*}r_{\mathcal{H}}\|_\rho^2 + \langle A_{\hat{h}_i}\hat{r} - A_{h_i^*}r_{\mathcal{H}}, A_{h_i^*}r_{\mathcal{H}} - \Gamma_i\rangle_\rho) \\ &=: 2((I) + (II) + (III)),\end{aligned} \tag{A.10}$$

We now provide universal consistency of $(I), (II)$ and (III) using Theorems A.5, A.6 and A.7.

Bound on (I) We have from the definition of the operator norm,

$$(I) \leq \|\hat{r}\|_{\mathcal{H}_{\bar{k}}}^2 \|(A_{\hat{h}_i} - A_{h_i^*})\|_{\mathcal{L}(L^2)}^2. \tag{A.11}$$

From the definition of $\hat{r}$ and from the fact that $\|(\hat{T}_{\hat{h}_i} + \lambda_{2,i})^{-1}\| \leq \frac{1}{\lambda_{2,i}}$,

$$\begin{aligned}\|\hat{r}\|_{\mathcal{H}_{\mathfrak{K}}} &\leq \|(\hat{T}_{\hat{h}_i} + \lambda_{2,i})^{-1}\|_{\mathcal{L}(\mathcal{H}_{\mathfrak{K}})} \|\frac{1}{J_{dr}}\sum_{j=1}^{J_{dr}} \mathfrak{K}(\cdot, \hat{h}_i(\hat{P}^{(j)}))\Gamma_i^{(j)}\| \\ &\leq \frac{1}{\lambda_{2,i}}\frac{1}{J_{dr}}\sum_{j=1}^{J_{dr}} \|\mathfrak{K}(\cdot, \hat{h}_i(\hat{P}^{(j)}))\|\|\Gamma_i^{(j)}\| \\ &\leq \frac{1}{\lambda_{2,i}} C_\Gamma B_{\mathfrak{K}}.\end{aligned} \tag{A.12}$$

Using the preceding argument, along with theorem A.7 we have

$$\begin{aligned}(I) &\leq \frac{1}{\lambda_{2,i}^2} C_\Gamma^2 B_{\mathfrak{K}}^2 \|(A_{\hat{h}_i} - A_{h_i^*})\|_{\mathcal{L}(L^2)}^2 \\ &\leq \frac{C_\Gamma^2 B_{\mathfrak{K}}^2 L_{\mathfrak{K}}}{\lambda_{2,i}^2}\left(\frac{2B_{\bar{k}}}{c_Y}\right)^{2\beta}\left(I(g, \ell, \infty) - I(g^*, \ell, \infty)\right)^{\beta}.\end{aligned} \tag{A.13}$$

Bound on (III): Adding and subtracting $A_{h_i^*}\hat{r}$, and then applying the projection theorem,

$$\begin{aligned}(III) &= \langle A_{\hat{h}_i}\hat{r} - A_{h_i^*}\hat{r}, A_{h_i^*}r_{\mathcal{H}} - \Gamma_i\rangle_\rho + \langle A_{h_i^*}\hat{r} - A_{h_i^*}r_{\mathcal{H}}, A_{h_i^*}r_{\mathcal{H}} - \Gamma_i\rangle_\rho \\ &= \langle A_{\hat{h}_i}\hat{r} - A_{h_i^*}\hat{r}, A_{h_i^*}r_{\mathcal{H}} - \Gamma_i\rangle_\rho.\end{aligned}$$

From the Cauchy-Schwarz inequality and the definition of the spectral norm,

$$(III) \leq \|A_{\hat{h}_i} - A_{h_i^*}\|_{\mathcal{L}(L^2)}\|\hat{r}\|_{\mathcal{H}_\Re}\|A_{h_i^*}r_{\mathcal{H}} - \Gamma_i\|_\rho. \tag{A.14}$$

From the derivation for term (I), $\|r\|_{\mathcal{H}} \leq \dfrac{1}{\lambda_{2,i}}C_\Gamma B_\Re$. We can bound $\|A_{h_i^*}r_{\mathcal{H}} - \Gamma_i\|_{\mathcal{J}}$ using the convexity of the norm and equation (A.12) as

$$\begin{aligned}\|A_{h^*}r_{\mathcal{H}} - \Gamma\|_\rho &\leq \|A_{h_i^*}r_{\mathcal{H}} - \Gamma_i\|_{\mathcal{J}} \\ &\leq \|A_{h_i^*}r_{\mathcal{H}}\| + \|\Gamma_i\| \\ &\leq C_\Gamma\left(1 + \frac{B_\Re}{\lambda_{2,i}}\right)\end{aligned} \tag{A.15}$$

Using theorem A.7 and the preceding arguments,

$$(III) \leq \frac{C_\Gamma^2 B_\Re\sqrt{L_\Re}}{\lambda_{2,i}}\left(1 + \frac{B_\Re}{\lambda_{2,i}}\right)\left(\frac{2B_{\bar{k}}}{c_Y}\right)^\beta\left(I(g, \ell_{logist}, \infty) - I(g^*, \ell_{logist}, \infty)\right)^{\beta/2} \tag{A.16}$$

Bound on (II):

$$\begin{aligned}(II) &= \|A_{h_i^*}(\hat{r} - r_{\mathcal{H}_\Re})\|_{\mathcal{H}_\Re}^2 \\ &= \|\sqrt{T_{h^*}}(\hat{r} - r_{\mathcal{H}_\Re})\|_{\mathcal{H}_\Re}^2\end{aligned}$$

Note that $\hat{r}$ is trained with two stage sampled data which has been classified by $\hat{h}_i$ and not by h_i^*. To distinguish between the two we shall make a change to the notation: $\hat{r}_{\hat{h}_i} = \hat{r}$ and we shall denote by $\hat{r}_{h_i^*}$ as the empirical two stage regressor trained using the optimal marginal

predictor. More specifically,

$$\hat{r}_{h_i^*} := (T_{h_i^*} + \lambda_{2,i})^{-1} \hat{s}_{h_i^*},$$

where $\hat{s}_{h_i^*} := [\Re(\cdot, h_i^*(P^{(J_{tl}+1)})), \Re(\cdot, h_i^*(P^{(J_{tl}+2)})), ..., \Re(\cdot, h_i^*(P^{(J_{tl}+J_{dr})}]'$ and

$$\hat{r}_{\hat{h}_i} := (T_{\hat{h}_i} + \lambda_{2,i})^{-1} \hat{s}_{\hat{h}_i},$$

where $\hat{s}_{\hat{h}_i} := [\Re(\cdot, \hat{h}_i(P^{(J_{tl}+1)})), \Re(\cdot, \hat{h}_i(P^{(J_{tl}+2)})), ..., \Re(\cdot, \hat{h}_i(P^{(J_{tl}+J_{dr})})]'$. We have

$$\begin{aligned}
(II) &= \|\sqrt{T_{h_i^*}}(\hat{r}_{\hat{h}_i} - r_{\mathcal{H}_\Re})\|^2_{\mathcal{H}_\Re} \\
&= \|\sqrt{T_{h_i^*}}(\hat{r}_{\hat{h}_i} - \hat{r}_{h_i^*} + \hat{r}_{h_i^*} - r_{\mathcal{H}})\|^2_{\mathcal{H}_\Re} \\
&\leq 2(\|\sqrt{T_{h_i^*}}(\hat{r}_{\hat{h}_i} - \hat{r}_{h_i^*})\|^2_{\mathcal{H}_\Re} + \|\sqrt{T_{h_i^*}}(\hat{r}_{h_i^*} - r_{\mathcal{H}})\|^2_{\mathcal{H}_\Re}) \\
&= (IIa) + (IIb),
\end{aligned}$$

where the inequality is due to $\|\sum_{i=1}^{N} f_i\|^2 \leq N \sum_{i=1}^{N} \|f_i\|^2$. Working with the first term (IIa), from the definitions of $\hat{r}_{\hat{h}_i}$ and $\hat{r}_{h_i^*}$,

$$\hat{r}_{\hat{h}_i} - \hat{r}_{h_i^*} = (\hat{T}_{\hat{h}_i} + \lambda_{2,i})^{-1} \hat{s}_{\hat{h}_i} - (\hat{T}_{h_i^*} + \lambda_{2,i})^{-1} \hat{s}_{h_i^*}.$$

Adding and subtracting $(\hat{T}_{h_i^*} + \lambda_{2,i})^{-1} \hat{s}_{\hat{h}_i}$,

$$\hat{r}_{\hat{h}_i} - \hat{r}_{h_i^*} = (\hat{T}_{h_i^*} + \lambda_{2,i})^{-1} (\hat{s}_{\hat{h}_i} - \hat{s}_{h_i^*}) - ((\hat{T}_{h_i^*} + \lambda_{2,i})^{-1} - (\hat{T}_{\hat{h}_i} + \lambda_{2,i})^{-1}) \hat{s}_{\hat{h}_i}.$$

Using the operator identity $T_1^{-1} - T_2^{-1} = T_1^{-1}(T_1 - T_2)T_2^{-1}$ and the definition of r, we have

$$\begin{aligned}
\hat{r}_{\hat{h}_i} - \hat{r}_{h_i^*} &= (\hat{T}_{h_i^*} + \lambda_{2,i})^{-1} (\hat{s}_{\hat{h}_i} - \hat{s}_{h_i^*}) - (\hat{T}_{h_i^*} + \lambda_{2,i})^{-1} (\hat{T}_{h_i^*} - \hat{T}_{\hat{h}_i}) (\hat{T}_{\hat{h}_i} + \lambda_{2,i})^{-1} \hat{s}_{\hat{h}_i} \\
&= (\hat{T}_{h_i^*} + \lambda_{2,i})^{-1} (\hat{s}_{\hat{h}_i} - \hat{s}_{h_i^*}) + (\hat{T}_{h_i^*} + \lambda_{2,i})^{-1} (\hat{T}_{\hat{h}_i} - \hat{T}_{h_i^*}) \hat{r}_{\hat{h}_i}
\end{aligned}$$

Using the definition of spectral norm and the squared sum-norm inequality,

$$(IIa) \leq 2\|\sqrt{T_{h_i^*}}(\hat{T}_{h_i^*} + \lambda_{2,i})^{-1}\|^2_{\mathcal{L}(\mathcal{H}_{\mathfrak{K}})}(\|\hat{s}_{\hat{h}_i} - \hat{s}_{h_i^*}\|^2 + \|\hat{T}_{\hat{h}_i} - \hat{T}_{h_i^*}\|^2_{\mathcal{L}(\mathcal{H}_{\mathfrak{K}})}\|\hat{r}_{\hat{h}_i}\|^2_{\mathcal{H}_{\mathfrak{K}}})$$

We know that for $\delta_2 > 0$, the term $\|\sqrt{T_{h_i^*}}(\hat{T}_{h_i^*} + \lambda_{2,i})^{-1}\|^2_{\mathcal{L}(\mathcal{H}_{\mathfrak{K}})} \leq \frac{4}{\lambda_{2,i}}$ with probability $1 - \delta_2/3$ provided $J_{dr} \geq 64\log(\frac{6}{\delta_2})\frac{B_{\mathfrak{K}}\mathcal{N}(\lambda_{2,i})}{\lambda_{2,i}}$ and $\lambda_{2,i} \leq \|T_{h_i^*}\|_{\mathcal{L}(\mathcal{H}_{\mathfrak{K}})}$ (See bound on $\|\sqrt{T}(T_x + \lambda)^{-1}\|^2$ in [151]).

Next, by definition of $\hat{s}_{\hat{h}_i}$, $\hat{s}_{h_i^*}$ and the squared sum-norm inequality,

$$\begin{aligned}
\|\hat{s}_{\hat{h}} - \hat{s}_{h^*}\|^2 &= \left\|\frac{1}{J_{dr}}\sum_{j=1}^{J_{dr}}(\mathfrak{K}_{(\hat{h}_i(P^{(j)})} - \mathfrak{K}_{h_i^*(P^{(j)})})\Gamma_i^{(j)}\right\|^2 \\
&\leq \frac{1}{J_{dr}}\sum_j \|(\mathfrak{K}_{(\hat{h}_i(P^{(j)})} - \mathfrak{K}_{h_i^*(P^{(j)})})\Gamma_i^{(j)}\|^2 \\
&\leq \frac{C_\Gamma^2}{J_{dr}}\sum_j \|\mathfrak{K}_{(\hat{h}_i(P^{(j)})} - \mathfrak{K}_{h_i^*(P^{(j)})}\|^2 \\
&\leq \frac{C_\Gamma^2 L_{\mathfrak{K}}}{J_{dr}}\sum_j \|\hat{h}_i(P^{(j)}) - h_i^*(P^{(j)})\|^{2\beta}
\end{aligned}$$

Using the simplifications similar to those used in Corollary A.2, we have with probability $1 - \delta$,

$$\|\hat{s}_{\hat{h}} - \hat{s}_{h^*}\|^2 \leq \frac{C_\Gamma^2 L_{\mathfrak{K}} 2^{2\beta} B_{\bar{k}}^{2\beta}}{c_Y^{2\beta}}\left(\sqrt{\frac{\log\delta^{-1}}{J_{dr}}} + \left(I(g, \ell_{logist}, \infty) - I(g^*, \ell_{logist}, \infty)\right)\right)^\beta.$$

Using the above bound along with Corollary A.2, we have, with probability $1 - 2\delta - \delta_2/3$,

$$(IIa) \leq \frac{4}{\lambda_{2,i}}\left(2C_\Gamma^2 L_{\mathfrak{K}} + \|\hat{r}_{\hat{h}_i}\|^2 B_{\mathfrak{K}}^2 L_{\mathfrak{K}}\right)\left(\frac{2B_{\bar{k}}}{c_Y}\right)^{2\beta}\left(\sqrt{\frac{\log\delta^{-1}}{J_{dr}}} + \left(I(g, \ell_{logist}, \infty) - I(g^*, \ell_{logist}, \infty)\right)\right)^\beta$$

Using the fact that $\|\hat{r}_{\hat{h}_i}\| \leq \frac{C_\Gamma B_\Re}{\lambda_{2,i}}$,

$$(IIa) \leq \frac{4}{\lambda_{2,i}}\left(2+\frac{B_\Re^4}{\lambda_{2,i}^2}\right)C_\Gamma^2 L_\Re\left(\frac{2B_{\bar{k}}}{c_Y}\right)^{2\beta}\left(\sqrt{\frac{\log\delta^{-1}}{J_{dr}}}+\big(I(g,\ell_{logist},\infty)-I(g^*,\ell_{logist},\infty)\big)\right)^{\beta}.$$

Term (IIb) is the direct application of distribution regression on the class conditional distribution for class i, therefore,

$$(IIb) \leq \mathcal{E}(\hat{r}\circ h_i^*)-\mathcal{E}(r_{\mathcal{H}}\circ h_i^*). \tag{A.17}$$

Let $\mathcal{S}_{tl} := I(g,\ell_{logist},\infty)-I(g^*,\ell_{logist},\infty)\big)$ and $\mathcal{S}_{dr} := \mathcal{E}(\hat{r}\circ h_i^*)-\mathcal{E}(r_{\mathcal{H}}\circ h_i^*)$. Then, with probability $1-2\delta-\delta_2/3$,

$$\mathcal{E}(\hat{r}\circ\hat{h}_i)-\mathcal{E}(r_{\mathcal{H}}\circ h_i^*) \leq C_1\mathcal{S}_{tl}^{\beta}+C_2\mathcal{S}_{tl}^{\beta/2}+C_3\left(\sqrt{\frac{\log\delta^{-1}}{J_{dr}}}+\mathcal{S}_{tl}\right)^{\beta}+4\mathcal{S}_{dr},$$

where, $C_1 := \frac{2C_\Gamma^2 B_\Re^2 L_\Re}{\lambda_{2,i}^2}\big(\frac{2B_{\bar{k}}}{c_Y}\big)^{2\beta}$, $C_2 := \frac{C_\Gamma^2 B_\Re\sqrt{L_\Re}}{\lambda_{2,i}}\left(1+\frac{B_\Re}{\lambda_{2,i}}\right)\big(\frac{2B_{\bar{k}}}{c_Y}\big)^{\beta}$, $C_3 := \frac{4}{\lambda_{2,i}}\left(2+\frac{B_\Re^4}{\lambda_{2,i}^2}\right)C_\Gamma^2 L_\Re\left(\frac{2B_{\bar{k}}}{c_Y}\right)^{2\beta}$

□

APPENDIX B

Appendix for Chapter 3

B.1 Algorithms for Tracking

The algorithms below provide a high level description of the tracking algorithms. Algorithm B.1 describes the dynamic profile construction for the ground stations. Algorithm B.2 describes the simple static allocation when $R_{static} < R_{thres}$ and Algorithm B.3 provides the complex static profiles for antenna pointing and allocation. Note that the selection between the profiles occur as described in Chapter III. In Algorithm B.3 if the greedy algorithm runs out of the ground station passes, then the algorithm is run again with initializing from the minimum inclination (instead of RAAN as described). If both procedures fail, the problem is declared infeasible.

Algorithm B.1: Dynamic profile

Input: Number of available ground stations n_G, Uncertainty net $\mathcal{J}_\epsilon$, net of observation intervals $\mathcal{T}_\tau$, Schedules $\{S_{jl}\}_{l=1,j=1}^{L_j,n_G}$, Antenna widths $\{w_G(A_{ref,jl})\}$.

for $j = 1, ..., n_G$ **do**
  for $l = 1, 2, ...L_j$ **do**
    $APP_{jl} = \{\}$
    for $t \in \mathcal{T}_\tau \bigcap S_{jl}$ **do**
      Compute $w_G(V_j(\mathcal{J}_\epsilon, t))$
      Compute $R_{dynamic,jl}$
      if $R_{dynamic,jl} < 1$ **then**
        $APP_{jl} \leftarrow \left(\frac{s_1'(t) + s_2'(t)}{\|s_1'(t) + s_2'(t)\|}, t\right), (s_1'(t), s_2'(t)) := \underset{s_1,s_2 \in V_j(\mathcal{J}_\epsilon,t) \cap H_j}{\arg\max} d_G(s_1, s_2)$
      end
    end
  end
end
if $\sum_{j,l} \mathbb{1}_{\{R_{dynamic,jl}<1\}} > n_P$ **then**
  Select n_P passes of largest length and discard the rest of the schedules and profiles.
end

Algorithm B.2: Simple static profile

Input: Number of available ground stations n_G, Uncertainty net $\mathcal{J}_\epsilon$, net of observation intervals $\mathcal{T}_\tau$, Schedules $\{S_{jl}\}_{l=1,j=1}^{L_j,n_G}$, Antenna widths $\{w_G(A_{ref,jl})\}$.

for $j = 1, 2, \cdots, n_G$ **do**
  for $l = 1, ..., L_j$ **do**
    $D_{avg,jl} = \{\}$
    for $\gamma \in H_{jl} := \{\gamma \in \mathcal{J}_\epsilon, \mathfrak{m}(V_j(\gamma, S_{jl}) \in H_j) > 0\}$ **do**
      Compute average Doppler time stamp $t_{avg,jl}(\gamma)$
      $D_{avg,jl} \leftarrow V_j(\gamma, t_{avg,jl}(\gamma))$
    end
    $R_{static,jl} = \dfrac{w_G(D_{avg,jl})}{w_G(A_{ref,jl})}$
    $s_1', s_2' = \underset{s_1,s_2 \in D_{avg,jl}}{\arg\max}\ d_G(s_1, s_2)$
    $APP_{jl} = \left(\dfrac{s_1' + s_2'}{\|s_1' + s_2'\|}, S_{jl}\right)$.
  end
end
Select n_P passes for which $H_{jl} = \mathcal{J}_\epsilon$ and $R_{static,jl} < R_{thres}$.

Algorithm B.3: Complex static profile

Input: Number of available ground stations n_G, Uncertainty net $\mathcal{J}_\epsilon$, net of observation intervals $\mathcal{T}_\tau$, Schedules $\{S_{jl}\}_{l=1,j=1}^{L_j,n_G}$, Antenna widths $\{w_G(A_{ref,jl})\}$.

for $j = 1, 2, \cdots, n_G$ **do**
  for $l = 1, ..., L_j$ **do**
    $D_{avg,jl} = \{\}$
    for $\gamma \in H_{jl} := \{\gamma \in \mathcal{J}_\epsilon, \mathfrak{m}(V_j(\gamma, S_{jl}) \in H_j) > 0\}$ **do**
      Compute average Doppler time stamp $t_{avg,jl}(\gamma)$ $D_{avg,jl} \leftarrow V_j(\gamma, t_{avg,jl}(\gamma))$
    end
  end
end
$\mathcal{G} = \{\}$
for $nn = 1, 2, ..., n_P$ **do**
  $\mathcal{I}_\epsilon = \{\}$
  while $\mathcal{J}_\epsilon \setminus \mathcal{I}_\epsilon \neq \varnothing$ *and* $|\mathcal{G}| < \sum_j L_j$ **do**
    $\gamma_{cand} = \underset{\gamma \in (\mathcal{J}_\epsilon \setminus \mathcal{I}_\epsilon)}{\arg\min} RAAN(s)$
    $jl_{cand} = \underset{j \in \{1,2,..n_G\}, l \in \{1,2,...,L_j\}: \gamma_{cand} \in H_{jl}}{\arg\min} \frac{w_G(D_{avg,jl})}{w_G(A_{ref,jl})}$
    Construct $MWST_{jl_{cand}}$: Minimum Width Spanning Tree on S^2 over datapoints $D_{avg,jl_{cand}}$ starting from point corresponding to γ_{cand} until maximum width less than $R_{thres} w_G(A_{ref,jl_{cand}})$
    $H_{cover,jl_{cand}} = \{\gamma \in \mathcal{J}_\epsilon : V_{j_{cand}}(\gamma, t_{avg,jl_{cand}}(\gamma)) \in MWST_{jl_{cand}}\}$
    $\mathcal{I}_\epsilon \leftarrow \mathcal{I}_\epsilon \bigcup H_{cover,jl_{cand}}$
    $\mathcal{G} \leftarrow jl_{cand}$
  end
end
Release pass intervals not used from the schedule

APPENDIX C

Appendix for Chapter 4

C.1 Calibration of Combined Magnetometer Measurements

In this section we discuss extension of calibration parameters to combined magnetometer measurements. We show that with modified signal parameters, the non-orthogonal spin calibration methods presented in [67, 66] can be applied directly to combined magnetometer measurements. We will present the model in the absence of interference. For a true magnetic field measurement of $Q_T(t)$, the sensor i measures

$$Q_S(t) = G_i O_t Q_T(t) + S_i,$$

where

$$G_i = \begin{bmatrix} G_{i,1}\sin\theta_{i,1}\cos\varphi_{i,1} & G_{i,1}\sin\theta_{i,1}\sin\varphi_{i,1} & G_{i,1}\cos\theta_{i,1} \\ G_{i,2}\sin\theta_{i,2}\cos\varphi_{i,2} & G_{i,2}\sin\theta_{i,2}\sin\varphi_{i,2} & G_{i,2}\cos\theta_{i,2} \\ G_{i,3}\sin\theta_{i,3}\cos\varphi_{i,3} & G_{i,3}\sin\theta_{i,3}\sin\varphi_{i,3} & G_{i,3}\cos\theta_{i,3} \end{bmatrix}$$

and $S = \begin{bmatrix} S_{i,1} & S_{i,2} & S_{i,3} \end{bmatrix}'$. All the angles except for $\varphi_{i,3}$ are expected to be small and this results in the small angle approximation [67, 66]:

$$G_i = \begin{bmatrix} G_{i,1} & G_{i,1}\Delta\varphi_{i,1} & G_{i,1}\Delta\theta_{i,1} \\ -G_{i,2}\Delta\varphi_{i,2} & G_{i,2} & G_{i,2}\Delta\theta_{i,2} \\ G_{i,3}\Delta\theta_{i,3}\cos(\varphi_{i,3}) & G_{i,3}\Delta\theta_{i,3}\sin(\varphi_{i,3}) & G_{i,3} \end{bmatrix}$$

For individual magnetometers, using a further simplification that $G_{i,2} = G_{i,1} + \Delta G_{21}$ and $\Delta\varphi_{i,2} = \Delta\varphi_{i,1} + \Delta\varphi_{i,21}$ and ignoring the second order terms we have

$$G_i = \begin{bmatrix} G_{i,1} & G_{i,1}\Delta\varphi_{i,1} & G_{i,1}\Delta\theta_{i,1} \\ -G_{i,1}(\Delta\varphi_{i,1} + \Delta\varphi_{i,21}) & G_{i,1} + \Delta G_{i,21} & G_{i,1}\Delta\theta_{i,2} \\ G_{i,3}\Delta\theta_{i,3}\cos(\varphi_{i,3}) & G_{i,3}\Delta\theta_{i,3}\sin(\varphi_{i,3}) & G_{i,3}. \end{bmatrix} \tag{C.1}$$

The parameters of equation (C.1) is computed by estimating the harmonics generated at multiples of the spin frequency $\omega, 2\omega$ (See the methods in [67, 66]). We will induce a similar structure to equation (C.1) for combined magnetometer measurements and discuss it's calibration. We shall focus on extension of the method by Kepko et. al [67], and similar extensions can be used for [66]. For a sensor combination $W = (W_1, W_2, \cdots, W_M)$, the small signal structure gives

$$G_W = \begin{bmatrix} \sum_m w_{m,1} G_{m,1} & \sum_m w_{m,1} G_{m,1} \Delta\varphi_{m,1} & \sum_m w_{m,1} G_{m,1} \Delta\theta_{m,1} \\ \sum_m w_{m,2} G_{m,2} \Delta\varphi_{m,2} & \sum_m w_{m,2} G_{m,2} & \sum_m w_{m,2} G_{m,1} \Delta\theta_{m,2} \\ \sum_m w_{m,3} G_{m,3} \Delta\theta_{m,3} \cos(\varphi_{m,3}) & \sum_m w_{m,3} G_{m,3} \Delta\theta_{m,3} \sin(\varphi_{m,3}) & \sum_m w_{m,3} G_{m,3} \end{bmatrix}.$$

For the small signal approximations of G_i,

$$G_W = \begin{bmatrix} G_{W,1} & G_{W,1} \Delta\varphi_{W,1} & G_{W,1} \Delta\theta_{W,1} \\ -G_{W,2} \Delta\varphi_{W,2} & G_{W,2} & G_{W,2} \Delta\theta_{W,2} \\ G_{W,3} \Delta\rho & G_{W,3} \Delta\xi & G_{W,3} \end{bmatrix}$$

where

$$\begin{aligned} G_{W,1} &= \sum_m w_{m,1} G_{m,1}, & \Delta\varphi_{W,1} &= \sum_m w_{m,1} \frac{G_{m,1}}{G_{W,1}} \Delta\varphi_{m,1}, \\ G_{W,2} &= \sum_m w_{m,2} G_{m,2}, & \Delta\varphi_{W,2} &= \sum_m w_{m,2} \frac{G_{m,2}}{G_{W,2}} \Delta\varphi_{m,2}, \\ G_{W,3} &= \sum_m w_{m,3} G_{m,3}, & \Delta\rho &= \sum_m w_{m,3} \frac{G_{m,3}}{G_{W,3}} \Delta\theta_{m,3} \cos(\varphi_{m,3}), \\ & & \Delta\theta_{W,1} &= \sum_m w_{m,1} \frac{G_{m,1}}{G_{W,1}} \Delta\theta_{m,1}, \\ & & \Delta\theta_{W,2} &= \sum_m w_{m,2} \frac{G_{m,1}}{G_{W,2}} \Delta\theta_{m,2}, \\ & & \Delta\xi &= \sum_m w_{m,3} \frac{G_{m,3}}{G_{W,3}} \Delta\theta_{m,3} \sin(\varphi_{m,3}), \end{aligned}$$

In the above equation, direct first order small angle approximation cannot be applied. However, by separating combined gain measurements, we can write the approximation

$$G_W = \begin{bmatrix} G_{W,1} & G_{W,1}\Delta\varphi_{W,1} & G_{W,1}\Delta\theta_{W,1} \\ -G_{W,1}(\Delta\varphi_{W,1} + \Delta\varphi_{W,21}) & G_{W,1} + \Delta G_{W,21} & G_{W,1}\Delta\theta_{W,2} \\ G_{W,3}\Delta\rho_W & G_{W,3}\Delta\xi_W & G_{W,3}. \end{bmatrix} \tag{C.2}$$

where

$$\begin{aligned} G_{W,1} &= \sum_m w_{m,1} G_{m,1}, & G_{W,3} &= \sum_m w_{m,3} G_{m,3}, \\ \Delta\theta_{W,1} &= \sum_m w_{m,1} \frac{G_{m,1}}{G_{W,1}} \Delta\theta_{m,1}, & \Delta\theta_{W,2} &= \sum_m w_{m,2} \frac{G_{m,2}}{G_{W,1}} \Delta\theta_{m,2}, \\ \Delta\varphi_{W,1} &= \sum_m w_{m,1} \frac{G_{m,1}}{G_{W,1}} \Delta\varphi_{m,1}, & \Delta\varphi_{W,21} &= \frac{1}{G_{W,1}} \sum_m w_{m,2} G_{m,2} \Delta\varphi_{m,2} - w_{m,1} G_{m,1} \Delta\varphi_{m,1}, \\ \Delta\rho_W &= \sum_m w_{m,3} \frac{G_{m,3}}{G_{W,3}} \Delta\theta_{m,3} \cos(\varphi_{m,3}), & \Delta\xi_W &= \sum_m w_{m,3} \frac{G_{m,3}}{G_{W,3}} \Delta\theta_{m,3} \sin(\varphi_{m,3}). \\ \Delta G_{W,21} &= \sum_m w_{m,2} G_{m,2} - w_{m,1} G_{m,1}. \end{aligned}$$

It is a natural question whether small angle structure holds for all the components of G_W, given that it holds for each of the individual sensors. We shall show that for a small angle $\Delta\gamma$, if the small angle approximation also holds for $2\frac{\sup_m G_{m,1}}{\inf_m G_{m,1}}\Delta\gamma$, then the small angle approximation also holds for G_W. The angle in question are $\Delta\theta_{W,2}$ and $\Delta\varphi_{W,21}$. Using first order approximations for each of the individual sensors,

$$\begin{aligned} \Delta\theta_{W,2} &= \sum_m w_{m,2} \frac{G_{m,2}}{G_{W,1}} \Delta\theta_{m,2} \\ &= \sum_m w_{m,2} \frac{G_{m,1} + \Delta G_{m,21}}{G_{W,1}} \Delta\theta_{m,2} \\ &= \frac{G_{m,1}}{G_{W,1}} \sum_m w_{m,2} \Delta\theta_{m,2} + o(\epsilon') \\ &\leq \frac{\sup_m G_{m,1}}{\inf_m G_{m,1}} \sum_m w_{m,2} \Delta\theta_{m,2} + o(\epsilon'). \end{aligned}$$

Similarly,

$$\begin{aligned}
\Delta\varphi_{W,21} &= \frac{1}{G_{W,1}} \sum_m w_{m,2} G_{m,2} \Delta\varphi_{m,2} - w_{m,1} G_{m,1} \Delta\varphi_{m,1} \\
&= \frac{1}{G_{W,1}} \sum_m w_{m,2} (G_{m,1} + \Delta G_{m,21}) \Delta\varphi_{m,2} - w_{m,1} G_{m,1} \Delta\varphi_{m,1} \\
&= \frac{1}{G_{W,1}} \sum_m G_{m,1} (w_{m,2} \Delta\varphi_{m,2} - w_{m,1} \Delta\varphi_{m,1}) + o(\epsilon') \\
&\leq \frac{\sup_m G_{m,1}}{G_{W,1}} \sum_m (w_{m,2} \Delta\varphi_{m,2} - w_{m,1} \Delta\varphi_{m,1}) + o(\epsilon') \\
&\leq 2 \frac{\sup_m G_{m,1}}{\inf_m G_{m,1}} \max \left(\sum_m w_{m,2} \Delta\varphi_{m,2}, \sum_m w_{m,1} \Delta\varphi_{m,1} \right) + o(\epsilon').
\end{aligned}$$

Since the affine combinations of the small angles produced by W are also small, from the above equations, the small angle approximation holds for G_W. The estimation of parameters using either [67] or [66] can be used for estimation of these modified small angle parameters with a modification for ρ_W, ξ_W. In both of these variables, the individual products cannot be resolved and they will have to be estimated directly as a sum. This modification should not change the solution for $\hat{G}_W$ recovered.

C.2 Decomposition of Loss

We show that under imperfect calibration due to spacecraft interference and with the spacecraft model under consideration, the loss l_W can be decomposed into two parts. The first is a function of the telemetry x_t and the second is composed of historical observed telemetry, spacecraft current loops that are not observable by the telemetry and the true magnetic field. The calibration parameters of the spacecraft G_W, S_W are dependent on the past L measurements of data.

In the spacecraft model under consideration, the interference is a function of spacecraft

telemetry and unobserved variables. For any $t \in \mathcal{T}$,

$$
\begin{aligned}
\ell_W &= \|Q_T(t) - O_t' \hat{G}_W^{-1}(t)(Q_W(t) - \hat{S}_W(t))\| \\
&= \|O_t' G_W^{-1} G_W O_t Q_T(t) - O_t' \hat{G}_W^{-1}(t)(G_W O_t Q_T(t) + G_W V_W(t) + S_W - \hat{S}_W(t))\| \\
&= \|(G_W^{-1} - \hat{G}_W^{-1}(t)) O_t Q_T(t) + \hat{G}_W^{-1}(t) \sum_m W_m G_m V_m(t) + S_W - \hat{S}_W(t)\| \\
&= \|\hat{G}_W^{-1}(t) \sum_m W_m G_m (h_m(x_t) + \xi_t) + (G_W^{-1} - \hat{G}_W^{-1}(t)) O_t Q_T(t) + S_W - \hat{S}_W(t)\| \\
&= \|\hat{G}_W^{-1}(t) \sum_m W_m G_m h_m(x_t) + \hat{G}_W^{-1}(t) \sum_m W_m G_m \xi_t + (G_W^{-1} - \hat{G}_W^{-1}(t)) O_t Q_T(t) + S_W - \hat{S}_W(t)\| \\
&= \|G_W^{-1} \sum_m W_m G_m h_m(x_t) \\
&\qquad + \hat{G}_W^{-1}(t) \sum_m W_m G_m \xi_t + (G_W^{-1} - \hat{G}_W^{-1}(t)) \left(O_t Q_T(t) + \sum_m W_m G_m h_m(x_t) \right) + S_W - \hat{S}_W(t)\| \\
&= f_W(x_t) - \zeta_t(x_{t-L}, x_{t-L+1}, \cdots, x_t, \xi_{t-L}, \xi_{t-L+1}, \cdots, \xi_t, Q_T(t-L), Q_T(t-L+1), \cdots, Q_T(t)),
\end{aligned}
$$

where $f_W(x_t) = \|G_W^{-1} \sum_m W_m G_m h_m(x_t)\|$ is the component of the interference that depends only on the telemetry at time t for a fixed sensor combination W and ζ_t is the perturbation from $f_W(x_t)$ based on unobserved parameters and imperfect calibration.

C.3 Additional Experimental Results

We present runs for the test datasets for $\beta = 0.1, 0.5$ and 2. The hyper parameters, kernel bandwidth and regularization, used for these different tests with β were from cross validation performed for $\beta = 1$.

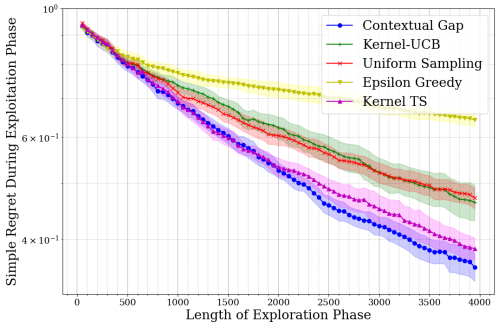

(a) Letter dataset

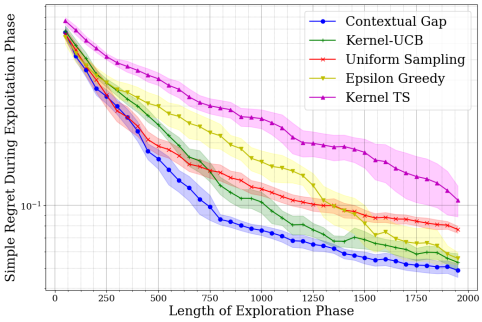

(b) USPS dataset

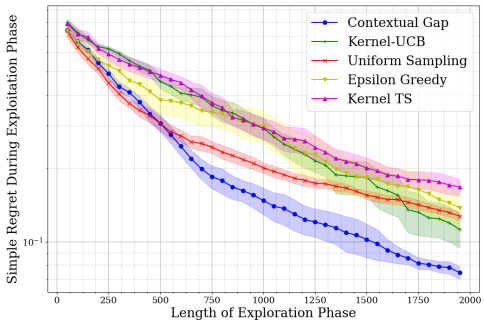

(c) MNIST dataset

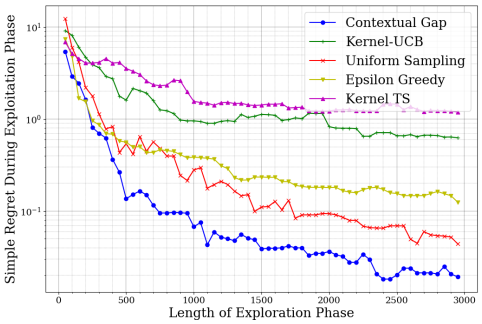

(d) Spacecraft dataset

Figure C.1: Simple regret evaluation with $\beta = 0.1$

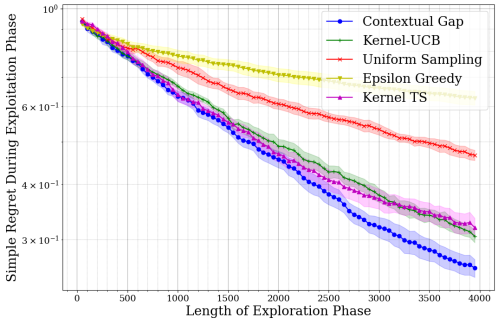

(a) Letter dataset

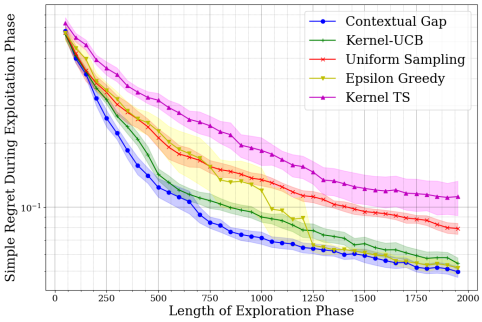

(b) USPS dataset

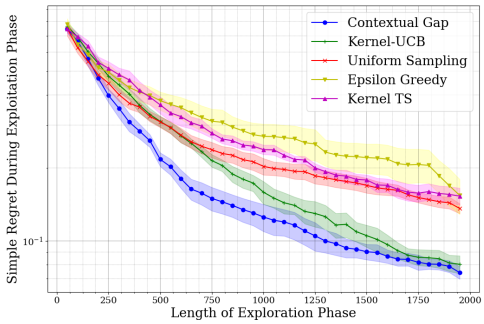

(c) MNIST dataset

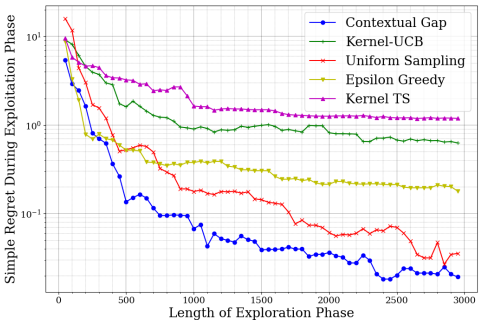

(d) Spacecraft dataset

Figure C.2: Simple regret evaluation with $\beta = 0.5$

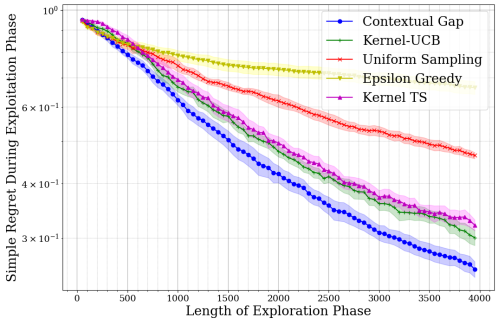

(a) Letter dataset

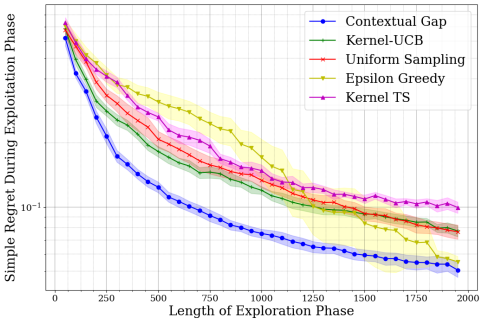

(b) USPS dataset

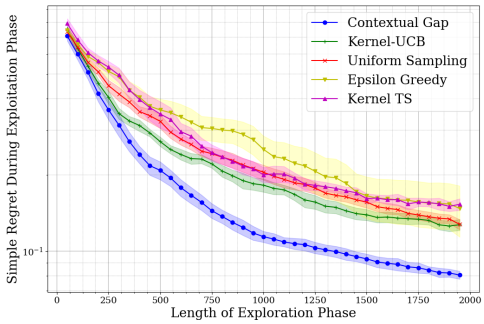

(c) MNIST dataset

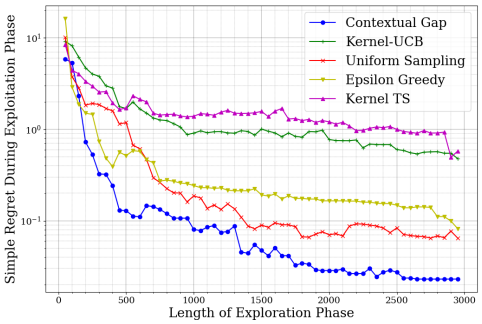

(d) Spacecraft dataset

Figure C.3: Simple regret evaluation with $\beta = 2$

The following runs compare the behavior of contextual gap with a history of 25 points and contextual gap by considering only the previous datapoint.

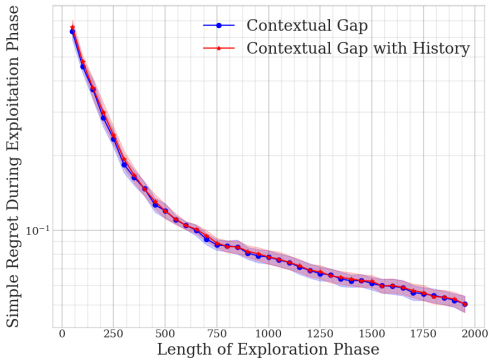

(a) USPS dataset

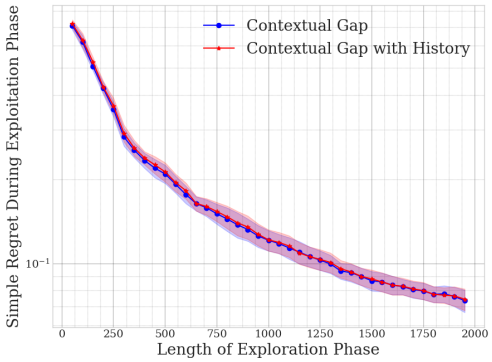

(b) MNIST dataset

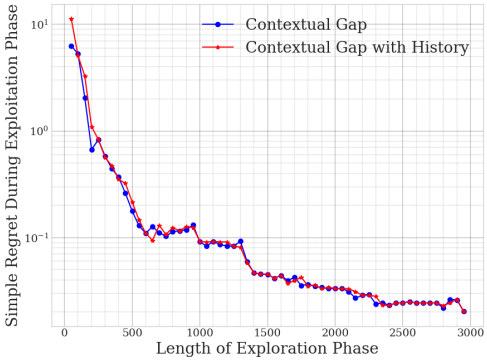

(c) Spacecraft dataset

Figure C.4: Simple regret for Contextual Gap with History of 25 points

The following plots provide the time series information for the magnetic field interference for the experimental dataset along the X, Y and Z directions in the body fixed frame.

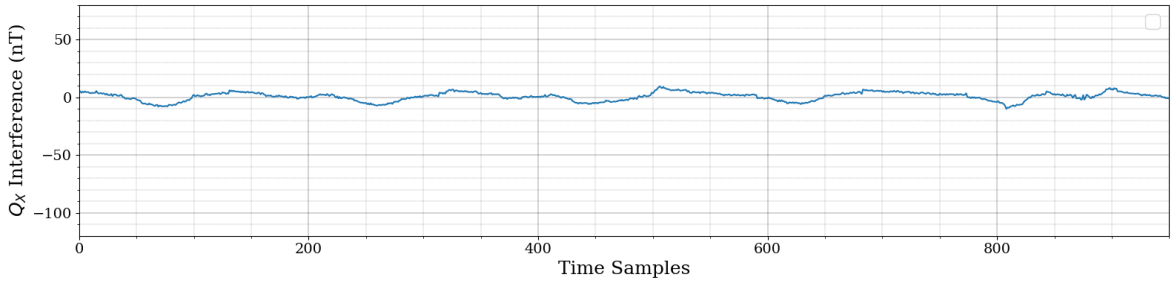

(a) Interference of Magnetometer 1

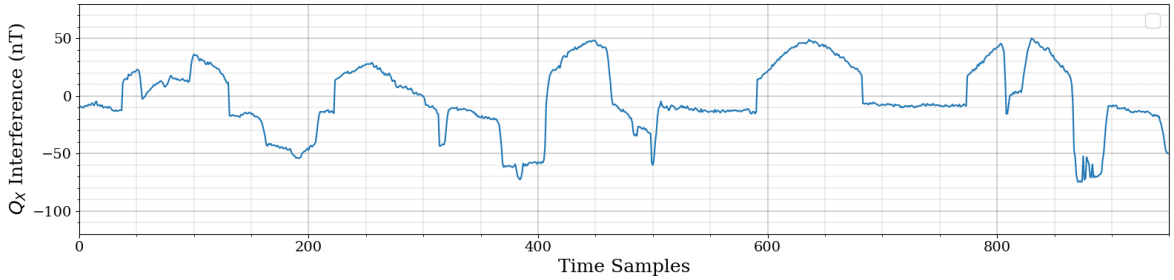

(b) Interference of Magnetometer 2

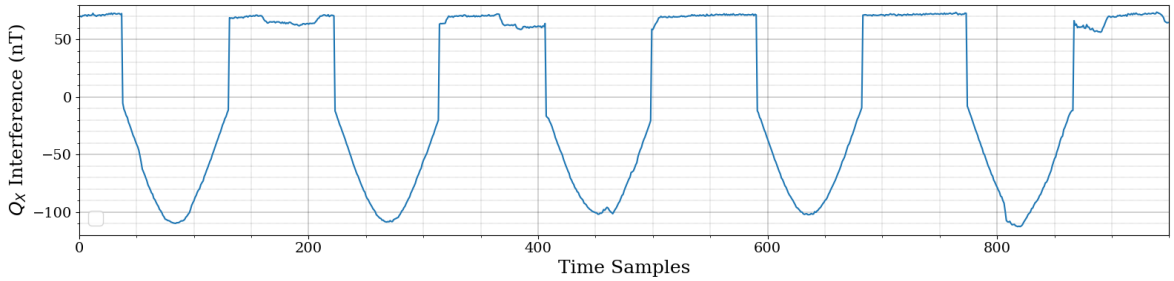

(c) Interference of Magnetometer 3

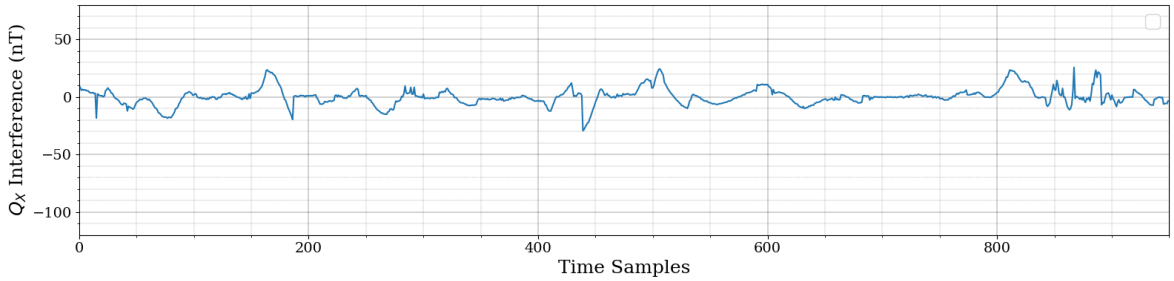

(d) Contextual Gap with 11 arms

Figure C.5: Time series of magnetic field interference - X direction

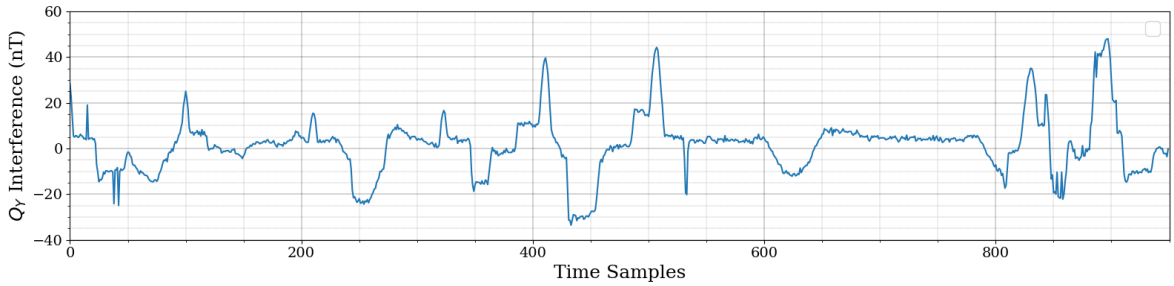

(a) Interference of Magnetometer 1

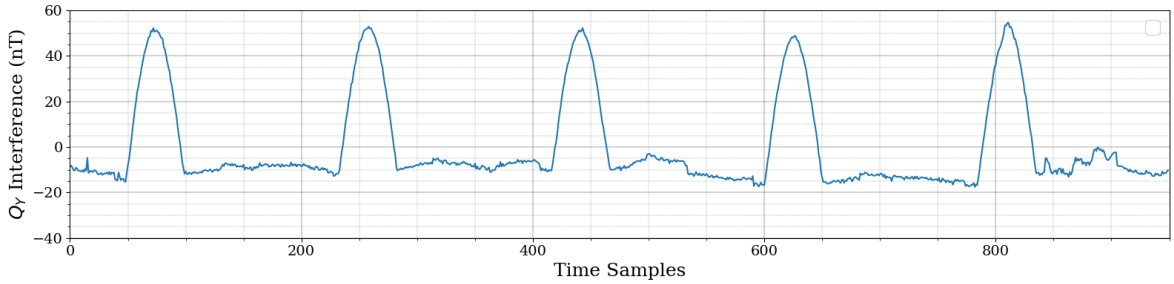

(b) Interference of Magnetometer 2

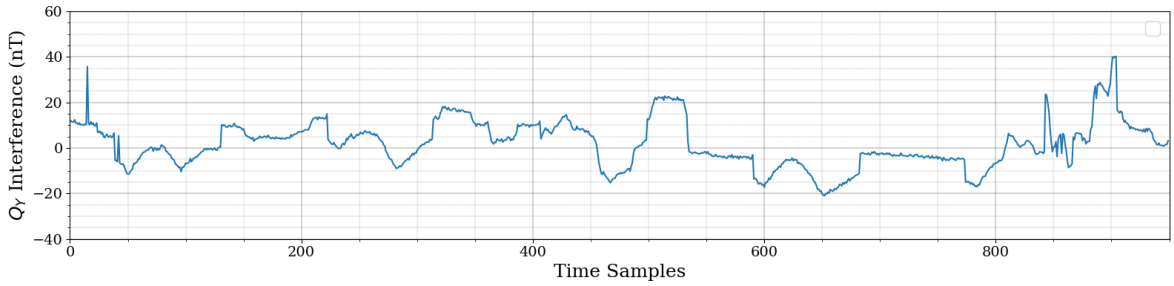

(c) Interference of Magnetometer 3

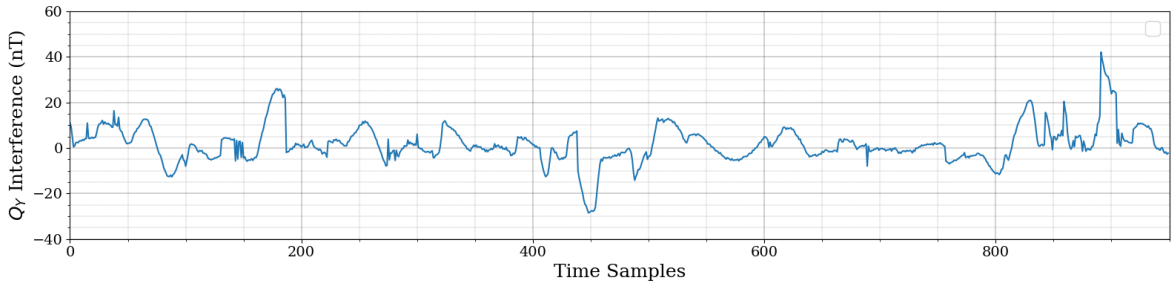

(d) Contextual Gap with 11 arms

Figure C.6: Time series of magnetic field interference - Y direction

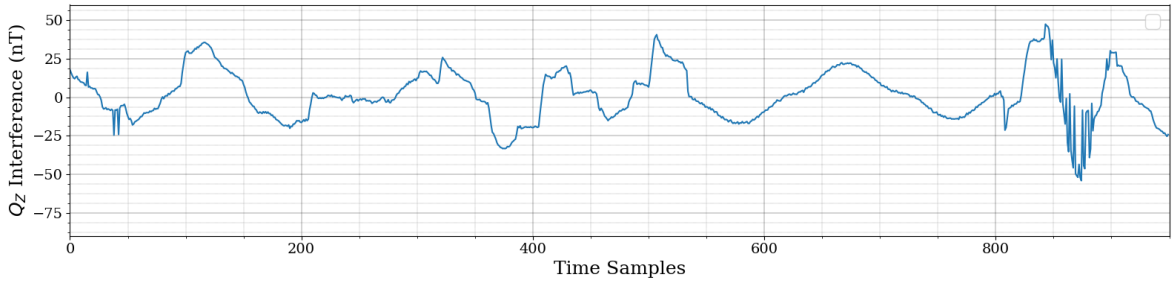

(a) Interference of Magnetometer 1

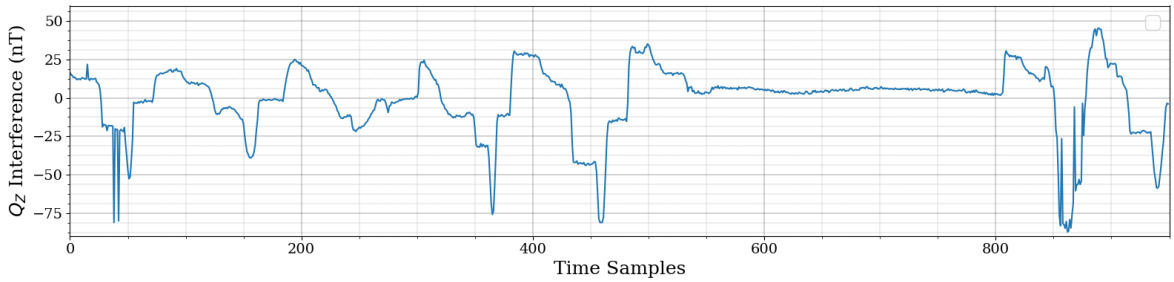

(b) Interference of Magnetometer 2

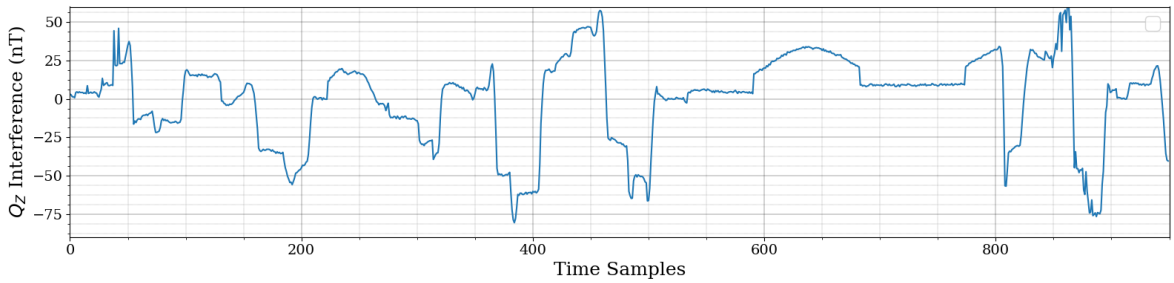

(c) Interference of Magnetometer 3

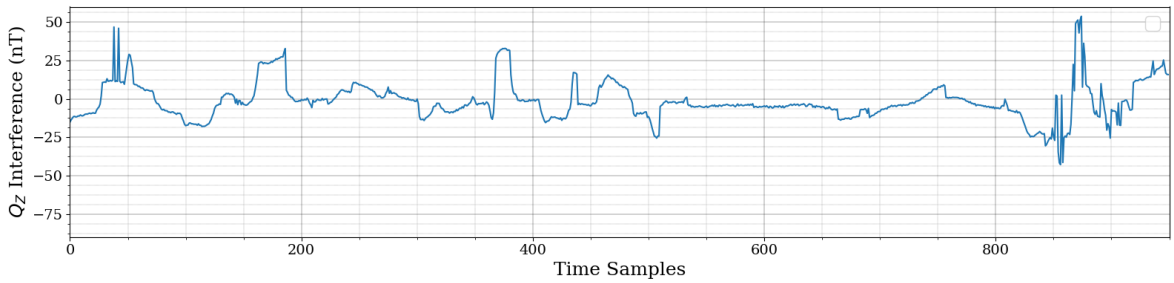

(d) Contextual Gap with 11 arms

Figure C.7: Time series of magnetic field interference - Z direction

BIBLIOGRAPHY

[1] R. Tsunoda, "Tilts and wave structure in the bottomside of the low-latitude f layer: Recent findings and future opportunities," in *AGU Fall Meeting Abstracts*, 2016.

[2] N. England, J. W. Cutler, and S. Sharma, "Tandom beacon experiment-tbex design overview and lessons learned," *Cubesat Developer's Workshop*, 2018.

[3] M. Swartwout, "University-class satellites: From marginal utility to'disruptive'research platforms," 2004.

[4] ——, "The first one hundred cubesats: A statistical look," *Journal of Small Satellites*, vol. 2, no. 2, pp. 213–233, 2013.

[5] G. Richardson, K. Schmitt, M. Covert, and C. Rogers, "Small satellite trends 2009-2013," in *Proceedings of the AIAA/USU Conf. on Small Satellites*, 2015.

[6] L. Berthoud and M. Schenk, "How to set up a CubeSat project-preliminary survey results," in *Proceedings of the AIAA/USU Conf. on Small Satellites*, 2016.

[7] S. Bandyopadhyay, R. Foust, G. P. Subramanian, S.-J. Chung, and F. Y. Hadaegh, "Review of formation flying and constellation missions using nanosatellites," *Journal of Spacecraft and Rockets*, vol. 53, no. 3, pp. 567–578, 2017/09/15 2016. [Online]. Available: https://doi.org/10.2514/1.A33291

[8] J. Schoolcraft, A. Klesh, and T. Werne, "MarCO: Interplanetary mission development on a CubeSat scale," in *Space Operations: Contributions from the Global Community*. Springer, 2017, pp. 221–231.

[9] J. W. Cutler and A. Fox, "A framework for robust and flexible ground station networks." *Journal of Aerospace Computing, Information and Communication*, vol. 3, March 2006.

[10] G. Minelli, "Mobile CubeSat command & control (MC3) ground stations," in *9th Annual CubeSat Summer Workshop*, 2012.

[11] K.-M. Cheung, D. Abraham, B. Arroyo, E. Basilio, A. Babuscia, C. Duncan, D. Lee, K. Oudrhiri, T. Pham, R. Staehle *et al.*, "Next-generation ground network architecture for communications and tracking of interplanetary smallsats," *Interplanetary Network Progress Report*, vol. 202, pp. 1–44, 2015.

[12] J. R. Vetter, "Fifty years of orbit determination," *Johns Hopkins APL technical digest*, vol. 27, no. 3, p. 239, 2007.

[13] J. R. Wright, "Orbit determination tool kit: Theory and algorithms," Analytical Graphics Inc., Tech. Rep., 2013.

[14] T. J. Martin-Mur, E. D. Gustafson, B. T. Young, and M. C. Jesick, "Interplanetary CubeSat navigational challenges," in *International Symposium Space Flight Dynamics, Munich, Germany*, 2016.

[15] H. Klinkrad, *Space debris*. Wiley Online Library, 2010.

[16] A. Rossi and G. Valsecchi, "Collision risk against space debris in earth orbits," *Periodic, Quasi-Periodic and Chaotic Motions in Celestial Mechanics: Theory and Applications*, pp. 345–356, 2006.

[17] G. Tommei, A. Milani, and A. Rossi, "Orbit determination of space debris: admissible regions," *Celestial Mechanics and Dynamical Astronomy*, vol. 97, no. 4, pp. 289–304, 2007.

[18] T. Schildknecht, "Optical surveys for space debris," *The Astronomy and Astrophysics Review*, vol. 14, no. 1, pp. 41–111, 2007.

[19] H. G. Lewis, G. G. Swinerd, and R. J. Newland, "The space debris environment: future evolution," *The Aeronautical Journal*, vol. 115, no. 1166, pp. 241–247, 2011.

[20] J. S. O. Center, "Space-track. org," *The Source for Space Surveillance Data,[www. space-track. org], USSTRATCOM*, 2012.

[21] M. Morton and T. Roberts, "Joint space operations center (jspoc) mission system (jms)," AIR FORCE SPACE COMMAND PETERSON AFB CO, Tech. Rep., 2011.

[22] N. F. Ness, "Magnetometers for space research," *Space Science Reviews*, vol. 11, no. 4, pp. 459–554, 1970.

[23] C. Russell, "The isee 1 and 2 fluxgate magnetometers," *IEEE Transactions on Geoscience Electronics*, vol. 16, no. 3, pp. 239–242, 1978.

[24] M. Kivelson, K. Khurana, J. Means, C. Russell, and R. Snare, "The galileo magnetic field investigation," *Space Science Reviews*, vol. 60, no. 1-4, pp. 357–383, 1992.

[25] F. J. Rich, "Fluxgate magnetometer (ssm) for the defense meteorological satellite program (dmsp) block 5d-2, flight 7," AIR FORCE GEOPHYSICS LAB HANSCOM AFB MA, Tech. Rep., 1984.

[26] M. H. Acuna, "Space-based magnetometers," *Review of scientific instruments*, vol. 73, no. 11, pp. 3717–3736, 2002.

[27] C. Russell, B. Anderson, W. Baumjohann, K. Bromund, D. Dearborn, D. Fischer, G. Le, H. Leinweber, D. Leneman, W. Magnes *et al.*, "The magnetospheric multiscale magnetometers," *Space Science Reviews*, vol. 199, no. 1-4, pp. 189–256, 2016.

[28] D. Miles, I. Mann, M. Ciurzynski, D. Barona, B. Narod, J. Bennest, I. Pakhotin, A. Kale, B. Bruner, C. Nokes *et al.*, "A miniature, low-power scientific fluxgate magnetometer: A stepping-stone to cube-satellite constellation missions," *Journal of Geophysical Research: Space Physics*, vol. 121, no. 12, 2016.

[29] N. F. Ness, K. W. Behannon, R. P. Lepping, and K. H. Schatten, "Use of two magnetometers for magnetic field measurements on a spacecraft," *Journal of Geophysical Research*, vol. 76, no. 16, pp. 3564–3573, 1971.

[30] A. Sheinker and M. B. Moldwin, "Adaptive interference cancelation using a pair of magnetometers," *IEEE Transactions on Aerospace and Electronic Systems*, vol. 52, no. 1, pp. 307–318, 2016.

[31] D. A. Vallado, "Fundamentals of astrodynamics and applications," *2nd ed. El Segundo, CA: Microcosm Press; Dordrecht: Kluwer Academic Publishers, 2001. Space technology library; v. 12*, 2001.

[32] A. Milani and G. Gronchi, *Theory of orbit determination*. Cambridge University Press, 2010.

[33] D.-J. Lee, "Nonlinear bayesian filtering with applications to estimation and navigation," Ph.D. dissertation, Texas A&M University, 2005.

[34] A. J. Krener, "The convergence of the extended kalman filter," in *Directions in mathematical systems theory and optimization*. Springer, 2003, pp. 173–182.

[35] J. L. Crassidis and J. L. Junkins, *Optimal estimation of dynamic systems*. CRC press, 2011.

[36] M. L. Psiaki, R. M. Weisman, and M. K. Jah, "Gaussian mixture approximation of angles-only initial orbit determination likelihood function," *Journal of Guidance, Control, and Dynamics*, pp. 1–13, 2017/09/13 2017. [Online]. Available: https://doi.org/10.2514/1.G002615

[37] K. J. DeMars and M. K. Jah, "Probabilistic initial orbit determination using gaussian mixture models," *Journal of Guidance, Control, and Dynamics*, vol. 36, no. 5, pp. 1324–1335, 2017/09/13 2013. [Online]. Available: https://doi.org/10.2514/1.59844

[38] A. Milani, G. F. Gronchi, M. d. Vitturi, and Z. Knežević, "Orbit determination with very short arcs. i admissible regions," *Celestial Mechanics and Dynamical Astronomy*, vol. 90, no. 1-2, pp. 57–85, 2004.

[39] L. Ansalone and F. Curti, "A genetic algorithm for initial orbit determination from a too short arc optical observation," *Advances in Space Research*, vol. 52, no. 3, pp. 477–489, 2013.

[40] D. A. Vallado and S. S. Carter, "Accurate orbit determination from short-arc dense observational data," *The Journal of the Astronautical Sciences*, vol. 46, no. 2, pp. 195–213, 1998.

[41] A. Milani, G. F. Gronchi, Z. Knežević, M. E. Sansaturio, and O. Arratia, "Orbit determination with very short arcs: Ii. identifications," *Icarus*, vol. 179, no. 2, pp. 350–374, 2005.

[42] J. Sang, J. C. Bennett, and C. Smith, "Experimental results of debris orbit predictions using sparse tracking data from mt. stromlo," *Acta Astronautica*, vol. 102, pp. 258–268, 2014.

[43] D. Farnocchia, G. Tommei, A. Milani, and A. Rossi, "Innovative methods of correlation and orbit determination for space debris," *Celestial Mechanics and Dynamical Astronomy*, vol. 107, no. 1-2, pp. 169–185, 2010.

[44] J. Taylor, *Deep Space Communications*, ser. JPL Deep-Space Communications and Navigation series. John Wiley & Sons, 2016.

[45] L. Barbulescu, J.-P. Watson, L. D. Whitley, and A. E. Howe, "Scheduling space–ground communications for the air force satellite control network," *Journal of Scheduling*, vol. 7, no. 1, pp. 7–34, 2004.

[46] S. Damiani, H. Dreihahn, J. Noll, M. Niézette, and G. P. Calzolari, "A planning and scheduling system to allocate esa ground station network services," in *The Int'l Conference on Automated Planning and Scheduling*, 2007.

[47] G. P. Calzolari, T. Beck, Y. Doat, M. Unal, H. Dreihahn, and M. Niezette, "From the ems concept to operations: First usage of automated planning and scheduling at esoc," in *SpaceOps 2008 Conference*, 2008, p. 3579.

[48] K. Leveque, J. Puig-Suari, and C. Turner, "Global educational network for satellite operations (genso)," in *Proceedings of the AIAA/USU Conf. on Small Satellites*, 2007.

[49] K.-M. Cheung, C. Lee, S. Waldherr, M. Lanucara, B. K. Malphrus, and W. Dove, *Architecture and Concept of Operation of Next-Generation Ground Network for Communications and Tracking of Interplanetary Smallsats*. American Institute of Aeronautics and Astronautics, 2017/10/16 2016. [Online]. Available: https://doi.org/10.2514/6.2016-2401

[50] Y. Nakamura, S. Nakasuka, and Y. Oda, "Low-cost and reliable ground station network to improve operation efficiency for micro/nano-satellites," in *56th International Astronautical Congress*, 2005.

[51] C. Kitts and M. Rasay, "A university-based distributed satellite mission control network for operating professional space missions," *Acta Astronautica*, vol. 120, pp. 229–238, 2016.

[52] M. Schmidt, "Ground station networks for efficient operation of distributed small satellite systems," doctoralthesis, Universität Würzburg, 2011.

[53] A. J. Vazquez and R. S. Erwin, "On the tractability of satellite range scheduling," *Optimization Letters*, vol. 9, no. 2, pp. 311–327, feb 2015.

[54] G. Pandolfi, R. Albi, J. Puglia, Q. Berdal, R. DeGroote, M. Messina, R. Di Battista, M. Emanuelli, D. Chiuri, T. Capitaine *et al.*, "Solution for a ground station network providing a high bandwidth and high accessibility data link for nano and microsatellites," in *67th international astronautical congress (IAC), Guadalajara, Mexico*, 2016.

[55] G. Shirville and B. Klofas, "Genso: A global ground station network," in *AMSAT Symposium*, 2007.

[56] T. Gooley, J. Borsi, and J. Moore, "Automating air force satellite control network (afscn) scheduling," *Mathematical and Computer Modelling: An International Journal*, vol. 24, no. 2, pp. 91–101, 1996.

[57] S. Spangelo, J. Cutler, K. Gilson, and A. Cohn, "Optimization-based scheduling for the single-satellite, multi-ground station communication problem," *Computers & Operations Research*, vol. 57, pp. 1–16, 2015.

[58] J. Castaing, "Scheduling downloads for multi-satellite, multi-ground station missions," *Proceedings of the 28th AIAA Small Satellite Conference*, 2014.

[59] ——, "Scheduling under uncertainty: Applications to aviation, healthcare and aerospace," Ph.D. dissertation, University of Michigan, 2017.

[60] R. Falone and G. Corrao, "Ground station network scheduling through genetic and deterministic combined algorithm," in *2018 SpaceOps Conference*, 2018, p. 2725.

[61] K. Cahoy and A. K. Kennedy, "Initial results from access: An autonomous cubesat constellation scheduling system for earth observation," *Proceedings of the 31st AIAA Small Satellite Conference*, 2017.

[62] X. Jia, T. Lv, F. He, and H. Huang, "Collaborative data downloading by using inter-satellite links in leo satellite networks." *IEEE Trans. Wireless Communications*, vol. 16, no. 3, pp. 1523–1532, 2017.

[63] D. M. Miles, "Advances in fluxgate magnetometry for space physics," Ph.D. dissertation, University of Alberta, 2017.

[64] J. C. Springmann and J. W. Cutler, "Attitude-independent magnetometer calibration with time-varying bias," *Journal of Guidance, Control, and Dynamics*, vol. 35, no. 4, pp. 1080–1088, 2012.

[65] C. C. Foster and G. H. Elkaim, "Extension of a two-step calibration methodology to include nonorthogonal sensor axes," *IEEE Transactions on Aerospace and Electronic Systems*, vol. 44, no. 3, 2008.

[66] H. K. Leinweber, "In-flight calibration of space-borne magnetometers," Ph.D. dissertation, Graz University of Technology, 2012.

[67] E. L. Kepko, K. K. Khurana, M. G. Kivelson, R. C. Elphic, and C. T. Russell, "Accurate determination of magnetic field gradients from four point vector measurements. i. use of natural constraints on vector data obtained from a single spinning spacecraft," *IEEE Transactions on Magnetics*, vol. 32, no. 2, pp. 377–385, 1996.

[68] B. J. Anderson, L. J. Zanetti, D. H. Lohr, J. R. Hayes, M. H. Acuna, C. T. Russell,

and T. Mulligan, "In-flight calibration of the near magnetometer," *IEEE transactions on geoscience and remote sensing*, vol. 39, no. 5, pp. 907–917, 2001.

[69] J. L. Crassidis, K.-L. Lai, and R. R. Harman, "Real-time attitude-independent three-axis magnetometer calibration," *Journal of Guidance control and dynamics*, vol. 28, no. 1, pp. 115–120, 2005.

[70] J. Vasconcelos, G. Elkaim, C. Silvestre, P. Oliveira, and B. Cardeira, "Geometric approach to strapdown magnetometer calibration in sensor frame," *IEEE Transactions on Aerospace and Electronic Systems*, vol. 47, no. 2, pp. 1293–1306, 2011.

[71] R. Alonso and M. D. Shuster, "Complete linear attitude-independent magnetometer calibration," *Journal of the Astronautical Sciences*, vol. 50, no. 4, pp. 477–490, 2002.

[72] K. Bromund, F. Plaschke, R. Strangeway, B. Anderson, B. Huang, W. Magnes, D. Fischer, R. Nakamura, H. Leinweber, C. Russell *et al.*, "In-flight calibration methods for temperature-dependendent offsets in the mms fluxgate magnetometers," in *6th Magnetometer Workshop, Insel Vielm, Germany*, 2017.

[73] J. C. Springmann, A. J. Sloboda, A. T. Klesh, M. W. Bennett, and J. W. Cutler, "The attitude determination system of the rax satellite," *Acta Astronautica*, vol. 75, pp. 120–135, 2012.

[74] M. Mohri, A. Rostamizadeh, and A. Talwalkar, *Foundations of machine learning*. MIT press, 2012.

[75] G. Blanchard, G. Lee, and C. Scott, "Generalizing from several related classification tasks to a new unlabeled sample," in *Advances in Neural Information Processing Systems*, 2011, pp. 2178–2186.

[76] Z. Szabó, B. Sriperumbudur, B. Póczos, and A. Gretton, "Learning theory for distri-

bution regression," *Journal of Machine Learning Research*, vol. 17, no. 152, pp. 1–40, 2016.

[77] J. Baxter, "A model of inductive bias learning," *Journal of Artificial Intelligence Research*, vol. 12, pp. 149–198, 2000.

[78] B. Poczos, A. Singh, A. Rinaldo, and L. Wasserman, "Distribution-free distribution regression," in *Artificial Intelligence and Statistics*, 2013, pp. 507–515.

[79] A. Maurer, "Transfer bounds for linear feature learning," *Machine learning*, vol. 75, no. 3, pp. 327–350, 2009.

[80] A. Pentina and S. Ben-David, "Multi-task and lifelong learning of kernels," in *International Conference on Algorithmic Learning Theory*. Springer, 2015, pp. 194–208.

[81] S. J. Pan, I. W. Tsang, J. T. Kwok, and Q. Yang, "Domain adaptation via transfer component analysis," *IEEE Transactions on Neural Networks*, vol. 22, no. 2, pp. 199–210, 2011.

[82] A. Maurer, M. Pontil, and B. Romera-Paredes, "Sparse coding for multitask and transfer learning," in *Proceedings of the 30th International Conference on Machine Learning (ICML-13)*, 2013, pp. 343–351.

[83] K. Muandet, D. Balduzzi, and B. Schölkopf, "Domain generalization via invariant feature representation," in *Proceedings of the 30th International Conference on Machine Learning (ICML-13)*, 2013, pp. 10–18.

[84] I. Steinwart and A. Christmann, *Support vector machines*. Springer Science & Business Media, 2008.

[85] G. Blanchard, A. A. Deshmukh, U. Dogan, G. Lee, and C. Scott, "Domain generalization by marginal transfer learning," *arXiv preprint arXiv:1711.07910*, 2017.

[86] C. Norton, S. Chien, P. Pingree, D. Rider, J. Bellardo, J. Cutler, and M. Pasciuto, "NasaâĂŹs earth science technology office cubesats for technology maturation," *Proceedings of the AIAA/USU Conf. on Small Satellites*, 2013.

[87] J. W. Cutler, C. Lacy, T. Rose, S.-h. Kang, D. Rider, and C. Norton, "An update on the grifex mission," *Cubesat Developer's Workshop*, 2015.

[88] C. D. Norton, M. P. Pasciuto, P. Pingree, S. Chien, and D. Rider, "Spaceborne flight validation of nasa esto technologies," in *Geoscience and Remote Sensing Symposium (IGARSS), 2012 IEEE International*. IEEE, 2012, pp. 5650–5653.

[89] M. Bkassiny, S. K. Jayaweera, Y. Li, and K. A. Avery, "Blind cyclostationary feature detection based spectrum sensing for autonomous self-learning cognitive radios," in *Communications (ICC), 2012 IEEE International Conference on*. IEEE, 2012, pp. 1507–1511.

[90] W. A. Gardner, W. Brown, and C.-K. Chen, "Spectral correlation of modulated signals: Part ii–digital modulation," *Communications, IEEE Transactions on*, vol. 35, no. 6, pp. 595–601, 1987.

[91] Z. Musielak and B. Quarles, "The three-body problem," *Reports on Progress in Physics*, vol. 77, no. 6, p. 065901, 2014.

[92] H. Poincaré, *Les méthodes nouvelles de la mécanique céleste: Méthodes de MM. Newcomb, Glydén, Lindstedt et Bohlin. 1893*. Gauthier-Villars, 1892, vol. 1,2.

[93] E. Belbruno, *Capture dynamics and chaotic motions in celestial mechanics: With applications to the construction of low energy transfers*. Princeton University Press, 2004.

[94] J. S. Parker and R. L. Anderson, *Low-energy lunar trajectory design*, ser. JPL Deep-Space Communications and Navigation series. John Wiley & Sons, 2014.

[95] A. V. Schaeperkoetter, "A comprehensive comparison between angles-only initial orbit determination techniques," Ph.D. dissertation, Texas A&M University, 2011.

[96] S. Sharma and J. W. Cutler, "Robust orbit determination and classification: A learning theoretic approach," *Interplanetary Network Progress Report*, vol. 203, pp. 1–20, 2015.

[97] W. A. Gardner, "Spectral correlation of modulated signals: Part i–analog modulation," *Communications, IEEE Transactions on*, vol. 35, no. 6, pp. 584–594, 1987.

[98] M. Bkassiny, S. K. Jayaweera, Y. Li, and K. A. Avery, "Wideband spectrum sensing and non-parametric signal classification for autonomous self-learning cognitive radios," *IEEE Transactions on Wireless Communications*, vol. 11, no. 7, pp. 2596–2605, July 2012.

[99] J. Cutler, "Ground station virtualization," in *The fifth international symposium on reducing the cost of spacecraft ground systems and operations, Pasadena*, 2003.

[100] J. H. Yuen, J. Hamkins, and M. K. Simon, *Autonomous software-defined radio receivers for deep space applications*. John Wiley & Sons, 2006, vol. 13.

[101] W. M. Jang, "Blind cyclostationary spectrum sensing in cognitive radios," *ieee communications letters*, vol. 18, no. 3, pp. 393–396, 2014.

[102] W. A. Sutherland, *Introduction to metric and topological spaces*. Oxford University Press, 2009.

[103] S. A. Whitmore and T. Smith, "Launch and deployment analysis for a small, meo, technology demonstration satellite," in *AIAA PAPER 2008-1131, Paper Presented at*

46th AIAA Aerospace Sciences Meeting and Exhibit, 7-10 Jan 2008, Reno, Nevada, 2009.

[104] J. M. Hanson, D. J. Coughlin, G. A. Dukeman, J. A. Mulqueen, and J. W. McCarter, "Ascent, transition, entry, and abort guidance algorithm design for the x-33 vehicle," *AIAA paper*, vol. 4409, p. 1998, 1998.

[105] G. A. Dukeman, "Atmospheric ascent guidance for rocket-powered launch vehicles," *AIAA paper*, vol. 4559, pp. 5–8, 2002.

[106] P. Lu and B. Pan, "Highly constrained optimal launch ascent guidance," *Journal of guidance, control, and dynamics*, vol. 33, no. 2, p. 404, 2010.

[107] U. L. Alliance, "Atlas v launch services userâĂŹs guide," *Lockheed Martin Commercial Launch Services*, 2010.

[108] S. Delavault, P. Legendre, R. Garmier, and B. Revelin, "Improvement of the tle accuracy model based on a gaussian mixture depending on the propagation duration," in *AIAA/AAS Astrodynamics Specialist Conference and Exhibit*, 2008, p. 6772.

[109] P. Auer, N. Cesa-Bianchi, and P. Fischer, "Finite-time analysis of the multiarmed bandit problem," *Machine learning*, vol. 47, no. 2-3, pp. 235–256, 2002.

[110] P. Auer, "Using confidence bounds for exploitation-exploration trade-offs," *Journal of Machine Learning Research*, vol. 3, no. Nov, pp. 397–422, 2002.

[111] P. Auer, N. Cesa-Bianchi, Y. Freund, and R. E. Schapire, "The nonstochastic multi-armed bandit problem," *SIAM journal on computing*, vol. 32, no. 1, pp. 48–77, 2002.

[112] S. Agrawal and N. Goyal, "Analysis of thompson sampling for the multi-armed bandit problem," in *Conference on Learning Theory*, 2012, pp. 39–1.

[113] S. Bubeck, N. Cesa-Bianchi *et al.*, "Regret analysis of stochastic and nonstochastic multi-armed bandit problems," *Foundations and Trends® in Machine Learning*, vol. 5, no. 1, pp. 1–122, 2012.

[114] A. O. Hero and D. Cochran, "Sensor management: Past, present, and future," *IEEE Sensors Journal*, vol. 11, no. 12, pp. 3064–3075, 2011.

[115] D. A. Castanon, "Approximate dynamic programming for sensor management," in *Decision and Control, 1997., Proceedings of the 36th IEEE Conference on*, vol. 2. IEEE, 1997, pp. 1202–1207.

[116] J. Evans and V. Krishnamurthy, "Optimal sensor scheduling for hidden Markov model state estimation," *International Journal of Control*, vol. 74, no. 18, pp. 1737–1742, 2001.

[117] V. Krishnamurthy, "Algorithms for optimal scheduling and management of hidden Markov model sensors," *IEEE Transactions on Signal Processing*, vol. 50, no. 6, pp. 1382–1397, 2002.

[118] E. K. Chong, C. M. Kreucher, and A. O. Hero, "Partially observable Markov decision process approximations for adaptive sensing," *Discrete Event Dynamic Systems*, vol. 19, no. 3, pp. 377–422, 2009.

[119] A. Mahajan and D. Teneketzis, "Multi-armed bandit problems," in *Foundations and Applications of Sensor Management*. Springer, 2008, pp. 121–151.

[120] L. Li, W. Chu, J. Langford, and R. E. Schapire, "A contextual-bandit approach to personalized news article recommendation," in *Proceedings of the 19th international conference on World wide web*. ACM, 2010, pp. 661–670.

[121] Y. Abbasi-Yadkori, D. Pál, and C. Szepesvári, "Improved algorithms for linear stochas-

tic bandits," in *Advances in Neural Information Processing Systems*, 2011, pp. 2312–2320.

[122] V. Gabillon, M. Ghavamzadeh, and A. Lazaric, "Best arm identification: A unified approach to fixed budget and fixed confidence," in *Advances in Neural Information Processing Systems*, 2012, pp. 3212–3220.

[123] K. Jamieson and R. Nowak, "Best-arm identification algorithms for multi-armed bandits in the fixed confidence setting," in *Information Sciences and Systems (CISS), 2014 48th Annual Conference on*. IEEE, 2014, pp. 1–6.

[124] A. Garivier and E. Kaufmann, "Optimal best arm identification with fixed confidence," in *Conference on Learning Theory*, 2016, pp. 998–1027.

[125] A. Carpentier and M. Valko, "Simple regret for infinitely many armed bandits," in *International Conference on Machine Learning*, 2015, pp. 1133–1141.

[126] M. Y. Guan and H. Jiang, "Nonparametric stochastic contextual bandits," in *The 32nd AAAI Conference on Artificial Intelligence*, 2018.

[127] M. Hoffman, B. Shahriari, and N. Freitas, "On correlation and budget constraints in model-based bandit optimization with application to automatic machine learning," in *Artificial Intelligence and Statistics*, 2014, pp. 365–374.

[128] M. Soare, A. Lazaric, and R. Munos, "Best-arm identification in linear bandits," in *Advances in Neural Information Processing Systems*, 2014, pp. 828–836.

[129] P. Libin, T. Verstraeten, D. M. Roijers, J. Grujic, K. Theys, P. Lemey, and A. Nowé, "Bayesian best-arm identification for selecting influenza mitigation strategies," *arXiv preprint arXiv:1711.06299*, 2017.

[130] L. Xu, J. Honda, and M. Sugiyama, "Fully adaptive algorithm for pure exploration in linear bandits," *arXiv preprint arXiv:1710.05552*, 2017.

[131] T. J. Sabaka, L. Tøffner-Clausen, N. Olsen, and C. C. Finlay, "A comprehensive model of earthâĂŹs magnetic field determined from 4 years of swarm satellite observations," *Earth, Planets and Space*, vol. 70, no. 1, p. 130, 2018.

[132] A. Durand, O.-A. Maillard, and J. Pineau, "Streaming kernel regression with provably adaptive mean, variance, and regularization," *arXiv preprint arXiv:1708.00768*, 2017.

[133] M. Valko, N. Korda, R. Munos, I. Flaounas, and N. Cristianini, "Finite-time analysis of kernelised contextual bandits," in *Uncertainty in Artificial Intelligence*. Citeseer, 2013, p. 654.

[134] Y. LeCun, L. Bottou, Y. Bengio, and P. Haffner, "Gradient-based learning applied to document recognition," *Proceedings of the IEEE*, vol. 86, no. 11, pp. 2278–2324, 1998.

[135] J. J. Hull, "A database for handwritten text recognition research," *IEEE Transactions on pattern analysis and machine intelligence*, vol. 16, no. 5, pp. 550–554, 1994.

[136] C.-W. Hsu and C.-J. Lin, "A comparison of methods for multiclass support vector machines," *IEEE transactions on Neural Networks*, vol. 13, no. 2, pp. 415–425, 2002.

[137] J. T. Hwang, D. Y. Lee, J. W. Cutler, and J. R. Martins, "Large-scale multidisciplinary optimization of a small satelliteâĂŹs design and operation," *Journal of Spacecraft and Rockets*, vol. 51, no. 5, pp. 1648–1663, 2014.

[138] J. Bauer, "The origins of non-ideal current-voltage characteristics of silicon solar cells," Ph.D. dissertation, Martin-Luther University Halle-Wittenberg, 2009.

[139] O. Breitenstein, "Understanding the current-voltage characteristics of industrial crystalline silicon solar cells by considering inhomogeneous current distributions," *Opto-*

Electronics Review, vol. 21, no. 3, pp. 259–282, 2013.

[140] S. Maus, M. Rother, C. Stolle, W. Mai, S. Choi, H. Lühr, D. Cooke, and C. Roth, "Third generation of the potsdam magnetic model of the earth (pomme)," *Geochemistry, Geophysics, Geosystems*, vol. 7, no. 7, 2006.

[141] V. I. Arnold, *Mathematical methods of classical mechanics*. Springer Science & Business Media, 2013, vol. 60.

[142] D. D. Holm, *Geometric Mechanics: Part II: Rotating, Translating and Rolling*. World Scientific Publishing Company, 2008.

[143] R. Hermann and A. Krener, "Nonlinear controllability and observability," *IEEE Transactions on automatic control*, vol. 22, no. 5, pp. 728–740, 1977.

[144] P. Billingsley, *Convergence of probability measures*. John Wiley & Sons, 2013.

[145] O. Kallenberg, *Foundations of modern probability*. Springer, 2002.

[146] A. Christmann and I. Steinwart, "Universal kernels on non-standard input spaces," in *Advances in Neural Information Processing Systems*, 2010, pp. 406–414.

[147] I. Steinwart, "On the influence of the kernel on the consistency of support vector machines," *The Journal of Machine Learning Research*, vol. 2, pp. 67–93, 2002.

[148] W. Rudin *et al.*, *Principles of mathematical analysis*. McGraw-Hill New York, 1964, vol. 3.

[149] A. Caponnetto and E. De Vito, "Optimal rates for the regularized least-squares algorithm," *Foundations of Computational Mathematics*, vol. 7, no. 3, pp. 331–368, 2007.

[150] E. De Vito and A. Caponnetto, "Risk bounds for regularized least-squares algorithm with operator-value kernels," Massachusetts Institude of Technology, Cambridge, Technical Report CBCL Paper No.249/AI Memo No.2005-015, May 2005.

[151] Z. Szabó, A. Gretton, B. Póczos, and B. Sriperumbudur, "Two-stage sampled learning theory on distributions," in *AISTATS-Proceedings of the Eighteenth International Conference on Artificial Intelligence and Statistics*, vol. 38, 2015, pp. 948–957.